Rotary-Linear Axes for High Speed Machining

by

Michael Kevin Liebman

A.B., Physics (1996)
Princeton University

S. M., Mechanical Engineering (1998)
Massachusetts Institute of Technology

Submitted to the Department of Mechanical Engineering
in partial fulfillment of the requirements for the degree of

Doctor of Philosophy in Mechanical Engineering

at the

MASSACHUSETTS INSTITUTE OF TECHNOLOGY

September 2001

Author .....
Department of Mechanical Engineering
July 10, 2001

Certified by .....
David L. Trumper
Asssociate Professor of Mechanical Engineering
Thesis Supervisor

Accepted by .....
Ain A. Sonin
Chairman, Departmental Committee on Graduate Students

Rotary-Linear Axes for High Speed Machining

by

Michael Kevin Liebman

Submitted to the Department of Mechanical Engineering
on July 10, 2001, in partial fulfillment of the
requirements for the degree of
Doctor of Philosophy in Mechanical Engineering

Abstract

This thesis presents the design, analysis, fabrication, and control of a rotary-linear axis; this axis is a key subsystem for high speed, 5-axis machine tools intended for fabricating centimeter-scale parts. The rotary-linear axis is a cylinder driven independently in rotation and translation. This hybridization minimizes machine inertias and thereby maximizes accelerations allowing for the production of parts with complex surfaces rapidly and accurately. Such parts might include dental restorations, molds, dies, and turbine blades.

The hybrid rotary and linear motion provides special challenges for precision actuation and sensing. Our prototype rotary-linear axis consists of a central shaft, 3/4 inch (1.91 cm) in diameter and 15 inches (38.10 cm) long, supported by two cylindrical air bearings. The axis has one inch (2.54 cm) of linear travel and unlimited rotary travel. Two frameless permanent magnet motors respectively provide up to 41 N continuous force and 0.45 N·m continuous torque. The rotary motor is composed of commercially available parts; the tubular linear motor is completely custom-built. The prototype axis achieves a linear acceleration of 3 g's and a rotary acceleration of 1,300 rad/s^2. With higher power current amplifiers and reduced sensor inertia, we predict the axis could attain peak accelerations of 12 g's and 17,500 rad/s^2 at low duty cycles.

This thesis also examines several concepts for developing a precision rotary-linear sensor that can tolerate axial translation. Our prototype rotary sensor uses two laser interferometers to measure the orientation of a slightly tilted mirror attached to the shaft. A third interferometer measures shaft translation. The rotary axis has a control bandwidth of 40 Hz; the linear axis has a bandwidth of 70 Hz. The rotary-linear axis has 2.5 nm rms linear positioning noise and 3.1 μrad rms rotary positioning noise.

This thesis presents one novel 5-axis machine topology which uses two rotary-linear axes. The first axis rotates and translates the part. The second axis carries the cutting tool and provides high speed spindle rotation as well as infeed along the axis of rotation. For use as a spindle, precision rotary sensing is not required, and a sensorless control scheme based on motor currents and voltages can be used.

Thesis Supervisor: David L. Trumper
Title: Asssociate Professor of Mechanical Engineering

Acknowledgments

I am extremely fortunate to have been able to work with so many fantastic people during the course of this research. I am most grateful to Professor David Trumper, my advisor for the past 5 years, for teaching me most of what I know about electromagnetics, controls, and design. He has been a constant source of inspiration and a great role model. He is also one of the most brilliant people I have ever met. I am particularly honored to be the first Doctoral student to graduate from his lab since he received tenure.

I thank my thesis committee for their help throughout this research and for teaching some of the best classes I have taken. Professor Sanjay Sarma was especially helpful in teaching me about toolpaths and machine topologies. His math class on random, cool topics introduced me to many interesting phenomena. Professor Jeffrey Lang helped me with several motor design issues and with implementing sensorless control. I thoroughly enjoyed his electromagnetics class with extremely clear lectures illustrated with colored chalk and containing a series of excellent demos. Professor Alex Slocum is a great resource who always has new ideas. His precision machine course and book have helped me in numerous ways over the last five years.

I am glad I had a chance to work with Marsette Vona, a Master's student, over the past year and a half. Marsette did a fantastic job designing and fabricating the sensor and making it work. He also built a custom link between the laser axis cards and the dSPACE board. Moreover, he was a sounding board for all aspects of the project and provided numerous valuable suggestions. I thank him for all his hard work on the project and will miss working with him.

Several people suggested and helped us develop various optical sensors. I thank Dr. Carl Zanoni, Vice President of R & D at Zygo Corporation, for suggesting the helicoid sensor concept to us. I also thank Dr. William Plummer, Director of Optical Engineering at Polaroid, and Donald Combs, Douglas Goodman, and Jeffrey Roblee, all of Polaroid, for meeting with us several times to discuss the possibility of fabricating the helicoid mirror. I thank Professor George Barbastathis in the Mechanical

Engineering Dept. at MIT for his help with various optical sensor concepts. Also, I thank Professor John Ziegert in the Mechanical Engineering Dept. at the University of Florida for suggesting the half-wave plate sensor concept to us.

During my five years in the Precision Motion Control Lab, I have had the pleasure of working with a fantastic group of graduate students. I have learned a tremendous amount from them and they have each helped me in some aspect of this work. In the early days, Won-jong Kim taught me about motor design and analysis. Pradeep Subrahmanyan and I discussed all sorts of things, and he taught me a great deal about controls. Paul Konkola was always ready to kick around new ideas as well. Steve Ludwick, David Ma, David Chargin, and Joe Calzaretta were always eager to show me the latest fast tool servo work and were valuable resources. I thank Katie Lilienkamp for her dynamic signal analyzer software which is incredibly useful. Ming-chih Weng was always ready to talk about electromagnetics. When he left, I turned to Xiaodong Lu, who also taught me about flexible modes. When I needed some practical advice on how to build something, I turned to Marten Byl. Rick Montesanti was another mechanical whiz who gave me many ideas. I have also enjoyed working along side Robin Ritter, Claudio Salvatore, Amar Kendale, and Andrew Stein.

I thank David Rodriguera and Maureen Lynch for their help ordering equipment and avoiding the MIT bureaucracy. I thank Gerry Wentworth, Mark Belanger, and Bob Kane for their assistance in the machine shop.

I thank my parents and sister for all their encouragement, love, and support.

Finally, I thank Coach Kandiah, my boxing coach, for training me for five years. Boxing helped me survive this long journey. I also thank all the MIT Boxing Club members whom I've had the pleasure of training with over the years.

This research was funded by NSF grant award number DMI-0084981, "Rotary-Linear Hybrid Axes for Meso-scale Machining," and the Charles E. Reed Faculty Initiatives Fund.

For Mom, Dad, and Judith

Contents

List of Figures

List of Tables

Chapter 1

Introduction

1.1 Background

This thesis describes the development of a rotary-linear axis for use as a key component in high-speed, 5-axis machine tools. We particularly focus on machine tools intended for fabricating centimeter-scale parts. This research was motivated by the desire to build a 5-axis machine tool for grinding customized dental restorations. Today, most dental restorations are manually fabricated by skilled technicians in a dental laboratory. If a machine existed which could automatically grind dental restorations

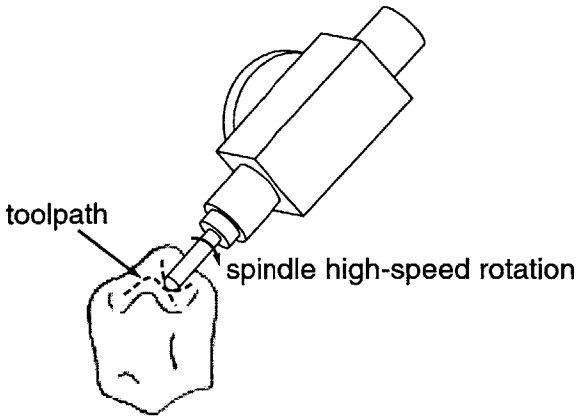

Figure 1-1: A 5-axis machine for grinding dental restorations requires high accelerations so that the spindle can rapidly traverse toolpaths on the complex occlusal surface of the dental restoration.

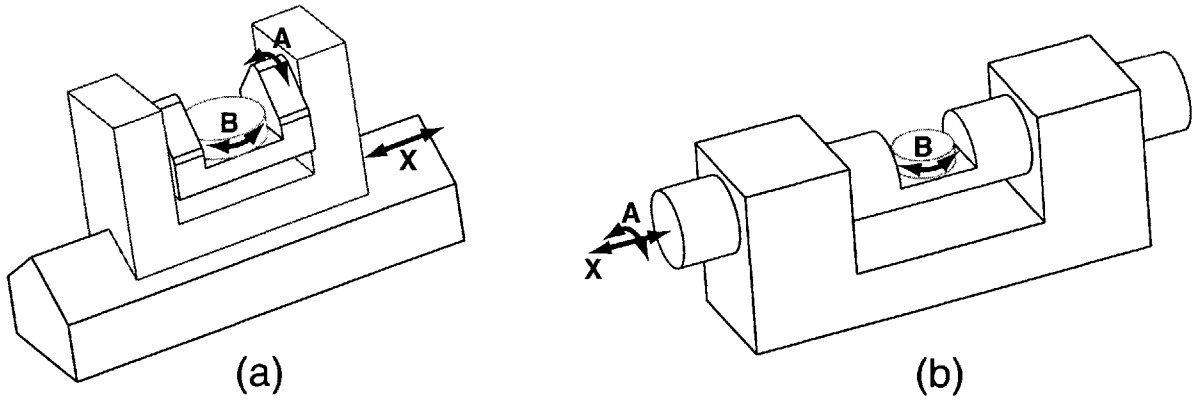

Figure 1-2: (a) Conventional stacked axis arrangement with a rotary table (B) stacked on a trunnion (A) stacked on an X-axis. (b) Rotary-linear (A-X) axis with a rotary table (B). Figure drawn by Marsette Vona.

from ceramic blanks, it would revolutionize dentistry by eliminating the high costs of manual fabrication. Such a machine needs 5 axes of motion to generate the complex shape of teeth, and it needs to obtain shape accuracies of 20 μm. Existing 5-axis machine tools are too big, slow, and expensive for this task. They cannot achieve the high feedrates required for fabrication in acceptable cycle times.

Thus, this research began by examining how best to design machine tools optimized for high-speed machining of centimeter-scale parts. In particular, we wanted to develop a machine which allows a spindle to follow complex toolpaths on a small part at high feedrates as depicted in Figure 1-1. We found that the key to being able to follow complex toolpaths at high feedrates is having high accelerations in multiple axes. This is because as the part and feature sizes shrink, changes in the cutting tool's velocity must occur over shorter distances. Furthermore, higher rotary accelerations are required to follow toolpaths with smaller radii at the same feedrates. Existing 5-axis machines have extremely slow rotary accelerations. Thus, machining of centimeter-scale parts with complex surfaces, requires higher rotary and linear accelerations than can be achieved on existing 5-axis machines.

Typically machine tools have axes stacked on top of each other, as shown in Figure 1-2 (a). In this situation the bottom axis must accelerate the mass of all the axes and actuators further up the kinematic chain. Thus, bottom axes tend to have

low accelerations. These low acceleration axes can limit the attainable feedrates and lengthen production times of small parts with complex surfaces. One way to achieve high accelerations in two axes is with a hybrid axis consisting of one moving part driven in two axes: the rotary-linear axis consists of a cylinder driven independently in rotation and translation as shown schematically in Figure 1-2 (b). We sometimes refer to this hybrid rotary-linear axis as a z-θ axis where z represents the linear degree of freedom and θ represents the rotary degree of freedom. Since the same moving part provides both degrees of freedom, we have eliminated the need to stack these two axes. Even though there may be some stacking of axes elsewhere in the 5-axis machine tool, we have eliminated one level in the kinematic chain. This improvement allows significantly higher accelerations than would otherwise be possible.

1.2 Thesis Overview

1.2.1 z-θ Horizontal Trunnion Machine Tool

We have invented a 5-axis machine topology which we envision will have higher accelerations, control bandwidths, and accuracies than are currently possible. This improved performance is achieved by using two hybrid rotary-linear axes, each of which eliminates one level of stacking from the machine's kinematic chain. The envisioned machine topology, shown in Figure 1-3, is named the *z-θ horizontal trunnion machine tool topology* since it is kinematically similar to existing horizontal spindle 5-axis machine tools with trunnions. In these conventional machines, the workpiece sits on a 360° rotary table, B, mounted on a trunnion, A, which slides on an X-axis as shown in Figure 1-2 (a). The horizontal spindle is mounted to a vertical slideway, Y, riding up and down a moving column that provides infeed motion, Z.

The *z-θ horizontal trunnion machine tool topology* combines the conventional trunnion, A, and conventional linear axis, X, into a rotary-linear axis, A-X. Furthermore, it eliminates the moving column, Z, by combining this infeed motion with the high speed spindle rotation using a second rotary-linear axis. The spindle is still mounted

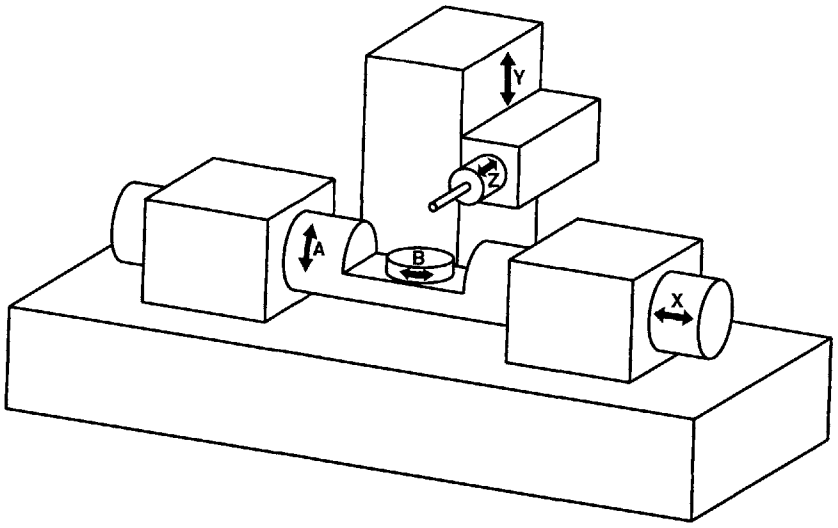

Figure 1-3: Envisioned z-θ horizontal trunnion 5-axis machine tool topology. The A-X rotary-linear axis allows us to achieve high accelerations in the A- and X-axes. The high speed rotation of the spindle and infeed, Z, are combined into a rotary-linear axis as well. The spindle moves up and down a fixed column on a conventional Y-axis linear slideway. The B-axis is envisioned as a small indexing head which provides a fifth axis with minimal inertia.

on a conventional vertical slideway, Y, riding up and down a fixed column. The conventional rotary table, B, is replaced by a small indexing rotary axis, B. By indexing this fifth axis, we lighten the A-X rotary-linear axis and thereby allow for higher accelerations in the A- and X-axes.

In this thesis we design, build, and test a prototype of the A-X rotary-linear axis of the *z-θ horizontal trunnion machine tool* shown in Figure 1-3. This axis carries the centimeter-scale part. The axis must have high rotary and linear accelerations to achieve high feedrates as well as high resolution rotary and linear sensing to achieve high shape accuracies. We use a second rotary-linear axis as a high speed spindle combined with infeed motion, Z. This application requires high rotary speed but only low resolution rotary sensing. In fact, it is possible to eliminate the rotary sensor in this spindle application and use a sensorless observer based on motor currents and voltages to commutate the rotary motor. We investigate this sensorless operation with our prototype rotary-linear axis even though this prototype is not intended for use as a spindle.

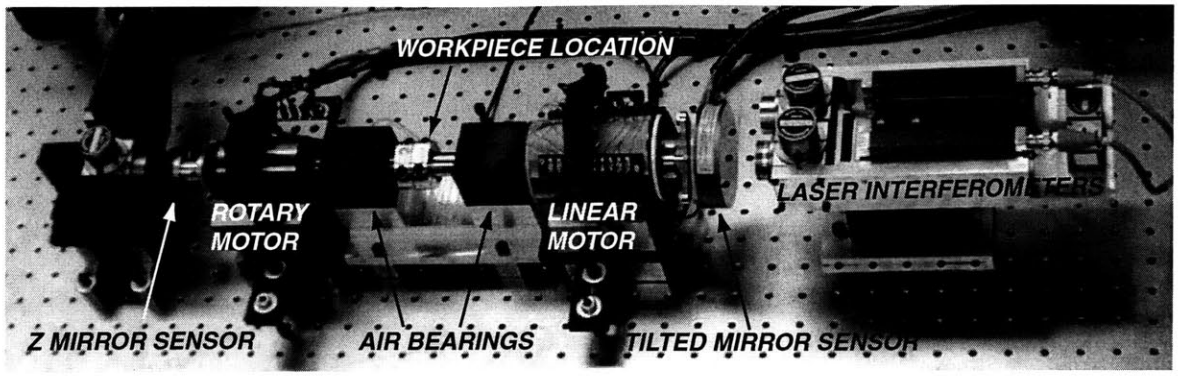

Figure 1-4: The prototype z-θ axis consists of a central shaft riding in two cylindrical air bearings. The frameless rotary motor on the left made from commercially available parts generates torque; the custom-built tubular linear motor on the right generates force. On the far left is a 1 inch (2.54 cm) diameter mirror for z measurement, and on the far right is a 3 inch (7.62 cm) diameter, slightly tilted mirror for θ measurement.

1.2.2 Prototype z-θ Axis

Our prototype rotary-linear axis is shown in Figure 1-4. It consists of a 3/4 inch (1.91 cm) diameter, 15.23 inches (38.68 cm) long stainless steel shaft supported by two cylindrical air bearings. The axis has one inch (2.54 cm) of linear travel and unlimited rotary travel. On the left side of the shaft, a frameless, permanent magnet rotary motor generates torque; on the right side of the shaft, a frameless, tubular, permanent magnet linear motor generates force. A laser interferometer on the far left measures axial distance, z, to a 1 inch (2.54 cm) diameter mirror mounted to the shaft. Two laser interferometers on the far right measure the orientation of a 3 inch (7.62 cm) diameter, slightly tilted mirror mounted to the shaft. Since this mirror rotates with the shaft, determining its orientation allows us to calculate the shaft's rotation angle θ.

The shaft geometry and assembled components are shown in Figure 1-5. The permanent magnet rotors of the rotary and linear motors are shorter than their stators so that the axis can translate axially without losing motor force. The magnetic rotors and mirror mounts are axially clamped to shoulders in the shaft. Thus, the components attached to the shaft can be disassembled and used on future prototypes.

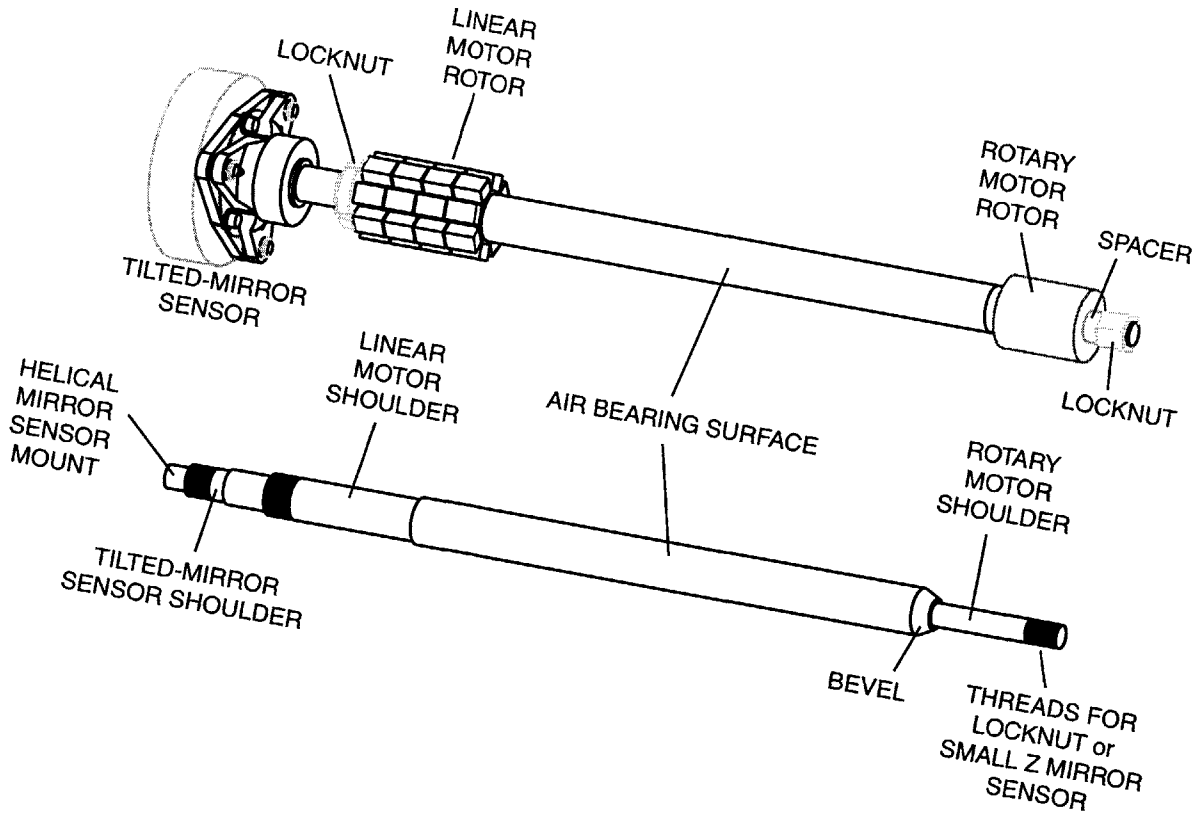

Figure 1-5: Shaft geometry and assembled components. The shaft is 0.75 inches (1.91 cm) in diameter in the center and 15.23 inches (38.68 cm) long.

	MASS	*ROTARY INERTIA*
Shaft	0.86 kg	3.9×10^{-5} kg·m^2
Linear Motor Magnets	0.23 kg	3.3×10^{-5} kg·m^2
Rotary Motor Magnets	0.06 kg	1.7×10^{-5} kg·m^2
Tilted-Mirror Sensor	0.29 kg	25.1×10^{-5} kg·m^2
Total	1.44 kg	34.0×10^{-5} kg·m^2

Table 1.1: Masses and rotary inertias of the shaft and attached elements shown in Figure 1-5.

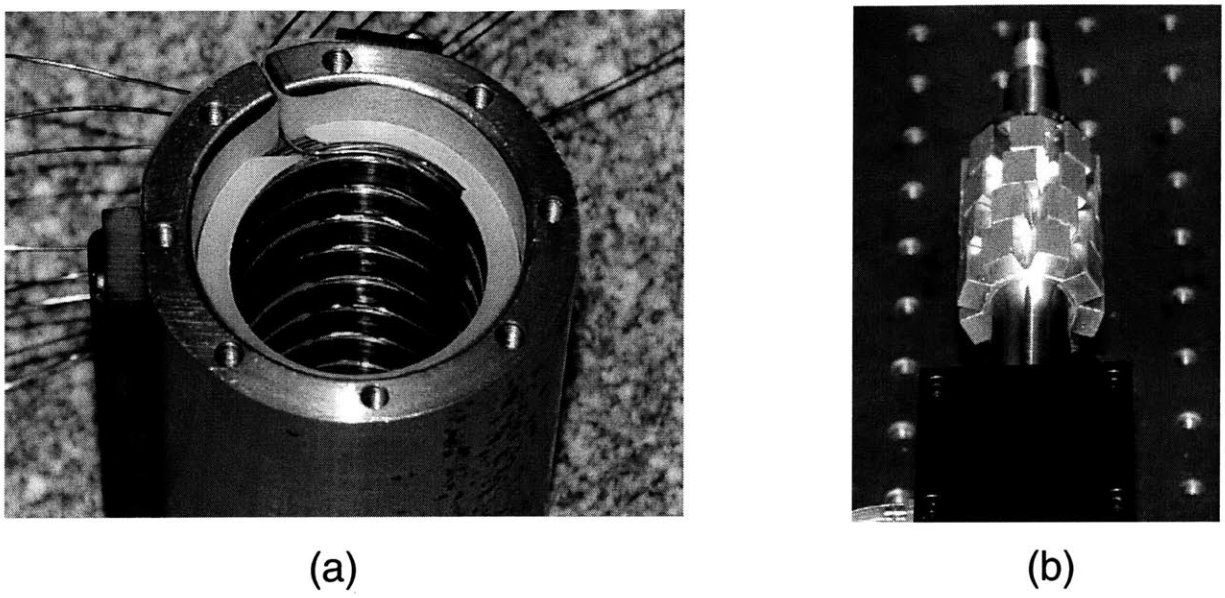

Figure 1-6: Custom-built tubular linear motor: (a) Stator consisting of ring coils separated by nylon inserts. The coil leads are routed through a slot in the back iron. (b) Magnetic Rotor consisting of four octagonal magnet rings each made of eight rectangular Neodymium Iron Boron (NdFeB) magnets.

If a permanent mounting method were used, the air bearings would be captured by the rotors, and the axis could not be disassembled. All components are designed for minimum mass and rotary inertia. The masses and rotary inertias of the shaft and its components are listed in Table 1.1. Note that the tilted-mirror sensor has almost three times the rotary inertia of the rest of the axis, and thus this component dominates the dynamics of the shaft in rotation. This sensor allows us to control and test our prototype axis. However, we expect future rotary-linear axes to use a different sensor such as a 2-D encoder with a much lower rotary inertia.

1.2.3 z-θ Motor

The z-θ motor consists of two separate motors—a rotary motor and a tubular linear motor. The rotary motor is composed of commercially available parts; the tubular linear motor shown in Figure 1-6 is completely custom-built. A continuum electromechanical analysis is used to optimize the linear motor's magnetic pitch length, coil

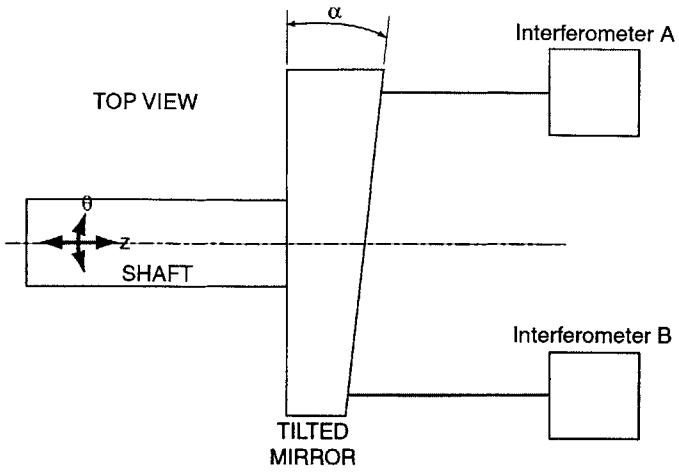

Figure 1-7: Tilted-mirror sensor schematic. The shaft's rotation angle θ is sensed by measuring the distance in two places to a slightly tilted mirror. The maximum mirror tilt is $\alpha = 4.7$ mrad.

thickness, and magnet thickness for high linear and rotary accelerations. The linear motor affects rotary accelerations since its magnet array adds inertia to the axis. For the rotary motor, we bought two frameless rotary motors of different lengths and combined the shorter rotor with the longer stator. Our power amplifiers can only provide 3 A continuous phase currents without overheating. At these current levels, we can produce a continuous linear force of 40.5 N and a continuous rotary torque of 0.45 N·m. This results in 2.9 g's of linear acceleration and 1320 rad/s^2 of rotary acceleration for our axis. At these current levels, the linear motor dissipates 43 W, and the rotary motor dissipates 92 W. These are sustainable power dissipation levels. Since the rotary motor dissipates approximately twice the power of the linear motor, it becomes hotter than the linear motor at these power dissipation levels.

1.2.4 z-θ Sensor

Marsette Vona worked closely with the author on the sensor design for the z-θ axis. He designed and built the prototype sensor and investigated several alternative sensors as part of his Master's thesis, *Metrology Techniques for Compound Rotary-Linear Motion* [70]. We use laser interferometry to measure axis translation; this measure-

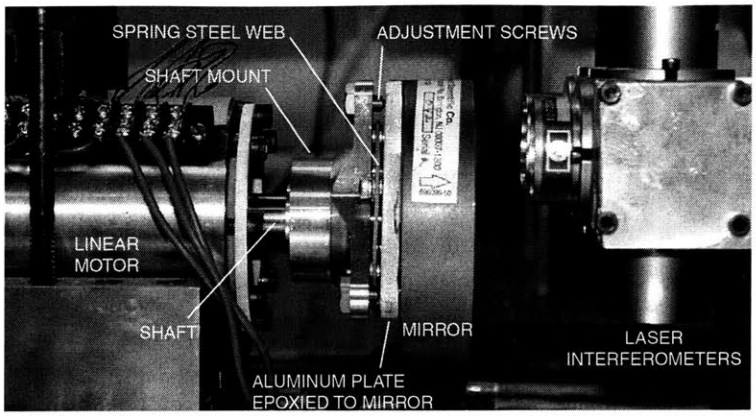

Figure 1-8: Prototype tilted-mirror sensor mounted on the z-θ axis. The sensor is mounted to a wobble plate so we can experiment with changing the mirror tilt angle.

ment is insensitive to rotation provided the mirror is adjusted perpendicular to the rotation axis. Finding a rotary sensor that can tolerate axial translation is, however, much more challenging. We examined several novel interferometric rotary sensors and implemented the tilted-mirror sensor shown schematically in Figure 1-7. The shaft's rotation angle θ is sensed by measuring distance to the slightly tilted mirror in two places. By measuring these distances, we can determine the mirror's orientation and therefore the shaft's rotation angle θ. Figure 1-8 shows a picture of our prototype tilted-mirror sensor integrated into the z-θ axis. This sensor provides an absolute angle measurement even though the laser interferometers provide only relative distance measurements. We can adjust the mirror's tilt angle α and found it can be as large as 4.7 mrad which results in a sensor resolution of 1,366,000 counts/rev or 4.6 μrad. This angular resolution corresponds to a linear resolution of 0.046 μm at a 1 cm radius from the rotation axis. The experimentally observed sensor random noise when the controller and air bearings are turned off is 2.6 μrad rms. We also developed an automatic calibration routine that measures the mirror's tilt angle and the location of the two interferometers each time the axis is turned on.

1.2.5 Prototype Axis Specifications

The prototype z-θ axis specifications are summarized in Table 1.2. The axis has 2.54 cm of linear travel and unlimited rotary travel. Its mass is 1.44 kg, and its rotary inertia is 34.0×10^{-5} kg·m^2. The linear axis has a control bandwidth of 70 Hz and has 2.5 nm rms linear positioning noise; the rotary axis has a control bandwidth of 40 Hz and has 3.1 μrad rms rotary positioning noise.

Parameter	*Specification*
Linear Travel	2.54 cm
z-θ Axis Mass	1.44 kg
Linear Motor Force Constant	13.5 N/A$_{peak}$
Linear Motor Constant	6.2 N/$\sqrt{\text{W}}$
Max Continuous Current	3 A$_{peak}$
Max Continuous Force	40.5 N
Max Linear Acceleration	2.9 g
Linear Sensor Resolution	0.625 nm
Linear Axis Closed-Loop Bandwidth	70 Hz
Linear Positioning Noise	2.5 nm rms
Rotary Travel	360° (unlimited)
z-θ Axis Inertia	34.0×10^{-5} kg·m^2
Rotary Motor Force Constant	0.15 N·m/A$_{peak}$
Rotary Motor Constant	0.047 N·m/$\sqrt{\text{W}}$
Max Continuous Current	3 A$_{peak}$
Max Continuous Torque	0.45 N·m
Max Rotary Acceleration	1320 rad/s^2
Rotary Sensor Resolution	4.6 μrad (1,366,000 counts/rev)
Rotary Axis Closed-Loop Bandwidth	40 Hz
Rotary Positioning Noise	3.1 μrad rms

Table 1.2: z-θ prototype specifications.

1.2.6 z-θ Axis Ultimate Performance Specifications

With two changes to our prototype axis—higher power current amplifiers and a different rotary sensor—we could achieve much higher accelerations:

- Our current amplifiers are thermally limited to about 3 A continuous current.

For safety, we do not allow higher currents, even for short time periods. The rotary motor is rated for up to 10.4 A of peak current; the linear motor can withstand similar peak currents. Thus, upgrading to higher power amplifiers would increase our peak force, torque, and acceleration levels by a factor of about 3. These extremely high peak accelerations can only be used at low duty cycles or the motors will overheat. Even at low duty cycles, high peak accelerations can improve machine tool performance significantly. They allow target feedrates to be reached in much shorter distances. They also enable the tool to follow toolpaths with smaller radii at higher feedrates.

- The tilted-mirror sensor works well and allows us to control the prototype axis. However, since its rotary inertia dominates that of the rest of the axis, we expect to use a different sensor in the future. A likely candidate is a 2-D encoder sensor which uses a 2-D encoder grid of negligible mass and rotary inertia. Replacing the tilted-mirror sensor with one of negligible mass and inertia eliminates 20% of the axis mass and *74%* of the axis inertia.

After making these changes, the z-θ axis could achieve peak linear accelerations of 11.7 g and peak rotary accelerations of 17,530 rad/s^2 for short time periods. The improved performance specifications are summarized in Table 1.3.

Parameter	*Specification*
Linear Travel	2.54 cm
z-θ Axis Mass	1.15 kg
Linear Motor Force Constant	13.5 N/A_{peak}
Linear Motor Constant	6.2 $N/\sqrt{W}$
Max Continuous Current	3 A_{peak}
Peak Current	10 A_{peak}
Max Continuous Force	40.5 N
Peak Force	135 N
Max Continuous Linear Acceleration	3.6 g
Peak Linear Acceleration	11.7 g
Linear Sensor Resolution	0.625 nm
Linear Axis Closed-Loop Bandwidth	120 Hz
Rotary Travel	360° (unlimited)
z-θ Axis Inertia	8.9×10^{-5} kg·m^2
Rotary Motor Force Constant	0.15 N·m/A_{peak}
Rotary Motor Constant	0.047 N·m/$\sqrt{W}$
Max Continuous Current	3 A_{peak}
Peak Current	10.4 A_{peak}
Max Continuous Torque	0.45 N·m
Peak Torque	1.56 N·m
Max Continuous Rotary Acceleration	5060 rad/s^2
Peak Rotary Acceleration	17,530 rad/s^2
Rotary Sensor Resolution	10 μrad
Rotary Axis Closed-Loop Bandwidth	120 Hz

Table 1.3: z-θ ultimate performance specifications. These specifications require higher power current amplifiers and a sensor with negligible mass and inertia such as a 2-D encoder.

1.3 Thesis Contributions

The main contribution of this thesis is the development of a rotary-linear axis for use as a key component in high-speed, 5-axis machine tools intended for fabricating centimeter-scale parts. We present design, analysis, fabrication, and control techniques for this axis. We envision that this axis can be used in novel 5-axis grinding machines to fabricate dental restorations and other such parts. This could change fabrication of dental restorations from a manual skilled art to a precise, fast, computer numerically controlled (CNC) process. Specific thesis contributions are listed below:

- Developed the rotary-linear axis as a key machine tool component especially suited for high-speed, multi-axis machine tools for fabricating centimeter-scale parts. (Chapter 2)
- Designed, analyzed (Chapters 4 & 5) and fabricated (Chapter 6) the prototype rotary-linear axis.
- Designed, fabricated, and tested a rotary-linear motor which includes a custom-built tubular-linear motor. (Chapters 4 & 6)
- Developed a continuum electromechanical analysis for permanent magnet synchronous motors with iron backing. (Appendix A)
- Developed a permanent magnet motor design procedure based on this motor analysis. This procedure explains how to optimize motor pitch length, coil thickness, magnet thickness, and air gap for maximum rotary and linear accelerations. (Chapter 4)
- Developed an analysis to compare permanent magnet and induction motors to allow selection for our application. (Section 3.2.1; Appendix B)
- Invented a 5-axis machine tool topology optimized for centimeter-scale parts that allows for accurate, high-speed machining. (Chapter 2)

- Investigated interferometric and other rotary sensor designs that can tolerate axial translation. (Chapter 5; section 3.4)
- Invented and tested a tilted-mirror interferometric rotary sensor that tolerates axial translation and integrated it into the prototype axis. (Chapters 5 & 9; section 6.4)
- Developed a controller for the rotary-linear axis. (Chapters 8 & 9)
- Developed a classification of 5-axis machine tool topologies based on their rotating axes. (Section 2.3)
- Wrote a comprehensive tutorial on field-oriented control of permanent magnet motors. (Chapter 7)
- Integrated across the mechanical, electrical, and control engineering disciplines to combine the z-θ motor and z-θ sensor into a clean, well-modeled structure that allows for accurate control. (Chapters 6 & 8)

1.4 Thesis Organization

Chapter 2, Five-Axis Machine Tools, explains why 5-axis machines are needed and reviews existing designs. We classify existing 5-axis machine tools into five categories based on their rotary axes: There are two classes of rotating spindle machines, two classes of rotating part machines, and one class in which both spindle and part rotate. We then look at some new 5-axis machine concepts that incorporate rotary-linear axes. The rest of the thesis focuses on the rotary-linear axis itself.

Chapter 3, Rotary-Linear Motion, begins by reviewing existing z-θ stage designs. We critique the actuators, sensors, and overall integration of these varied designs, and point out the many challenges inherent in building rotary-linear stages. Next we consider possible motor, bearing, and sensor concepts for our stage. We present an analysis showing that in our force range permanent magnet motors are more power

efficient than induction motors. We also present several concepts for rotary sensors that allow axial movement.

Chapter 4, Rotary-Linear Motor Design & Analysis, starts off by developing simple motor scaling laws for achieving high accelerations. We then summarize the results of the continuum electromechanical analysis of permanent magnet motors provided in Appendix A. Using the results of this analysis, we show how to optimize motor parameters such as pitch length, coil thickness, air gap, and magnet thickness for achieving high rotary and linear accelerations. We measure the linear motor force constant with a load cell and measure the rotary motor force constant via its back electromotive force (EMF).

Chapter 5, Tilted-Mirror Sensor Design, explains how the tilted-mirror sensor works. We first provide a simple analysis of an ideal sensor and then provide a complete analysis to handle the complications of the practical implementation.

Chapter 6, Prototype z-θ Axis, describes the fabrication of the prototype axis. We look at the shaft design and how the motors and sensors attach to it. We also look at the construction of the sensor mirror mounts. The second half of this chapter describes the complete fabrication of the custom-built tubular linear motor. We show how high-strength magnets are assembled to form the magnetic rotor and how the stator is designed and built.

Chapter 7, Field Orientation Principle, is a tutorial on the dq transformations used to simplify AC motor control. It starts off by reviewing DC motor modeling and control. The remainder of the chapter focuses on the 3-phase permanent magnet motor. We show how to model this motor in the 3-phase abc frame and how to transform the model to a frame moving with the rotor, the dq frame. We show that in the dq frame, motor torque is proportional to q-axis current so that the 3-phase motor is as easy to control as a DC motor.

Chapter 8, Control System, describes the modeling and compensation of the rotary and linear axes and shows closed-loop step responses and Bode plots of the final controller designs. This chapter also describes the design of analog power amplifier circuits used to provide motor phase currents and the implementation of a sensorless

observer for the rotary axis.

Chapter 9, Control Implementation, describes how the control system is implemented on the digital signal processor (DSP). We explain how we built up the control code from initial motor testing through the final control scheme. We describe the top-level finite state controller used to sequence events and respond to events. We also look at motor control, sensor processing, an automatic sensor calibration routine, and sensorless processing.

Chapter 10, Conclusions & Suggestions for Future Work, describes several paths for continuing the research on the rotary-linear axis and its integration into a small 5-axis machine tool.

Appendix A, Continuum Electromechanical Analysis of Permanent Magnet Synchronous Linear Motor with Iron Backing, presents this detailed analysis. The results of this analysis are used in Chapter 4 to optimize the linear motor design.

Appendix B, Induction Motor Optimization, shows how to select the power optimal rotor slip speed and rotor thickness for an induction motor. This analysis is used to compare permanent magnet motors and induction motors in Chapter 3.

Appendix C, Magnetic Circuit Analysis Approximation of Magnetic Fields, derives a convenient approximation for magnetic fields due to permanent magnets. It can be used to estimate magnetic fields in iron-backed motors.

Appendix D, Mechanical Drawings, contains detailed mechanical drawings of the shaft, machine base, and linear motor parts.

Appendix E, Electrical Schematics, lists electrical connections between the motors, the power amplifiers, and the DSP board.

Appendix F, Vendors, lists key vendors who provided parts for the prototype axis.

Chapter 2

Five-Axis Machine Tools

Our research began with the desire to design a five-axis machine tool optimized for centimeter-scale parts. This chapter starts off by describing why five-axis machine tools are needed and by giving some example applications. Next, we survey and classify existing five-axis machine tool topologies. We will see that existing machine topologies do not readily scale down for the production of centimeter-scale parts. We also look at toolpath generation and see how the need for high accelerations drives the design of a machine topology optimized for small parts. In particular, we develop the idea of a hybrid axis to minimize machine inertias and maximize accelerations. We show several new machine topologies incorporating such a hybrid axis. The chapter ends with a discussion of the machine topology we think is the best candidate, which incorporates two hybrid rotary-linear axes—one to provide rotary and linear motion of the part, the other to provide high speed rotation of the spindle and infeed.

2.1 Introduction

An ordinary vertical milling machine is a three-axis machine tool. The table holding the workpiece can be moved in three linear axes, X, Y, and Z, relative to the milling spindle as shown in Figure 2-1 (a). By convention the z-axis is aligned with the spindle's rotation axis, which is the vertical axis in this instance. The spindle's high-speed rotation is not counted as one of the machine tool's axes.

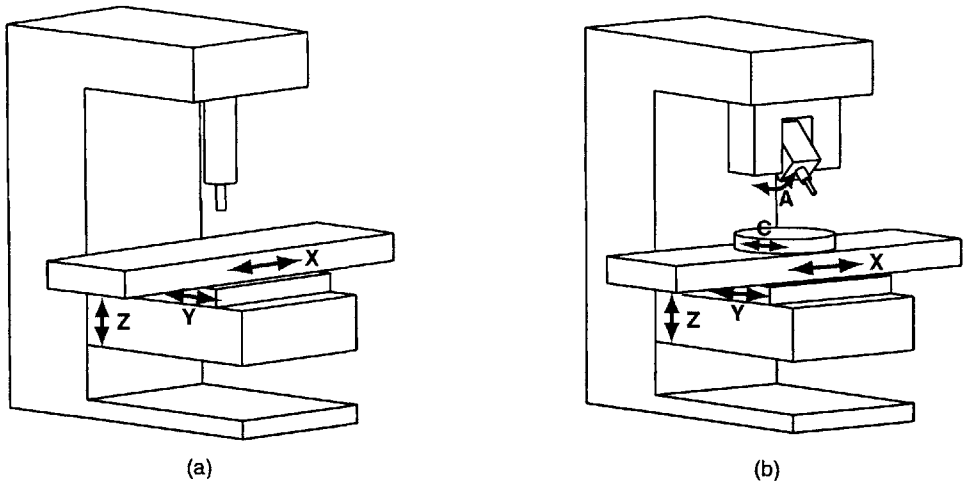

Figure 2-1: Two examples of milling machines: (a) vertical 3-axis machine (b) vertical 5-axis machine with swiveling spindle (A) and rotating part (C).

A five-axis machine tool has five degrees of freedom—three linear and two rotary. An ordinary vertical 3-axis milling machine can be turned into a five-axis milling machine by adding two rotary degrees of freedom. For example, Figure 2-1 (b) shows a five-axis milling machine with a swiveling spindle (A), and a rotating part (C).

Five-axis machine tools have much more capability than three-axis machine tools. They can machine complex parts with sculptured surfaces with fewer passes and with better surface finishes than three-axis machines. This is because the spindle's angle relative to the workpiece can be adjusted to match curvatures in the part. Additionally, changing the spindle's angle allows different surfaces of the tool to engage in machining so that the tool does not wear out in one spot. For example, a ball end mill has zero velocity at its tip so machining with an inclined ball end mill produces a better surface finish and reduces cutting forces. An inclined spindle also provides better access to cavities so that shorter, stiffer, standard tools can be used compared to the specialized tools needed to do the job on a three-axis machine. Five-axis machines can also machine complex features such as undercuts and angled holes, which cannot be made on three-axis machines. Another benefit is that the part can be machined with fewer re-fixturings since a five-axis machine can access five sides of the part in a single setup.

2.2 Applications

2.2.1 Fabricating Customized Dental Restorations

The main application for our research is to develop a high-speed machine tool for automatically fabricating customized dental restorations. This machine tool could revolutionize dentistry by allowing dentists to rapidly fabricate restorations in their office. Automatic fabrication will significantly reduce the cost of dental restorations, improve their quality, and make the experience much more efficient and comfortable for the patient. Since the restorations no longer need to be manually fabricated by skilled technicians in a dental laboratory, the restoration can be accomplished in one appointment, without the need for temporary restorations.

Today, most dental restorations are produced using the lost-wax or investment casting method. This method requires that the patient make two visits to the dentist. During the first visit, the dentist prepares the problematic tooth, takes impressions of the patient's teeth, and places a temporary restoration on the prepared tooth. He then sends the impressions to a dental laboratory where a dental technician builds a model of the patient's teeth by pouring plaster into the impressions. The technician carves a wax model of the replacement tooth such that it fits with the neighboring and occluding teeth. This wax model is then invested to form a mold, the wax is melted out, and the restoration metal is cast in the cavity vacated by the wax. Typically, the technician spends 9 hours making a restoration with the lost-wax method. After 1–2 weeks, the dentist receives the fabricated restoration, and the patient returns for a second visit. The temporary restoration is removed, and the permanent restoration is bonded to the patient's tooth.

Computer-Aided Design and Manufacturing (CAD/CAM) of dental restorations is an alternative to the lost-wax method which promises production of dental restorations in under an hour. In the envisioned CAD/CAM system, the dentist uses optical techniques to obtain a computer model of the patient's teeth. Next, a Computer-Aided Design (CAD) program creates a computer model of the restoration using a database of ideal teeth and the computer model of the patient's teeth. A CAM pro-

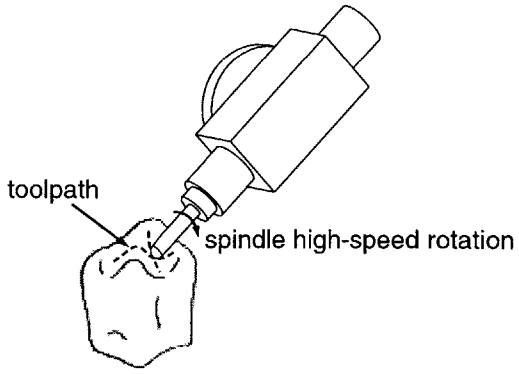

Figure 2-2: A 5-axis grinding machine must be designed so that the spindle can rapidly traverse optimal toolpaths on the complex occlusal surface of a dental restoration.

gram generates the toolpaths required to machine the restoration on a Computer Numerically Controlled (CNC) 5-axis machine tool, and the machining takes place. Finally, the dentist bonds the restoration in place in the patient's jaw.

The CAD/CAM system of producing dental restorations offers significant advantages over the existing lost-wax production method. The entire restoration procedure is accomplished in one visit with CAD/CAM, greatly increasing customer convenience. Temporary restorations are no longer needed, thus reducing cost and the time previously required to install and remove these temporaries. With the current lost-wax technique, each dental lab has its own way of making restorations using the same basic techniques. Dental technicians require a great deal of skill and experience to create high quality restorations. The automation of production holds the promise of standardized high quality restorations without relying on the expertise of dental technicians.

A key component in the CAD/CAM system is a 5-axis machine tool capable of grinding ceramic restorations. Since ceramic is very hard, it must be cut at high spindle speeds exceeding 30,000 rpm with very low chip loads. To achieve time-economical production at low chip loads requires very high feed rates. Figure 2-2 shows a spindle traversing toolpaths on the complex occlusal surface of a dental restoration. The machine tool needs 5 axes of motion to be able to generate the complex shape of teeth, produce good surface finish, and avoid excessive tool wear.

The shape accuracy desired is on the order of 20 μm. The machine should also be small enough to fit easily into a dentist's office. These requirements rule out the use of any existing small machine tools. Large machine tools, besides requiring a large amount of space, cannot possibly achieve the high feedrates required due to their large inertias. Designers of existing machine tools think big, and their designs do not readily scale down to the centimeter-scale range required for restorations.

2.2.2 Fabricating Other Small, Complex Parts

The manufacturing, medical, automotive, aerospace, and electronics industries require many small parts with delicate features and demanding tolerances. Often each part required has a unique geometry. This makes it inefficient to produce parts such as molds, dies, and dental restorations with electrical-discharge machining or investment casting techniques as is the current practice. A direct 5-axis CNC machining operation will be a superior way of producing these parts. It will allow for faster and easier fabrication, lower costs, more accurate parts, and more flexibility. Unfortunately no small, accurate 5-axis machine tools exist today which can produce these parts efficiently.

In addition to dental restorations, examples of small, complex parts that require 5-axis machining are aerospace components, heart valves, EDM electrodes, gear set pinions and wheels, indexing cams, jewelry, optical lenses, musical instrument components, compressor screw pairs, turbines, mold cavities, impellers, and prosthetics.

2.3 Classification of Existing Topologies

Before embarking on the design of a new five-axis machine tool, in this section we survey and classify existing five-axis machine tool topologies. The American Society of Mechanical Engineers's (ASME) *Methods for Performance Evaluation of Computer Numerically Controlled Machining Centers* [3] provides a nice classification of three-axis machine tools. Three-axis machine tools, like the vertical three-axis mill of Figure 2-1 (a), generally provide three linear degrees of freedom between the spindle

and the workpiece. The ASME standard first differentiates between horizontal spindle and vertical spindle machines. Horizontal spindle machines are further classified based on the column's motion. There are horizontal machines with a fixed column, a traveling column, and a traveling column with a fixed table. Vertical machines are classified based on column or gantry motion. There are vertical machines with a fixed column, a traveling column, and a movable column with a fixed table. The vertical gantry machines are split into fixed bridge machines and traveling gantry machines.

A five-axis machine provides five degrees of freedom—three linear and two rotary—between the tool and the part. Figure 2-1 (b) shows a five-axis milling machine with a swiveling spindle and a rotating part. The ASME standard provides only two representative examples of five-axis machines and does not attempt a full classification of five-axis machines. This may be because there are so many permutations of axes possible in a five-axis machine tool that we cannot hope to distinctly classify every possible configuration. For example, there are 720 ways of placing the X, Y,Z, A, and B axes on either the spindle or the workpiece when different stacking orders of the axes are distinct:

$$ {}_5P_5 \cdot 1 + {}_5P_4 \cdot {}_1P_1 + {}_5P_3 \cdot {}_2P_2 + {}_5P_2 \cdot {}_3P_3 + {}_5P_1 \cdot {}_4P_4 + 1 \cdot {}_5P_5 = 720 $$

Here ${}_nP_k$ is the number of permutations of n objects taken k at a time,

$$ {}_nP_k = \frac{n!}{(n-k)!}. $$

We propose a classification of existing serial five-axis machines based mainly on their rotary axes. It is the rotary axes, after all, that distinguish five-axis machines from their more ordinary cousins, the three-axis machines. The classification of existing five-axis machines is further simplified by the fact that rotary axes are usually stacked on top of linear axes and not vice versa. For example, it is common to stack a rotary axis on top of an X-Y table, but rarely, if ever, would the X-Y table be stacked on top of a rotary axis. Since our classification is based on the two rotary axes, each of our five-axis machine categories includes a large number of permutations based on

the arrangements of the three underlying linear axes. If desired, these permutations can be specified according to ASME's three-axis machine tool classification.

We use the standard naming convention for machine tool axes. The Z-axis is the linear axis aligned with the spindle's rotation axis. Hence, for vertical machines the Z-axis is vertical, and for horizontal machines the Z-axis is horizontal. The X-axis is usually the longer of the two remaining linear axes as shown in Figure 2-1, and the Y-axis is the third linear axis. A rotary axis rotating about the X-axis is labeled A, a rotary axis rotating about the Y-axis is labeled B, and a rotary axis rotating about the Z-axis is labeled C. Note that the rotary axes in Figure 2-1 (b) conform to this convention.

We next describe each of our five classes of five-axis machine tools. The first and second classes assign both rotary degrees of freedom to the spindle, but in different ways: We call these *Rotating, Swivel Spindle Machines* and *Swivel, Tilt Spindle Machines*, respectively. The third class—*Swivel Spindle, Rotating Part Machines*—give one rotary degree of freedom to both the spindle and the part. The fourth and fifth classes assign both rotary degrees of freedom to the part, using a rotary axis mounted on a trunnion: The fourth class is *Horizontal Machines with Rotary Tables on Trunnions*, and the fifth class is *Vertical Machines with Rotary Tables on Trunnions*.

2.3.1 Rotating, Swivel Spindle Machines

A *rotating, swivel spindle* is shown in Figure 2-3. The spindle has two rotary degrees of freedom. One is a rotation, C, about the nominal spindle axis, and the other is a swiveling motion, A, about an axis perpendicular to the nominal spindle axis. The swiveling motion is nominally about the X-axis but could also be about the Y-axis if the C-axis rotates by 90°. Thus, in general, the swiveling motion could be labeled either an A- or B-axis.

This type of five-axis machine is best suited for machining extremely large workpieces: it is much easier to rotate a small spindle than a large workpiece. In general, as the workpiece increases in size, fewer of the machine's degrees of freedom are assigned

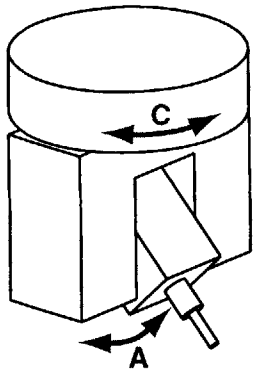

Figure 2-3: Rotating (C), swivel (A/B) spindle.

to it. An extremely large workpiece such as an aluminum part for an aircraft may move in one linear degree of freedom or may even be stationary. Thus, the *rotating, swivel spindle* is likely stacked on top of 2 or 3 linear axes. This stacking requires large stiff structures and big actuators to achieve high accelerations in the linear axes.

While the *rotating, swivel spindle* allows five-axis machining of large workpieces, it has several disadvantages. The spindle rotation is coupled to translation: if the C axis rotates 45° degrees to change the spindle angle, the spindle tip is now in a different X and Y location. This is undesirable especially as feature sizes shrink. This coupling causes a sine error as well: an angular error in the spindle axis is magnified by the distance between the spindle's axis of rotation and the tooltip.

Another disadvantage of this topology is that the machine has a singularity in its nominal position with no swivel angle. A singularity is a machine configuration in which two or more axes line up and degrees of freedom are lost. In this case, for example, the C-axis rotation does not affect the spindle's orientation when the spindle has zero swivel (A) angle. It is thus impossible to rotate the spindle along the C-axis, no matter how much control effort is expended in any of the machine's axes. Such singularities cause control and kinematic difficulties in their vicinity and therefore should be avoided in precision machining. Machine topologies, like this one, which have singularities in the middle of their workspaces are undesirable.

An example of a *rotating, swivel spindle* machine is Ingersoll's High Velocity Pro-

filer [27], one of the first linear motor machines designed for the aerospace industry. This machine has an X-axis travel of 4.5 m, a Y-axis travel of 2.5 m, and a Z-axis travel of 0.6 m. It uses linear motors to achieve linear accelerations of 0.3 g, and feed rates of 0.50 m/s. The rotating and swiveling axes spin at only 20 rpm or 2.1 rad/s. In this horizontal machine, the workpiece moves along the X-axis. The rotating (C), swivel (B) spindle is attached to a ram that moves in its housing along the Z axis. The ram's housing moves up and down a stationary column along the Y axis. The C-axis can rotate $\pm 185°$, and the swivel B-axis can rotate $\pm 45°$.

Another *rotating, swivel spindle* machine is Ingersoll's High Velocity Gantry [27] used for producing automotive dies. This is a vertical spindle machine with a fixed workpiece and a traveling gantry (X-axis). Its workspace is 6 m $\times$ 3 m $\times$ 1.35 m. A saddle (Y-axis) rides on the gantry, and a ram moves vertically (Z-axis) relative to the saddle. The rotating (C), swivel (B) spindle is mounted to the ram. The C axis has $\pm 180°$ rotation capability, and the B axis moves in 1° increments. The Jobs Jo 'Tech and Jo 'Mach [28] five axis gantry machines have a similar configuration to Ingersoll's High Velocity Gantry. Jobs labels the rotating, swivel spindle, "a spiral, twist head."

2.3.2 Swivel, Tilt Spindle Machines

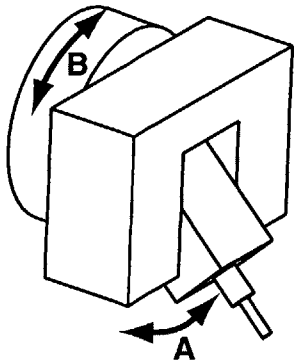

Figure 2-4: Swivel (A), tilt (B) spindle.

A *swivel, tilt spindle* has two rotary degrees of freedom. As shown in Figure 2-4

neither of these rotary degrees of freedom is the C-axis. This distinguishes the class of swivel (A), tilt (B) spindle machines from the rotating (C), swivel (A) spindle machines of the previous section. In our nomenclature, the words "swivel" and "tilt" are the same and can represent either the A- or B-axes, but the word "rotary" represents only the C-axis when applied to spindles.

Like the rotary, swivel spindle machines, swivel, tilt spindle machines are well-suited for handling large parts. The swivel, tilt spindle machine topology is better since it does not have a singularity in the nominal spindle position. However its swivel and tilt angles are generally limited to avoid interference with the rest of the machine structure. The spindle swivel or tilt still does couple to translation. This coupling can be reduced by pivoting the spindle about its tooltip.

An example of a *swivel, tilt spindle* machine is the Toshiba MPF-5A Double Column High Speed 5-axis Machining Center [65] used for producing complicated monolithic aircraft parts. The large workpiece moves on an X-axis underneath a fixed bridge. A saddle moves along the Y-axis of the bridge and carries the Z-axis. The swivel (A), tilt (B) spindle is mounted to the Z-axis. The spindle can swivel $\pm 30°$ and tilt $\pm 30°$. The maximum linear axis feedrate is 0.17 m/s, and the maximum rotary feedrate is 2.8 rpm (0.29 rad/s).

Another *swivel, tilt spindle* machine is the Mazak Mazatech V-815 5X 5-axis Tilting Spindle Vertical Machining Center [47]. It is designed for machining aerospace components and molds and dies. It also allows a swivel of $\pm 30°$ and a tilt of $\pm 30°$. It can achieve maximum feedrates of 0.33 m/s and 10 rpm (1.0 rad/s).

2.3.3 Swivel Spindle, Rotating Part Machines

Swivel spindle, rotating part machines assign one rotary degree of freedom to the spindle and one to the workpiece. The spindle's swiveling motion is usually along the B-axis. The workpiece may rotate on a rotary table (C) as shown on the left in Figure 2-5 or it may rotate on a servo controlled tail stock (A) as shown on the right in Figure 2-5.

Swivel spindle, rotating part machines offer more flexibility than other five-axis

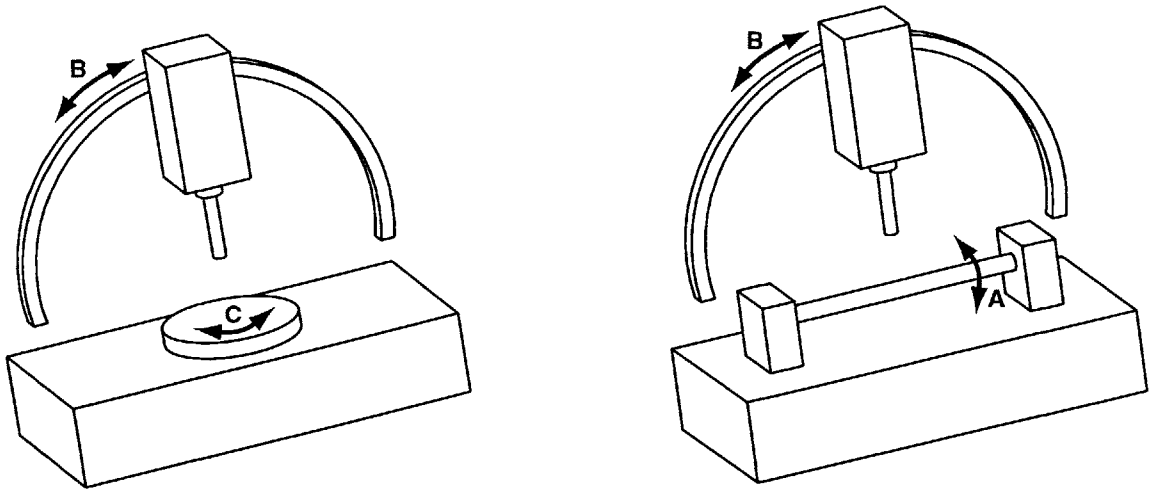

Figure 2-5: Two examples of swivel (B) spindle, rotating (C/A) part topologies.

machine classes since the two rotation axes are separate. The machine can be outfitted with various rotary axes for the part including an A-axis rotary table, a C-axis rotary table, an A-axis servo-controlled tail stock, or even an A-axis trunnion. These machines thus have the flexibility to handle many different kinds and sizes of parts.

The Boston Digital Bostomatic 505 [7] is an example of a *swivel spindle, rotating part* machine tool. It is nominally a vertical machining center, but the spindle can swivel $\pm 100°$ in the B-axis so that it can also function as a horizontal machining center. The spindle swivels about the tooltip as shown in Figure 2-5; this eliminates coupling between the swivel axis (B) and the linear axes. Also, since cutting takes place near the center of spindle rotation, the machining forces produce only a small torque on the swiveling B-axis. Furthermore, sine errors are reduced relative to a spindle which does not rotate about its tooltip: an angular error in spindle orientation is not magnified into a linear position error if the spindle axis is located near the tooltip. The machine's workspace is 1.02 m $\times$ 0.32 m $\times$ 0.43 m; it has a maximum contouring speed of 0.063 m/s. It can accomodate a high-speed rotary table which can turn at 33 rpm (3.46 rad/s). Another *swivel spindle, rotating part* machine is the Deckel Maho DMC U Series Universal Machining Center [13]. It has a vertical milling head which swivels from vertical to horizontal in 5 seconds (3 rpm or 0.31

rad/s).

2.3.4 Horizontal Machines with Rotary Tables on Trunnions

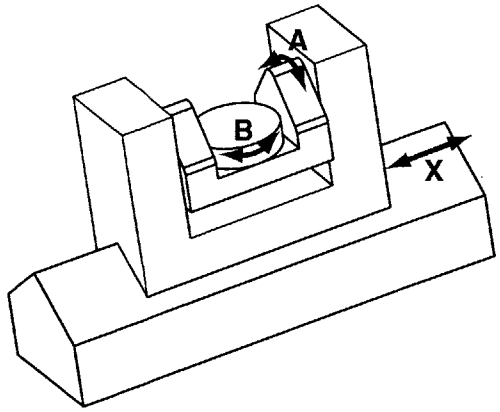

Figure 2-6: Rotary table (B), mounted on a trunnion (A) in a horizontal machine tool. Figure drawn by Marsette Vona.

The remaining five-axis machine tool topologies use rotary tables mounted on trunnions. We divide these machine tools into two classes based on whether the underlying machine tool has a horizontal spindle or a vertical spindle. In this section we consider *horizontal machines with rotary tables on trunnions.* Figure 2-6 shows a rotary table (B) mounted on a trunnion (A). As is common in horizontal machine tools, the trunnion is stacked on the X-axis. The horizontal spindle is usually mounted on a vertical slide (Y) riding up and down a moving column that provides infeed motion (Z).

Whereas machine topologies with both rotary degrees of freedom assigned to the spindle are required for extremely large parts, machine topologies with both rotary degrees of freedom assigned to the workpiece are best for medium and small parts. This is because it is much easier to rotate small parts themselves rather than the spindle. Also, machines with rotary tables on trunnions tend to have smaller workspaces since the workspace size is limited by the dimensions of the rotary table.

Rotary, trunnion machines allow easier manual operation than machines with rotary degrees of freedom assigned to the spindle. To machine a tilted cut manually,

the workpiece is tilted and rotated to the appropriate plane, and the operator can proceed as if he were using a 3-axis machine. In a rotating, swivel spindle machine, however, the spindle is at an angle, so it is not easy to make a tilted cut manually.

Horizontal rotary trunnion machines do not have a singularity in the nominal position of the rotary axes. Vertical rotary trunnion machines do have a singularity since the spindle axis is aligned with the rotary table's axis (C for vertical machines). Also, chips fall off of horizontal spindle machines better than vertical spindle machines.

Makino's MC-5XA series of 5-axis machining centers [45] are examples of *horizontal machines with rotary tables on trunnions.* They have the standard configuration of axes mentioned for this machine tool topology: the trunnion is on an X-axis slide, and the spindle is on a vertical slide (Y) on a moving column (Z). The smallest machine in the series, the MC56-5XA has a maximum workpiece diameter of 0.6 m. The trunnion (A) has a 120° travel (+20° to -100°), and the rotary table (B) can rotate 360°. The maximum feedrates for the linear axes are 0.2 m/s; for the trunnion axis the maximum feedrate is 2.8 rpm (0.3 rad/s), and for the rotary table it is 4.7 rpm (0.5 rad/s).

Many other machine tools have a similar topology:

- Toshiba's BMC 1000 (5), Horizontal Machining Center (5-Axis Control) [65]
- Mazak's Mazatech H-630 5X, 5-Axis Simultaneously Controlled Horizontal Machining Center [47]
- Yasda's YBM700/900-NTT, 5-Axis Precision Center [78]
- Deckel Maho's DMU-P Series with NC swivel rotary table [13]

Most horizontal machines have a rotary axis (B) mounted on a trunnion (A). However, Makino's MC-5XB [45] has a trunnion-like axis (A) mounted on a rotary axis (B). This machine topology reverses the order of the two rotary axes, so we classify it as a sub-class within *horizontal machines with rotary tables on trunnions.* It allows for larger workpieces, up to 2.2 m in diameter, than Makino's MC-5XA line of regular rotary on trunnion machines. However, the feedrates, are much slower since

the stacked rotary structure is huge. Yasda's H30i [78] also has a rotary A-axis (360°) mounted on a rotary B-axis (165°) and so falls within this sub-class of horizontal machines with A-axes on B-axes.

At the end of this chapter we propose a new machine tool topology based on the popular horizontal machine with a rotary table on a trunnion: We combine the trunnion (A) and linear (X) axes into a combined rotary-linear (A-X) axis which can both rotate and translate. We also replace the spindle and column infeed motion by a rotary-linear axis that can provide high-speed spindle rotation as well as infeed (Z). Now we turn to the last class of serial five-axis machines.

2.3.5 Vertical Machines with Rotary Tables on Trunnions

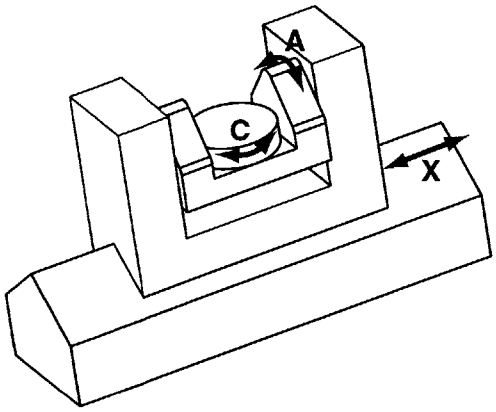

Figure 2-7: Rotary table (C), mounted on a trunnion (A) in a vertical machine tool. Figure drawn by Marsette Vona.

These machines are similar to the previous class, but the spindle is now vertical, so that the rotary table is a C-axis as shown in Figure 2-7. This creates a singularity in the nominal position, and swarf removal is more difficult. The Hermle U series [26] are examples of *vertical machines with rotary tables on trunnions.* In these machines all three linear axes are assigned to the spindle, and the rotary trunnion axis holds the workpiece. The spindle slides vertically (Z) on the cross-slide (X) of a moving gantry (Y). The trunnion can rotate ±110°, and the rotary table can rotate 360°.

Other vertical rotary, trunnion machines include Mikron's UCP710 [49] and Makino's V55-5XA [45].

The Mori Seiki M-400C1 [50] and Deckel Maho DMU50 [13] machines have slightly different topologies. In both these machines the trunnion is arranged sideways so that the trunnion axis is a B-axis rather than an A-axis. These two machines form a subclass of sideways trunnion vertical machines.

2.4 Toolpath Generation

Usually a machine is designed without regard for toolpaths, and then the Computer-Aided Manufacturing (CAM) program must make do with the machine's limited feedrates and accelerations. In machining complex centimeter-scale parts, the accelerations are so high that the machine must be specifically designed with the toolpaths in mind in order to achieve good performance. High rotary accelerations are especially crucial as the part size decreases, and most existing machine tools have very low rotary accelerations. Our rotary-linear axis can achieve high rotary and linear accelerations since it reduces the coupling and stacking of axes and keeps inertias low. Thus, it is a natural choice for use in machining small, complex parts.

Many researchers have investigated aspects of toolpath generation. In practice, most toolpaths are currently generated by using isocurves of the parametric surface representation or by intersecting the desired surface with equally-spaced planes resulting in a contour plot suitable for 3-axis milling. Two main goals of toolpath generation are to achieve the minimum toolpath length and the minimum cusp height. These are competing goals since cusp height can be reduced by moving toolpaths closer together, but this increases the toolpath length. Elber and Cohen [17] present an algorithm to adaptively develop isocurves for 5-axis milling. Choi [9] addresses the issue of generating the cutter location data, the tool's orientation at each point along the toolpath, in 5-axis machining given a specified toolpath. The goal is to minimize cusp height. Morishige [51] presents a collision avoidance algorithm for use in generating cutter location data.

Kim and Sarma [33, 32] seek optimal toolpaths that incorporate the machine kinematics and dynamics as well as the tool-surface geometry. Their goal is not to minimize toolpath length, but to minimize total cutting time subject to maximum cusp heights and actuator limits. Vickers [69], Elber [16], and Warkentin [71] examine curvature matching between the tool and the freeform surface. Vickers [69] points out that for efficient machining of surfaces, the cutter shape should be as close as possible to the surface shape. Elbers [16] divides the surface into convex, concave, and saddle regions, and advocates the use of a flat end-mill for the convex regions and a ball end-mill for the concave and saddle regions. Warkentin [71] presents an unconventional method for machining spherical surfaces which does not try to match the local surface curvature. His method is best described as dropping a coin in a spherical dish. The coin, which represents a flat endmill, makes perfect contact with the dish.

2.5 Acceleration Scaling Laws

2.5.1 Linear Accelerations

Machine tools for centimeter-scale parts must have higher accelerations in all axes to maintain the same feedrates used on larger parts. The reason for this is indicated in the simple analysis presented below. First, define the part characteristic dimension as l. An arbitrary surface on this part could be represented via its Fourier components. For this simple example, we will ignore rotational motion and concentrate on one-axis infeed (z) and crossfeed (x). Then, the n-th Fourier component of the surface could be expressed as

$$z(x) = A\sin(\frac{n\pi x}{l}). \tag{2.1}$$

The first Fourier component is sketched in Figure 2-8. The second derivative of z with respect to time t while assuming a constant horizontal feedrate $\dot{x}$ is

$$\ddot{z} = -A(\frac{n\pi}{l}\dot{x})^2\sin(\frac{n\pi x}{l}). \tag{2.2}$$

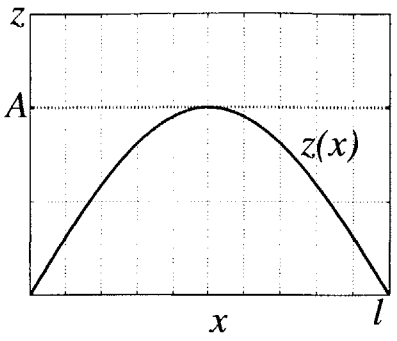

Figure 2-8: First Fourier component of a toolpath on the surface of a part with characteristic dimension l and amplitude A. Infeed motion is along the z-axis and crossfeed motion is along the x-axis.

We further assume that the amplitude A is proportional to the length, $A \propto l$, so that the surface amplitude scales with part size. With this assumption we see that the required infeed acceleration scales as the inverse of the part size l,

$$\ddot{z} \propto \frac{1}{l}. \tag{2.3}$$

Next we consider how the acceleration requirements on the crossfeed axis (x) scale with part size l. For simplicity we assume a constant acceleration $\ddot{x}$ from rest up to a maximum feedrate v_m. As a function of time t, we have $v = \ddot{x}t$. The distance l required to attain a speed v in a time t is $l = \frac{1}{2}\ddot{x}t^2$. If we assume that we need to reach the maximum feedrate in a distance $l/2$, then we find

$$v_m = \sqrt{\ddot{x}l}. \tag{2.4}$$

Thus to maintain the same maximum feedrate v_m as the distance l shrinks, the acceleration $\ddot{x}$ must increase inversely with l,

$$\ddot{x} \propto \frac{1}{l}. \tag{2.5}$$

This simple scaling analysis shows that the acceleration in the both the infeed (z)

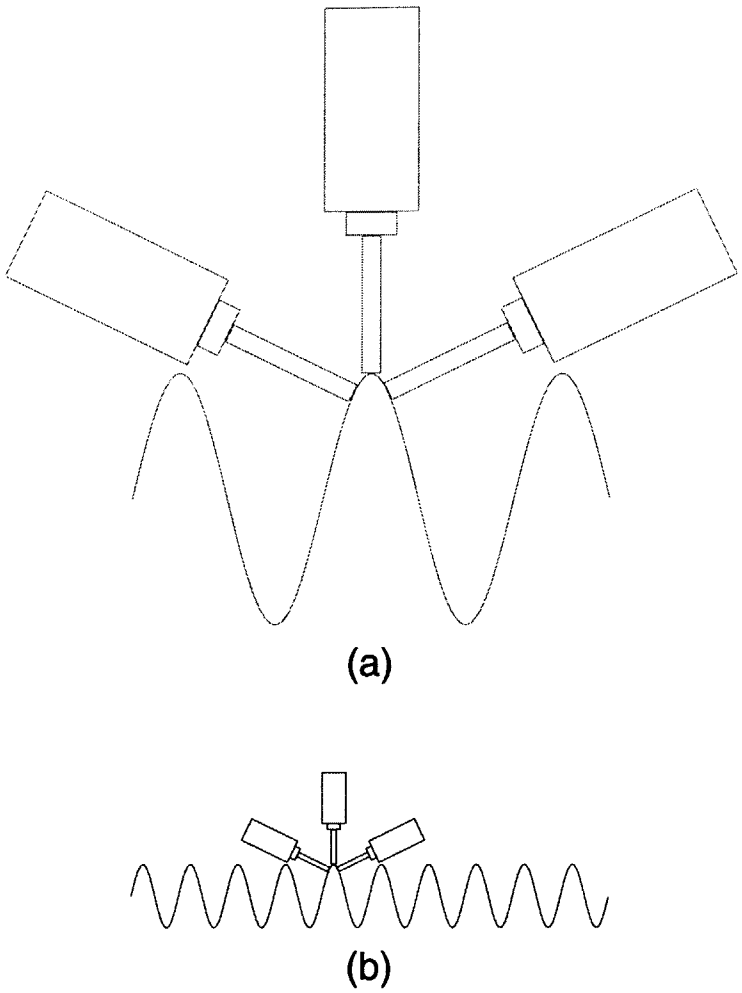

Figure 2-9: Spindles cutting the crests of sinusoidal surfaces and maintaining their angular positions normal to the part surfaces. For the same crossfeed velocity, the spindle in (b) must have higher angular accelerations than spindle in (a).

and crossfeed (x) axes of the machine tool must increase inversely with the part size to maintain given maximum feedrates.

2.5.2 Rotary Accelerations

Consider the situation shown in Figure 2-9 in which a spindle traverses a sinusoidal crest. As is common in 5-axis machining, the spindle is maintained normal to the part surface to achieve better surface finish. In this example we are interested in the rotary acceleration of the spindle as it rounds the crests of the sinewave. As shown,

the spindle cannot cut the entire sinewave surface while maintaining a normal angular position because the spindle will hit another part of the surface. We are interested in determining how the rotary acceleration of the spindle scales as the feature size shrinks. We write the sinewave as

$$z(x) = A\sin(\frac{\pi x}{l}), \tag{2.6}$$

where again x is the crossfeed direction, z is the infeed, and l is the characteristic part dimension.

The spindle is always perpendicular to the slope of the sinewave which is dz/dx. Since we are only interested in the angular acceleration of the spindle, we can use this slope to represent the spindle's angular orientation, even though it really is perpendicular to this angle. The spindle's angle is $\arctan(dz/dx)$, but for small angles this is approximately equal to dz/dx. The spindle's angular acceleration α is then the second derivative of angle with respect to time t,

$$\alpha \approx \frac{d^2}{dt^2}\left(\frac{dz}{dx}\right). \tag{2.7}$$

If we assume a constant crossfeed $\dot{x}$, then plugging (2.6) into (2.7) yields

$$\alpha \approx -A\left(\frac{\pi}{l}\right)^3 \dot{x}^2 \cos(\frac{\pi x}{l}). \tag{2.8}$$

We again make the assumption that amplitude A is proportional to the characteristic dimension l, $A \propto l$, so that the surface amplitude scales with part size. With this assumption, and also assuming a constant crossfeed $\dot{x}$, we have that the spindle angular acceleration scales as the inverse of the square of part size,

$$\alpha \propto \frac{1}{l^2}. \tag{2.9}$$

Note that at the peak of the sinewave, at $x = l/2$, $\alpha = 0$ since the surface locally approximates a circular path and no angular acceleration is required right

at this point. However for small angles away from the peak, our approximation $\arctan(dz/dx) \approx dz/dx$ is valid, and we see that $\alpha \propto 1/l^2$ at these points. Thus, this simple analysis shows that small parts require very high angular accelerations if we try to maintain constant feedrates. Also note that although we considered the spindle to be rotating in deriving this analysis, it could just have well have been the part that was rotating about a stationary spindle.

2.6 New Topology Concepts with Integrated Axes

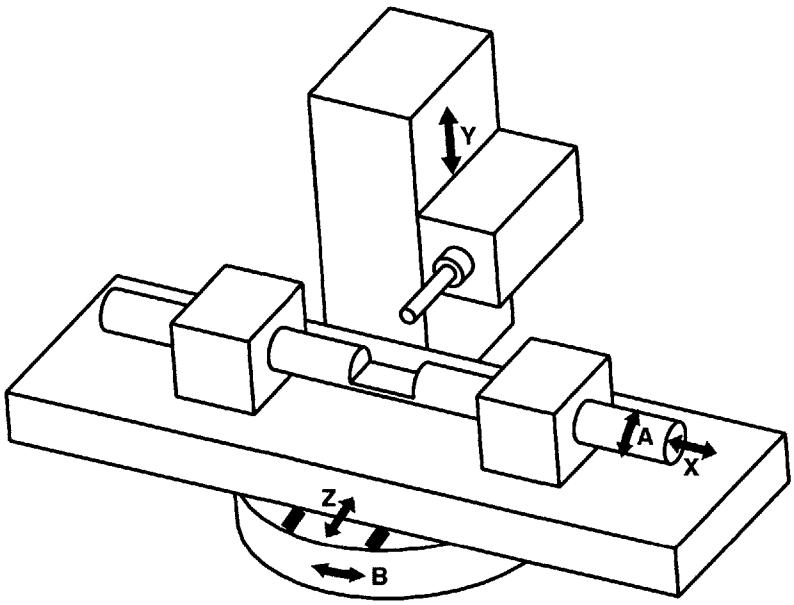

Figure 2-10: Possible 5-axis machine topology using a rotary-linear axis.

In this section we present some examples of machine topologies that incorporate rotary-linear axes to achieve high accelerations. One such topology is shown in Figure 2-10. In this topology, the rotary-linear (A-X) axis carries the part. The entire rotary-linear axis slides along a guideway in the Z-direction, and is mounted on a large rotary table (B). The spindle moves up and down a fixed column to provide Y motion. In this topology, the X- and A-axes have extremely high accelerations, and the Z- and Y-axes have high accelerations. The B-axis, however, will have, a low acceleration since it has to rotate a large inertia.

This topology is unusual since it has linear axes stacked on a rotary axis. Usually rotary axes are stacked on linear axes. In fact, our survey of five-axis machine tools did not find any that stack linear axes on rotary axes. As the rotary, B-axis, turns, the orientation of the Z- and X-axes change which makes it harder to keep track of position. With today's computing power, dealing with this coordinate transformation should be possible. However, infeed motion now requires a simultaneous actuation of the Z- and X-axes which is undesirable. Also, since angular errors in the B-axis are magnified, the B-axis must be accurate.

Many interesting variations of this topology are possible:

- We can place the B axis directly underneath the part, on the rotary-linear axis. This would eliminate rotating the linear axes, and would increase the B-axis acceleration. The disadvantage is that the rotary-linear axis has to carry this small rotary axis.

- We could move Z motion to the spindle.

- We can interchange the stacking of the B- and Z-axes. This results in a changing angle between the X- and Z-axes as B rotates, but infeed is always directed along the Z-axis.

We now look at a different topology in which a rotary-linear axis is mounted crosswise in another rotary-linear axis. This crossed rotary-linear axis topology is shown in Figure 2-11. This topology offers very high accelerations in the A-, X-, and Z-axes, and high accelerations in the B- and Y-axes. The major challenge with this topology is packaging the smaller B-Y rotary-linear axis crosswise in the larger A-X rotary-linear axis. One possible variation on this topology is to move the spindle in the Y direction instead of the part. Then, only a rotary B-axis is mounted in the A-X rotary-linear axis.

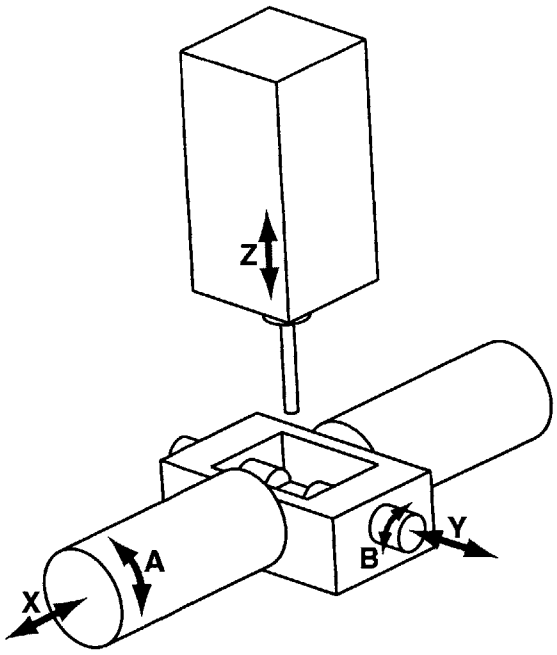

Figure 2-11: Crossed rotary-linear axes 5-axis machine topology.

2.7 z-θ Horizontal Trunnion Topology

Conventionally, machine tool designers have implemented multiple degrees of freedom by stacking axes. An example of such a serial arrangement is shown in Figure 2-12 (a). Machine tool manufacturers such as Makino [45], Mazak [47], Toshiba [65], and Yasda [78] use this arrangement in their horizontal 5-axis machine tools as described in section 2.3.4. This configuration uses a rotary index table (B) mounted on a trunnion (A) which is mounted on a linear axis (X). The stacking of axes quickly leads to a large machine tool with correspondingly large inertias. There are thus significant inherent acceleration limits in stacked axis designs like this one. For example, the trunnion motor can be made very large to achieve high rotary acceleration, but then the X-axis which carries this trunnion will see a very large inertia and hence have slow acceleration. Furthermore, stacked axes lead to large machine tools even for small working volumes which is undesirable and expensive. In addition, the errors developed in the individual axes accumulate in such serial machine structures.

Recently, machine tool designers have developed parallel machine configurations

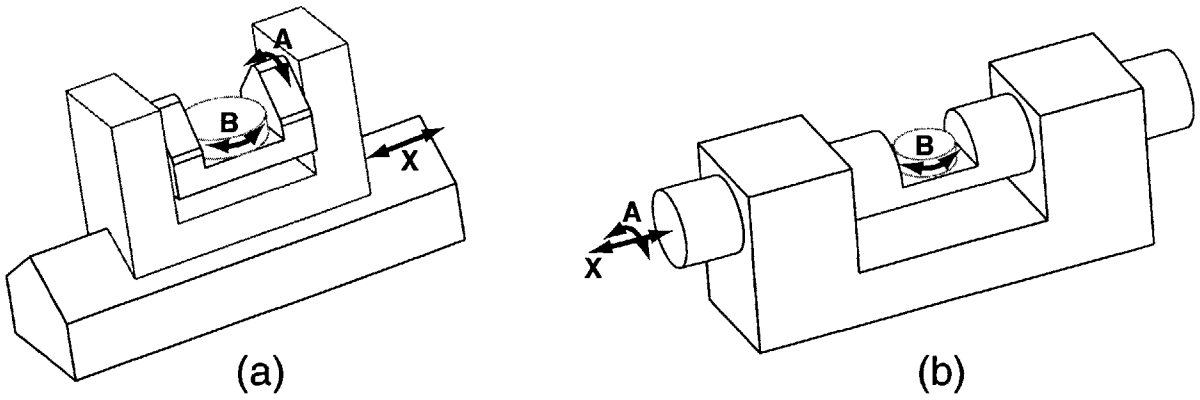

Figure 2-12: A common stacked-axis arrangement used in horizontal multi-axis machine tools is compared to our proposed rotary-linear axis. (a) Rotary index table (B) is mounted on a trunnion (A) which is moved by a linear axis (X). (b) Our rotary-linear (A-X) axis eliminates the conventional stacking of axes. Figure drawn by Marsette Vona.

such as the hexapod [6]. In such parallel machine tools, a number of struts attach to a platform which can be moved and rotated by changing the length or position of the struts. While these machines are still actively being researched by a number of groups, they have some problems, particularly in the small-scale, high-speed arena [64]. In parallel structures, the machine stiffness changes drastically throughout the workspace, and when machining complex surfaces, the machine often will approach singular positions in its workspace. Singular positions are locations in which at least one degree of freedom is lost, usually because two axes have lined up. Parallel structures remain much larger than serial structures as the workspace shrinks which is another reason why we do not consider them further for small parts.

Our proposed rotary-linear axis eliminates the problems associated with conventional stacked axis arrangements. It is shown schematically in Figure 2-12 (b). By combining the X- and A- axes into one moving cylinder, we have drastically reduced the rotary and linear inertias compared to the stacked axis case. The resulting machine structure is also much smaller, which allows for smaller actuators and a reduced machine footprint. This simple, small combined axis has a much higher structural resonant frequency than a large stacked arrangement of axes. This allows for significantly

higher machine control bandwidth and thus the ability to track the high-frequency surface features of centimeter-scale parts with improved machine accuracy.

The combined rotary-linear axis can also be used to provide rotation and infeed for a spindle. In this application it will allow much higher infeed acceleration than is possible by moving a whole spindle on an independent infeed stage as in current practice. We only have to move the rotating spindle linearly, not the entire spindle housing with motor, bearings, and sensor. Since the rotating spindle has much less mass than its entire housing, we can achieve significantly higher accelerations than we could by moving the spindle housing back and forth.

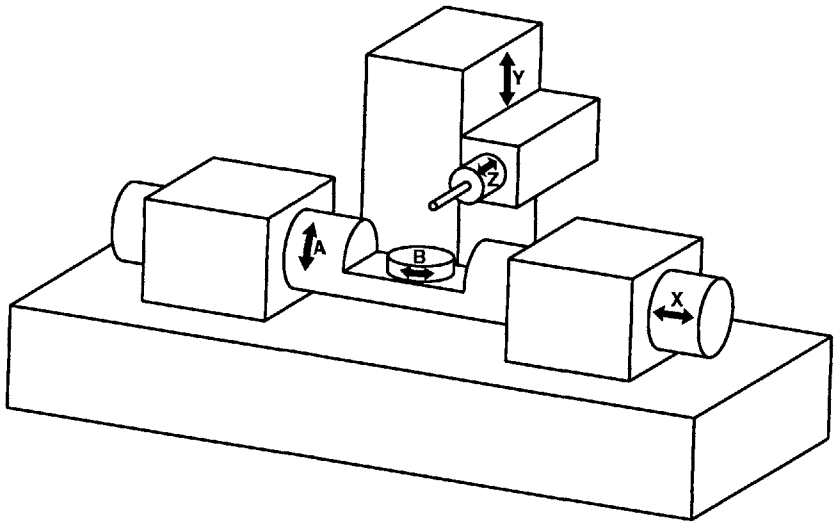

Figure 2-13: Envisioned z-θ horizontal trunnion 5-axis machine tool topology. The A-X rotary-linear axis allows us to achieve high accelerations in the A- and X-axes. The high speed rotation of the spindle and infeed, Z, are combined into a rotary-linear axis as well. The spindle moves up and down a fixed column on a conventional Y-axis linear slideway. The B-axis is envisioned as a small indexing head which provides the fifth axis with minimal inertia.

The 5-axis machine topology we think is best for small parts is shown in Figure 2-13. It is similar to existing horizontal 5-axis machines with 360° rotary tables, B, mounted on a trunnion, A. In our design, however, the trunnion, A, and linear axis, X, are combined into an A-X rotary-linear axis. This allows us to achieve high accelerations in these axes and eliminates the control problems associated with stacked axes. Also, we have combined the spindle high-speed rotation and infeed, Z,

into a rotary-linear axis as well. For this spindle application, the rotary-linear axis does not require precision rotary sensing, only precision linear sensing.

The inclusion of a continuous B-axis may add considerable inertia to the rotary-linear axis. Thus, we have chosen to use an indexed B-axis instead of a continuous axis. This indexed axis allows for five-sided machining and allows the rotary-linear axis to achieve higher accelerations. The only functionality lost by indexing this axis is the ability to drill arbitrarily angled holes which is not often required. It is still possible to machine freeform surfaces with three or four continuous axes when the other axes are indexed. Suh and Lee [62] present a method for machining freeform surfaces with one or two indexed axes that minimizes the number of times the index table needs to be indexed. Our design further reduces the added inertia of this index table by offloading its actuator. Thus, in order to index the table, the rotary-linear axis would return to a home position, and a mechanical reach-in actuator would engage the index table.

Our design assigns both rotary degrees of freedom to the centimeter-scale part since it has a much smaller rotary inertia than the spindle. This is because the part is roughly a centimeter cube, whereas the spindle is larger and has significant length. The rotary inertia of a long cylinder with mass m and length l about one end is $ml^2/3$. Thus, since the spindle has more mass than the part and has a length longer than a centimeter it will have a much higher rotary inertia than the part does.

The combined rotary-linear axis with index table that carries the workpiece provides three degrees of freedom for nearly the mass and inertia of one conventional rotary degree of freedom. The spindle combined with infeed motion allows us to just move the rotating spindle, not the whole spindle housing. In effect, we get the spindle infeed motion for free, whereas in a conventional horizontal spindle machine, spindle infeed requires moving a massive column.

2.8 Summary

In this chapter we presented a classification of existing 5-axis machine tools based mainly on their rotary axes. These machines all have many levels of stacked axes in their kinematic chains which results in limited linear accelerations and low rotary accelerations. For machining complex centimeter-scale parts, we require high rotary and linear accelerations to be able to follow toolpaths at high feedrates. We derived some simple scaling laws that show that infeed and crossfeed accelerations are inversely proportional to the part size, l. Also, we derived that rotary accelerations are inversely proportional to the square of the part size, l^2, if we want to maintain constant feedrates as the part size and features shrink.

Thus, it is key to have high accelerations for machining centimeter-scale parts. In particular since the rotary accelerations are inversely proportional to the square of the part size, we need higher rotary accelerations more than higher linear accelerations. This intuitively makes sense since if you want to write with a pen on a small centimeter-scale object you are holding in the palm of your hand, you know you will have to rotate either the pen or the object a lot. A bigger object, however, is easier to write on.

The rotary-linear axis is a key component that allows for higher accelerations in two axes since it eliminates one level in the machine's kinematic chain. This axis can be incorporated into many novel machine tool topologies. The z-θ horizontal trunnion topology is one topology that seems promising. It uses one rotary-linear axis to carry the part. This rotary-linear axis gives us the very high angular acceleration that we need for small parts. Without using a rotary-linear axis, the only way to achieve high rotary acceleration is to use a large rotary motor. The linear axis carrying the rotary motor then has to move the entire large rotary motor, and the linear axis will have reduced acceleration. Our machine topology also uses the rotary-linear axis as a high speed spindle combined with infeed motion. In this application, we get the linear degree of freedom almost for free compared to a conventional solution which requires moving the entire spindle housing for infeed.

In the remainder of this thesis we focus on the rotary-linear axis itself. Our prototype axis is mainly intended as the precision axis for carrying the workpiece. However, we also use this testbed to examine some aspects of using a rotary-linear axis in a spindle application. In the next chapter we review existing rotary-linear stage designs and examine concepts for rotary-linear motors, bearings, and sensors.

Chapter 3

Rotary-Linear Motion

3.1 Review of Existing z-θ Stage Designs

3.1.1 Teletype Positioning Mechanism

In 1973, Teletype Corporation patented a rotary and linear magnetomotive positioning mechanism for telegraph receivers and printers [31]. As shown in Figure 3-1 this device positions a cylinder carrying an array of alphanumeric character dies. The desired character die is rotationally and axially aligned with a hammer. The hammer prints the character by pressing a piece of paper and an inking ribbon into the die. This patent attempts to increase printing speed and accuracy by replacing the complex mechanical means for rotary and linear positioning used previously.

The rotary and linear motion is created by two one-phase, Lorentz force motors located on either end of the type carrier cylinder. These motors are both of the moving coil type. Two fixed C-shaped magnets produce radial magnetic fields at both ends of the cylinder. The coils are attached to the cylinder and produce a Lorentz force density, $\vec{J} \times \vec{B}$, where $\vec{J}$ is current density in the coils and $\vec{B}$ is the radial magnetic field produced by the magnets. The linear motor coil **23** generates a linear force, but the portion of the coil in the open section of the C-shaped magnet does not generate any force since there is no magnetic field there. This open section is required so that the printhead can access the paper. The rotary motor is simple but quite inefficient.

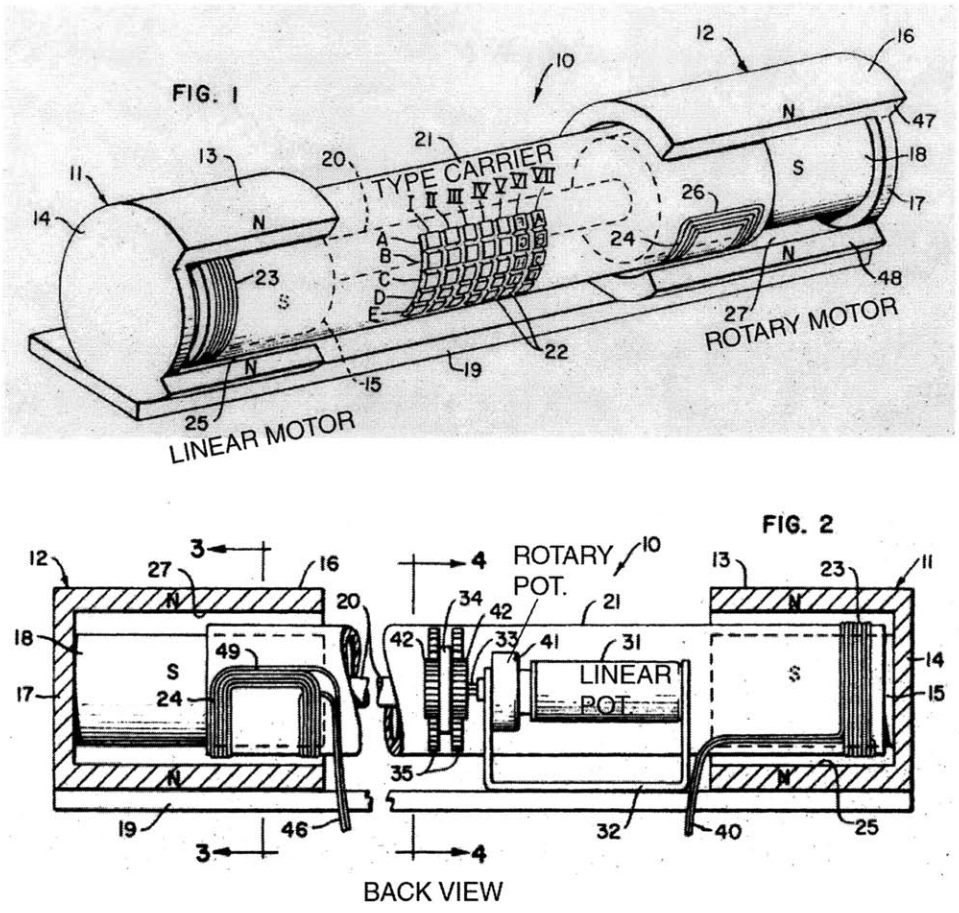

Figure 3-1: Rotary & linear magnetomotive positioning mechanism for printers patented by Teletype Corporation in 1973. Figure from U. S. Patent 3,745,433 [31].

The rotary motor coil **24** is rectangular and fit onto the curved surface of the cylinder. The two sides of **24** parallel to the linear motor coil **23** actually generate equal and opposite linear forces. The coil section **26** generates no force since it is in an area with no magnetic field, and only coil section **49** generates a rotation force. Thus, approximately only 1/4 of the rotary motor coil generates useful force. Since coil section **26** must remain in the open section of the magnet, the allowable rotation is limited.

Sliding contact bearings are used and are integrated into the motor structures. The inside of the hollow plastic type carrier cylinder slides along the south magnetic poles of both motors. Linear and rotary potentiometers are used to sense linear and rotary displacements. These sensors are placed on an axis parallel to the axis of

the type carrier but displaced from it. The sensors are coupled to the cylinder by a pair of rack gears **35**. These gears rotate gears on a shaft attached to a rotary potentiometer. They also capture a boss **34** so that linear motion of the cylinder is transferred to the same shaft and thus the linear potentiometer. The friction in the sliding contact bearings and especially the mechanical couplings to the sensors limits the achievable resolution and speed of the device. Nonetheless, it provides a simple design for generating coarse linear-rotary motion.

3.1.2 Philips Electromagnetic Actuator

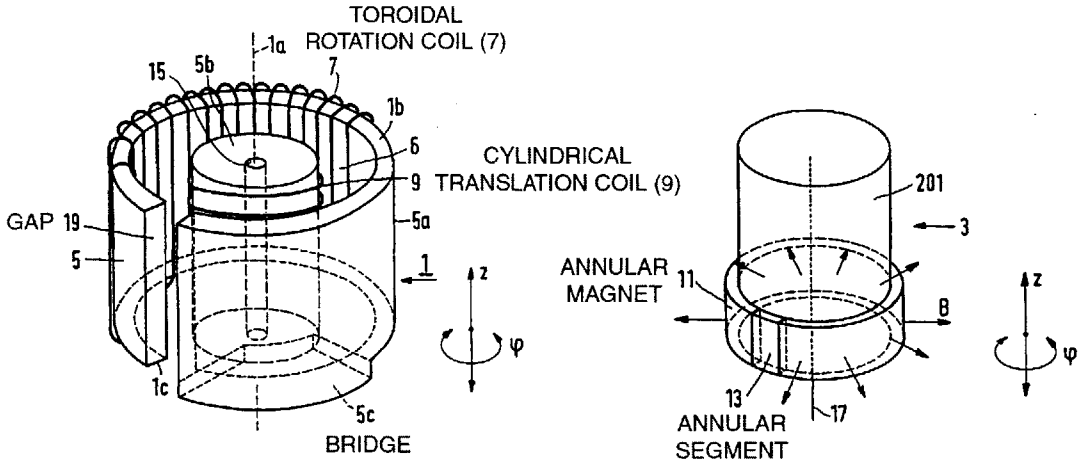

Figure 3-2: Electromagnetic actuator with a cylindrical translation coil and a toroidal rotation coil patented by Philips Corporation in 1997. Figure from U. S. Patent 5,600,189 [68].

In 1997, U. S. Philips Corporation patented an electromagnetic actuator for placing electronic components on printed circuit boards (PCB's) [68]. The actuator, shown in Figure 3-2, provides rotary and linear positioning. A suction pad attached to the moving part of the actuator picks up a surface mounted electronic component from a feed area. Then the component is positioned over a printed circuit board by conventional actuators. The rotational degree of freedom in the electromagnetic actuator adjusts the component's orientation; the linear degree of freedom presses the component into an adhesive layer on the PCB.

The electromagnetic actuator shown in Figure 3-2 consists of two single-phase Lorentz force actuators. The rotor, which rotates and translates, includes a radially magnetized annular magnet. This magnet is interrupted by an annular segment magnetized in the opposite direction. The stator consists of a ferromagnetic central core and shell connected by a bridge at the bottom. The core has a cylindrical coil wound on it for producing a translation force; the shell has a toroidal coil wound on it for producing a rotation force.

Next we examine how force is produced in this actuator. The Lorentz force, $\vec{J} \times \vec{B}$, can be calculated and is the force on the coils in the actuator. For typical surface wound synchronous motors, a reaction force equal and opposite to the Lorentz force is applied to the magnetic rotor. However, in this actuator, the reaction force for the rotary motor is split between the magnetic rotor and the stator back iron. Since the Lorentz force law does not tell us anything about forces on magnetic materials, we must use a different method for understanding the forces, such as the energy method.

Linear motion is produced by the interaction of the cylindrical coil and the annular magnet. The flux path of the radially magnetized annular magnet crosses the cylindrical translation coil and returns from the shell to the core via the bridge. As the magnet moves axially, the flux linked by the cylindrical coil changes. We will see that the annular segment which is magnetized opposite the rest of the magnet is necessary for rotary motion; as far as linear motion is concerned, however, it serves no purpose and in fact reduces the motor's efficiency. Next we will show that rotary motion changes the flux linkage in the toroidal coil. After that we use the energy method to qualitatively show that a changing flux linkage in the cylindrical or toroidal coils results in a force or torque on the rotor.

Rotary motion is produced by the interaction of the toroidal coil and the magnetic rotor. The magnetic flux leaves the rotor and crosses into the shell where it links the toroidal coil. The flux then passes through the bridge to the core and back to the magnetic rotor. The gap in the shell forces the flux to always link the toroidal coil in the same direction. The flux linkage of the toroidal coil changes with rotation of the rotor due to the oppositely magnetized annular segment. Thus, the annular segment

must always be located within the angular extent of the toroidal coil. Note that if the rotor were symmetric and did not have an annular segment, no torque would be generated on the magnetic rotor. The toroidal coil would feel a Lorentz force, but the reaction force would be on the shell.

It now remains to use the energy method to show that a changing flux linkage in this actuator results in a force or torque. We consider the linear motion case; the rotary case is similar. The energy method [76] applies to lossless electromagnetic systems like this one. In this example the annular magnet is the moving part. The force f and displacement x at the mechanical terminal of the lossless electromagnetic system correspond to the rotor. The electromagnetic system has two electrical terminals with flux linkages, λ_1 and λ_2, and currents, i_1 and i_2. The first coil is a fictitious coil which replaces the annular magnet since the energy method doesn't deal directly with permanent magnets.[1] A constant current i_1 in this coil results in the same magnetomotive force as would be provided by the permanent magnet. The second coil is the cylindrical translation coil.

Thus, we have a two coil system: the first coil represents the magnet and the second coil represents the physical coil. The system's coenergy, $w'(i_1, i_2, x)$ is

$$w'(i_1, i_2, x) = \int_0^{i_1} \lambda_1(\tilde{i_1}, i_2 = 0, x)\, d\tilde{i_1} + \int_0^{i_2} \lambda_2(i_1, \tilde{i_2}, x)\, d\tilde{i_2}, \tag{3.1}$$

where $\tilde{i_1}$ and $\tilde{i_2}$ are dummy variables in the integration. According to the energy method, force is the partial derivative of the coenergy with respect to position,

$$f = \left.\frac{\partial w'(i_1, i_2, x)}{\partial x}\right|_{i_1, i_2}. \tag{3.2}$$

The first integral in equation (3.1) evaluates the flux linkage of the fictitious magnet coil as its current is increased from zero while the physical coil has no current in it. This term is independent of the translation of the rotor, x, and thus will not

[1]It is also possible to use a (different) fictitious coil in addition to the permanent magnet [18]. This coil nulls out the effect of the permanent magnet so that the initial flux linkage and force in the system are zero. Under normal conditions this fictitious coil has zero current.

contribute to the force. The second term integrates the flux linkage of the physical cylindrical coil once the fictitious magnet coil has reached its constant current i_1. As long as this flux linkage changes with x, the coenergy's derivative with respect to x will be non-zero and force will be generated on the rotor. Thus we have shown that a changing flux linkage in the cylindrical coil results in a translation force on the magnetic rotor. Likewise, a changing flux linkage in the toroidal coil results in a rotation torque on the magnetic rotor.

This actuator provides a compact and simple way of generating rotary and linear motion. The rotary and linear motors use the same magnet array which reduces the axial extent of the actuator and the moving mass. Furthermore, the coils need not be wound on top of each other, but can be wound separately on the shell and core as shown in Figure 3-2. In order to obtain this simplicity, the actuator gives up power efficiency and translational and rotational travel.

Power efficiency is reduced by large air gaps and incomplete use of the magnet array. Both motors have large air gaps; for example, the linear motor sees the toroidal coil as an extra air gap. Also, the magnet array is not fully utilized by either motor: the annular segment reduces the force capability of the linear motor; the rotary motor only uses the part of the annular magnet within the angular extent of the toroidal coil.

The single phase nature of each motor eliminates the need for commutation, but also reduces the translational and rotational travel. The rotational travel is limited to approximately the angular extent of the toroidal coil since the annular segment must remain opposite this coil.

The two degree of freedom optical sensor developed for this actuator is shown in Figure 3-3. The figure shows a developed part of a cylindrical encoder attached to the magnetic rotor. The 2-D pattern is created by vacuum depositing aluminum on a transparent substrate and using a laser beam to selectively remove the aluminum. The pattern's linewidth is roughly 50 μm. LED's shine light through the encoder grid and fixed masks modulate the light as the encoder grid moves in translation or rotation. Photodiodes behind the masks detect the intensity of the modulated light.

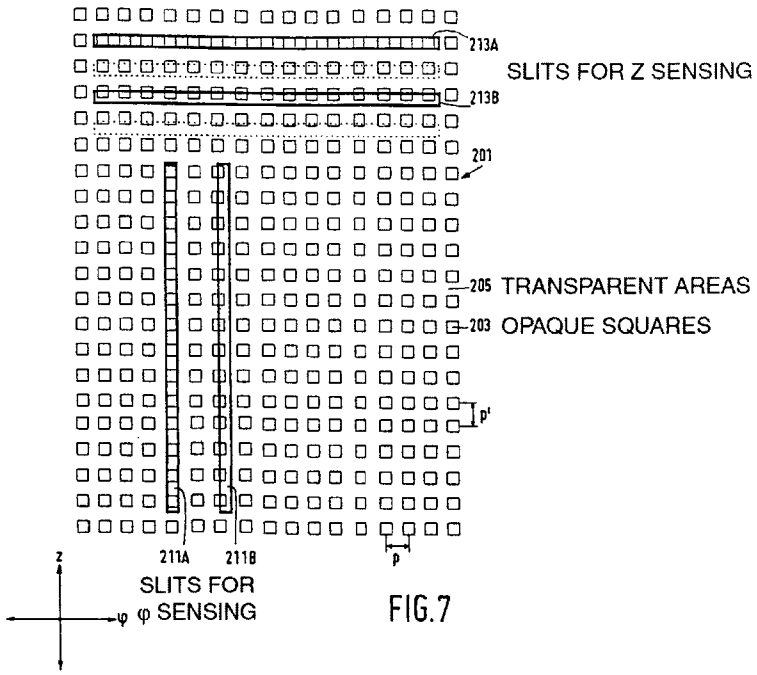

Figure 3-3: A 2-D optical encoder for rotary φ and linear z sensing. Two masks with slits are used for each degree of freedom. The slits in the two masks are displaced by one-quarter pitch of the encoder grid to provide quadrature signals. Figure from U. S. Patent 5,600,189 [68].

The masks are made of parallel transparent slits; Figure 3-3 shows a representative slit for each mask. The masks for z sensing have slits elongated in the φ direction so that the modulated light is insensitive to φ movement. The masks for φ sensing similarly are elongated in the z direction. For each direction of sensing, two masks are used with slits offset by one-quarter pitch of the encoder grid to provide quadrature signals.

3.1.3 z-ϕ Induction Actuator

Paul de Wit et al. at the University of Twente [12] designed and built a z-ϕ induction actuator shown in Figure 3-4. This actuator is meant to replace a pneumatic device used to position surface mounted devices on printed circuit boards in a laser welding system. The two most interesting aspects of the design are the use of induction motors and the use of a rotation sensor based on crossed polarizers. Table 3.1 lists some of

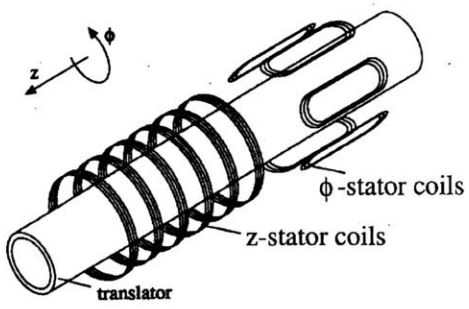

Figure 3-4: z-ϕ induction actuator. Figure from [12].

the device's reported parameters.

Parameter	*Specification*
Linear Travel	70 mm
Maximum Force	16 N
Translator Mass	0.1 kg
Maximum Linear Acceleration	10 g
Linear Sensor Resolution	23 μm
Linear Axis Closed Loop Bandwidth	50 Hz
Rotary Travel	360°
Maximum Torque	0.03 N·m
Translator Inertia	2.5×10^{-5} kg·m^2
Maximum Angular Acceleration	1200 rad/s^2
Rotary Sensor Resolution	48 μrad
Rotary Axis Closed Loop Bandwidth	40 Hz

Table 3.1: z-ϕ induction actuator specifications [12].

Figure 3-5 shows a cross-section of the z-ϕ induction actuator. A hollow aluminum translator rides inside of two radial air bearings. A long tube is attached to the inside of the translator; it is part of the z sensor and is also used to carry vacuum to the nozzle holder. The tubular linear induction motor (TLIM) and tubular rotary induction motor (TRIM) coils are located outside the translator and between the air bearings. The hollow back iron behind the aluminum translator is stationary and attached to the housing.

The simplicity of an induction motor's rotor provides some advantages when used

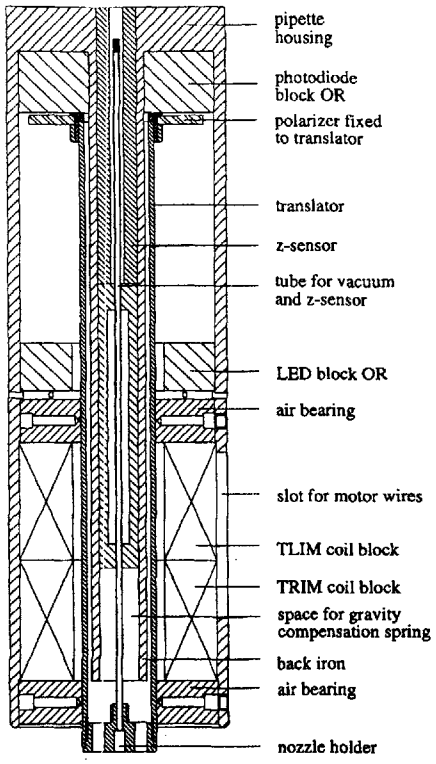

Figure 3-5: Cross-section of z-ϕ induction actuator. Figure from [12].

in a linear-rotary stage. First, since the rotor can be as simple as a piece of aluminum, it does not require permanent magnets. This reduces the mass and inertia of the rotor. Second, since the same aluminum rotor will work for a linear induction motor and a rotary induction motor, the linear and rotary stators can be located directly on top of each other without any axial gap.

Induction motors have several disadvantages. First, in small sizes, they are considerably less power efficient than permanent magnet synchronous motors and generate much less force. Second, heat is generated not only in the stator coils, but directly on the moving part which is undesirable. For example, in the z-ϕ induction actuator shown in Figure 3-5, if the linear motor produces a 10 N force for three seconds, the translator expands by 11 μm. This requires that the air bearings have very large air gaps of 18 μm to accomodate the thermal expansion. Due to this large air gap, the air bearing stiffness is only 2 N/μm. Third, induction motors can be more challenging

to model and control than synchronous motors.

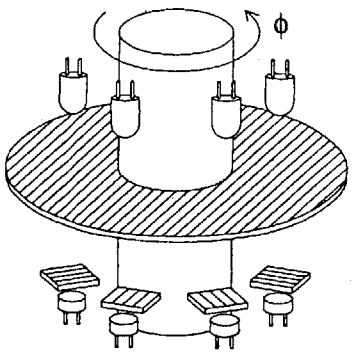

Figure 3-6: Optical rotation sensor based on crossed polarizers. Figure from [12].

The induction actuator uses a variable inductance sensor to measure translation. A long tube attached to the translator is a magnetizable core for the sensor. A look-up table is used to determine position since the inductance is a non-linear function of the translation. This sensor has a resolution of 23 μm.

The optical rotation sensor, which is based on crossed polarizers, is shown in Figure 3-6. This sensor consists of four high intensity LED's and four photodiodes. A linear polarizer is attached to the tranlator shaft and polarizes the light from the photodiodes in a direction based on the translator's rotation angle. This polarized light is analyzed by fixed polarizers mounted above photodiodes. These polarizers have angles of 0°, 45°, 90°, and 135°. This sensor has a resolution of 48 μrad. One disadvantage of this sensor is that the sensor must take up an axial distance on the shaft equivalent to the linear travel. This is necessary to keep the polarizer mounted to the translator from hitting the LED's or the photodiodes as can be seen in Figure 3-6.

3.1.4 Electro-Scientific Industries Drilling Spindle

Electro-Scientific Industries patented a high speed drilling spindle with a reciprocating ceramic shaft in 1999 [36]. The invention, shown in Figure 3-7, is designed for high speed, precision drilling of very small diameter holes in printed circuit boards. The linear and rotary motion of the spindle is decoupled through the use of a magnetically

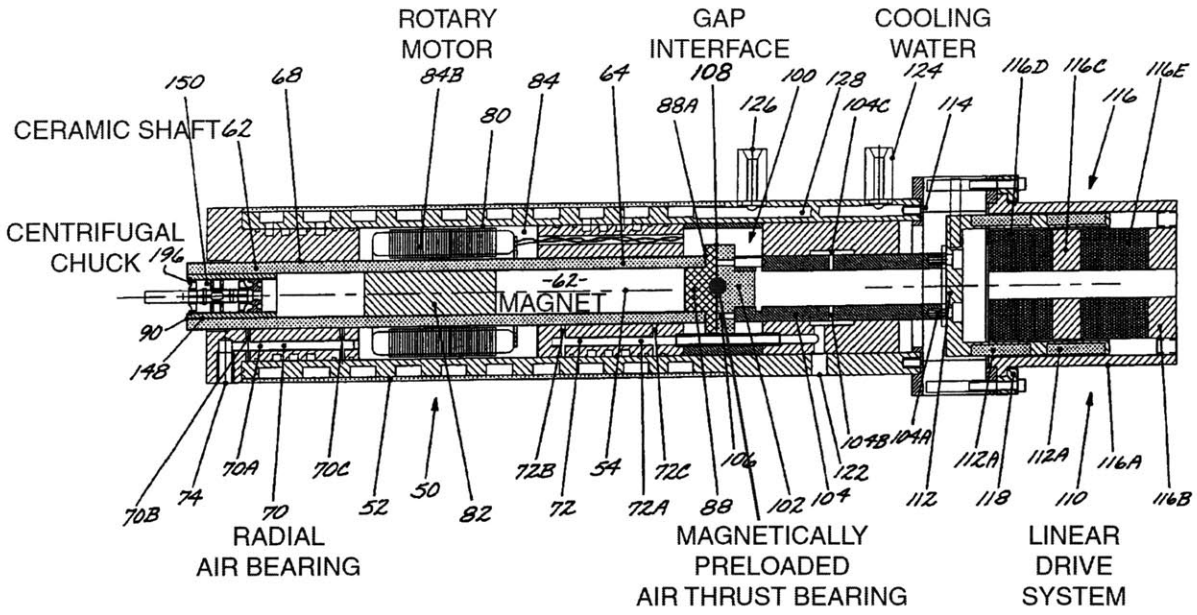

Figure 3-7: High speed drilling spindle with reciprocating ceramic shaft patented by Electro-Scientific Industries in 1999. Figure from U. S. Patent 5,997,223 [36].

pre-loaded air thrust bearing. This design is fascinating and presents an alternative to the coupled design described in this thesis. We next explore the design in detail and note its advantages and disadvantages.

The spindle rotates at high speeds of up to 200,000 revolutions per minute. It is supported by two radial air bearings with close tolerances. At such high rotation rates, the centrifugal forces on the spindle cause the diameter to grow which can lead to seizure of the spindle in the air bearings. Thus, the patent advocates the use of ceramic instead of steel since ceramic has a higher Young's modulus and lower density and therefore less diametric growth than steel. The ceramic spindle is hollow to minimize its mass and inertia.

The rotary motor for the spindle is a permanent magnet, brushless, synchronous motor. It is a moving magnet design, and the magnet array is placed inside the hollow spindle. This has distinct advantages over attaching a magnet array to the outside of the spindle. The hollow spindle acts as a strong retaining structure for the magnet. If the magnet were bonded outside the spindle, the centrifugal forces on it could cause it to break off at high speeds. Furthermore, the hollow cylinder

is stiff enough to reduce the diametral growth of the magnet at high speeds. The disadvantage of this mounting method is that the air gap of the motor is increased by the thickness of the ceramic shaft; this reduces motor efficiency and achievable torque. Also, the radius of the rotary motor is limited to that of the shaft which also limits achievable accelerations. In a spindle motor such as this one, the rotary motor may not need to provide high torque, but in a high acceleration machine tool, this is necessary. Overall, the magnet placement inside the spindle tube seems quite beneficial for a high-speed spindle application.

Linear thrust is generated by a single-phase permanent magnet voice coil motor. It consists of stationary permanent magnets and a moving cup structure housing two circular coils. The cup is attached to a thrust bearing slider **104** mounted in a radial air bearing. This slider attaches to the rotating spindle with a magnetically preloaded air thrust bearing. The air gap interface between the spindle and the thrust bearing slider allows the spindle to rotate relative to the linear drive system. The linear drive system is constrained from rotating by a pin sliding in a slot lined with Teflon. The linear drive system is designed for 0.4 inches of linear travel. As shown in Figure 3-7 the linear motor coils and magnets are the same length. In the extreme travel positions, some of the coils will not be interacting with the magnets. Thus, it seems that the motor force constant will vary over the linear travel. The patent does not address this issue for either the rotary or linear motors.

The Electro-Scientific Industries spindle is nearly a stacked-axis design for linear and rotary motion. If the rotary motor stator moved linearly with the spindle, it would be a conventional stacked axis design. By offloading this actuator mass, they have improved the stacked axis design. One of the main advantages of stacked-axis designs is that sensing of the two axes is decoupled and therefore easy. The Electro-Scientific Industries patent does not address sensing means, but any standard linear and rotary sensors could be used. Their cleverly stacked design also has some disadvantages. The large number of air bearings, three radial and one thrust, add complexity and cost to the machine. Also, the magnetically-preloaded air bearing acts as an undamped spring and could limit the linear-motor control bandwidth as

well as the attainable linear precision. For a drilling spindle high precision linear motion may not be required, but for a grinding spindle it is.

3.1.5 Anorad Rotary-Linear Actuator

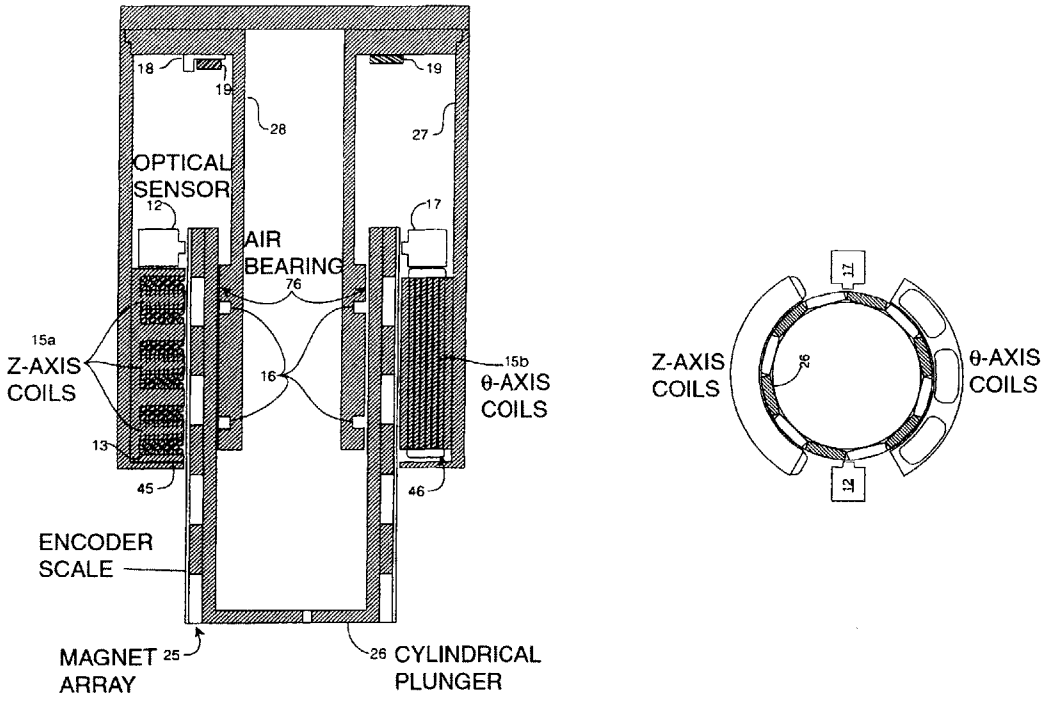

Figure 3-8: Rotary-linear actuator patented by Anorad Corporation in 1999. The view on the right is a cross-section through the motor. Figures from U. S. Patent 5,982,053 [8].

Anorad Corporation patented a rotary-linear actuator shown in Figure 3-8 in 1999 [8]. We consider this design last since, of all the prior art designs, this one is the closest to the z-θ axis described in this thesis. The Anorad design seems mainly aimed at pick-and-place applications as it has high accelerations but produces relatively small forces, for example, 3 N continuous in z, compared with over 45 N for our axis.

The strong points of the Anorad design include the sensor, bearings, and overall packaging. The sensor design is particularly nicely done; it is based on a 2-D optical encoder grid and obtains resolutions of 0.4 μm in z and 35 μrad in θ. Also, the packaging of the actuator provides for a compact stage: it has interior air bearings,

and the encoder grid is overlaid over the magnet array. The motor design, however, is inefficient, and this is the weakest part of the design. Essentially Anorad has taken its 2-axis planar servo motor technology and rotated it around a cylinder. While this technology based on a checkerboard magnet array pattern has some merit for a stage with large planar travels, it is not a good solution for a cylindrical stage, especially one with a short linear travel.

We obtained some preliminary specifications of Anorad's "Cyclone High Performance Air Bearing z-θ Stage" in late 1999, some of which are shown in Table 3.2. As of mid-2001 this product is not listed on their web page, nor has it been the subject of any press releases or articles; it does not appear to be a readily available commercial product yet.

Parameter	*Specification*
Linear Travel	50 mm
Maximum Linear Velocity	1 m/s
Peak Acceleration with 70 gram load	2.0 g
Moving mass	270 g
Linear Continuous Force	2.9 N
Linear Sensor Resolution	0.4 μm
Rotary Travel	360°
Maximum Angular Velocity	60 rad/s
Maximum Angular Acceleration	1250 rad/s^2
Angular Sensor Resolution	35 μrad

Table 3.2: Anorad Cyclone S50 preliminary specifications.

As shown in Figure 3-8 the moving part of the rotary-linear actuator is a hollow cylindrical plunger. It is supported by internal air bearings. The rotary and linear motors are slotted, permanent magnet synchronous motors. These motors have stationary coils and moving magnets. We now examine the magnet array, the stator coils, and the 2-D encoder.

A checkerboard magnet array shown in Figure 3-9 is mounted on the plunger. The useful feature of this array is that it forms rows and columns of magnetic poles. On a cylindrical surface these become rings and columns. The effective ring magnets

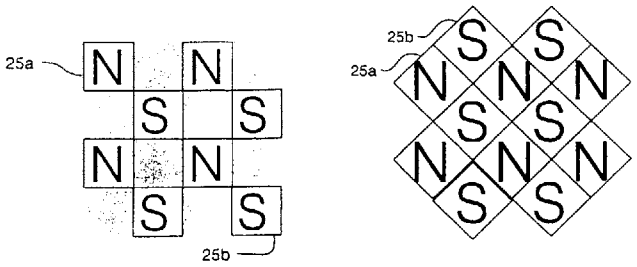

Figure 3-9: Two possible realizations of a checkboard magnet array are shown. Anorad's Rotary-Linear Actuator uses this type of magnet array. Figures from U. S. Patent 5,982,053 [8].

form the magnetic rotor of a linear motor while the effective column magnets form the magnetic rotor for a rotary motor. A benefit of this magnet array pattern is that the same magnet array can be used for both the linear and rotary motors. Its chief drawback, however, is that it achieves only a 50% packing density and hence 50% efficiency for a given surface area compared to a regular motor. To see this note that the checkerboard array on the left in Figure 3-9 uses only 50% of the available surface area. It is possible to fill in more of the surface area with magnets as shown on the right in Figure 3-9; this, however, does not improve the motor efficiency since the added magnets produce forces that, on average, cancel each other.

The arrangement of stator coils shown on the right in Figure 3-8 is peculiar. Since the z-axis coils extend only partway around the motor, the linear motor force is produced off axis and will also produce a torque that tends to cock the plunger in the air bearing. Likewise since the θ-axis coils extend only partway around the motor, the rotary motor will produce a linear force in addition to a torque. This coupling is clearly undesirable in a precision stage. Perhaps, this arrangement was chosen for packaging reasons, but it is possible to eliminate these problems while using approximately the same amount of space: the two motors should be stacked axially and the z-axis and θ-axis coils should extend completely around the plunger's circumference. This would also allow the z-axis coils to be ring coils rather than bent rectangular coils. Ring coils are easier to wind and result in a higher efficiency motor since they do not have end-turns.

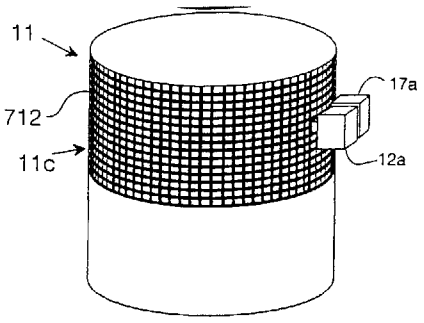

Figure 3-10: 2-D optical encoder for use as a rotary and linear sensor. Figure from U. S. Patent 5,982,053 [8].

Anorad's design and integration of a 2-D encoder for rotary and linear sensors is excellent. The 2-D encoder grid and two optical sensors are shown in Figure 3-10. Although this sensor does take up significant area on the cylinder, especially for longer linear travels, it provides a decoupled z and θ measurement without adding mass and inertia to the moving part. Furthermore, if the grid can be integrated into the air bearing surface or the motor surface, as Anorad has done, it does not increase the moving plunger's length. To achieve this integration Anorad needed to attach the encoder scale to the surface of the magnet array as shown in Figure 3-8. This was possible since they first coated the magnet array in epoxy and then, after it hardened, machined it to a precision round surface.

3.2 Rotary-Linear Motor Concepts

In this section we look at rotary-linear motor concepts. We first compare permanent magnet motors and induction motors. We find that permanent magnet motors are more power efficient at small force levels like ours. Second, we compare combining the linear and rotary permanent magnet motors into a stacked configuration versus using two separate motors. The separate motors are a better solution for short axial travels so we use this design in our prototype.

3.2.1 Permanent Magnet Motor vs. Induction Motor

In this section we compare the power efficiency of permanent magnet and induction motors. We show that for use in our z-θ axis, permanent magnet motors are significantly more power efficient. Of course, there are other factors to be considered in comparing permanent magnet and induction motors. In general, permanent magnet motors are easier to model and control than induction motors. Induction motors dissipate power on the rotor whereas permanent magnet motors do not, except for power dissipated by eddy currents in the magnets. Neither induction motors nor brushless permanent magnet motors require external connections to their rotors. Induction motor rotors are, in simplest form, just a conductor, and therefore can be rugged and inexpensive. Furthermore, in induction motors the same surface can be used for z and θ motors and possibly even as a bearing surface. However, as we shall see, induction motors are significantly less power efficient than permanent magnet motors for small sizes and forces, and this is the deciding factor.

As shown in Figure 3-11, the permanent magnet synchronous motor we consider consists of a magnetic rotor with back iron and a surface-wound stator also with back iron. We use the analysis developed in Appendix A, Continuum Electromechanical Analysis of Permanent Magnet Synchronous Linear Motor with Iron Backing, to predict this motor's force and power dissipation. Table 3.3 lists the parameters describing the permanent magnet motor.

We model the induction motor as shown in Figure 3-11. We use a thin current-sheet model for the stator and rotor currents. This is convenient since we can find an equivalent circuit model when the induction motor rotor is modeled as a thin current sheet but not when it is modeled as a thick current sheet [48]. The induction motor is analyzed in [48] and Appendix B. Table 3.4 lists the parameters describing the induction motor.

Our models compare permanent magnet and induction linear motors with planar geometries. We use these same analyses to compare cylindrical motor geometries such as tubular linear motors and rotary motors. The planar analysis approximates

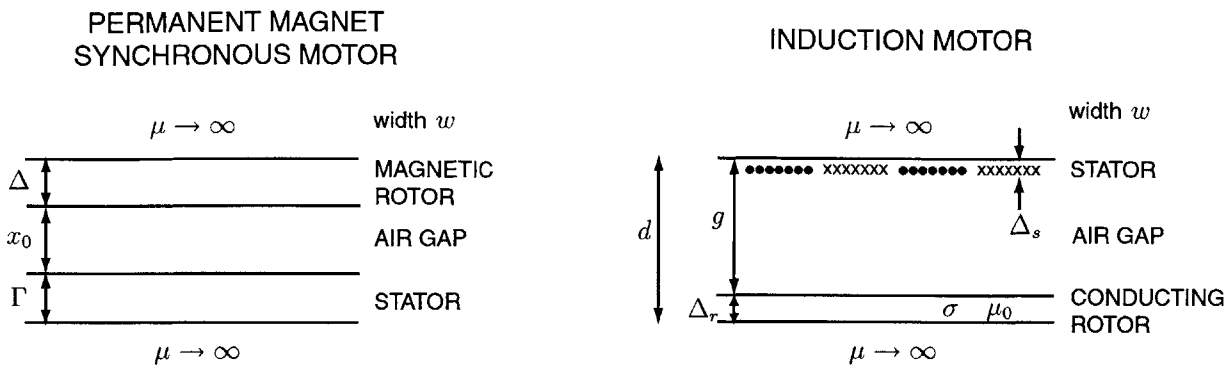

Figure 3-11: Schematic showing layers in a permanent magnet motor and an induction motor. The permanent magnet motor has a surface-wound stator, and the induction motor has a slotted stator.

Parameter	*Description*
Δ	Magnet Thickness
x_0	Air Gap
Γ	Coil Thickness
w	Width

Table 3.3: Permanent magnet motor parameters.

Parameter	*Description*
Δ_r	Rotor Thickness
Δ_s	Coil Thickness
g	Physical Air Gap
d	Effective Air Gap, $d = g + \Delta_r$
σ	Rotor Conductivity
w	Width

Table 3.4: Induction motor parameters.

a cylindrical analysis but avoids the complexities of using Bessel functions.

Force and Power Scaling Laws

In a permanent magnet synchronous motor, force is produced by stator currents interacting with the magnetic field created by the magnets. Thus, the permanent magnet motor force, F_{pm}, is proportional to stator current, I,

$$F_{pm} \propto I. \tag{3.3}$$

Power dissipation in the permanent magnet motor, P_{pm}, is due to Joule heating in the stator and so is proportional to current squared,

$$P_{pm} \propto I^2. \tag{3.4}$$

In an induction motor, force is produced by the interaction between stator and rotor currents. Since rotor currents are induced by stator currents, induction motor force, F_{ind}, is proportional to stator current squared,

$$F_{ind} \propto I^2. \tag{3.5}$$

Power dissipation in the stator and rotor is also proportional to current squared, so total induction motor power dissipation is

$$P_{ind} \propto I^2. \tag{3.6}$$

Thus, for an induction motor, power is proportional to force,

$$P_{ind} \propto F_{ind}, \tag{3.7}$$

but for a permanent magnet motor, power is proportional to force squared,

$$P_{pm} \propto F_{pm}^2. \tag{3.8}$$

Thus, permanent magnet motors are more power efficient at lower force levels, and induction motors are more power efficient at higher force levels.

Motor Comparison

In order to determine which motor is best for a given force range, we find the proportionality constants in equations (3.7) and (3.8) and use these to plot power dissipation as a function of force. The motor with the lowest power dissipation in the given force range is the best for our purposes.

Perhaps the easiest way to determine the proportionality constants between motor force and power is to use values from existing motors. Here, however, we calculate these constants using motor models for the permanent magnet and induction motors.

For the permanent magnet motor we choose a motor pitch length, $l = 6$ cm, and width, $w = 6$ cm, which is typical for our application. We assume a typical permanent magnet remanence for Neodymium Iron Boron (NdFeB) magnets of $\mu_0 M_0 = 1.2$ T. We choose the power optimal coil thickness, $\Gamma = l/10$, as described in Appendix A, and let the windings be copper so that their conductivity is $\sigma = 5.6 \times 10^7\ (\Omega\cdot\text{m})^{-1}$. We choose a magnet thickness of $\Delta = l/8$ and let the motor air gap be $x_0 = 1$ mm. We can now use equation (A.46) to find that for one pitch length of the motor

$$\frac{P_{pm}}{F_{pm}^2} = 0.00389\ \frac{\text{W}}{\text{N}^2}. \tag{3.9}$$

For the induction motor we choose the same motor pitch length, l, stator thickness, $\Delta_s = \Gamma$, and air gap, $g = x_0$, as for the permanent magnet motor. We choose the power optimal rotor thickness, $\Delta_r = 0.8$ mm, by graphing power as a function of Δ_r as explained in Appendix B. Futhermore, we choose to operate the induction motor at the power optimal dimensionless slip frequency $\tilde{S}_+$ which is derived in Appendix B. Using equation (B.5) we calculate that for one pitch length

$$\frac{P_{ind}}{F_{ind}} = 2.62\ \frac{\text{W}}{\text{N}}. \tag{3.10}$$

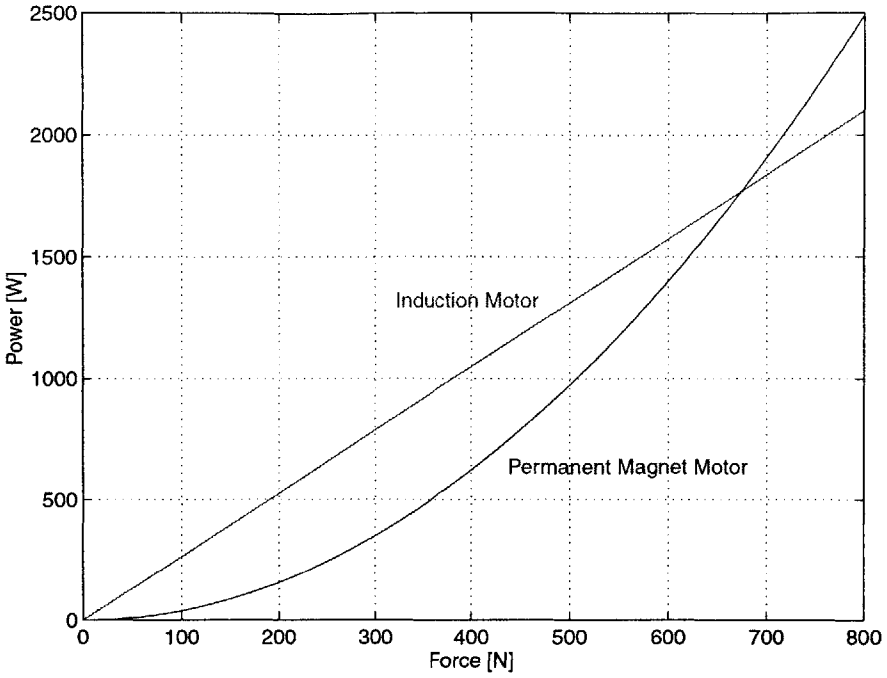

Figure 3-12: Power vs. force for comparable permanent magnet and induction motors. Both motors have a spatial wavelength of $l = 6$ cm, and a working area of 36 cm^2.

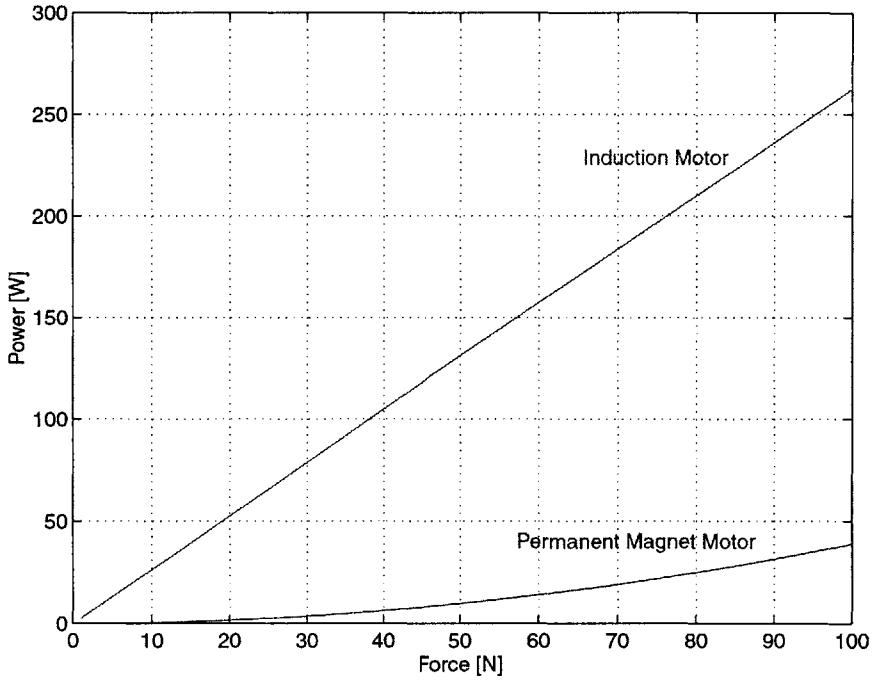

Figure 3-13: Power vs. force for comparable permanent magnet and induction motors. This figure zooms in on the force range of 0–100 N in Figure 3-12.

We plot power as a function of force in Figures 3-12 and 3-13 for these two comparable motors. In the range of 0–50 N that concerns us, the permanent magnet motor is considerably more power efficient than the induction motor. In general, at small enough force levels, permanent magnet motors are always more power efficient. In this particular comparison, both motors dissipate the same power at a force of 674 N, and at higher force levels, the induction motor is more power efficient. This is shown in Figure 3-12. In general, induction motors are more power efficient at higher force levels. Based on this analysis, we choose to use permanent magnet motors in our axis since they are much more power efficient for the force range required.

3.2.2 Stacked vs. Separated Motor Configurations

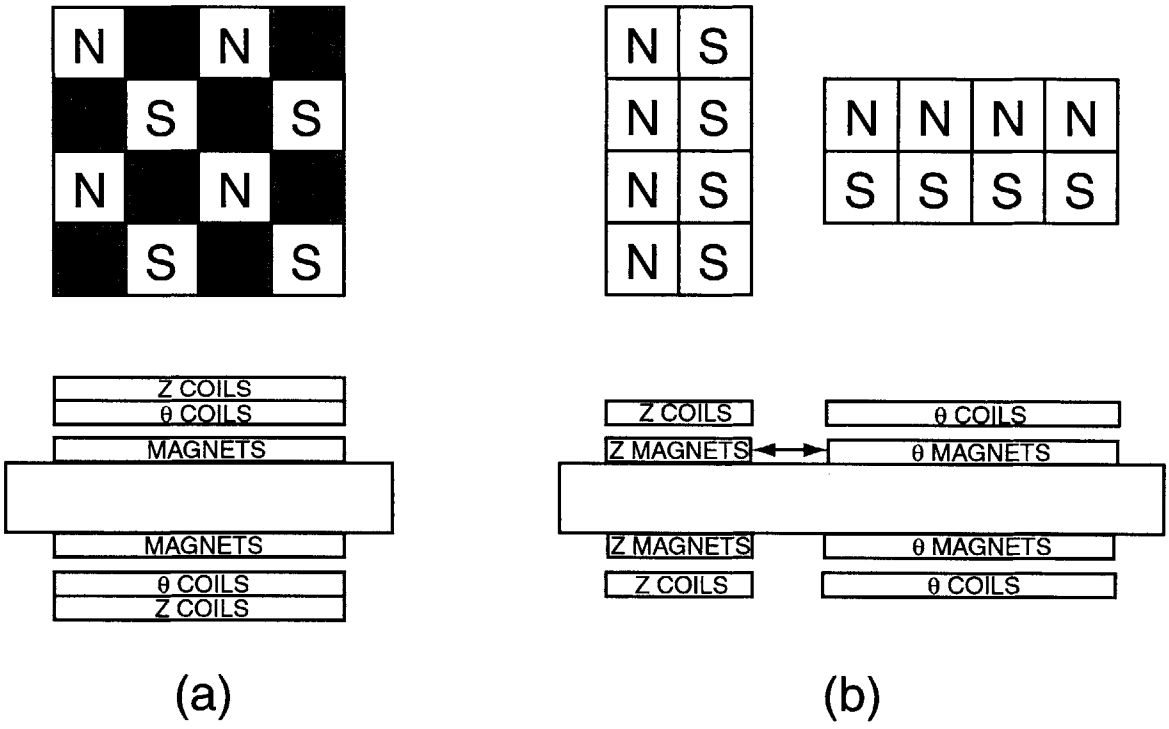

Figure 3-14: (a) Stacked motor and (b) separated motor configurations. The checkerboard magnet array used in the stacked motor can have only a 50% packing density.

Two possible configurations for a z-θ motor are shown in Figure 3-14. In Figure 3-14 (a), a checkerboard magnet array is used like the one in the Anorad design discussed

in section 3.1.5. This same magnet array can interact with either z or θ coils to produce force since it has both rows and columns of magnetic poles. If we filled in the magnet array this would no longer be the case, so this magnet array can have only a 50% packing density.[2] An alternative, more conventional, design is to use two separate magnet arrays as shown in Figure 3-14 (b). In this case 100% magnet packing density is achieved, but two different magnet arrays are required.

Although the stacked motor with a checkerboard magnet array appears more axially compact at first, it is less power efficient than two separate motors for short axial travels. First, note that since the checkerboard magnet array has a 50% packing density, it needs twice the area to have the same number of magnets as the separated motors. Second, since the z coils see the θ coils as an additional air gap, and vice versa, the combined motor is less power efficient than the separated motors. The one disadvantage of the separated motors is the wasted axial travel between them. In fact, however, it is allowable for the z magnets to go under the θ coils, or vice versa, since no net force will be produced.

Since our axis has a short axial travel, we choose to use two separate motors. We design the motors so that the magnetic rotors are axially shorter than their corresponding stators by at least our one inch of axial travel. Thus, the rotors always produce full force inside their stators even as they translate axially with the z-θ shaft. We look at the detailed motor design and optimization in the next chapter, Rotary-Linear Motor Design & Analysis.

3.3 Rotary-Linear Bearing Concepts

Air bearings and hydrostatic bearings are natural choices for providing smooth translation and rotation. Rolling element bearings and sliding contact bearings have excessive friction for high-speed precision motion control. This friction reduces positioning accuracy, limits achievable accelerations, and generates unwanted heat. Magnetic

[2] A checkerboard array of north and south poles without gaps does not have rows and columns of north and south poles and produces no force when interacting with z or θ coils.

bearings would work, but they are too costly and are not required. Thus, we focus on air and hydrostatic bearings.

3.3.1 Hydrostatic Bearings

Hydrostatic bearings offer significantly more damping than air bearings. This is desirable in axes of grinding machines to eliminate chatter and high frequency excitation. However, at high speeds, hydrostatic bearings dissipate a lot of power as heat. Thus, high speed spindles are made with air bearings, not hydrostatic bearings. The other downside of hydrostatic bearings is that they require an oil pump and recirculation system. Since we could implement air bearings without this added overhead, this was the deciding factor in choosing air bearings for our prototype axis.

Kotilainen and Slocum [38, 37] recently investigated modular self-compensating hydrostatic bearings. These cast bearings have self-compensating grooves located on the internal bearing surface which makes them simple to use and inexpensive. They would be a good choice for bearings in future rotary-linear axes. This type of self-compensated bearing was developed by Wasson [72]. He located the self-compensating geometry on the outer surface of the shaft rather than the inner surface of the bearing. It is desirable to have the geometry on the inner surface of the bearing when the shaft travels axially as it does in a rotary-linear axis.

3.3.2 Orifice Air Bearings

The two major air bearing technologies are orifice and porous graphite air bearings. We examine both these technologies and choose porous graphite air bearings since they are cheaper, less sensitive to debris, and easier to integrate into our prototype. Professional Instruments (see Appendix F) makes cylindrical orifice air bearings. Although many orifice air bearings use the orifice to restrict air flow, Professional Instruments' air bearings are elementally compensated with a proprietary groove technology in the bearing surface. Orifice and groove compensated air bearings are sensitive to debris which can block the orifices or grooves and crash the bearing. This is especially

a concern for us since the translation of the shaft can bring debris into the bearing. Professional Instruments suggests using a custom bearing with a special low-pressure region in front of the actual bearing. The clearance in this region would be small, but larger than that of the actual air bearing. The length of this region would be half the travel of the axis, about 1 centimeter, so that the shaft would never bring debris into the air bearing region as it translated axially. The Professional Instruments cylindrical air bearings each consist of two discrete bearing regions so that the bearing can exert a moment on the shaft. Since we want to use two air bearings in our design, the system would be over-constrained. The design could still work if a flexure, such as a circular diaphragm, is used to position one bearing and eliminate the over-constraint. The cost of the orifice bearing is higher than the porous graphite bearing; the need for a special clearance region and mounting method would make this a much more expensive and complex option.

3.3.3 Porous Graphite Air Bearings

An alternative air bearing technology commercialized by New Way Bearings (see Appendix F) uses porous graphite. The air pressure is uniformly distributed at the bearing surface, and the porous graphite restricts and dampens the air flow [14]. For small air gaps below 4 μm the air film in porous graphite bearings can provide squeeze film damping, while orifice air bearings do not have much damping. Also, if debris do get into the bearing, the soft graphite will scratch locally, but the rest of the bearing can carry the load and the bearing will not crash. Furthermore, if there is a loss of air, the porous graphite bearing can tolerate some sliding contact since the graphite is soft compared to a steel shaft. In an orifice bearing, the bearing is typically hard coated aluminum or stainless steel which can mar and scratch a steel shaft. Another advantage of the porous graphite air bearings is that they are packaged with O-rings that are compliant enough to allow the bearings to self-align. This eliminates the overconstraint problem faced with Professional Instruments' bearings. In addition to their crash resistance, added damping, and self-alignment properties, the New Way bearings are also cheaper and more readily available, so we choose them for our

prototype.

3.4 Rotary-Linear Sensor Concepts

We need to measure rotation and translation of the z-θ axis so that we can control the axis position. Although many types of rotary sensors and linear sensors exist, few of them allow the moving part to both rotate and translate. Among common linear sensors, laser interferometers and linear variable differential transformers (LVDT's) allow rotation movement as well as translation. However, common rotary sensors do not allow translation. For example, a standard optical encoder does not allow the encoder disk to translate axially in its housing.

In this section we investigate various rotary-linear sensor concepts. Since linear sensors that can tolerate rotation exist, we particularly focus on developing a rotary sensor that can tolerate translation. In section 3.1, Review of Existing z-θ Stages, we already saw a number of rotary-linear sensor concepts such as a rotating polarizer and a 2-D optical encoder. We briefly review these and present additional concepts in this section.

For our initial prototype, we choose to implement the tilted-mirror sensor. The design and analysis of this sensor is described in detail in chapter 5, Tilted-Mirror Sensor Design, and its fabrication is described in section 6.4 of Chapter 6, Prototype z-θ Axis. This sensor works very well for our initial prototype but is not intended to be the final sensor solution due to its large mass and inertia. The tilted-mirror's inertia is 2.8 times greater than the inertia of the entire rest of the axis, and its mass causes a cantilever resonance that limits the bandwidth of the rotary controller. Originally, we planned to replace this sensor with the helicoid mirror sensor. That did not happen, however, since the the helicoid mirror proved too expensive to fabricate. Also, implementing the tilted-mirror sensor proved more challenging than we initially thought. The next generation rotary-linear axis prototype will likely use a 2-D encoder as a sensor.

3.4.1 Sensor Specifications

Parameter	*Specification*
Linear Travel	2.5 cm
Linear Resolution	0.1 μm
Max. Linear Speed	1.5 m/s
Update Rate	10 kHz
Rotary Travel	360° (unlimited)
Rotary Resolution	10 μrad
Max. Rotary Speed	235 rad/s (2240 rpm)
Update Rate	10 kHz

Table 3.5: Desired z-θ sensor specifications.

In general, the z-θ axis can be used either as a positioning axis or as a high-speed spindle. Our first prototype is mainly intended to be a positioning axis, but we also plan to use it to study some aspects of the spindle application. The sensor specifications for these two different applications are quite different. For use as a positioning axis, we require high resolution and accuracy in both translation and rotation. The axis will have extremely high accelerations, but the velocities will not be that large since the distance traveled is small. For use as a high-speed spindle, we still need high resolution z sensing, but we only need low resolution θ sensing so that we can commutate the rotary motor. In fact, it is possible to use sensorless control in this case as described in section 8.5. The spindle application requires very high rotary speeds which our first prototype cannot attain.

Our prototype sensor specifications are overly stringent so that we can investigate using the prototype z-θ axis as a positioning axis and as a spindle. Desired sensor specifications are listed in Table 3.5. The sensor must accomodate the full range of axis motion, 2.5 cm in z, and unlimited in θ. For use as a positioning axis, we do not require full rotation capability. The linear resolution is 0.1 μm, and the rotary resolution is 0.1 μm at a radius of 1 cm, or 10 μrad. The maximum linear velocity,

v_{max}, is reached after peak acceleration of $a_{max} = 12$ g's over a distance of $x = 1$ cm,

$$v_{max} = \sqrt{2a_{max}x} = 1.5\ m/s. \tag{3.11}$$

The maximum rotary velocity, ω_{max}, due to a 90° rotation, $\theta = \pi/2$, at a peak rotary acceleration of $\alpha_{max} = 17,530$ rad/s^2 is

$$\omega_{max} = \sqrt{2\alpha_{max}\theta} = 235 \text{ rad/s (2,240 rpm)}. \tag{3.12}$$

3.4.2 Introduction to Rotary-Linear Interferometric Sensors

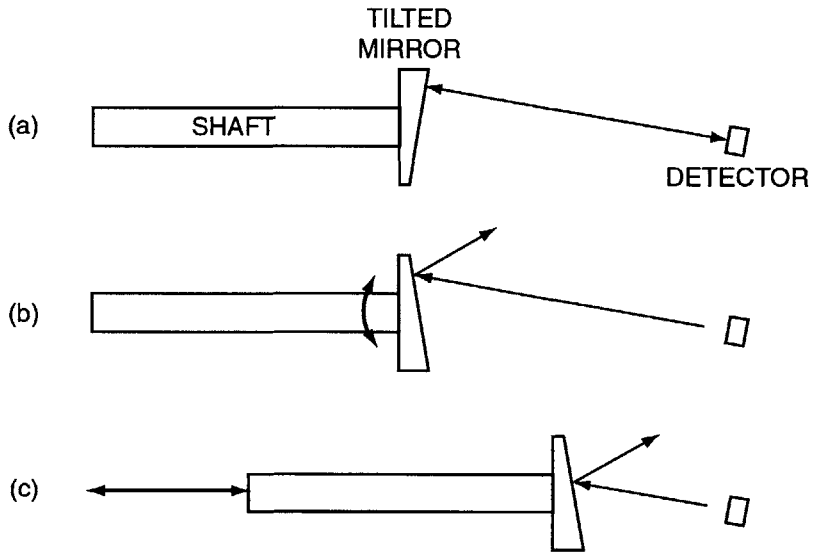

Figure 3-15: Schematic showing general difficulties with designing an interferometric rotary-linear sensor: (a) A laser beam is directed normally at a tilted mirror so that it returns to the detector. (b) As the shaft and mirror rotate, the beam traces out an ellipse in the measurement plane and so misses the detector. (c) As the shaft and mirror translate, the major and minor diameters of the ellipse change.

Many of our rotary-linear design concepts are based on plane mirror interferometry. These include the prism-mirror sensor, tilted-mirror sensor, helicoid mirror sensor, and rotating half wave plate sensor. This is because plane mirror interferometry is an excellent solution for linear sensing, and it seems reasonable to try to adapt it to rotary sensing as well.

One of the main difficulties in designing a rotary interferometric sensor that can tolerate rotary and linear movement is getting the laser beam to hit the detector. For example, consider the situation shown in Figure 3-15 (a): We measure distance to a tilted mirror attached to a rotating shaft. As the shaft rotates, the path length of the laser beam changes. In order to achieve high resolution we would like to tilt the mirror by several degrees. We send the beam in at a slight tilt as shown in Figure 3-15 (a) so that it reflects normally off the mirror and hits a detector. However, as shown in Figure 3-15 (b), when the mirror has rotated, the beam no longer returns to the sensor. Furthermore, as shown in Figure 3-15 (c), when the shaft translates axially, the beam walks along the mirror since the beam is tilted.

Each of our sensor concepts deals with this issue. The prism-mirror sensor sends the laser beam in parallel to the rotation axis so that the beam does not walk. It uses a prism to refract the beam so that the beam always reflects normally off the tilted mirror. Unfortunately, as is shown in section 3.4.3, the optical path length is constant as the shaft rotates, so that the sensor will, in fact, not sense rotation. The tilted-mirror sensor avoids the problems shown in Figure 3-15 by limiting the mirror tilt to very small angles of milliradians. This is the sensor we implement on our prototype axis. It is described in detail in Chapter 5.

The helicoid mirror sensor provides a radial ramp surface to the beam so that the beam sees a constant mirror tilt as the shaft rotates. Thus it is possible to reflect the beam normally off the helicoid, although the angle is still limited by beam walk. The rotating half-wave plate sensor uses a beam parallel to the axis of rotation which reflects normally off a mirror so that the problems of Figure 3-15 are avoided. We now look at these concepts in greater detail.

3.4.3 Prism-Mirror Sensor

One of our first ideas for a rotary-linear sensor is shown in cross-section in Figure 3-16. Initially, we were excited by this idea since it avoids the problems shown in Figure 3-15:

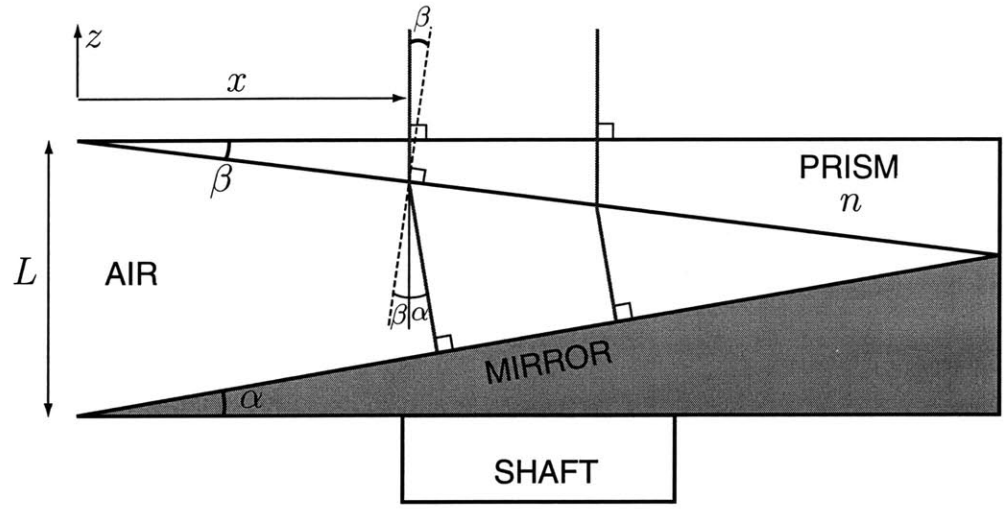

Figure 3-16: Prism-mirror sensor. A prism with apex angle β deviates a laser beam to reflect normally from a mirror tilted at an angle of α. Unfortunately, the optical path distance does not change with x so the sensor cannot measure x motion.

- The incoming beam does not walk as the z-θ axis is translated in z since the incoming beam is parallel to the axis of rotation.

- The returning beam is coincident with the incoming beam since it reflects off the mirror normally. This allows the returning beam to always hit the detector.

Unfortunately we were disappointed to discover that this configuration does not sense rotation as will be clear from the following discussion.

A mirror with a tilt, α, of several degrees is attached to the z-θ shaft. As the shaft rotates, the stationary laser beam traces a circular path on the prism. The cross-section shown in Figure 3-16 rotates with the shaft. Thus, in the cross-section shown, the incoming laser beam appears to translate in the x direction as the shaft rotates.[3] It is easiest to analyze the sensor from this perspective. A prism attached to the mirror refracts the incoming beam so that it reflects normally from the mirror.

We now show that the total optical path length is unfortunately invariant to changes in the coordinate x. We choose the prism angle β so that the prism refracts the beam to hit the mirror at normal incidence. Applying Snell's Law to the prism/air

[3]In fact, the coordinate x varies as the cosine of shaft rotation angle.

interface in Figure 3-16 yields the relationship,

$$n \sin \beta = \sin(\alpha + \beta), \tag{3.13}$$

where n is the prism's index of refraction. The total optical path length, d, is

$$d = nx \tan \beta + (L - x \tan \beta - x \tan \alpha) \cos \alpha. \tag{3.14}$$

The first term in equation (3.14) is the path length in glass, and the second term is the path length in air. We can show that equation (3.14) is invariant to x by using Snell's Law, equation (3.13). After some algebra, we obtain

$$d = L \cos \alpha. \tag{3.15}$$

This says that the optical path length, d, is invariant to x movement. This sensor thus does not detect shaft rotation.

3.4.4 Tilted-Mirror Sensor

A schematic of the tilted-mirror sensor is shown in Figure 3-17. The slightly tilted mirror rotates with the z-θ shaft. Two interferometers measure distance to the tilted mirror. From these two measurements we calculate the mirror's spatial orientation. Since the mirror is fixtured to the shaft, the mirror's orientation is directly related to the shaft's rotation angle, θ.

This is the sensor we use on our z-θ prototype axis. It's design and analysis are contained in Chapter 5, Tilted-Mirror Sensor Design & Analysis. It's fabrication is described in section 6.4. Marsette Vona describes the detailed implementation of this sensor in his Master's thesis [70]. The sensor resolution is limited by its tilt angle, α. In our prototype axis, we use a sensor tilt of $\alpha = 4.7$ mrad which yields an angular resolution of 1,366,000 counts/rev or 4.6 μrad (0.95 arcsec). Although the two interferometers only provide relative distance measurements, the tilted-mirror sensor provides an absolute angular measurement since it measures mirror orientation.

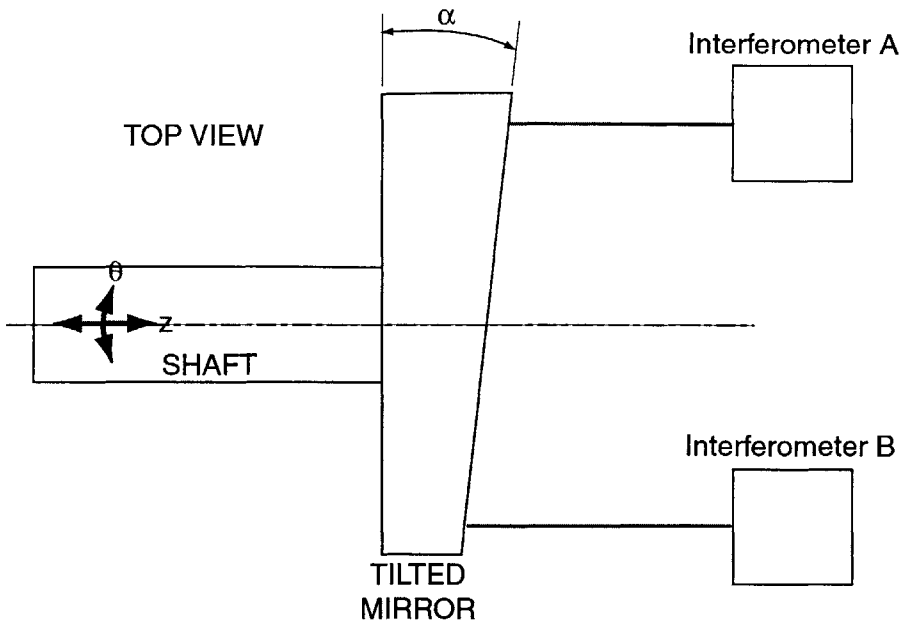

Figure 3-17: Tilted-mirror sensor. Two interferometers measure distance to a slightly tilted mirror. The mirror tilt, α, is 4.7 milliradians.

3.4.5 Helicoid Mirror Sensor

The helicoid sensor idea was first proposed to us by Dr. Carl Zanoni, Vice President of R & D at Zygo Corporation. Dr. William Plummer, Director of Optical Engineering at Polaroid, also met with us several times to discuss the idea and the possibility of grinding the helicoid mirror. Marsette Vona also analyzed the helicoid mirror concept in his Master's thesis [70].

The basic idea is to mount a mirror in the shape of a radial wedge, or helicoid, to the end of the rotary-linear axis as shown in Figure 3-18. The radial wedge has a constant tilt angle α at a given radius as it rotates, unlike a tilted plane mirror. Thus, the beam can be normal to the radial wedge mirror surface and will still return to the detector as the shaft is rotated: we have avoided the problem shown in Figure 3-15 (b). However the beam will still walk on the mirror slightly as shown in Figure 3-15 (c) as the shaft translates. The helicoid sensor cannot provide 360° measurement since approximately 10° of the helicoid mirror is unusable at the transition from high to low point. For use on the rotary-linear positioning axis, this is not a problem since

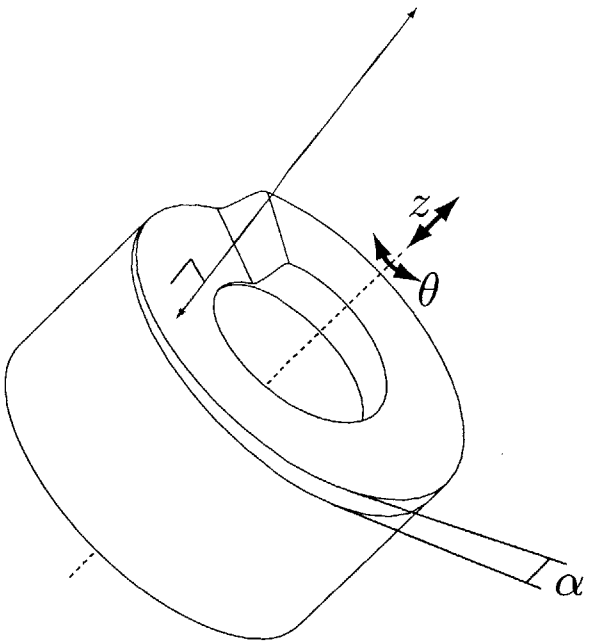

Figure 3-18: Helicoid Miror Sensor. The laser interferometer measurement beam is directed normal to a radial wedge, or helicoid, mirror so that shaft rotation is measured. Another beam measures translation by reflecting off the flat mirror in the center. A detailed mechanical drawing of the helicoid mirror is shown in Figure D-6. Figure drawn by Marsette Vona.

we do not need to spin the part all the way around.

We designed on paper a helicoid sensor with a 1 mm pitch and a 1.5 inch radius. This results in a tilt angle of $\alpha = 4.2$ mrad. One of the main benefits of the helicoid sensor is that it can have a macroscopic tilt angle, whereas the tilted-mirror sensor must have a small tilt angle so that the beam returns to the detector. In fact, however, the tilt angle for the helicoid mirror is roughly the same as that of the tilted-mirror sensor. Thus, the helicoid mirror sensor offers roughly the same resolution as the tilted-mirror sensor. Before testing the tilted-mirror sensor we did not know we would be able to achieve such a large tilt, and so the helicoid sensor seemed to promise much higher resolution at that time.

Another complication with the helicoid mirror sensor is that the helicoid surface has small principal curvatures, whereas the tilted-mirror is globally flat. We estimate that for our proposed helicoid mirror the principal curvatures are 0.110 m^{-1}

and $-0.110\ \mathrm{m}^{-1}$. We may be able to correct for this curvature using a weak cylindrical lenses. For example, 1/8 diopter cylindrical spectacle lenses are commercially available, and are very close to the correction we require.

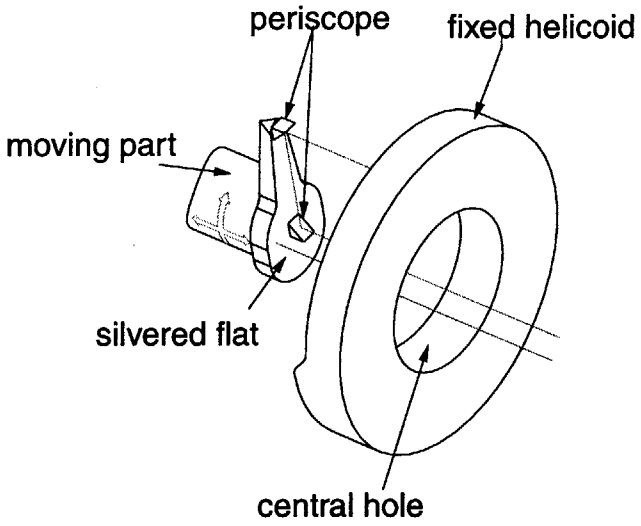

Figure 3-19: Helicoid sensor periscope concept. A small periscope is attached to the rotary-linear axis, and the massive helicoid mirror is held stationary. The periscope optics scan the surface of the helicoid. Figure drawn by Marsette Vona [70].

One significant benefit of the helicoid sensor over the tilted-mirror sensor is that the helicoid needn't be attached to the shaft. Instead, it is possible to use a stationary helicoid and have only a small periscope attach to the shaft as shown in Figure 3-19. In this configuration, the sensor mass and inertia are significantly reduced. One beam which is offset from the rotation axis measures z distance off the silvered flat. The other beam is aligned with the rotation axis and is scanned across the helicoid by the periscope. We met with Dr. William Plummer and his team at Polaroid twice to discuss fabricating the helicoid mirror. Since grinding the helicoid mirror on an aspheric optics grinding machine would take a long time and be expensive, we were not able to fabricate a prototype helicoid mirror.

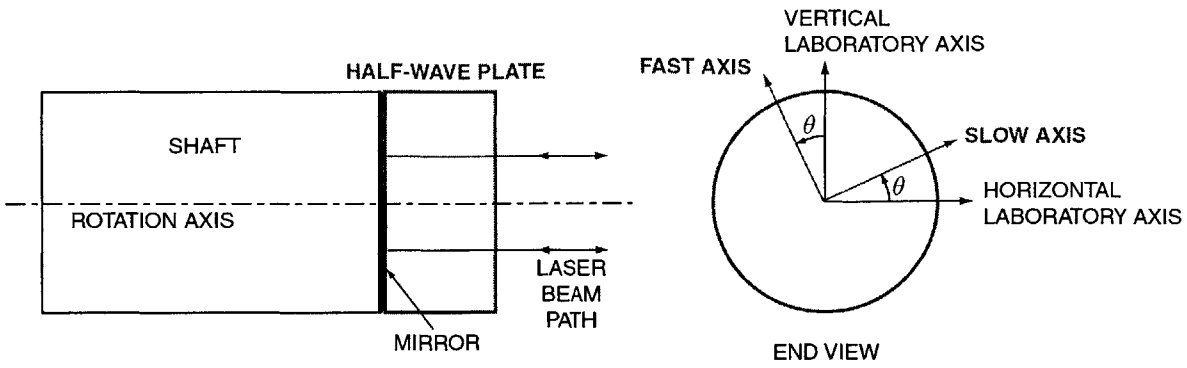

Figure 3-20: Rotating half-wave plate sensor. The optical path length of the measurement beams changes as the half-wave plate rotates. Two beams polarized in different ways are needed for quadrature sensing.

Crystal	n_s	n_f
Muscovite Mica	1.599	1.594
Quartz	1.5534	1.5443
Calcite	1.6584	1.4864

Table 3.6: Slow and fast refractive indices, n_s and n_f, of some birefringent crystals. Data from [24].

3.4.6 Rotating Half-Wave Plate Sensor

A half-wave plate imparts a phase shift to a polarized measurement beam that is a function of the half-wave plate's rotation angle θ. We will show that we can use a half-wave plate to measure shaft rotation angle θ by mounting it to the z-θ shaft and including it in the path of the measurement beam of an interferometer as shown in Figure 3-20. This concept was suggested to us by Professor John Ziegert of the University of Florida. In this section we present a preliminary analysis which shows how the phase of the measurement beam varies with θ.

A half-wave plate is a birefringent crystal which retards light polarized along its slow axis by an integer number of full wavelengths plus one half of a wavelength compared to light polarized along its fast axis. Birefringent crystals have a slightly different index of refraction for light polarized along their fast and slow axes, which are

perpendicular. Table 3.6 lists fast and slow indices of refraction, n_f and n_s, for some common crystals used to make half-wave plates. In general, the phase retardation, Γ, of a phase retarder plate is a function of the wavelength of light in vacuum, λ, the plate thickness, d, and the difference between the slow and fast indices of refraction, $n_s - n_f$,

$$\Gamma = \frac{(n_s - n_f)d}{\lambda}. \tag{3.16}$$

For a half-wave plate we choose the plate thickness, d, so that $\Gamma = (2m + 1)\pi$ where m is any integer. Such a half-wave plate rotates the polarization direction of linearly polarized light by twice the angle between the polarization direction of the incoming light and the half-wave plate's fast axis. Also, half-wave plates change the handedness of circularly polarized light. We shall derive this result next.

We use the Jones calculus [77] to represent the polarization state of light as it passes through a half-wave plate. In this formalism, the polarization state of light is represented as a vector,

$$V = \begin{bmatrix} V_h \\ V_v \end{bmatrix} \tag{3.17}$$

where V_h is the complex electric field amplitude in the horizontal laboratory direction, and V_v is the complex field amplitude in the vertical laboratory direction as shown in Figure 3-20. For example, horizontally polarized light is represented by the vector,

$$\begin{bmatrix} 1 \\ 0 \end{bmatrix}, \tag{3.18}$$

and right-hand circularly polarized light is represented by the vector,

$$\begin{bmatrix} 1 \\ -i \end{bmatrix}. \tag{3.19}$$

In the Jones formalism we represent optical elements by 2×2 matrices. We can multiply several matrices together to obtain the overall transfer matrix of a complex system. We can derive a matrix model for a phase retarder with phase retardation, Γ,

and rotation angle, θ, (see Figure 3-20). First, we resolve the incoming light along the retarder's fast and slow axes. Second, we propagate the light along these axes using the fast and slow indices of refraction. Third, we express the emerging polarization state in the laboratory frame. The first and third steps are just coordinate rotations between the laboratory frame and the frame of the phase retarder. The resulting Jones matrix is, from [77],

$$\begin{bmatrix} e^{-i(\Gamma/2)}\cos^2\theta + e^{i(\Gamma/2)}\sin^2\theta & -i\sin\frac{\Gamma}{2}\sin(2\theta) \\ -i\sin\frac{\Gamma}{2}\sin(2\theta) & e^{-i(\Gamma/2)}\sin^2\theta + e^{i(\Gamma/2)}\cos^2\theta \end{bmatrix}. \tag{3.20}$$

The Jones matrix for a half-wave plate, W, is found by setting $\Gamma = \pi$ in equation (3.20), and simplifying,

$$W = \begin{bmatrix} -i\cos(2\theta) & -i\sin(2\theta) \\ -i\sin(2\theta) & i\cos(2\theta) \end{bmatrix}. \tag{3.21}$$

In our HP plane mirror interferometers, the measurement beam has circularly polarized light. We assume that the outgoing beam is circularly polarized in a right-handed sense, $[\ 1 \quad -i\ ]^T$. After emerging from the half-wave plate it is polarized in a left-handed sense, $[\ 1 \quad i\ ]^T$. To derive this, we apply the matrix W to a beam of circularly polarized left-handed light:

$$W\begin{bmatrix} 1 \\ -i \end{bmatrix} = (-i\cos 2\theta - \sin 2\theta)\begin{bmatrix} 1 \\ i \end{bmatrix} = -ie^{-2\theta i}\begin{bmatrix} 1 \\ i \end{bmatrix}. \tag{3.22}$$

Note that the handedness of the light is changed independently of the half-wave plate's orientation angle, θ. The beam also receives a phase lag of 2θ. This phase lag varies linearly with angle, θ, and thus allows us to sense θ. As shown in Figure 3-20, the beam reflects off a mirror and passes through the half-wave plate again. The handedness of the light is again inverted so that the interferometer sees no change in the polarization state of light returning to it, and the phase is delayed a further 2θ.

Our interferometer uses a He-Ne laser which produces light with a wavelength of

$\lambda = 632.8$ nm. A rotation of $\theta = \pi/2$ delays the measurement beam by λ. Since the interferometers have a resolution of 0.625 nm, this sensor achieves a rotary resolution of

$$\frac{632.8 \text{ nm}}{0.625 \text{ nm}} \times \frac{2\pi}{\pi/2} = 4050 \text{ counts/rev.} \tag{3.23}$$

This resolution is too low for our application. However, it may be possible to increase the resolution by using a half-wave plate that delays the phase by $\Gamma = (2m + 1)\pi$, where the integer m is made as large as possible. For this purpose it is desirable to use a material that has a large difference between its fast and slow indices of refraction so that the thickness required is not too great.

3.4.7 Rotating Polarizer Sensor

An optical sensor based on crossed polarizers is shown in Figure 3-6 and discussed on page 80 of section 3.1.3, "z-ϕ Induction Actuator." This sensor has a reported resolution of 48 μrad.

3.4.8 2-D Encoder

A 2-D transmissive optical encoder is shown in Figure 3-3 and discussed on page 76 of section 3.1.2, "Philips Electromagnetic Actuator." This 2-D encoder transmits light through a grid of transmissive and opaque sections and uses masks with elongated slits to modulate the light.

A 2-D reflective optical encoder is shown in Figure 3-10 and discussed on page 86 of section 3.1.5, "Anorad Rotary-Linear Actuator." This sensor provides a resolution of 0.4 μm in translation and 35 μrad in rotation.

3.5 Summary

In this chapter we first reviewed existing rotary-linear stage designs. Two of the more interesting designs were the Electro-Scientific Industries spindle and the Anorad actuator. The Electro-Scientific Industries spindle has permanent magnets for the

rotary motor inside of a hollow ceramic shaft so that they would not fly off of the shaft at high rotary speeds. This spindle also uses a magnetically preloaded air thrust bearing to couple the linear drive system to the rotating spindle. The Anorad design implements a 2-D encoder and integrates it into the motor surface.

We then developed rotary-linear motor concepts. We showed that permanent magnet motors are much more power efficient than induction motors for our application. We also showed that for short axial travels, separate permanent magnet motors are more power efficient than a motor with a combined magnet array. We then examined several rotary interferometric sensors that can tolerate axial translation. We showed that the prism-mirror sensor unfortunately does not sense rotation. The tilted-mirror sensor is incorporated into our prototype axis but has significant rotary inertia. The helicoid mirror sensor is not readily manufacturable. The rotating half-wave plate sensor concept is promising and should be investigated further.

A 2-D encoder may be the simplest and most cost-effective solution for use on future rotary-linear axes. Initially, we gravitated towards an end-on interferometric-based sensor since we wanted to save the added shaft length required for a sensor with a 2-D grid. In implementing the tilted-mirror sensor, however, we ended up adding at least as much shaft length and significant mass and inertia. The added inertia reduces the axis's angular acceleration; the added mass creates a cantilever resonance which limits the achievable rotary axis bandwidth. Although a 2-D encoder requires some area on the surface of the shaft, the 2-D grid adds an insignificant mass and inertia to the shaft. Furthermore, it is possible to create the 2-D grid on the same surface used for a magnetic rotor [8] or air bearing. This reduces the shaft length further. In the next chapter we look at the design and analysis of the rotary and linear motors.

Chapter 4

Rotary-Linear Motor Design & Analysis

This chapter discusses the design and analysis of the rotary and linear motors which rotate and translate the z-θ axis. Although both motors are permanent magnet synchronous motors, there are many differences between them. We designed and fabricated the linear motor and therefore had a great deal of freedom in optimizing this motor for the z-θ axis. Most of this chapter is therefore concerned with the design and analysis of the linear motor. We purchased the rotary motor which limited our available options. We explain how we selected this motor to achieve maximum axis accelerations.

Our main goal in designing the motors is to maximize achievable linear and rotary accelerations. These high accelerations are required for high-speed machining of small, complex parts. We use frameless motors with the rotors mounted on the moving axis and stators fixed to the machine base. It is the mass and inertia of the rotors that mainly concern us since these add to the mass and inertia of the moving part. Within reason, the sizes of the stators do not matter since they are mounted to the machine base.

In this chapter, we first present some simple scaling laws for achieving high rotary and linear accelerations. Next, we summarize the continuum electromechanical analysis for permanent magnet motors which is presented in detail in Appendix A. We

then use this analysis to design the linear motor for high accelerations: We explain how we choose motor pitch length, coil thickness, air gap, magnet thickness, and the magnet array configuration. We then calculate a theoretical force constant using our analysis and see that it agrees well with the measured force constant. We turn next to the rotary motor and explain how we selected it for high accelerations. Finally, we measure the rotary motor torque constant by measuring its back electromotive force.

4.1 Motor Scaling Laws for High Accelerations

In this section we develop some simple scaling laws to guide us in designing the motors for high rotary and linear accelerations. In particular we are interested in whether the motors should be long and skinny or short and fat. We show that long, skinny motors allow higher accelerations.

The z-θ shaft has a mass, M_s, and inertia, I_s. The linear motor rotor has a radius, R_z, and length, L_z; the rotary motor rotor has a radius, R_θ, and length, L_θ. We approximate the shear stress generated in the two motors as being directly proportional to motor surface area. We will see in section 4.3.2 that for permanent magnet synchronous motors, motor shear stress is proportional to the motor's magnetic pitch length, l. Thus, in this scaling analysis we are assuming a fixed motor magnetic pitch length, l, as the motors radii and lengths change. Futhermore, we are assuming a constant coil thickness as the motors radii and lengths change. The temperature rise due to Joule heating in stator coils is proportional to the square of the coil's thickness [41]. Thus, motors with constant coil thicknesses can withstand the same current levels, and our scaling analysis is thermally neutral. With these assumptions, the linear motor force, F_z, is proportional to its rotor's surface area,

$$F_z \propto 2\pi R_z L_z, \tag{4.1}$$

and that the rotary motor torque, τ, is proportional to its rotor's radius, R_θ, times

its rotor's surface area,

$$\tau \propto 2\pi R_\theta^2 L_\theta. \tag{4.2}$$

The total system mass, M, is

$$M = \pi\rho(R_z^2 L_z + R_\theta^2 L_\theta) + M_s, \tag{4.3}$$

where ρ is the density of the rotor. The total system inertia, I, is

$$I = \frac{1}{2}\pi\rho(R_z^4 L_z + R_\theta^4 L_\theta) + I_s. \tag{4.4}$$

Thus, the linear acceleration, a, is related to the rotors' geometries by

$$a \propto \frac{2\pi R_z L_z}{\pi\rho(R_z^2 L_z + R_\theta^2 L_\theta) + M_s}, \tag{4.5}$$

and the rotary acceleration, α, is related to the rotors' geometries by

$$\alpha \propto \frac{2\pi R_\theta^2 L_\theta}{\frac{1}{2}\pi\rho(R_z^4 L_z + R_\theta^4 L_\theta) + I_s}. \tag{4.6}$$

We would like to choose the radii and lengths of the two rotors, R_z, L_z, R_θ, and L_θ, such that the linear and rotary accelerations, a and α, are both large. The design will need to be balanced so that both a and α are large. For example, a design with a big linear motor and small rotary motor will have a high linear acceleration but low rotary acceleration. If either motor is too small, it will not contribute to the system mass and inertia much, and we can increase the corresponding acceleration by making this motor larger. Once the motor's mass and inertia are no longer insignificant compared to that of the rest of the system, we want to know if it is better to increase the motor's length or radius.

First, consider the choice of the linear motor's radius, R_z, and length, L_z. One way to think about this optimization is to maximize linear force, $F_z \propto R_z L_z$, without letting the total system mass and inertia get too large. The linear motor contributes a mass proportional to $R_z^2 L_z$ to the system mass, and an inertia proportional to $R_z^4 L_z$

to the system inertia. Thus, we are much better off choosing a larger value of L_z and a smaller value of R_z which corresponds to a long, skinny motor.

Second, consider the choice of the rotary motor's radius, R_θ, and length, L_θ. We want to maximize rotary motor torque, $R_\theta^2 L_\theta$, without letting the total system mass and inertia get too large. The rotary motor contributes a mass proportional to $R_\theta^2 L_\theta$ to the system mass, and an inertia proportional to $R_\theta^4 L_\theta$ to the system inertia. The inertia term again leads us favor increases in L_θ over R_θ resulting in a long, skinny motor. In this chapter, we use a similar scaling analysis to optimize the magnet thickness of the linear motor for high accelerations, and to select a rotary motor for high accelerations.

4.2 Linear Motor Electromechanical Analysis

In this section we present the results of an electromechanical analysis of an iron-backed permanent magnet synchronous motor. We use the analytical framework of Melcher [48] in which layers of electromagnetic material—such as magnets, air gap, coils, and iron—are described by transfer relations. Prior analyses by Trumper [66, 67] and Kim [34] have investigated ironless motors with a variety of magnet arrays. This type of analysis provides a wealth of information for optimization and design of motors. The author's Master's thesis, *Thermally Efficient Linear Motor Analysis & Design* [41] extends the analysis presented by Trumper, Kim, and Williams [66] to include an iron backing behind both the magnet array and the coils. In this section we present the framework for this analysis and its key results. We use the key results—analytical expressions for motor force and power consumption—to design the z-axis motor of the z-θ axis. The details of the continuum electromechanical analysis are presented in Appendix A.

4.2.1 Analytical Framework

Figure 4-1 shows a schematic of the layers of electromagnetic material in an iron-backed, surface-wound, permanent magnet motor. An air gap separates the stator

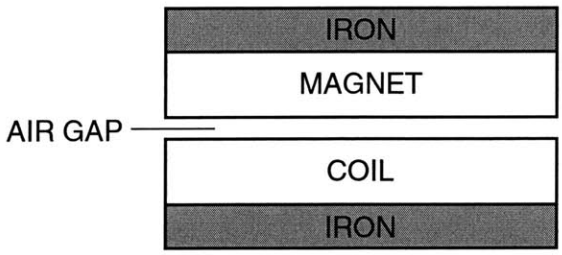

Figure 4-1: Layers of electromagnetic material in a surface wound permanent magnet motor.

from the permanent magnet rotor. The stator is said to be surface-wound since it consists of a uniform coil layer and does not have iron pole pieces. The iron backing behind the magnets and coils increases the strength of the magnetic fields produced and thus increases the motor's force capability compared to an ironless motor. *In fact we will show that a motor with iron backing produces the same force as an ironless motor having twice the coil thickness and twice the magnet thickness.* Thus an iron-bakced motor is far more efficient for our purposes.

Figure 4-2 shows a cross-section of the motor. The three middle layers represent the magnet array, air gap, and coils of the motor. In previous analyses [66, 67, 34] the outer two layers are semi-infinite free space since the authors are modeling ironless motors. Here, we model a motor with iron layers behind the magnets and coils. The thickness of the coils is denoted Γ, the thickness of the air gap is denoted x_0, and the thickness of the magnet array is denoted Δ. The unprimed xyz coordinate frame is afixed to the stator, and the primed $x'y'z'$ coordinate frame is attached to the permanent magnet rotor. The primed coordinate frame is displaced from the unprimed coordinate frame by a distance z_0 in the z direction; this coordinate allows for relative motion between the stator and rotor. The air gap x_0 is held constant in our analysis.

As shown in Figure 4-2 we represent the magnetization of the magnet array and the current density in the coils by Fourier series. Thus, we assume a periodic system with periodic fields. We further assume that the fields and currents do not vary in the y direction since we are analyzing a 2-D cross-section of the motor. In general

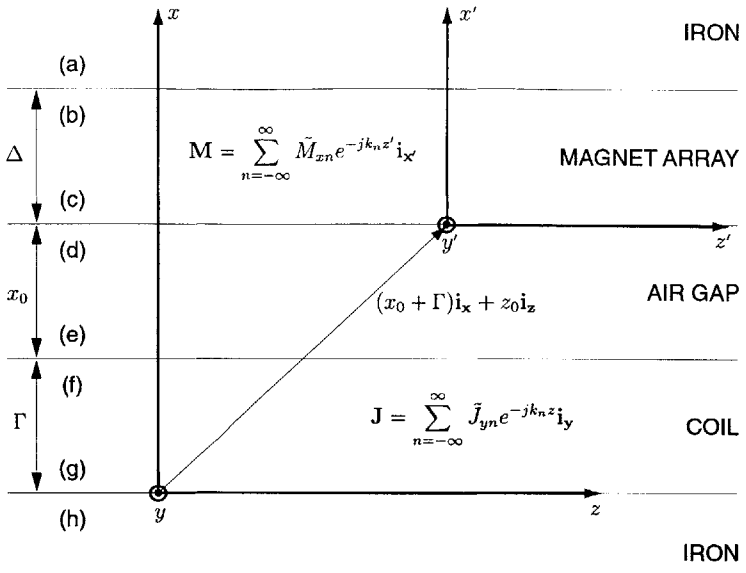

Figure 4-2: Here are the five layers used for the continuum electromechanical analysis of the linear motor. The Fourier expansions for the magnetization and current density are given. The layer thicknesses are Γ, x_0, and Δ. The unprimed coordinate frame is fixed to the stator, and the primed coordinate frame moves with the magnetic rotor.

this is a good approximation, but it ignores end effects. We are also assuming that the motor radius is sufficiently large that we can approximate the actual cylindrical geometry by the planar geometry shown in Figure 4-2. We follow Melcher's notation [48] for Fourier Series in which a periodic quantity such as the current density $\mathbf{J}(z,t)$ which varies periodically in z is written

$$\mathbf{J}(z,t) = \sum_{n=-\infty}^{\infty} \tilde{J}_{yn} e^{-jk_n z} \mathbf{i_y} \tag{4.7}$$

where $\tilde{J}_{yn}$ is the time dependent nth Fourier Series coefficient of the y component of $\mathbf{J}(z,t)$. The wavenumber k_n is

$$k_n = \frac{2\pi n}{l} \tag{4.8}$$

for a quantity whose period is l. Further, γ_n is defined as the absolute value of the wavenumber,

$$\gamma_n = |k_n|. \tag{4.9}$$

The upper and lower sides of the boundaries in Figure 4-2 are labeled with the letters (a) through (h). We are interested in finding the vector potential A_y and the magnetic field intensity H_z at the top and bottom of each surface. Melcher's transfer relations describe the fields within the layers. They relate the H_z's and A_y's for the two edges of a layer via two coupled equations. We also use jump conditions for A_y and H_z across the four layer boundaries. Our goal is to find $\tilde{H}^d_{zn}$ and $\tilde{H}^d_{xn}$ on the (d) surface so that we can evaluate the Maxwell stress tensor along this plane to find an expression for the force produced on the rotor of the motor. In order to simplify the analysis, we solve the layer problem first for the fields due to the magnets and then for the fields due to the coils. These two solutions can then be superposed because the problem is linear. Appendix A, "Continuum Electromechanical Analysis of a Permanent Magnet Synchronous Linear Motor with Iron Backing," carries out this analysis in detail.

Although we represent the magnetization **M** and the current density **J** by Fourier series with infinite harmonics, in order to obtain simple analytic results we consider only the fundamental harmonics of these periodic distributions. Even with this assumption considerable algebra is necessary and we use Maple [73, 25], a symbolic math software package, to do the algebra.

For a magnet array of alternating N-S poles, the fundamental Fourier coefficients for the square wave representing the magnetization are

$$\begin{aligned} \tilde{M}_{x(1)} &= \frac{2}{\pi} M_0 j \\ \tilde{M}_{x(-1)} &= -\frac{2}{\pi} M_0 j, \end{aligned} \tag{4.10}$$

where $\mu_0 M_0$ is the remanence of the permanent magnets. We write the fundamental Fourier coefficients of the current density as

$$\begin{aligned} \tilde{J}_{y(1)} &= J_a + j J_b \\ \tilde{J}_{y(-1)} &= J_a - j J_b. \end{aligned} \tag{4.11}$$

$\mu_0 M_0$	Magnetic Remanence
l	Magnetic Pitch (distance between North poles in N-S-N-S magnet array)
γ	Wavenumber of fundamental harmonic ($= \gamma_1 = 2\pi/l$)
Γ	Coil Thickness
Δ	Magnet Thickness
x_0	Air Gap Thickness
w	Motor Width
z_0	Translation of Rotor Relative to Stator
$2J_a$	Peak Current Density of Phase a
$2J_b$	Peak Current Density of Phase b

Table 4.1: Electromechanical model variables

where $2J_a$ and $2J_b$ are peak current densities of two sinusoidally distributed phases.

4.2.2 Force

In Appendix A, we derive that the force per spatial wavelength, l, produced by a motor of width, w, with iron behind the magnets and coils, and with sinusoidally distributed two-phase stator windings is

$$F_z = \mu_0 M_0 \frac{wl^2}{\pi^2} \left[\frac{e^{\gamma x_0}(e^{2\gamma\Delta} - 1)(e^{2\gamma\Gamma} - 1)}{e^{2\gamma(\Delta+\Gamma+x_0)} - 1} \right] (J_a \cos\gamma z_0 + J_b \sin\gamma z_0). \tag{4.12}$$

This result is an extension of the results in [66, 67] which accounts for the back iron. Table 4.1 lists the variables used in this equation.

It is illuminating to examine the limit of the force produced by an iron-backed motor, equation (4.12), when

$$e^{2\gamma(\Delta+\Gamma+x_0)} \gg 1, \tag{4.13}$$

or, for instance,

$$e^{2\gamma(\Delta+\Gamma+x_0)} > 10, \tag{4.14}$$

which can be re-written as

$$\Delta + \Gamma + x_0 > (0.18)l. \tag{4.15}$$

Since the sum of the magnet thickness, Δ, coil thickness, Γ, and air gap, x_0, in a

motor is usually greater than 0.18 times the motor's magnetic pitch, l, this condition is usually satisfied. Under this approximation, equation (4.12) simplifies to

$$F_z = \mu M_0 \frac{wl^2}{\pi^2} \left[(1 - e^{-2\gamma\Gamma})(1 - e^{-2\gamma\Delta})e^{-\gamma x_0}\right] (J_a \cos\gamma z_0 + J_b \sin\gamma z_0). \tag{4.16}$$

For comparison, we repeat—in suggestive form—the solution for the ironless case with a Halbach magnet array which has appeared in several papers, [66, 67]:

$$F_z = \mu M_0 \frac{\sqrt{2}wl^2}{\pi^2} \left[(1 - e^{-\gamma\Gamma})(1 - e^{-\gamma\Delta})e^{-\gamma x_0}\right] (J_a \cos\gamma z_0 + J_b \sin\gamma z_0). \tag{4.17}$$

The $\sqrt{2}$ in equation (4.17) is there since this equation applies to a motor using a Halbach magnet array. For ironless motors, the Halbach magnet array produces a field that is $\sqrt{2}$ times stronger than a conventional N-S magnet array.

Equations (4.16) for the iron-backed motor and (4.17) for the ironless motor are quite similar. Apart from the $\sqrt{2}$, which was discussed previously, they can be made identical by the following equalities:

$$\Gamma_{ironless} = 2\Gamma_{iron} \tag{4.18}$$

$$\Delta_{ironless} = 2\Delta_{iron} \tag{4.19}$$

The advantages of an iron-backed motor are clear: We can achieve the same force in an iron-backed motor with half the magnet thickness and half the coil thickness of an ironless motor. This result is reasonable since an iron layer behind a magnet produces the image of that magnet, thus effectively doubling its size. The same is true for the coil. This result is only strictly true when the limit of equation (4.13) holds, as will be the case in most motors.

4.2.3 Power

In this section, we derive an expression for the power dissipation in the motor as a function of the various motor parameters. We can invert equation (4.12) to yield the

commutation law for our motor. We then can calculate the power dissipation using an average value of J^2/σ [67]. We introduce the variables N_s for the number of spatial periods l of the coils and N_m for the number of spatial periods l of the magnets which interact with the coils. The power dissipation P_t for the motor with iron is thereby found to be

$$P_t = \frac{(3)2N_s\pi^4\Gamma}{N_m^2\sigma(\mu_0 M_0)^2 w l^3}\left[\frac{e^{2\gamma(\Delta+\Gamma+x_0)}-1}{e^{\gamma x_0}(e^{2\gamma\Delta}-1)(e^{2\gamma\Gamma}-1)}\right]^2 F_z^2. \tag{4.20}$$

For comparison, we repeat the result from [67] for the ironless motor as well:

$$P_t = \frac{(3)N_s\pi^4\Gamma}{N_m^2\sigma(\mu_0 M_0)^2 w l^3}\left[\frac{e^{2\gamma x_0}}{(1-e^{-\gamma\Gamma})^2(1-e^{-\gamma\Delta})^2}\right] F_z^2. \tag{4.21}$$

The factor of three in equations (4.20) and (4.21) is added in the original analysis by Trumper, Williams, and Nguyen [67] to account for non-idealities in the packing factor of the windings, winding length in the end-turns, and fringing fields. Applying the approximation of equation (4.13) to the power dissipation expression for the motor with iron backing, equation (4.20), yields

$$P_t = \frac{(3)2N_s\pi^4\Gamma}{N_m^2\sigma(\mu_0 M_0)^2 w l^3}\left[\frac{e^{2\gamma x_0}}{(1-e^{-2\gamma\Gamma})^2(1-e^{-2\gamma\Delta})^2}\right] F_z^2. \tag{4.22}$$

We use this result in the next section to design our motor for minimum power dissipation.

4.3 Linear Motor Design for High Accelerations

The first step of our linear motor design procedure is to estimate the approximate motor area needed to produce the required 40 N of force. We then select the motor magnetic pitch length, $l \approx 5.0$ cm, which is a key motor design parameter. Next, we use the motor model of the previous section to find the power optimal coil thickness, Γ. To find the power optimal magnet thickness, Δ, we use an analysis similar to the scaling analysis of section 4.1. However, we incorporate the motor model to predict

force produced as a function of Δ instead of assuming force produced is proportional to motor area as is done in equation (4.1).

Once we have determined the motor's ideal parameters, it remains to set the motor's actual parameters as close to these as possible subject to availability of materials and other system design constraints. In section 4.4 we calculate the linear motor force constant using the motor's actual parameters and the motor model of section 4.2. In section 4.5, we experimentally measure the linear motor force constant and verify our theoretical calculation.

4.3.1 Motor Sizing

We size our motor using an estimated shear force density of 1 N/cm^2 (1.4 psi). To arrive at this value, we use the Lorentz force density,

$$\vec{F} = \vec{J} \times \vec{B}, \tag{4.23}$$

where $\vec{F}$ is the volume force density, $\vec{J}$ is current density in the armature windings, and $\vec{B}$ is air gap magnetic flux. Based on our prior experience with motors, we estimate that we can achieve a thermally limited current density of

$$J = 5 \times 10^6 \text{ A/m}^2 \tag{4.24}$$

in the motor coils. To estimate the magnetic field, B, we use the simple magnetic circuit analysis of Appendix C which says that B is a fraction of the magnet's remanent magnetic field, B_r. The fraction is the ratio of the magnet thickness, Δ, to the total effective air gap, $\Delta + \Gamma + x_0$, comprised of the magnet thickness, Δ, actual air gap, x_0, and coil thickness, Γ:

$$B = B_r \left(\frac{\Delta}{\Delta + x_0 + \Gamma} \right). \tag{4.25}$$

For NdFeB rare-earth permanent magnets, $B_r \approx 1.2$ T, so that after allowing for some leakage we assume we can achieve an average magnetic field of

$$B = 0.4 \text{ T} \tag{4.26}$$

over the coil region. Inserting these values of J and B into the Lorentz force density, equation (4.23), we calculate an average volume force density of

$$F = 2 \text{ N/cm}^3. \tag{4.27}$$

in the coil volume. To turn this volume force density into a shear force density we multiply by an estimated coil thickness of

$$\Gamma = 0.5 \text{ cm}. \tag{4.28}$$

The estimated shear force density is

$$f' = 1 \text{ N/cm}^2 \text{ (1.4 psi)}. \tag{4.29}$$

This is the shear force density for small, surface-wound permanent magnet motors like the one we design in this thesis. For larger motors, force densities can be as high as 10 N/cm^2. This is because the coil thickness will be much larger than $\Gamma = 0.5$ cm. Also, motors with slotted stators have higher magnetic fields, B, since the coil thickness does not contribute to the effective air gap seen by the magnets in equation (4.25). Thus slotted motors can achieve magnetic fields closer to the remanent magnetic field strength.

We use the shear force density to determine how large a tubular area the motor requires to achieve its target of 40 N force. We choose a rotor outside diameter of approximately $d = 3$ cm, so that the rotor circumference is $\pi d = 9.4$ cm. Thus, to

achieve a 40 N force, the motor length should be approximately

$$\frac{40 \text{ N}}{f'\pi d} = \frac{40 \text{ N}}{(1 \text{ N/cm}^2)(9.4\ cm)} = 4.2 \text{ cm}. \tag{4.30}$$

This motor size is quite reasonable for our z-θ axis.

4.3.2 Magnetic Pitch Length Selection

The magnetic pitch length, l, is the periodicity length of the magnet array; it is the distance between two north poles in the alternating north-south permanent magnet array of the rotor. The whole motor can be scaled with this parameter. For example, we can imagine a family of motor designs in which the coil thickness, Γ, magnet thickness, Δ, and air gap, x_0, all scale with magnetic pitch, l. This scaling makes sense since it is inherent in the force equation (4.16) and power equation (4.22) of our motor model: The motor force and power depend only on the ratios Γ/l, Δ/l, and x_0/l, and not directly on Γ, Δ, or x_0. Recall that $\gamma = 2\pi/l$, so that the factors, $\gamma\Gamma$, $\gamma\Delta$, and γx_0, are all ratios with respect to l.

The motor force and power do, of course, depend on l itself in addition to the ratios Γ/l, Δ/l, and x_0/l. It is this dependence that can guide our selection of l and thus the motor's overall scale. We are also interested in how the force and power depend on the motor's width, w. First, we look at the motor force for a family of motors in which we maintain constant ratios Γ/l, Δ/l, and x_0/l as l varies. We also assume the current densities in the two-phase windings, J_a and J_b, are constant as l varies. For this family of motors, the force per unit area of motor, f', is proportional to l,

$$f' = \frac{F_z}{lw} \propto l. \tag{4.31}$$

This may at first seem surprising since it says that motor force per area increases as the pitch length inreases. It can be understood as follows: As the pitch length increases, the magnet thickness increases proportionally to maintain the same magnetic field in the air gap. The force increases proportionally to l since the coil carries the same

current density in the same magnetic field but is now proportionally thicker. This explains why the shear force density for our motor is 1 N/cm^2 but can increase up to 10 N/cm^2 for larger motors. The shear force density should be roughly proportional to l.

We now look at how power dissipation varies for this family of motors. Setting the ratios Γ/l, Δ/l, and x_0/l constant in equation (4.22), the power, P_t, per force level squared, F_z^2, is

$$\frac{P_t}{F_z^2} \propto \frac{N_s}{N_m^2 w l^2}. \tag{4.32}$$

Here, N_s is the number of spatial periods l of coils, and N_m is the number of spatial periods l of magnets which interact with the coils. First, let's consider how to design for minimum power dissipation if we had no other design constraints. According to equation (4.32), we want to decrease N_s and increase N_m. However, the number of magnet periods interacting with coils must be less than or equal to the number of coil periods, $N_m \leq N_s$. The best we can do is to set $N_m = N_s$. The power scaling law, equation (4.32), also tells us that power dissipation is inversely proportional to motor width w and the square of the magnetic pitch length, l. With no other constraints we choose the largest motor possible to minimize power dissipation.

Of course, however, motor size is limited so we should really re-phrase the optimization problem as follows: Given a fixed motor length, L, how should we choose l to improve power efficiency? Do we want only one magnetic wavelength, $N_m = 1$, with $l = L$, or is it better to have k wavelengths, $N_m = k$, each of length, $l = L/k$? We add the fixed motor length constraint by setting the number of magnetic wavelengths, N_m, times the length of each wavelength, l, to be constant. The same condition holds for the stator wavelengths N_s. Our fixed motor length constraint is

$$N_s l = N_m l = \text{const.} \tag{4.33}$$

We also fix the motor width,

$$w = \text{const.} \tag{4.34}$$

Applying these two constraints to the power scaling law, equation (4.32), we arrive at an expression for how power dissipation varies with l given a fixed total motor length and width,

$$\frac{P_t}{F_z^2} \propto \frac{1}{l}. \tag{4.35}$$

Thus, we should choose the magnetic pitch length, l, to be as large as possible.

Both the shear force density and power scaling results tell us to increase l. The shear force density is proportional to l (4.31), and power dissipation for a motor of fixed size is inversely proportional to l (4.35). The downside of increasing l is that the whole motor scales up with l. For our motor size this is not a problem, and we set l equal to the length of our motor, L, and $N_m = 1$. Our motor sizing analysis results in a desired motor length of roughly 4.2 cm. Since magnets are readily available in 0.5 inch and 1 inch sizes, we choose a magnetic pitch length and motor length of approximately 2 inches (5.08 cm). With gaps of twenty thousandths of an inch between 0.5 inch magnets, our final magnetic pitch length is 2.080 inches, or

$$l = 5.283 \text{ cm}. \tag{4.36}$$

4.3.3 Coil Thickness

By selecting the magnetic pitch length, l, we have selected an overall scaling for our motor. We now need to determine optimum thicknesses for the coil, Γ, and magnets, Δ. We optimize the coil thickness for minimum power dissipation at a given force level. The Γ dependence in the power equation (4.22) holding all other variables constant is

$$P_t(\Gamma) \propto \Gamma \frac{1}{(1 - e^{-2\gamma\Gamma})^2}. \tag{4.37}$$

For comparison, the result in the ironless case is [67]:

$$P_t(\Gamma) \propto \Gamma \frac{1}{(1 - e^{-\gamma\Gamma})^2}. \tag{4.38}$$

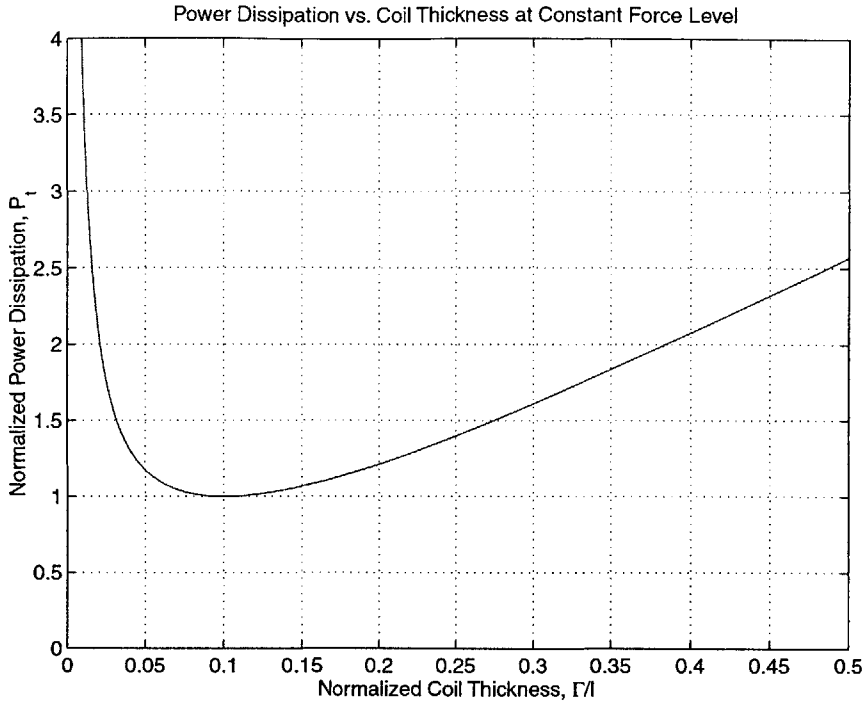

Figure 4-3: Power dissipation as a function of coil thickness.

The difference between the expressions for the iron-backed and ironless cases is a factor of 2 in front of the Γ in the exponent. Setting $\partial P_t/\partial\Gamma = 0$ yields a transcendental equation whose solution is $2\gamma\Gamma \approx 1.25$, or

$$\Gamma_{optimal} \approx \frac{l}{10}. \tag{4.39}$$

For the ironless case, the power optimal thickness is $l/5$ [67]. The power optimal coil thickness for an iron-backed motor is half that of an equivalent ironless motor.

Although we have found the optimal thickness, it is important to realize that the power vs. coil thickness plot is very flat near this minimum. Figure 4-3 plots normalized power dissipation as a function of normalized coil thickness, Γ/l. We see that the region, $0.06 \leq \Gamma/l \leq 0.16$, yields power dissipation within 10% of the minimum at $\Gamma/l = 0.10$. We choose the power optimal coil thickness, $\Gamma/l = 0.10$, for our motor.

	No Air Gap	*Small Air Gap*	*Large Air Gap*
Air Gap, x_0 [mm]	0	0.38	0.76
Force, F_z	100%	96%	91%
Power Dissipation, P_t	100%	109%	120%

Table 4.2: Motor force and power dissipation at different air gaps. The calculations assume a motor magnetic pitch length of $l = 5.283$ cm.

4.3.4 Air Gap

Motor force and power efficiency increase as the air gap between the stator and rotor decreases. However, a smaller air gap requires higher tolerances and better mechanical alignment. For these reasons, it is desirable to have a larger air gap, especially in a prototype machine. A larger air gap also provides better thermal insulation between a hot stator and the rotor. In this section we look at how much force and power efficiency we lose by using a larger air gap. We have already noted that force and power efficiency depend only on the ratio of the air gap, x_0, to the magnetic pitch length, l. We choose a larger magnetic pitch length, l, to maximize force and power efficiency; it also allows us to have a larger air gap.

From the force equation (4.16), the force, F_z, decreases with increasing air gap, x_0, as

$$F_z \propto e^{-\gamma x_0}. \tag{4.40}$$

From equation (4.22), power dissipation, P_t, increases with increasing air gap, x_0, as

$$P_t \propto e^{2\gamma x_0}. \tag{4.41}$$

As shown in Table 4.2, a small air gap of $x_0 = 0.38$ mm (0.015 inch) reduces motor force by 4% and increases power dissipation by 9% over an ideal motor with zero air gap. By doubling the size of the air gap to $x_0 = 0.76$ mm (0.030 inch), we reduce motor force by 5% and increase power dissipation by 10%[1] over a motor with an air

[1] 120%/109% = 110%

gap of $x_0 = 0.38$ mm. Since for mechanical reasons it is desirable to have a larger air gap in a prototype motor, and the decrease in motor performance is not great, we choose a larger air gap of

$$x_0 = 0.84 \text{ mm}. \tag{4.42}$$

4.3.5 Magnet Thickness

Thicker magnets increase the motor's force and decrease its power dissipation. From equation (4.16), with all other variables constant, the force approaches a maximum value exponentially as magnet thickness, Δ, increases,

$$F_z \propto \left(1 - e^{-2\gamma\Delta}\right). \tag{4.43}$$

This proportionality assumes constant currents and hence constant power dissipation. From equation (4.22), with all other variables constant, the power dissipation approaches a minimum value exponentially as magnet thickness increases,

$$P_t \propto \frac{1}{\left(1 - e^{-2\gamma\Delta}\right)^2}. \tag{4.44}$$

This proportionality assumes constant motor force. Thus, in general, one should choose magnets as thick as possible subject to motor size and magnet cost constraints. Since the additional force and power efficiency gained with increasing magnet thickness fall off exponentially, there will be an optimum magnet thickness; for any further increase in magnet thickness, the increased motor size and magnet cost outweight the improvement in motor force and power efficiency.

In the design of the z-θ axis, however, we must also take into account that added magnet thickness increases the mass and inertia of the moving shaft. In particular, we are not so much interested in minimizing power dissipation for a given force level, but rather we are interested in minimizing power dissipation for a given acceleration level. Thus, instead of using power dissipation per force squared, P_t/F_z^2, as an optimization metric, we use linear motor power dissipation per linear acceleration, P_t/a^2, and

Shaft Density (steel)	ρ_s	7806 kg/m^3
Shaft Length	L_s	36.6 cm
Shaft Radius	R_s	0.95 cm
Rotary Motor Magnet Mass	M_θ	0.19 kg
Rotary Motor Inertia	I_θ	3.6×10^{-5} kg·m^2
Magnet Density (NdFeB)	ρ_m	7500 kg/m^3
Linear Motor Magnet Length	L_m	5 cm
Linear Motor Magnet Pitch	l	5 cm
Linear Motor Magnet Thickness	Δ	(variable)
Linear Motor Magnet Outer Radius	R_o	$R_s + \Delta$

Table 4.3: Parameters used in the linear motor magnet thickness optimization. Note that these are approximations of parameters used during the design process and not the final parameter values.

rotary motor power dissipation per angular acceleration, P_r/α^2, as metrics. The linear motor magnet thickness affects angular acceleration since thicker magnets increase the the total shaft inertia.

The moving shaft of radius, R_s, length, L_s, and density, ρ_s, has mass,

$$M_s = \pi \rho_s R_s^2 L_s + M_\theta, \tag{4.45}$$

and inertia,

$$I_s = \frac{1}{2} \pi \rho_s R_s^4 L_s + I_\theta, \tag{4.46}$$

where we have included the mass, M_θ, and inertia, I_θ of the rotary motor's rotor. We model the magnet layer as an annular ring with an inner radius equal to that of the shaft, R_s, and outer radius, R_o, determined by the thickness of the magnet layer, Δ,

$$R_o = R_s + \Delta. \tag{4.47}$$

The annular magnet ring of density, ρ_m, and length, L_m, has mass,

$$M_m = \pi \rho_m \left(R_o^2 - R_s^2 \right) L_m, \tag{4.48}$$

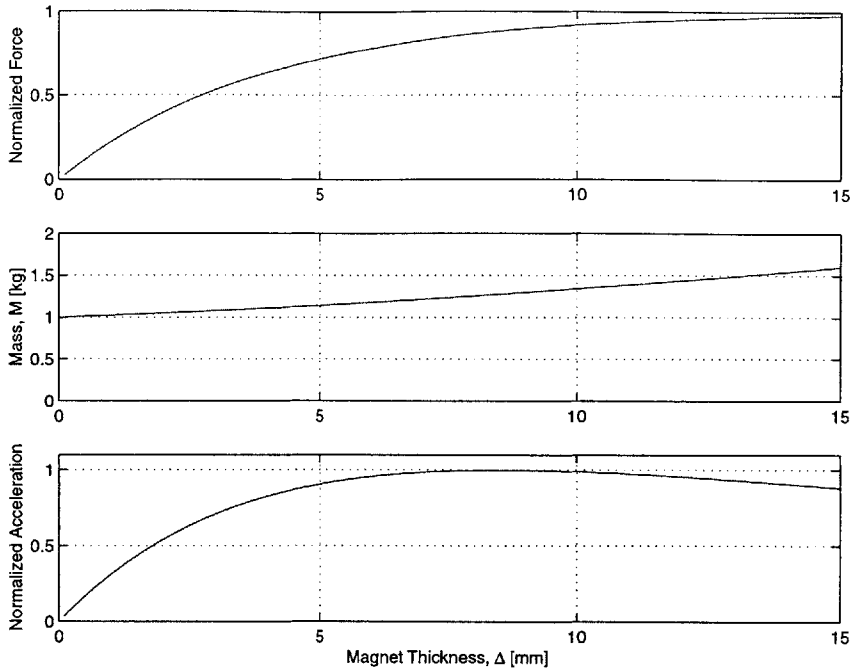

Figure 4-4: Motor force at constant power, total mass, and linear acceleration as functions of linear motor magnet thickness.

and inertia,

$$I_m = \frac{1}{2}\pi\rho_m \left(R_o^4 - R_s^4\right) L_m. \tag{4.49}$$

The total moving mass is the sum of that due to the shaft and the magnet ring

$$M = M_s + M_m, \tag{4.50}$$

and the total inertia is

$$I = I_s + I_m. \tag{4.51}$$

Table 4.3 lists the values of the parameters used in this analysis.

The linear motor force at constant power, total moving mass, M, and linear acceleration, a, are plotted as functions of magnet thickness, Δ, in Figure 4-4. Linear motor force exponentially approaches its maximum value as magnet thickness increases, but the moving mass increases almost linearly with magnet thickness as well. Thus, for thick magnets, the increase in mass is greater than the increase in force, and

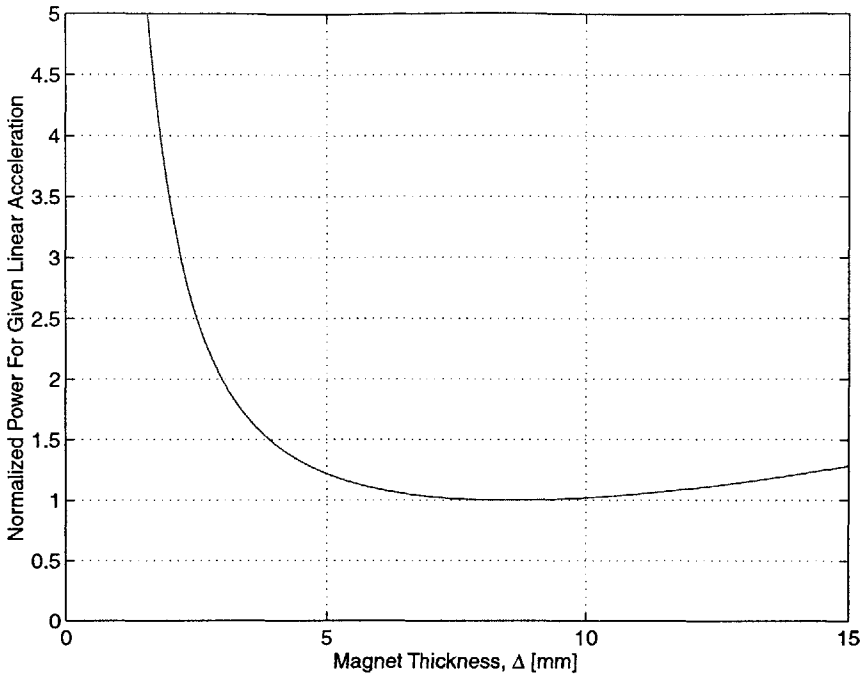

Figure 4-5: Linear motor power for a given linear acceleration vs. magnet thickness.

acceleration is reduced. The linear acceleration is maximum at a magnet thickness of $\Delta = 8.5$ mm.

Another way of looking at this optimization problem is to plot power required for a given linear acceleration as a function of magnet thickness as shown in Figure 4-5. From this plot we see that $\Delta \geq 3$ mm to achieve low power dissipation. We also have the requirement that $\Delta \leq 22$ mm, but this is not shown on the plot because we have a more stringent requirement on Δ's maximum value due to the rotary accelerations which we examine next.

The linear motor magnets do not affect the rotary motor's torque, but they do increase the total system inertia. Thus, angular acceleration decreases with increasing linear motor magnet thickness. The constant rotary motor torque, total rotating inertia, I, and angular acceleration, α, are plotted as functions of magnet thickness in Figure 4-6.

We can also plot the rotary motor's power required for a given angular acceleration as a function of linear motor magnet thickness as shown in Figure 4-7. At zero magnet

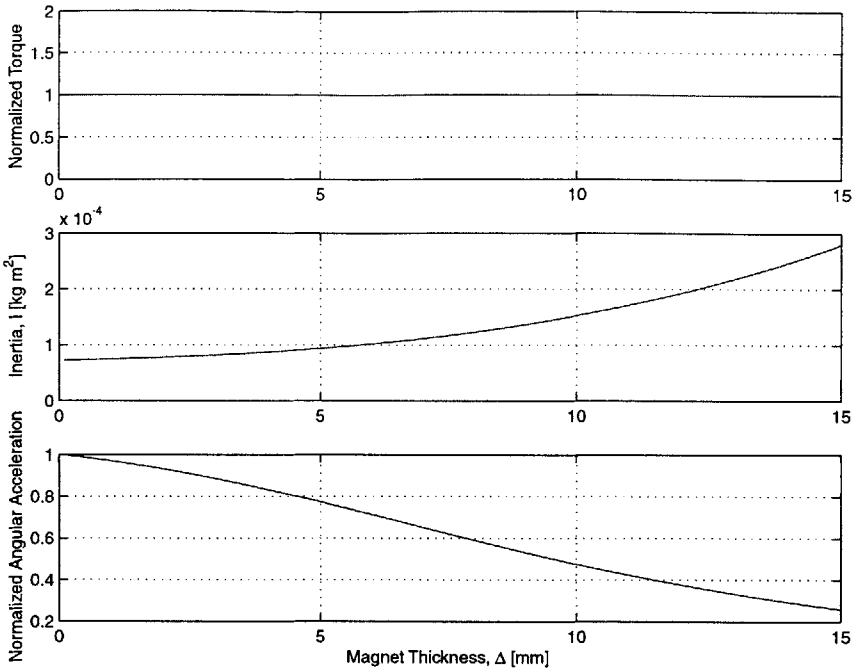

Figure 4-6: Rotary motor torque, total inertia, and rotary acceleration as functions of linear motor magnet thickness.

thickness, the rotary motor is most power efficient, but then we will not have a linear motor. At large magnet thicknesses, the rotary motor requires much higher power to produce the same angular acceleration. From the plot, we see that $\Delta \leq 8$ mm will keep the rotary motor power dissipation within a factor of 3 of the power required with no linear motor.

Thus combining the requirements from minimizing linear motor power dissipation and rotary motor power dissipation we have a range of magnet thicknesses which minimizes power in both motors,

$$3 \text{ mm} \leq \Delta \leq 8 \text{ mm}. \tag{4.52}$$

This analysis is performed for a magnetic pitch length of $l = 5$ cm, so

$$0.06 \leq \Delta/l \leq 0.16. \tag{4.53}$$

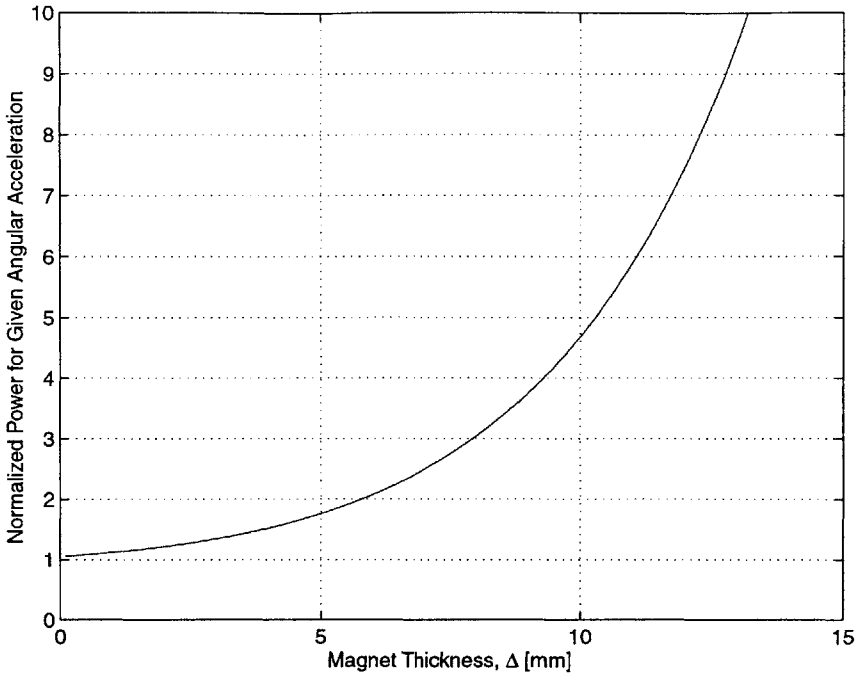

Figure 4-7: Rotary motor power for a given rotary acceleration vs. linear motor magnet thickness

Unlike the coil thickness optimization of the previous section, the magnet thickness optimization requires specific masses and inertias from our application, and so is a less general result. However, this same methodology can be used in other applications. For our motor we choose 0.25 inch thick magnets since they are within the acceptable range and are readily available,

$$\Delta = 6.35 \text{ mm}. \tag{4.54}$$

4.3.6 Magnet Array

We have modeled our motor as if the magnet array consists of an infinitely repeating pattern of north and south poles. The magnet flux lines for this ideal magnet array are shown in Figure 4-8 (a). Here the south pole is blue, the north poles are green, and the permeable stator and rotor back irons are grey. The dotted lines on the edges of magnet array (a) represent boundaries of perfect symmetry. The stator coils are

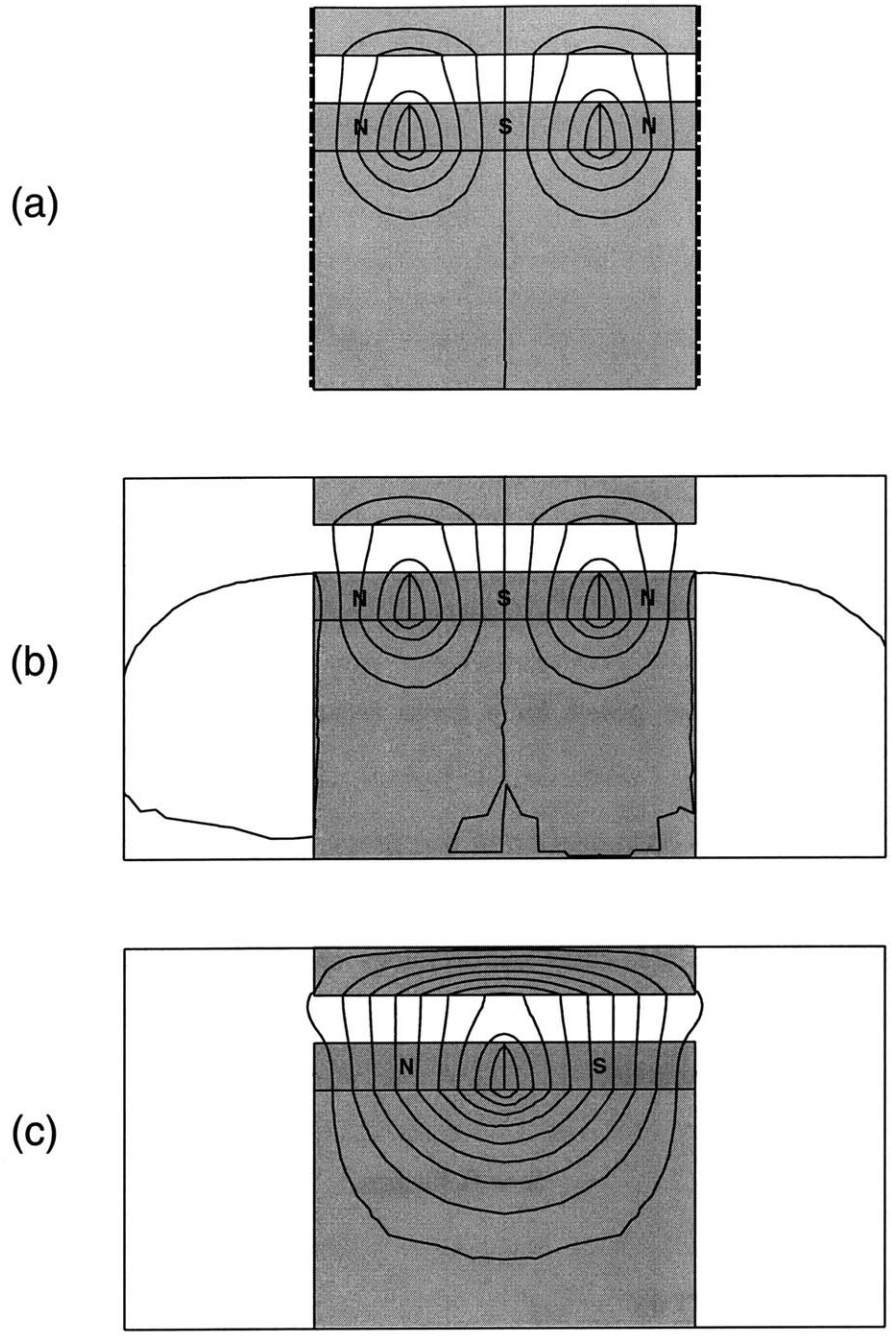

Figure 4-8: Finite-element plots of magnetic flux lines for three different magnet arrays: (a) Ideal infinitely repeating magnet array. (b) N-S-N single pitch magnet array. (c) N-S single pitch magnet array. Magnet array (b) approximates the ideal array (a) better than magnet array (c). Grey areas are permeable back iron. The dotted lines in (a) represent boundaries of perfect symmetry.

not shown but would be in the air gap which the magnet flux crosses.

In section 4.3.2, we choose to use only one magnetic pitch length in our motor so the rotor will have only one north and one south pole—not an infinite array. Two possible ways of arranging the magnets in one pitch length are shown in Figure 4-8 (b) and (c). In array (b) the north magnet is divided into two halves placed symmetrically on either side of the south pole, but in array (c) the north and south poles are placed side-by-side. Magnet array (b) approximates the ideal array better than magnet array (c) due to its symmetry. Both arrays (b) and (c) suffer from end-effects. However, the stator and rotor back irons in array (c) carry much more magnetic flux than in the ideal array. We implement magnet array (b) in our linear motor since it better approximates the ideal array. In addition to reducing the thickness of back iron required, array (b) has shorter magnetic flux paths than array (c). Since back iron has some finite permeability, the shorter flux paths in array (b) result in higher magnetic fields in the air gap.

The north and south poles in the arrays in Figure 4-8 are adjacent to each other. The magnetic material near the boundaries between magnets of opposite magnetization is wasted since it produces little flux that crosses the air gap. In effect, the adjacent edges of magnets of opposite magnetization short each other out and provide little useful magnetic flux. Thus, in retrospect, it would have been desirable to have small gaps between the magnets. This would eliminate magnet mass without affecting force much, thus boosting overall system acceleration. The range of obtainable magnet sizes is limited: this change could be made most easily by increasing the magnetic pitch length and introducing space between the north and south magnets.

4.4 Linear Motor Force Constant Calculation

This section calculates the linear motor force constant using the force equation (4.16),

$$F_z = \mu M_0 \frac{wl^2}{\pi^2} \left[(1 - e^{-2\gamma\Gamma})(1 - e^{-2\gamma\Delta})e^{-\gamma x_0}\right] (J_a \cos\gamma z_0 + J_b \sin\gamma z_0). \qquad (4.55)$$

Magnetic Remanence	$\mu_0 M_0$	1.2 T
Magnetic Pitch	l	52.83 mm
Coil Thickness	Γ	5.08 mm
Magnet Thickness	Δ	6.35 mm
Air Gap Thickness	x_0	0.84 mm
Motor Width	w	66.04 mm
Quadrature Current Density	J_q	$(2.57 \times 10^6) i_q$ A/m^2

Table 4.4: Linear motor parameters

Table 4.4 lists our motor's parameters. The Neodymium Iron Boron (NdFeB) magnets have a remanence of $\mu_o M_0 = 1.2$ T. The selection of magnetic pitch, l, coil thickness, Γ, magnet thickness, Δ, and air gap, x_0, are described in the previous section. The motor width, w, is tricky to calculate since the motor analysis leading to equation (4.16) is for a flat motor, but we are applying it to a tubular motor. If we use ring magnets, then the width would be the ring's circumference. However, we fabricate our motor with an octagonal arrangement of rectangular magnets to approximate a radially magnetized ring (Figure 6-19). Thus, a more accurate calculation of width is the sum of the lengths of the eight rectangular magnets around the magnet ring. Each magnet has a length of 8.255 mm (0.325 inches) so that the motor width is

$$w = 8 \times 8.255 \text{ mm} = 66.04 \text{ mm}. \tag{4.56}$$

We now relate the two-phase current density term, $(J_a \cos \gamma z_0 + J_b \sin \gamma z_0)$, to physical three-phase currents. We do this using the dq transformation developed in Chapter 7. We define a quadrature current density as

$$J_q = (2J_a \cos \gamma z_0 + 2J_b \sin \gamma z_0), \tag{4.57}$$

where $2J_a$ and $2J_b$ are peak current densities in the two-phase system.[2] If we can find the proportionality constant that relates quadrature current density, J_q, to quadrature

[2]This definition corresponds to the $\alpha\beta \rightarrow dq$ transformation described in Chapter 7. The two-phase ab frame which J_a and J_b are in leads the two-phase $\alpha\beta$ frame of Chapter 7 by $\pi/2$, but they are analogous frames.

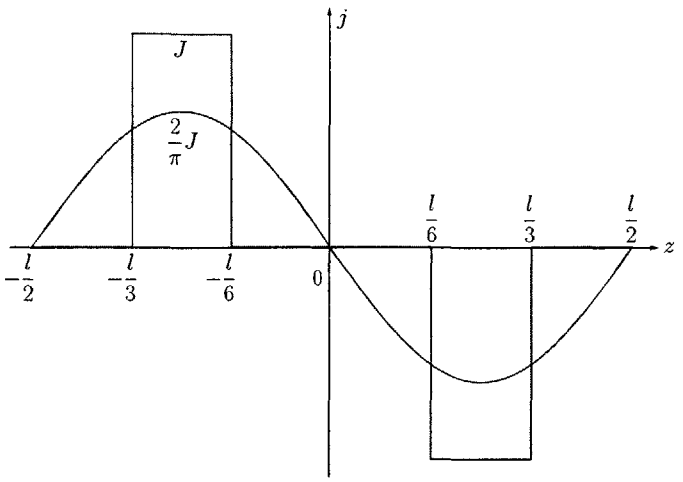

Figure 4-9: The first harmonic component of current density is shown in red superposed over the actual rectangular distribution of current density in the stator shown in blue. Current density is plotted as a function of axial distance, z.

current, i_q, we can express the motor force in terms of i_q. This is convenient since i_q corresponds to the peak phase currents in the motor when the phases are sinusoidally commutated. Also, our controller uses i_q internally, so we can command a given quadrature current and measure the force output as is done in section 4.5.

The motor's physical three-phase windings are ring coils. The current density, J, in a rectangular cross-section of the ring is

$$J = \frac{NI}{A}, \tag{4.58}$$

when the coil is carrying a current, I. Each of the coils has

$$N = 104 \text{ turns}, \tag{4.59}$$

and a cross-sectional area of

$$A = 0.0000387 \text{ m}^2. \tag{4.60}$$

The motor's actual three-phase windings provide the rectangular current density distribution shown in blue in Figure 4-9. The motor analysis leading to equation (4.16)

assumes that the stator windings produce sinusoidal current density distributions. Thus, we use the first harmonic component of the actual rectangular current density distribution. The first harmonic component[3] is shown in blue in Figure 4-9. It has a peak amplitude $2/\pi$ times that of the actual current density in the coils, J.

We can now express quadrature current density, J_q, in terms of quadrature current, i_q,

$$J_q = \left(\frac{2}{\pi}\right)\left(\frac{3}{2}\right)\frac{N}{A}i_q \tag{4.61}$$

$$= (2.57 \times 10^6)i_q. \tag{4.62}$$

The factor of $2/\pi$ accounts for taking the first harmonic of the rectangular current density distribution. The factor of $3/2$ accounts for the greater number of turns in the two-phase frame than the three-phase frame as explained in section 7.4.2.

Evaluating the force equation (4.16), with the motor parameters in Table 4.4 we obtain a predicted force constant of

$$K_t = 14.23 \text{ N/A}_{peak}, \tag{4.63}$$

where the force constant K_t is defined by

$$F_z = K_t i_q. \tag{4.64}$$

It is interesting to also calculate the force constant using the more accurate force equation (4.12) which does not make the approximation, $e^{2\gamma(\Delta+\Gamma+x_0)} \gg 1$. In this case we find $K_t = 15.02$ N/A$_{peak}$ which is within 6% of the approximate value given by equation (4.16).

[3]The easiest way to calculate the Fourier coefficients of a rectangular function is to find the Fourier coefficients of its derivative and relate these to the coefficients of the original signal. It is easy to find the Fourier coefficients of the derivative since this sequence consists of impulses. For details, see, for example, Oppenheim & Willsky [56]

4.5 Linear Motor Force Constant Measurement

The motor force constant, K_t, for a three-phase motor is the force produced when the motor phases are supplied with sinusoidally commutated currents. The force constant can be expressed in terms of the peak or root mean square (rms) amplitudes of these currents. In general motor force constants can be measured in two ways:

- The force can be directly measured as a function of phase current amplitude.
- The back-EMF voltage at a constant velocity can be measured and related to the motor force constant.

Since our linear motor has only a limited travel, we cannot maintain a constant velocity over several pitch lengths of the motor. Therefore, we measure the motor's force directly as a function of phase current amplitude. In the rotary motor case, it is harder to measure torque or force at a radius without a special setup, but it is easy to spin the rotary motor at constant velocity and measure the back EMF voltage. Thus, we use the back-EMF method to determine the rotary motor force constant in section 4.7.

We measure linear motor force as a function of quadrature current, i_q. A constant quadrature current corresponds to three-phase sinusoidal commutation with peak phase current amplitudes of i_q. The quadrature current and its relation to phase currents is discussed in Chapter 7. The axis's linear position, z, is measured and used to commutate the linear motor.

We measure linear motor force with a Kistler model 9212 load cell. This piezoelectric device produces 53.45 pC/lbf and has a load capacity of 5000 lbf. A Kistler Dual Mode Amplifier with a long time constant is used to measure the charge produced by the load cell. The load cell is mounted to an aluminum plate on an L-block which is bolted to the optical table. The load cell is fixtured to the aluminum plate with a double-ended screw. The z-θ axis pushes against the other end as shown in Figure 4-10. The small z-mirror is removed from the end of the axis for this test so z is measured from the tilted-mirror and used to commutate the motor.

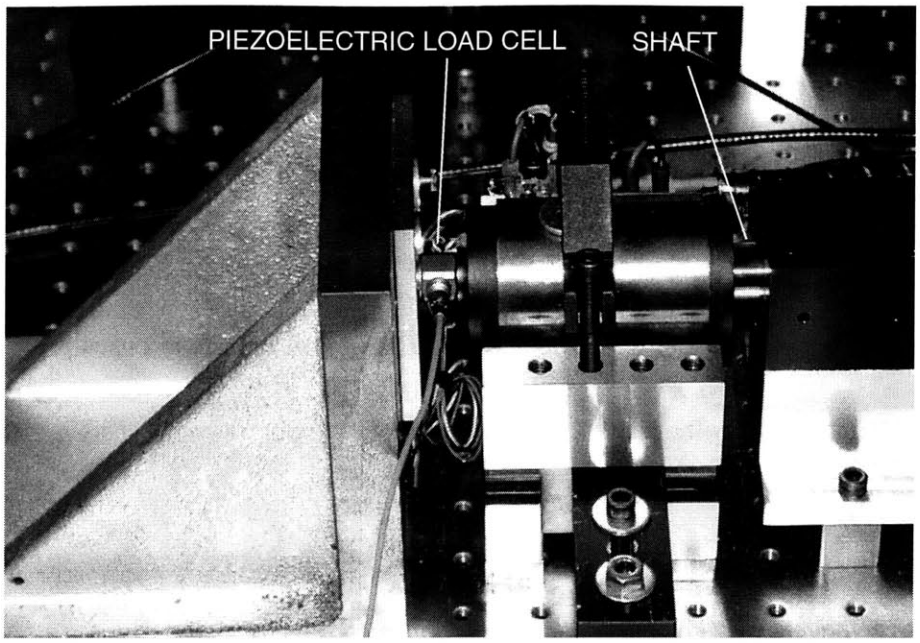

Figure 4-10: Measuring linear force with a piezoelectric load cell.

The results of this force test are shown in Figure 4-11. At a quadrature current of 3 A, corresponding to sinusoidal commutation with peak phase current amplitudes of 3 A, the motor produces 40.9 N of force. The motor temperature rises only a few degrees Celsius at this force level, but the power amplifiers are hot so we did not test higher current levels. The data is linear and yields a force constant,

$$K_t = 13.5 \text{ N/A}_{peak}. \tag{4.65}$$

This value agrees well with the predicted force constant, $K_t = 14.23$ N/A$_{peak}$, calculated in section 4.4.

4.6 Rotary Motor Selection for High Accelerations

We choose to buy the rotary permanent magnet synchronous motor rather than fabricate one ourselves. As related in section 6.7 we had considerable difficulty finding a vendor willing to sell us a single frameless rotary motor. Thus, our choices were

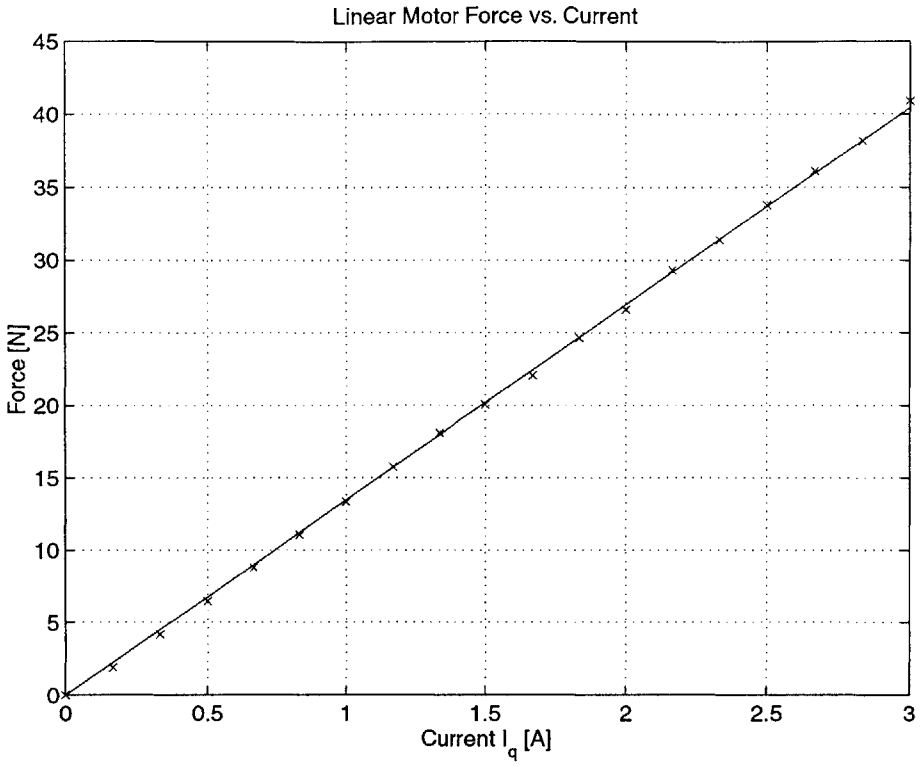

Figure 4-11: Linear motor force vs. current.

limited to frameless motors from a single vendor, Aerotech (see Appendix F). Their motor models come in different diameters, and each diameter has at least two different lengths. We bought two motors with the same diameter but different lengths. Then we used the shorter motor's rotor and the longer motor's stator for the rotary motor on the z-θ axis. This allows axial (z) travel of the axis while still allowing the rotary motor to produce full torque.

We wish to select the motor that provides the highest angular acceleration for the z-θ axis without adding too much mass to the axis. Table 4.5 calculates the angular accelerations achievable with the four smallest frameless motors. The total axis inertia is the sum of the approximate shaft and linear motor inertia, 7.5×10^{-5} kg·m^2, and the inertia of the rotary motor's rotor. We do not include the large sensor inertia in this calculation. It is clear from the table that the smallest diameter motor, the S-50-52, provides the highest angular acceleration. The last two models are too large

Motor Model	*Continuous Torque*	*Rotor Inertia*	*Total Inertia*	*Angular Acceleration*
	[N·m]	[kg·m^2]	[kg·m^2]	[rad/s^2]
S-50-52	0.42	1.7×10^{-5}	9.2×10^{-5}	4565
S-76-85	1.9	42×10^{-5}	49.5×10^{-5}	3838
S-130-39	2.8	160×10^{-5}	167.5×10^{-5}	1672
S-180-44	7.41	740×10^{-5}	747.5×10^{-5}	991

Table 4.5: Calculation of achievable angular accelerations with different Aerotech frameless rotary motors. Total Inertia includes the shaft and linear motor inertias of 7.5×10^{-5} kg·m^2.

anyhow, but they show the trend of decreasing angular acceleration with increasing motor diameter. This trend is expected based on the scaling analysis of section 4.1. Equation (4.6) indicates how angular acceleration, α, scales with rotary motor radius, R_θ,

$$\alpha \propto \frac{2\pi R_\theta^2 L_\theta}{\frac{1}{2}\pi\rho(R_z^4 L_z + R_\theta^4 L_\theta) + I_s}.$$

This scaling analysis led to the conclusion that long, skinny motors provide the highest acceleration. In the limit that the rotary motor's inertia dominates, which is the case for the S-76, S-130, and S-180 motors, the angular acceleration is inversely proportional to the square of the motor radius, R_θ^2. By choosing the smallest diameter motor, we also minimize axis mass which maximizes linear acceleration.

4.7 Rotary Motor Torque Constant Measurement

In section 4.5 we directly measure linear motor force with a load cell as a function of phase current amplitude. Although we could directly measure rotary motor torque by building a lever arm to push against the load cell, it is easier to use the back-EMF method for measuring the torque constant.

For DC motors, the back-EMF constant, K_e, is the same as the motor force constant, K_t, if both are expressed in SI units. This can easily be derived by equating mechanical power with electrical power. Setting torque, τ, times mechanical speed,

Ω, equal to current, i, times voltage, v, yields

$$\begin{aligned} \tau\Omega &= iv && (4.66) \\ (K_t i)\Omega &= i(K_e\Omega) && (4.67) \\ K_t &= K_e && (4.68) \end{aligned}$$

where we have used $\tau = K_t i$ and $v = K_e\Omega$.

The same physics goes on in a three-phase permanent magnet motor, but the bookkeeping is more difficult. We use the permanent magnet synchronous motor model in *abc* phase variables developed in section 7.3 to compute the torque constant. We spin the motor at constant electrical speed, $\omega = \dot{\theta}$, and measure the open-circuit voltage with $i_a = 0$. From equations (7.24) and (7.12), the phase a voltage, v_a, is sinusoidal with an amplitude proportional to electrical speed, ω,

$$v_a = -(\lambda_f \omega)\sin\theta. \tag{4.69}$$

Here λ_f is the maximum rotor flux linked by the stator phases. The mechanical speed, Ω, is related to electrical speed, ω, by the number of pole pairs p: $\omega = p\Omega$. Our rotary motor has 4 pole pairs so $p = 4$.

Figure 4-12 shows the three phase voltages, v_a, v_b, and v_c, measured while the motor is spinning at 20 rev/s. As expected the period, T, of each phase's back-EMF voltage is

$$T = \frac{1}{(20 \text{ rev/s})(4 \text{ pole pairs})} = 12.5 \text{ ms}. \tag{4.70}$$

The peak amplitude of the phase voltages is 12.5 V. Setting this equal to the peak amplitude, $\lambda_f\omega$, in equation (4.69) we have

$$\lambda_f = \frac{12.5 \text{ V}}{(4 \text{ pole pairs})2\pi(20 \text{ rev/s})} = 0.0248 \text{ Wb}. \tag{4.71}$$

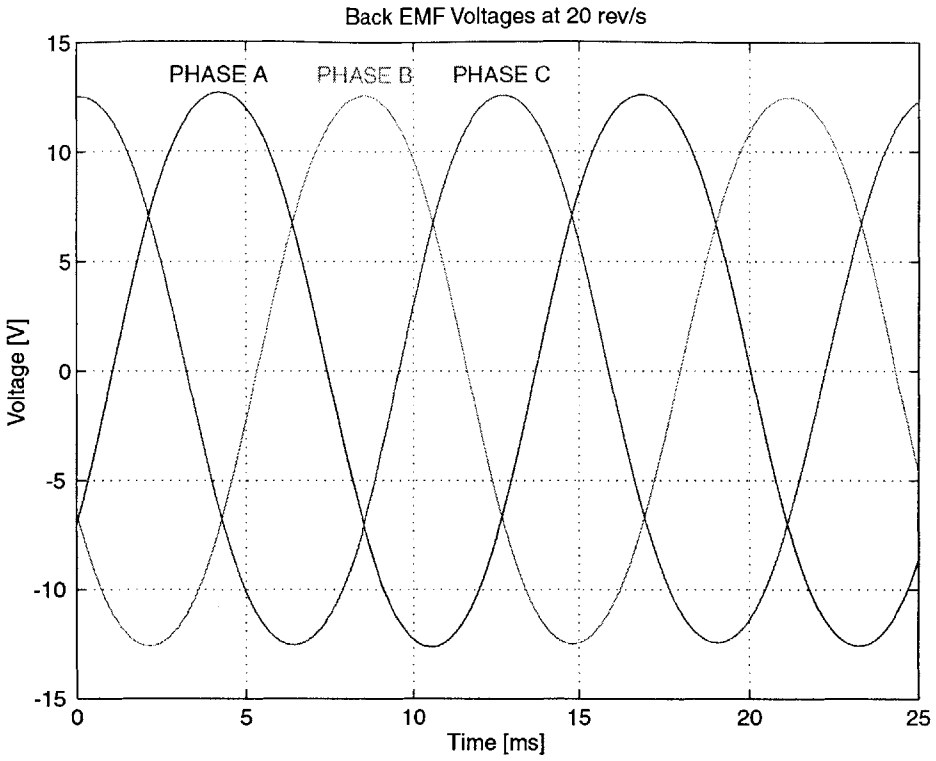

Figure 4-12: Measured rotary motor back EMF waveforms. The 8-pole motor is spinning at 20 rev/s.

We can now use equation (7.84) to find the motor torque constant,

$$K_t = p\frac{3}{2}\lambda_f = 0.15 \text{ N} \cdot \text{m/A}_{peak}. \tag{4.72}$$

This agrees with the torque constant specified in the Aerotech motor manual [2],

$$K_t = 0.16 \text{ N} \cdot \text{m/A}_{peak}. \tag{4.73}$$

4.8 Summary

In this chapter we looked at the design of the linear and rotary permanent magnet motors. We used a simple scaling analysis to show that higher linear and rotary accelerations are achieved when the motors are long and skinny rather than being short and fat. We estimated the motor's size using the Lorentz force density. We

then proceeded to design the permanent magnet synchronous linear motor using the results of a continuum electromechanical analysis contained in Appendix A.

We chose the motor magnetic pitch length l to be as large as possible, the full length of the motor. This is because the motor's shear stress is proportional to l, and it's power dissipation is inversely proportional to l for a fixed total motor length and width. In general, one wants to choose as large a motor pitch length as possible. However, as l increases, the coil thickness and magnet thickness must increase proportionally. Therefore, for large motors it makes sense to limit the size of l and have a motor with many pitch lengths rather than just one. We used the analytical expression for power dissipation to find the power optimal coil thickness range which is $0.06 \leq \Gamma/l \leq 0.16$ where Γ is the coil thickness. We selected the motor's magnet thickness by optimizing power dissipation for given linear and rotary acceleration levels. For our application the optimal linear motor magnet thickness range happens to be the same as the coil thickness range, $0.06 \leq \Delta/l \leq 0.16$, where Δ is the magnet thickness. The coil thickness optimization is a general result, but the magnet thickness optimization uses specific masses and inertias for our rotary axis.

We showed two ways of measuring motor force constants. We measured the linear motor force constant directly with a piezoelectric load cell. We found that the measured force constant of 13.5 $\mathrm{N/A}_{peak}$ agreed well with the predicted force constant of 14.23 $\mathrm{N/A}_{peak}$. We measured the rotay motor force constant by looking at its back EMF while the motor was spinning at 20 rev/s. This measurement corresponded to a motor force constant of 0.15 $\mathrm{N{\cdot}m/A}_{peak}$ which agrees with the value specified by the vendor, 0.16 $\mathrm{N{\cdot}m/A}_{peak}$.

One change we would make to the linear motor is to leave gaps between the north and south magnets since these adjacent portions of the magnets short each other out and produce no useful magnetic field. This change would reduce the magnet weight with negligible effects on the motor operation or power efficiency.

In the next chapter we look at how we can precisely measure the translation and rotation of our axis. These measurements are necessary not only to position the workpiece on a precision rotary-linear axis, but also to commutate the rotary and

linear motors.

Chapter 5

Tilted-Mirror Sensor Design & Analysis

This chapter presents, the design, analysis, and implementation of a tilted-mirror sensor to measure shaft rotation, θ, and translation, z. Precision rotary measurement is necessary for our prototype axis since it is intended for positioning the workpiece. Rotary-linear axes intended for use as spindles do not require precision rotary measurement; instead, a sensorless control scheme can be used as described in section 8.5.

The tilted-mirror sensor consists of a 3 inch (7.62 cm) diameter mirror mounted on the end of the rotary-linear shaft. It has a slight tilt of 4.7 mrad (16 arcmin) with respect to a plane normal to the shaft's axis of rotation. Two plane-mirror interferometers measure distance to the tilted-mirror, and from these measurements we can calculate shaft rotation, θ, and translation, z. In order to avoid singularities in this sensor implementation, we also directly measure translation, z, with a third laser interferometer; this interferometer measures distance to a small, non-tilted mirror on the opposite end of the shaft. Table 5.1 summarizes the performance of the tilted-mirror sensor.

In section 3.4 we examined several possible sensor concepts for measuring rotary-linear motion. These included the prism-mirror sensor, the tilted-mirror sensor, the helicoid mirror sensor, the rotating half-wave plate sensor, the rotating polarizer sensor, and the 2-D encoder. In this chapter we focus on the design and analysis

Parameter	*Specification*
Linear Travel	2.5 cm
Linear Resolution	0.625 nm
Linear Noise Level	0.35 nm rms
Max. Linear Speed	0.25 m/s
Update Rate	10 kHz
Rotary Travel	360° (unlimited)
Rotary Resolution	4.6 μrad (1,366,000 counts/rev)
Rotary Noise Level	2.6 μrad rms
Max. Rotary Speed	1850 rad/s (17,700 rpm)
Update Rate	10 kHz

Table 5.1: Tilted-mirror sensor specifications.

of the tilted-mirror sensor. The mechanical design and fabrication of this sensor is discussed in section 6.4.

Marsette Vona developed the tilted-mirror sensor as part of his Master's thesis, *Metrology Techniques for Compound Rotary-Linear Motion* [70], while working closely with the author on sensor design for the z-θ axis. He derived and implemented the tilted-mirror metrology relationships and the calibration algorithms. He also designed and fabricated the sensor hardware—the mirror and interferometer mounts described in section 6.4. In addition, he developed a combined software and hardware solution which connects the HP interferometer laser axis boards to the dSPACE 1103 board via a custom high-speed parallel link.

5.1 Tilted-Mirror Sensor Basic Analysis

This section presents a simplified analysis of the tilted-mirror sensor. We postpone consideration of several complicating details to the following section. We mount a slightly tilted plane mirror to the z-θ shaft as shown in Figure 5-1. The mirror is attached to the shaft with an adjustable wobble plate described in section 6.4.1. The mirror is only slightly tilted, with a tilt angle of $\alpha = 4.7$ mrad (16 arcmin). Two interferometers measure distance to the surface of the mirror. As the shaft

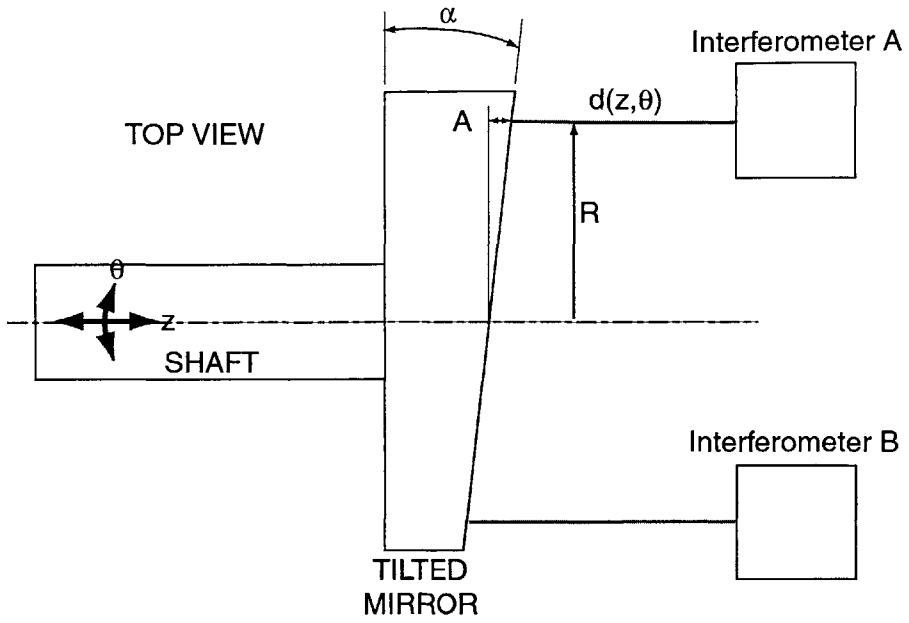

Figure 5-1: Schematic of the tilted-mirror sensor. The shaft's translation z and rotation θ are sensed by measuring the distance to a slightly tilted mirror in two places.

rotates, the mirror's orientation changes and so the distances measured by the two interferometers change.

5.1.1 Determining Rotation Angle

In this section we assume that both interferometers are at the same radius R. We further assume that the two interferometers are displaced by exactly 90° around a circle of radius R. Thus, they are in quadrature. The distances between the interferometers and the mirror surface, $d_1(z,\theta)$ and $d_2(z,\theta)$, vary linearly with shaft translation, z, and vary sinusoidally with shaft rotation, θ,

$$d_1(z,\theta) = z + A\sin\theta \tag{5.1}$$

$$d_2(z,\theta) = z + A\cos\theta. \tag{5.2}$$

Here A is the amplitude of the sinsusoidal variation with θ as shown in Figure 5-1. The amplitude, A, is related to the radius, R, and mirror tilt angle, α, by

$$A = R \tan \alpha. \tag{5.3}$$

Linear position, z, is measured with a third interferometer to a small z-mirror on the opposite end of the shaft. We also know A from equation (5.3) since we know R and α. Thus, the tilted-mirror sensor provides information about $\sin\theta$ and $\cos\theta$ just like an encoder does. We can find θ using the arctangent function,

$$\theta = \arctan\left(\frac{d_1 - z}{d_2 - z}\right). \tag{5.4}$$

5.1.2 Sensor Resolution

We use Smith and Chetwynd's [61] definition of sensor resolution as "the smallest discernible change in the parameter of interest that can be registered by a particular instrument." In our case, we are interested in the smallest angular change we can measure with the tilted-mirror sensor. We use the analysis of the previous section to estimate our sensor's resolution. The mirror's tilt angle is

$$\alpha = 4.7 \text{ mrad } (16 \text{ arcmin}). \tag{5.5}$$

The measurement radius is

$$R = 2.87 \text{ cm}, \tag{5.6}$$

so the amplitude of the sinsusoidal variation with θ is

$$A = R \tan \alpha = 135 \ \mu\text{m}. \tag{5.7}$$

Both $d_1 - z$ and $d_2 - z$ change in increments of 0.625 nm since d_1, d_2, and z are measured by laser interferometers which have resolutions of 0.625 nm. It is convenient to picture equation (5.4) by plotting the two distances $d_1 - z$ and $d_2 - z$ on the y-

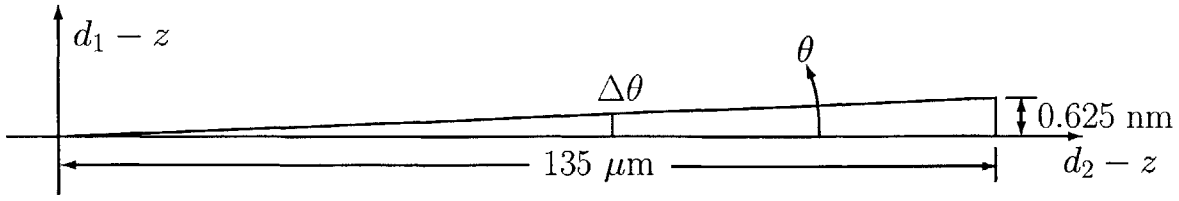

Figure 5-2: Determination of tilted-mirror sensor resolution. The rotation angle, θ, is calculated by $\theta = \arctan(d_1 - z)/(d_2 - z)$. Both $d_1 - z$ and $d_2 - z$ change in increments of 0.625 nm. The maximum change in θ occurs when $d_2 - z$ is equal to its maximum value, 135 μm, and $d_1 - z$ changes from 0 to 0.625 nm. The resolution is $\Delta\theta = 4.6$ μrad.

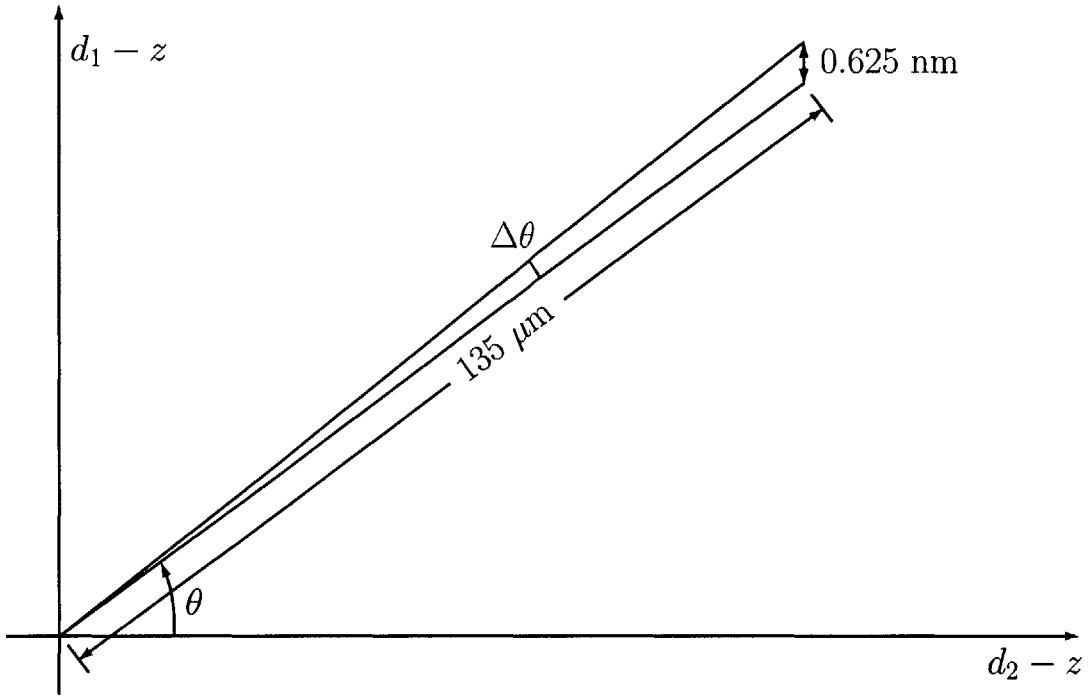

Figure 5-3: In general, the observed resolution due to an incremental change in $d_1 - z$ or $d_2 - z$ is a function of angle θ. For $\theta = 36.9°$, an incremental change in $d_1 - z$ results in an angle change of $\Delta\theta = 3.7$ μrad. This is the resolution observed experimentally at one angle and shown in Figure 5-7.

and x-axes respectively as shown in Figure 5-2. We would like to define the sensor's resolution as the angle change that results when either $d_1 - z$ or $d_2 - z$ changes by one increment. Unfortunately, we will demonstrate that this angle change is not constant but varies with the mirror's rotation angle, θ. Thus, we use the maximum angle change as our definition of sensor resolution; this is a conservative, worst-case estimate of the actual resolution which we will show varies between this value and zero.

We now show that the tilted-mirror sensor's resolution depends on the mirror's rotation angle, θ, which is measured counter-clockwise from the x-axis. Figure 5-2 depicts a situation that results in the coarsest resolution for an incremental change in one laser interferometer. In this case, $d_2 - z$ is equal to its maximum value of 135 μm, and $d_1 - z$ changes from 0 to 0.625 nm. The resulting angle change is $\Delta\theta = 4.6$ μrad. This is an upper limit on the sensor's resolution since any other incremental change in $d_1 - z$ or $d_2 - z$ at any other angle θ would result in a smaller change in θ. We provide an example of this next.

Consider the case shown in Figure 5-3 where $\theta = 36.9°$. The reason for this specific choice of θ will be made clear shortly. At this angle, an increase in $d_1 - z$ by 0.625 nm results in an angle change of $\Delta\theta = 3.7$ μrad. As θ increases from 0° to 90° the angle change, $\Delta\theta$, due to an incremental change in $d_1 - z$ decreases from a maximum of 4.6 μrad to zero. (At the same time, the angle change, $\Delta\theta$, due to an incremental change in $d_2 - z$ increases from zero to 4.6 μrad.)

Since the sensor resolution varies continuously with θ, we claim the worst case sensor resolution of 4.6 μrad (0.95 arcsec) for our sensor to be conservative. Every observable change in angle will be less than or equal to this value. This resolution is equivalent to 1,366,000 counts/rev. In section 5.6 we show an experimental measurement of the sensor noise in Figure 5-7. At the angle θ of this measurement, it is apparent that the sensor resolution is 3.7 μrad which is less than our conservative maximum value of 4.6 μrad derived above. This makes sense since, as shown in Figure 5-3, for the specific value of $\theta = 36.9°$, an incremental change in $d_1 - z$ results in an angle change of $\Delta\theta = 3.7$ μrad.

In closing, we note another way of defining resolution that is sometimes used. When $\theta = 45°$, a small angle change would, in theory, change both $d_1 - z$ and $d_2 - z$ by one increment simultaneously. This would result in an angle change $\Delta\theta$ that is $\sqrt{2}$ times higher than the 4.6 μrad value derived above for a single change in either $d_1 - z$ or $d_2 - z$. This method is somewhat unsatisfying, however, since it assumes that the two quadrature channels, $d_1 - z$ and $d_2 - z$, change simultaneously. In reality, these two signals have some noise levels, and their changes are not correlated.

5.1.3 Sensor Maximum Angular Velocity

Our sensor's maximum angular velocity is limited by the the maximum linear velocity of our plane mirror interferometers. When the linear, z, position of the axis is held constant, and the shaft spins with angular velocity, ω, the interferometers measure a sinusoidal variation in distance with amplitude, A. From equation (5.1) the distance to the first interferometer is

$$d_1(z) = A \sin \omega t. \tag{5.8}$$

The velocity sensed by this interferometer is therefore

$$\dot{d}_1(z) = A\omega \cos \omega t. \tag{5.9}$$

Since the interferometers have a maximum velocity limit of 0.254 m/s, our maximum sensor angular velocity is

$$\omega = \frac{\dot{d}_1(z)}{A} = \frac{0.25 \text{ m/s}}{135\ \mu\text{m}} = 1850 \text{ rad/s } (17,700 \text{ rpm}). \tag{5.10}$$

5.2 Tilted-Mirror Sensor Full Analysis

In the previous section we saw that since we know z, the two tilted-mirror interferometer distance measurements provide information about $\sin\theta$ and $\cos\theta$. We can thus recover θ by taking the arctangent of the ratio of $\sin\theta$ to $\cos\theta$. The tilted-mirror sensor uses this basic algorithm to compute θ. However, there are several additional

details that we consider in this section. In particular, we allow the two beams to have different radii and also allow them to be close to, but not exactly, in quadrature. Also, the laser interferometers only provide a relative distance measurement. Thus, it is important for us to know what orientation the mirror is in when the two interferometer beams read zero.

5.2.1 Path Length Equations

We let each interferometer beam[1] have a different radius, R_1 and R_2, and phase offset with respect to a horizontal plane, ϕ_1 and ϕ_2. We can now re-write the path length equations (5.1) and (5.2) as

$$d_1(z,\theta) = z + A_1 \sin(\theta - \phi_1) + C_1 \tag{5.11}$$

$$d_2(z,\theta) = z + A_2 \sin(\theta - \phi_2) + C_2. \tag{5.12}$$

Here C_1 and C_2 are constants that depend on when the laser interface electronics are zeroed. The two amplitudes, A_1 and A_2, are related to mirror tilt, α, and beam radii, R_1 and R_2, by

$$A_1 = R_1 \tan\alpha \tag{5.13}$$

$$A_2 = R_2 \tan\alpha. \tag{5.14}$$

5.2.2 Calibration Constants

There are six constants in the path length equations (5.11) and (5.12) which we need to know in order to calculate θ. They are the amplitudes, A_1 and A_2, the phases, ϕ_1 and ϕ_2, and the zero offsets, C_1 and C_2. These parameters are listed in Table 5.2. In section 5.3 we describe an automatic calibration procedure we use to determine these six constants. For now, we assume they are known.

[1] In fact, we are using two-pass plane mirror interferometers so that each beam that we talk about really consists of two beams. By considering their average radius and phase offset, we can treat each interferometer as if it had only one beam halfway between the two actual beams.

Parameter	*Description*
A_1, A_2	Amplitude of Sinusoidal Variation in Distance with Mirror Rotation
ϕ_1, ϕ_2	Phase Offset of Measurement Beam from Horizontal Plane
C_1, C_2	Zero Offset of Measurement Beam

Table 5.2: Tilted-mirror sensor calibration constants. The constants listed apply to the two interferometer measurement beams.

5.2.3 Compensation for Non-Ideal Measurement Beam Locations

In the simplified analysis of section 5.1 we assume that the two beams have the same radii and are perfectly in quadrature. In reality, the beams have different radii, and their phase difference is not exactly 90°. These non-idealities are included in equations (5.11) and (5.12). We solve equations (5.11) and (5.12) for the two signals, $\sin(\theta - \phi_1)$ and $\sin(\theta - \phi_2)$,

$$\sin(\theta - \phi_1) = \frac{d_1(z,\theta) - z - C_1}{A_1} \tag{5.15}$$

$$\sin(\theta - \phi_2) = \frac{d_2(z,\theta) - z - C_2}{A_2}. \tag{5.16}$$

By dividing by the amplitudes, A_1 and A_2, which are proportional to beam radii, R_1 and R_2, we compensate for the different beam radii.

We now show how to find θ using $\sin(\theta-\phi_1)$ and $\sin(\theta-\phi_2)$ given that we know ϕ_1 and ϕ_2. It is convenient to solve the problem in a frame rotated by ϕ_1. We introduce the angle, θ', which is 0 when $\theta = \phi_1$,

$$\theta' = \theta - \phi_1. \tag{5.17}$$

We also introduce the phase difference between the two measurement beams,

$$\phi_d = \phi_1 - \phi_2, \tag{5.18}$$

which is close to 90°. Using these transformations, equations (5.15) and (5.16) become

$$\sin\theta' = \frac{d_1(z,\theta) - z - C_1}{A_1} \tag{5.19}$$

$$\sin(\theta' - \phi_d) = \frac{d_2(z,\theta) - z - C_2}{A_2}. \tag{5.20}$$

Equation (5.19) provides $\sin\theta'$. We can find $\cos\theta'$ by expanding $\sin(\theta' - \phi_d)$ in equation (5.20) using the trigonometric identity for the sine of the difference of two angles and solving for $\cos\theta'$,

$$\cos\theta' = \frac{\sin(\theta' - \phi_d) - \sin\theta'\cos\theta_d}{\sin\theta_d}. \tag{5.21}$$

We can now use the arctangent function to find θ' and add ϕ_1 to transform back to θ,

$$\theta = \arctan\left(\frac{\sin\theta'}{\cos\theta'}\right) + \phi_1, \tag{5.22}$$

where $\sin\theta'$ and $\cos\theta'$ are given by equations (5.19) and (5.21).

5.3 Automatic Calibration Routine

We develop an automatic calibration routine to measure the calibration constants listed in Table 5.2. These constants are the amplitudes of sinusoidal variations in distance with mirror rotation, A_1 and A_2, the phase offsets of the measurement beams from the horizontal plane, ϕ_1 and ϕ_2, and the zero offsets of the measurement beams, C_1 and C_2. The amplitudes, A_1 and A_2, are related to the radii of the measurement beams and mirror tilt angle by equations (5.13) and (5.14). We perform this calibration routine each time the rotary-linear axis is turned on. Once these constants have been determined, we can use equations (5.18)–(5.22) to calculate shaft rotation angle, θ.

The automatic calibration routine first homes both motors by energizing one phase in each motor and waiting for the resulting rotary and linear stage oscillations to die down. Then the laser interferometers are zeroed in the software. At this time, the

z-axis controller is turned on, and holds the z-axis at a constant position. The θ-axis controller is also turned on and spins the axis under closed-loop control at 2.5 rev/s. Since the calibration constants have not yet been determined, the sensor processing software uses an inital guess for the set of calibration constants listed in Table 5.2.

As the rotor spins, the software records the distances measured by the two tilted-mirror interferometers, d_1 and d_2, for 5 seconds at a 5 kHz rate. This data is fit to the model described by equations (5.11) and (5.12). We assume that the rotor spins at a constant rate of $\omega = 15.708$ rad/s (2.5 rev/s). This assumption allows us fit the data to the model using a linear least-squares algorithm described in Marsette Vona's thesis [70]. From the least-squares fit, we determine A_1, A_2, ϕ_1, ϕ_2, C_1, and C_2. We then compare the model using these parameters to the data and determine the maximum error.

Typically, after one fit, the maximum error is higher than our threshold value of 150 nm. This is because the axis is not spinning at exactly $\omega = 15.708$ rad/s since the metrology equations are using initial guess calibration parameters. To improve the fit, we take another data set, but this time we use the calibration parameters we just determined from the least-squares fit. We continue this bootstrapping process until the maximum error is under 150 nm. This usually requires 4–8 iterations. Periodically we update the initial guess parameters with a set of final fit parameters, and this usually decreases the number of iterations required till the error is below the threshold.

5.4 Singularities without Direct z Measurement

In our prototype axis, we measure z with a third interferometer. It is also possible to determine z using just the two tilted-mirror beams, but this results in a singularity at two angular positions [70]. One of these singular positions is shown in Figure 5-4, and the other occurs when the shaft is rotated 180° from this angle. The singularity occurs when the line connecting the two interferometers is parallel to the line connecting the mirror's high and low points. At this angle a small clockwise rotation of the

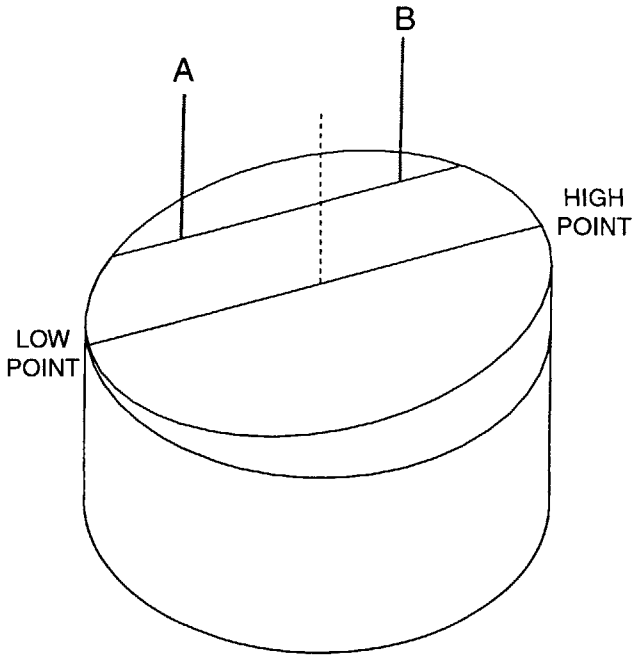

Figure 5-4: It is possible to measure rotation angle and translation of the rotary-linear axis without using a third beam to directly measure translation. However, at the angle depicted in the figure, a small clockwise rotation of the mirror increases the distance measured by the A and B inteferometers by the same amount; thus, it cannot be distinguished from a translation of the axis away from the interferometers. This singularity occurs when the line connecting the two interferometer beams is parallel to the line connecting the mirror's high and low points. Another singularity occurs when the shaft is rotated 180° from the orientation shown.

mirror increases the distance measured by the A and B inteferometers by the same amount; thus, it cannot be distinguished from a translation of the axis away from the interferometers. Likewise, a small counter-clockwise rotation cannot be distinguished from a translation of the axis toward the interferometers.

5.5 Interferometer Angular Tolerance

Our tilted-mirror sensor relies on the fact that two-pass plane mirror interferometers can tolerate a tilted-mirror. If the returning measurement beam hit the detector at an angle relative to the reference beam the fringes would be washed out. In fact, the interferometer is designed such that the returning measurement beam is parallel to

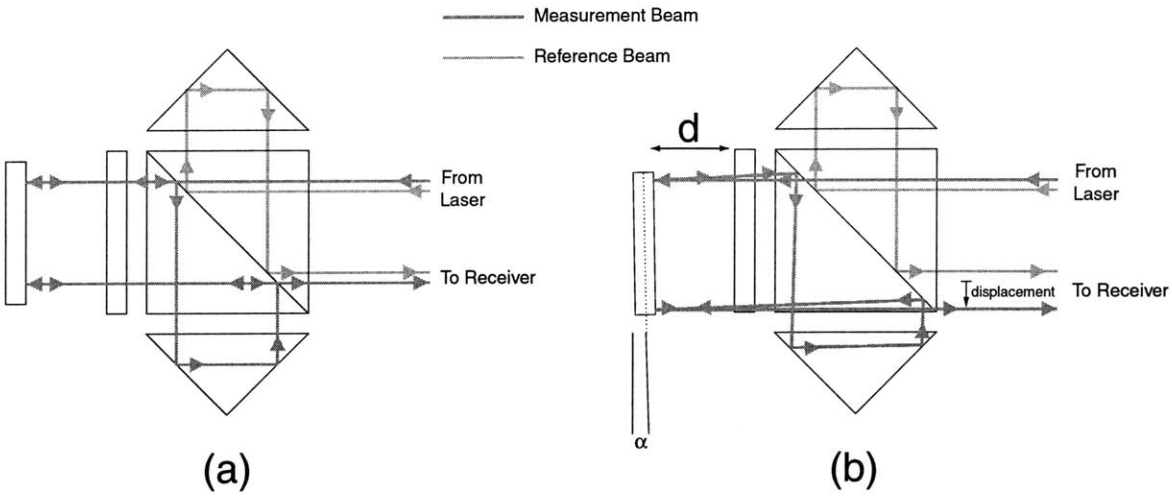

Figure 5-5: Measurement and reference beam paths in a 2-pass laser interferometer when the target mirror is (a) perfectly normal to the measurement beam and (b) tilted by a small angle, α. In case (b) the measurement beam is displaced from the reference beam by an amount proportional to mirror tilt, α, and distance between the interferometer and the target mirror, d. Figure drawn by Marsette Vona.

the reference beam even when reflecting off of a tilted-mirror. This is possible since the interferometer is a two-pass interferometer: On the first pass the beam reflects off the tilted mirror at an angle, but on the second pass the beam approaches the tilted mirror at an angle and reflects back parallel to its initial direction. This ingenious design is shown in Figure 5-5. The mirror tilt does affect the returning beam by displacing it (as shown in Figure 5-5) an amount proportional to the mirror tilt, α, and to the distance from the interferometer to the mirror, d.[2] The maximum beam displacement allowed by our interferometers corresponds to a value of αd that is roughly 250 mrad·mm. To maximize α, we minimize d by placing the interferometer as close as possible to the tilted-mirror.

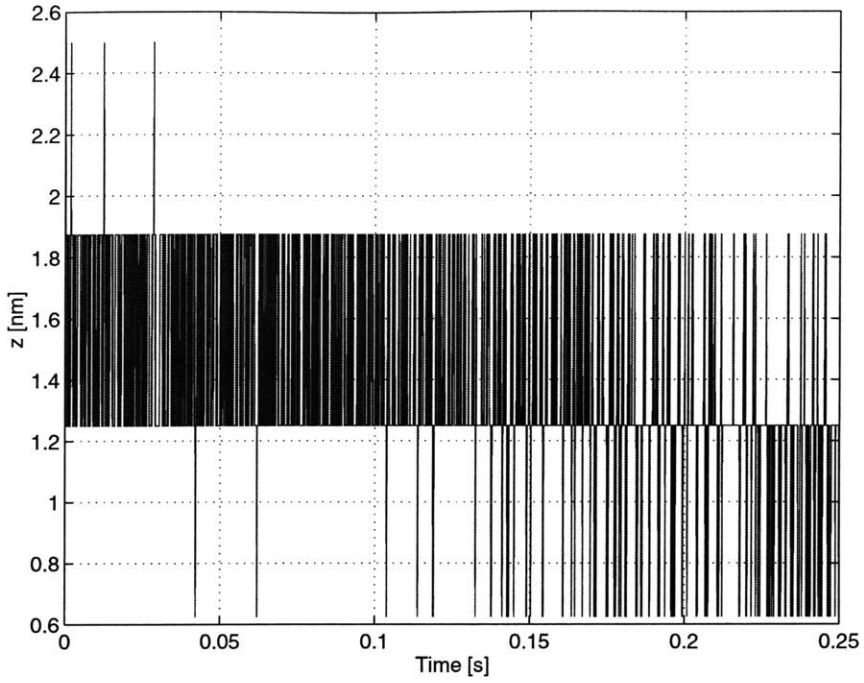

Figure 5-6: Linear axis interferometer sensor noise. The controller and air bearings are turned off. The rms noise level is 0.35 nm.

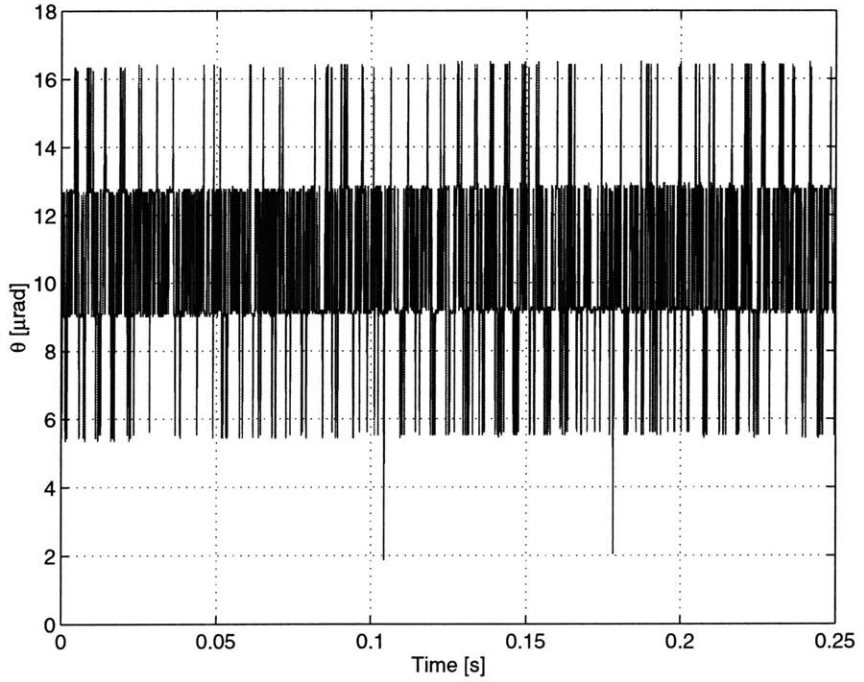

Figure 5-7: Rotary axis tilted-mirror sensor noise. The controller and air bearings are turned off. The rms noise level is 2.6 μrad.

5.6 Experimental Measurement of Sensor Noise

In this section we look at the measured linear axis and rotary axis sensor noise. We turn off the rotary and linear axis controllers and the air bearings for this measurement so that we only measure sensor noise. Of course, external disturbances such as vibrations and thermal gradients in the materials and atmosphere still affect the measurement. The measured linear axis interferometer sensor noise is shown in Figure 5-6. It has 0.35 nm rms of noise over the 1/4 second of data. The individual interferometer counts are clearly visible. This is a very low noise level. The rotary axis tilted-mirror sensor noise is shown in Figure 5-7. It has 2.6 μrad rms of noise over the 1/4 second of data. This, too, is extremely low.

It is also interesting to note the height of one quanta in Figure 5-7 which is the observed rotary sensor resolution. The sensor is quantized in units of 3.7 μrad at this rotary position. In section 5.1.2 we saw that the resolution depends on the shaft's rotation angle. We calculated that the worst case resolution is 4.6 μrad as shown in Figure 5-2. Our observed sensor resolution of 3.7 μrad at this angle is less than or equal to this maximum value of 4.6 μrad as expected. We can explain this particular resolution as occurring at a rotation angle of $\theta = 36.9°$ as shown in Figure 5-3.

5.7 Summary

This chapter explained the operation of the tilted-mirror sensor. This sensor measures the angular position of the rotary-linear axis by determining the orientation of a mirror tilted slightly with respect to a plane normal to the axis of rotation. The sensor provides an absolute measurement of angle and has an angular resolution of 1,366,000 counts/rev. The sensor noise level is 2.6 μrad rms.

Although this sensor functions well, it is not likely to be used in future rotary-linear axes. This is because in order to achieve high resolution, it requires a flat and hence

[2]Actually, the displacement is proportional to α and the path length of the measurement beam between its two reflections off the target mirror. This distance is usually only slightly larger than $2d$. Since we reduce d to just over an inch, however, this is important.

thick mirror with a large, 3 inch diameter. The inertia of this mirror is 3 times that of the rest of the axis and therefore dominates the rotary axis dynamics. Also, its mass of 0.29 kg at the end of an 8.4 inch length of shaft causes a resonance at 1000 rad/s which severely limits the closed-loop bandwidth of the rotary axis controller. We will investigate this resonance further in section 8.3.1.

Analyzing the beam paths in this sensor led us to learn about an interesting aspect of plane mirror interferometer design. As shown in Figure 5-5, two-pass plane mirror interferometers are insensitive to small angular tilts in the target mirror. This is because the first beam approaches parallel to the rotation axis and returns from the tilted mirror at an angle; on the second pass, the laser beam approaches at an angle and then returns parallel to the rotation axis. Thus, even if the target mirror is tilted the measurement beam returns parallel to the reference beam, but is offset from it an amount proportional to the tilt (see Figure 5-5).

This effect was initially unknown to us, but once discovered allowed us to achieve higher mirror tilt angles (of 4.6 mrad) than we initially expected. In fact, the tilted mirror achieves roughly the same tilt as the helicoid mirror sensor discussed in section 3.4.5 (4.2 mrad for an example design). This was surprising since the helicoid was designed to have a "macroscopic" tilt angle whereas the tilted-mirror sensor was supposed to have a very slight tilt angle. In retrospect, since our tilted-mirror sensor achieved such a high tilt angle and resolution, the helicoid sensor would not have provided much better performance.

In the next chapter we look at the mechanical design and fabrication of the prototype z-θ axis. We see how the sensors and mirror mounts are constructed as well as the motors and the rest of the rotary-linear axis.

Chapter 6

Prototype z-θ Axis

This chapter describes the fabrication and assembly of our prototype z-θ axis shown in Figure 6-1. The moving part is a stainless steel shaft, 15 inches long and 3/4 of an inch in diameter. It rotates and translates in cylindrical air bearings. Linear and rotary frameless permanent magnet motors are located on either end of the shaft. Their magnetic rotors are attached to the shaft while their stators are clamped in V-blocks. On the far left is a 1 inch (2.54 cm) diameter mirror for z measurement, and on the far right is a 3 inch (7.62 cm) diameter, slightly tilted mirror for θ measurement. One interferometer on the left measures distance to the z mirror, and two more

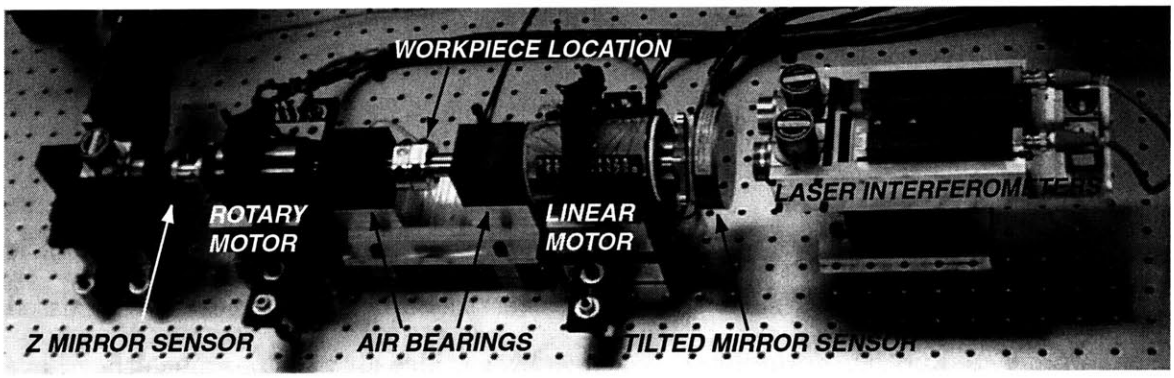

Figure 6-1: The prototype z-θ axis consists of a central shaft riding in two cylindrical air bearings. A frameless rotary motor on the left generates torque, and the custom-built tubular linear motor on the right generates force. On the far left is a 1 inch (2.54 cm) diameter mirror for z measurement, and on the far right is a 3 inch (7.62 cm) diameter, slightly tilted mirror for θ measurement.

interferometers on the right measure the tilt of the tilted mirror.

In this chapter we examine the design and fabrication of each component of the prototype. We point out how the components are designed with system-level goals in mind. For example, the system-level goal of minimizing moving mass and inertia affects the design of many components. We also stress innovative fabrication techniques. For example, arrays of high strength rare-earth permanent magnets pose many fabrication and assembly challenges. Finally, we examine how well our design and fabrication technique succeeds for each component and explain what we have learned.

This chapter's organization parallels the fabrication of the actual prototype axis. We start off discussing the air bearings and machine base. Then we examine the shaft which is the heart of the axis and see how the magnetic rotors and sensors are attached to the shaft. In the next section we look at the design of the tilted-mirror sensor and small z-mirror sensor and how they fit into the prototype axis design. After that we describe the fabrication of the custom tubular linear motor. We show how we assemble high strength Neodymium Iron Boron (NdFeB) magnets to form the magnetic rotor. We also look at the design and fabrication of the stator with emphasis on routing coil start and finish leads and protecting the wires from nicks and shorts. We finish the chapter with a description of the rotary motor and its assembly into the z-θ axis.

6.1 Air Bearing

As discussed in section 3.3 we choose to use air bearings rather than hydrostatic bearings in our prototype since they are easier to implement. We also discussed that we selected porous graphite air bearings over orifice air bearings since they have better crash resistance, higher damping, and self-alignment features. They are also less expensive and more readily available.

We use 3/4 inch New Way (see Appendix F) air bushings with a max load of 111 N and a stiffness of 18 N/μm. Figure 6-2 shows how the load capability varies with air

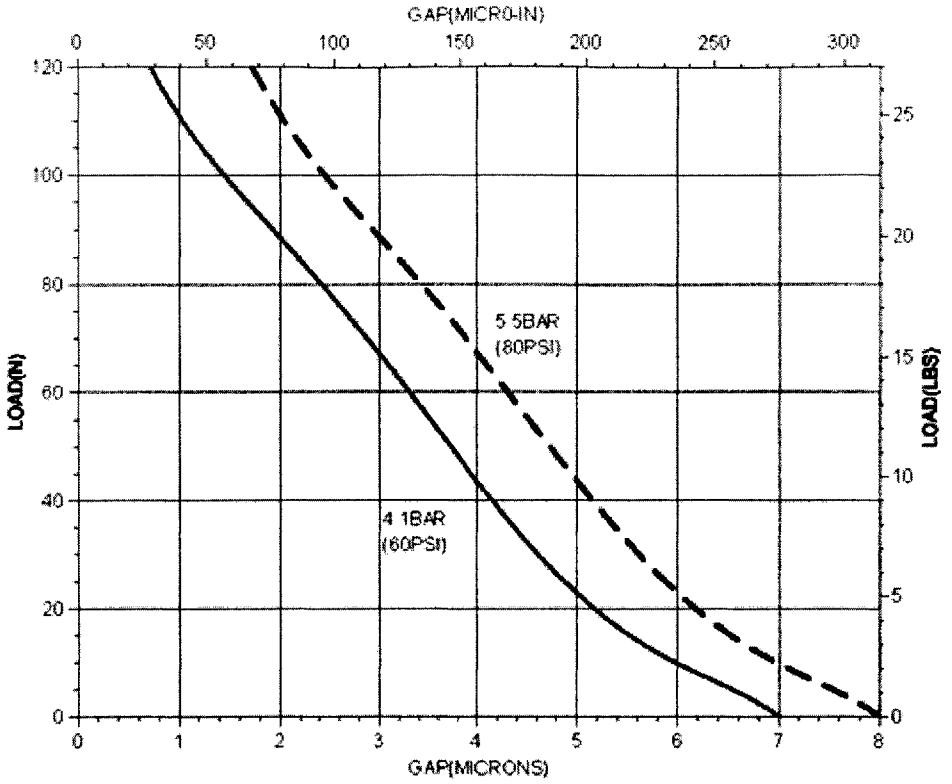

Figure 6-2: Load vs. air gap in 3/4 inch New Way air bushing. Figure from New Way Bearings (see Appendix F).

gap for 60 psi and 80 psi. The higher supply pressure has a higher load capability for a given air gap, but the air bearing stiffness is in general the same at the two different pressures.

The New Way air bushing and pillow block are shown in Figure 6-3. The bushing is sprayed with alochol and pressed into the pillow block. The O-rings can get caught and broken during the pressing process if the bearing is not pressed in straight. The four O-rings surrounding the bushing are compliant enough to allow the bearing to self-align inside the pillow block. The air pressure fitting is connected to the central hole on the pillow block. The region bounded by the two middle O-rings, the bushing, and the pillow block is also at supply pressure. The regions bounded by the top two O-rings and bottom two O-rings can be filled with a low-expansion replicating epoxy to increase the bearing's stiffness. At first we did not pot the bearings with epoxy, and the bearings worked nicely with only the O-rings for support. Later, we increased

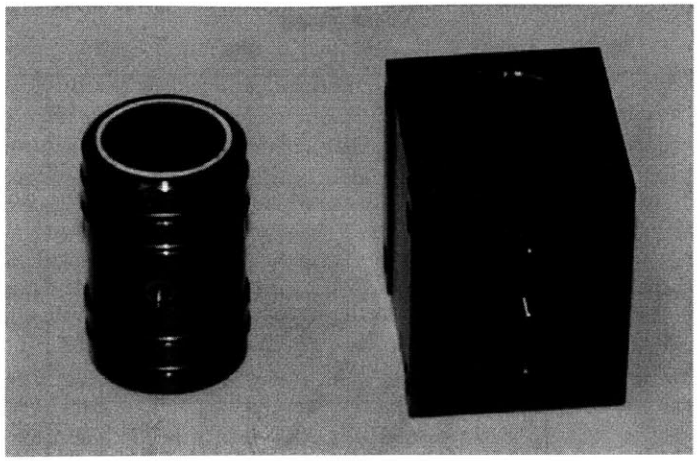

Figure 6-3: New Way Bearings (Appendix F) 3/4 inch porous graphite air bushing (left) and pillow block (right).

the stiffness by injecting epoxy.

In the course of characterizing the axis's rotary behavior, we discovered a low-frequency resonance at 100 Hz. We reasoned that if the shaft were unbalanced, the bearings would have to exert forces on the shaft as it rotated. These forces could act across the compliant O-rings to generate the resonance. To achieve higher bearing stiffness, we potted the bearings in Moglice, a low-expansion replicating epoxy, sold by Devitt Machinery Company (Appendix F). The first Moglice formulation we tried, Moglice 628, was almost a putty, and was much too thick for injecting into the pillow block. A more fluid formulation, Moglice FL/P, worked much better. We first mixed the epoxy well for several minutes, and then carefully poured it into an injector cartridge so that no air was trapped. Next, the injector was fit into the opening on the front of the pillow block, and Moglice was injected until it flowed out the opening on the back. It was viscous enough to fill the entire annular region between each set of two O-rings. Potting the bearings increased the resonant frequency from 100 Hz to 160 Hz. At this point, we identified the resonance as a cantilever mode of the beam. New Way's website (Appendix F) warns that "the potting procedure is only effective in relatively short travels because in most applications over one inch in travel, the air film and o-rings are stiffer than the bending strength of the guide rod." This agrees

with our experience related above.

6.2 Base

A base piece supports both of the air bearing pillow blocks as shown in Figure 6-4. It is made of aluminum to match the thermal expansion in the aluminum pillow blocks and also because aluminum is easily machinable. We milled the base from a solid aluminum block. It contains a cutout section in the center to increase space around the workpiece. This space will be especially needed if the shaft has a cradle section in between the two air bearings to hold the workpiece. This cradle might also have a small index table mounted on it, and a reach-in actuator to rotate the index table could be mounted to the base piece. After the base is machined, we take a finishing pass of the top surface with a fly-cutter to ensure that the two surfaces supporting the air bearing pillow blocks are at the same height and parallel. A mechanical drawing of the machine base is shown in Figure D-2 of Appendix D.

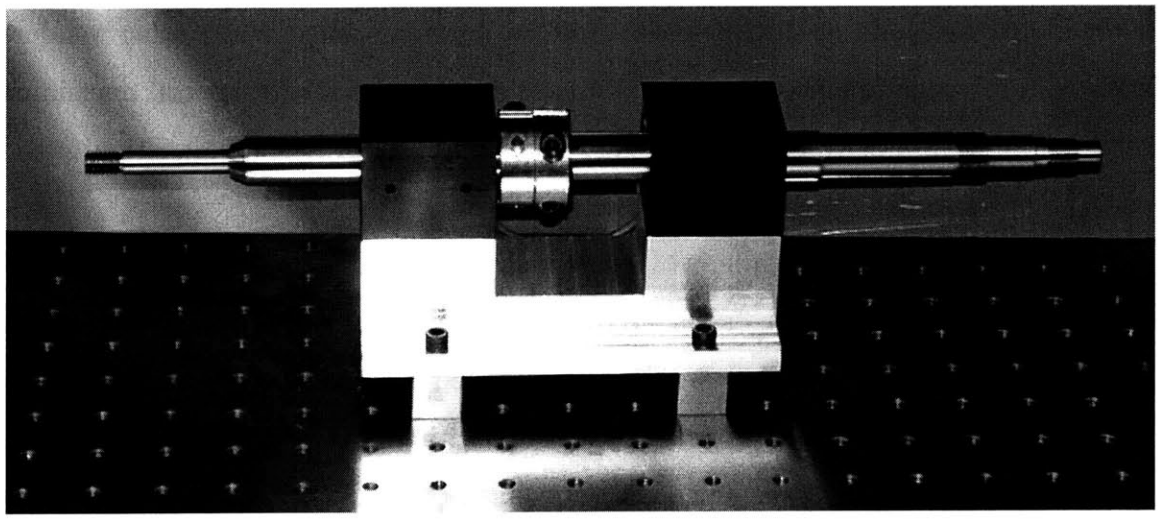

Figure 6-4: The precision ground stainless steel shaft rides in two air bushings. Shoulders and threads are machined into the shaft for attaching the magnetic rotors and sensor mirror mounts.

6.3 Shaft

The shaft, shown in Figure 6-4, is the heart of the axis. It holds the workpiece and accelerates it in translation and rotation. The magnetic rotors of the two frameless motors are both attached to the shaft to provide force and torque. A two degree of freedom position sensor is also mounted to the shaft.

Our primary concern in designing the shaft is minimizing its mass and rotary inertia to maximize achievable accelerations. We must also ensure that the resulting shaft is stiff enough to handle the accelerating forces and machining forces without deflecting. A stiffer structure with a lower mass and inertia also has a higher natural frequency which allows for higher control bandwidth. Finally, the shaft must be designed so that it can be fabricated economically and quickly.

6.3.1 Material & Form

The shaft is made from solid precision ground stainless steel. We were fortunate to find a vendor, Thomson Industries (Appendix F), which would sell us a custom machined shaft at a reasonable cost with a very fast turnaround time. Most other vendors were not interested in our order, asked for exorbitant prices for the special machining required, and gave delivery dates of many months. This practical restriction forced us to compromise on the shaft's material and form.

Initially it seemed the stiffness of a 3/4 inch solid stainless steel shaft was significantly higher than required. Thus we considered aluminum solid shafts and hollow stainless steel shafts since they would have reduced mass and inertia and yet they have sufficient stiffness. As it turned out, even with the solid stainless steel shaft, stiffness has become an issue since the rotary sensor is much heavier than initially envisioned. In order to work in air bearings, an aluminum shaft would need a hard coat of roughly one-half thousandth of an inch. The shaft would need to be custom precision ground and machined for us and then hard coated. No vendor we contacted was willing to do this quickly and inexpensively.

Next we considered using tubular shafting instead of solid shafting to attempt

to reduce mass and inertia without affecting stiffness significantly. Unfortunately, Thomson's tubular steel shafting, unlike its solid shafting, is not available in the ultraprecision N Class which has a tolerance of two ten thousandths of an inch. This tolerance is required for the shaft to work with the New Way air bushings. Thomson could precision grind a tubular shaft for us to this tolerance level, but the costs were very high since they would have to grind an entire twelve foot length of shafting. In addition, a tubular shaft cannot have deep shoulders machined into it; our final design does have deep shoulders to accommodate the magnet array of the rotary motor.

The shaft's magnetic properties also affect the machine design. We use a 440EH stainless steel, which is ferromagnetic. This enables us to use the shaft indirectly as back iron for the linear motor magnet array. The linear motor magnets are mounted on thin octagonal pieces of steel with circular cutouts so that they can be mounted on the shaft (see Figure 6-15). The octagonal back iron would surely saturate if not for the presence of the magnetic shaft inside it. If the shaft is made of a non-magnetic material, the octagonal pieces would have to be significantly thicker adding mass and inertia to the axis.

6.3.2 Geometry

As explained in the previous section, we first selected the shaft's material and form—a stainless steel, solid shaft. In this section, we explain the design of the shaft's geometry—its precision machined shoulders and threads. These features must provide some means for attaching the two magnetic rotors and the sensor mirror mounts. Furthermore, we must carefully examine the allowed axial travel of the shaft and make sure that a rotor will not crash into an air bearing, or a sensor mirror into a stator as the shaft translates. Thus, designing the shaft's geometry required us to envision the entire machine and design many other key parts concurrently. It also required careful attention to details.

We attached the magnetic rotors to the shaft by axially clamping them against shoulders machined into the shaft. The shoulders' diameters are a few ten-thousandths of an inch smaller than the rotors' inner diameters so that the rotors slide on with

a loose fit. Locknuts axially clamp the rotors against the shaft's shoulders. This mounting method both locates the rotors on the shaft and provides for torque and force transfer between the rotors and the shaft. The rotors can easily be disassembled from the shaft. This allows replacement of one of the motors or the shaft without having to rebuild the entire setup. If a permanent mounting method were used, the air bearings would be captured by the rotors, and the axis could not be disassembled.

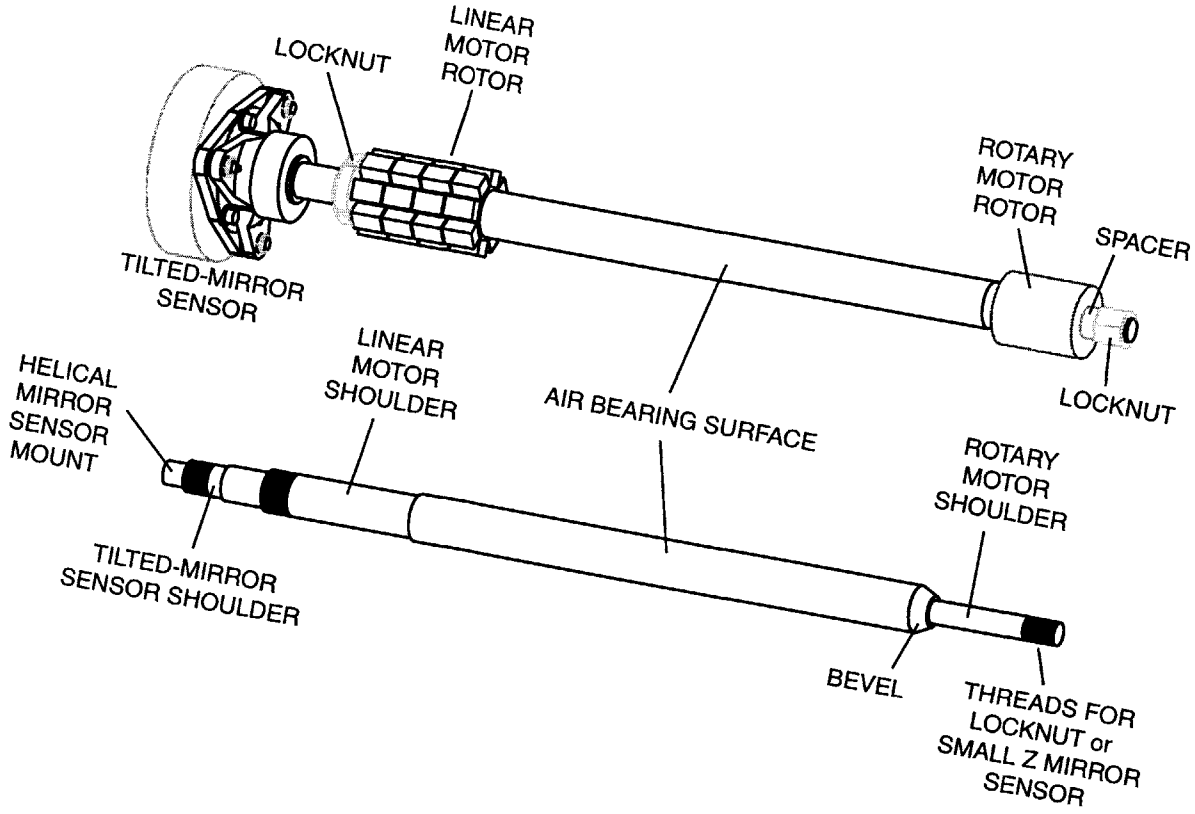

Figure 6-5: Shaft geometry and assembled components. The shaft is 0.75 inch in diameter in the center and 15.23 inches long. Figure D-1 shows a detailed mechanical drawing of the shaft.

The shaft's geometric features and some assembled components are shown in Figure 6-5. A detailed mechanical drawing of the shaft is shown in Figure D-1 of Appendix D. The central part of the shaft which rides in the air bearings is precision ground to 0.7500 +0.0000/-0.0002 inch. On the right side of the shaft in Figure 6-5 is a 0.375 inch shoulder for mounting the rotary motor. A bevel reduces stress con-

centrations resulting from the abrupt change in shaft diameter. The rotary motor shoulder is made roughly 1/4 inch longer than the rotor so that a spacer is needed between the rotor and locknut. This spacer allows for the addition of an auxiliary component to the axis. We initially envisioned this component to be either a small mirror for direct z sensing or an eddy current damper. Although not shown in Figure 6-5, we did decide to add a small z mirror sensor in this location. However, we did not axially clamp the z mirror sensor mount between the locknut and the rotor; instead, the z mirror sensor mount is threaded and replaces the locknut.

On the left side of the shaft in Figure 6-5 is the shoulder for the linear motor rotor. The linear motor rotor consists of four magnet rings which are slid onto the shoulder and axially clamped with a locknut. The next smaller shoulder is for the tilted-mirror sensor mount. We will explain this sensor's mechanical design and mounting in the following section. At the time we designed this shaft, we anticipated using the tilted-mirror sensor for the first stage of the project and then switching to the helical mirror sensor. Thus, our shaft design also provides a mounting surface for the helical mirror sensor which would replace the tilted-mirror sensor. The helical mirror sensor uses a stationary helical mirror and requires a small arm to be mounted to the shaft. We planned to use a two-piece shaft clamp to attach this arm. In fact, the helical mirror was never manufactured, so we have not used this mounting surface.

6.4 Sensor

Now, we turn to the mechanical design of the two interferometer-based sensors. Both sensors require mounting mirrors to the shaft and allowing the tilt of these mirrors to be adjusted. The tilted-mirror requires more tilt adjustment than the smaller z-mirror. Fixturing and packaging the interferometer optics is another challenge. Throughout the sensor design process, we tried to balance increased sensor resolution with the desire to minimize the added mass and inertia of the sensor mirrors. For example, increasing the diameter of the tilted mirror increases the rotary sensor's resolution, but also increases the mass and inertia of the moving axis. Marsette Vona

designed and fabricated the mirror mounts and interferometer mounts as part of his Master's thesis, *Metrology Techniques for Compound Rotary-Linear Motion* [70].

6.4.1 Tilted-Mirror Sensor

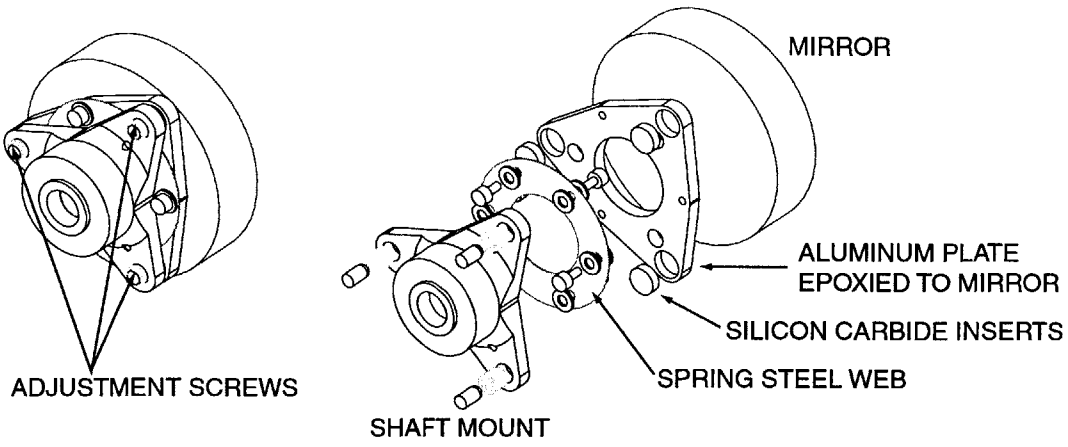

Figure 6-6: Tilted-mirror mount. Figure drawn by Marsette Vona [70].

Shaft rotation and translation can be determined by measuring the tilt of a slightly tilted mirror mounted to the shaft. The tilt is determined by measuring the distance to the mirror at two locations with plane mirror interferometers. For our prototype axis, we want to be able to adjust the mirror tilt so that we could determine the sensor's limitations; in general, however, a fixed tilt mount would work. The mounting method also needs to be removable so that the axis can be partially or wholly disassembled.

Figure 6-6 shows the design of the tilted-mirror mount. It consists of two parts, a shaft mount and a mirror, connected by a spring steel web. The spring steel web attaches to the shaft mount with three screws and to an aluminum plate epoxied to the mirror with three additional screws. The web pre-loads the mirror and silicon carbide inserts in its aluminum backing plate against three fine-pitch adjustment screws in the mount. These three adjustment screws set the mirror's tilt. The shaft mount and aluminum backing plate are designed to have as small an inertia as possible while supporting the mirror. This is why we fixture the mirror from the back rather than from its circumference. Also note that the shaft mount is a cuplike structure so that

the smaller diameter portion of the mount can fit inside the linear motor stator if the axis is translated. This reduces the shaft's length.

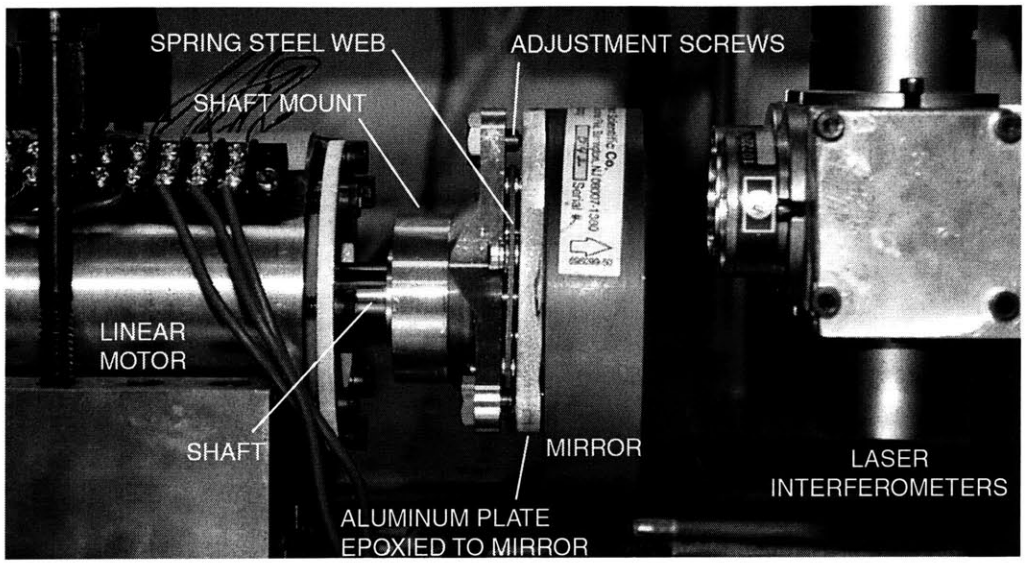

Figure 6-7: Tilted-mirror mount assembled on the z-θ axis.

This modular mount can be assembled and disassembled from the shaft. First, the shaft mount is placed onto a shoulder of the shaft labeled the "tilted-mirror sensor shoulder" in Figure 6-5. Then, a locknut is tightened against the mount using a custom-machined spanner wrench which is required due to the limited space around the locknut. Next, the spring steel web is attached to the shaft mount and then the mirror's aluminum backing plate. The mirror extends just beyond the end of the shaft. The adjustment screws can now be turned to achieve the desired mirror tilt. Figure 6-7 shows the tilted-mirror mount assembled on the shaft.

This tilted-mirror mount is successful at mounting the mirror and allowing the tilt to be adjusted. The mass and inertia of the sensor are also significantly reduced over other possible designs. Nonetheless, the sensor adds considerable inertia to the axis: The sensor's inertia is 25.1×10^{-5} kg·m^2 compared to 8.9×10^{-5} kg·m^2 for the shaft and two rotors. The sensor inertia reduces the angular acceleration of the axis by almost a factor of four compared to a sensor with negligible inertia. The sensor's mass, 0.29 kg, does not significantly reduce the axis's linear acceleration since the

mass of the shaft and two rotors is 1.15 kg. However, the location of the mass at the end of the shaft causes a low-frequency 160 Hz cantilever mode of the shaft which couples to the shaft's rotation and reduces the achievable bandwidth of the rotary axis controller as described in section 8.3.

6.4.2 Small Z-Mirror Sensor

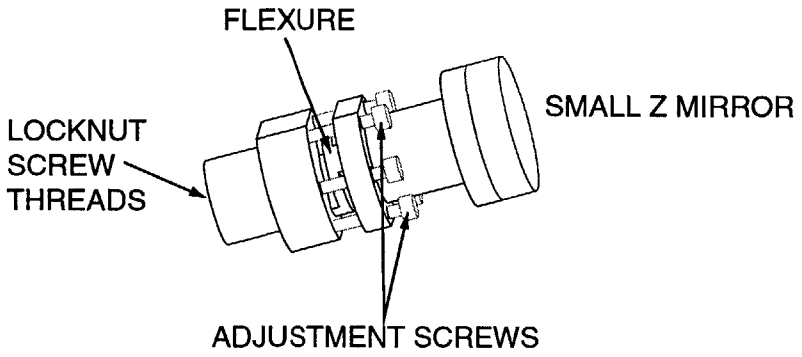

Figure 6-8: Small z mirror mount. Figure drawn by Marsette Vona [70].

The small z-mirror sensor provides a direct measurement of shaft translation, z. Although the tilted-mirror sensor also provides an indirect z measurement, this sensor suffers from singularity at two angles, and an independent z measurement removes this singularity. If the small z-mirror has an uncorrected tilt and the interferometer beams are not centered, a pure rotation of the shaft would cause a change in measured z. Thus, this sensor has a very slight adjustable tilt which is used to ensure perpendicularity between the mirror and the shaft.

Figure 6-8 shows the small z-mirror mount. A two degree-of-freedom flexure allows for slight tilt adjustment. Six adjustment screws—three for pushing and three for pulling—are used to adjust the mirror's tilt. The mount contains locknut screw threads and replaces the locknut shown in Figure 6-5. Thus, it is a removable mount. Furthermore, the entire mount fits inside the rotary motor stator as can be seen in Figure 6-9. This is desirable since it reduces the shaft's length which reduces mass and inertia and increases natural vibration frequencies.

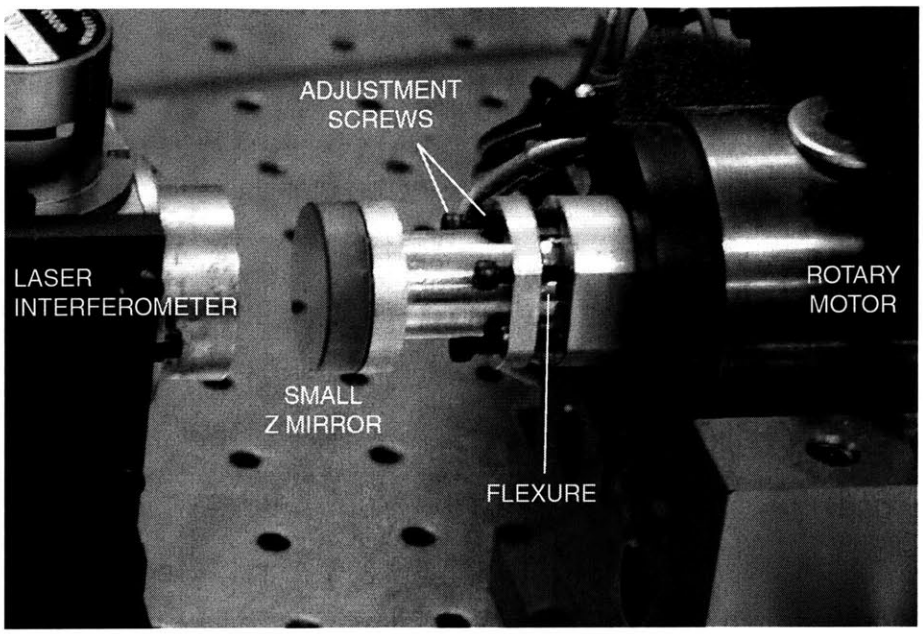

Figure 6-9: Small z mirror mount assembled on the z-θ axis.

6.4.3 Interferometer Mounts

Figure 6-10 shows the location of the Plane Mirror Interferometer (PMI) optics and receivers. The optics and receiver for the small z mirror sensor are mounted in the standard way. However, the tilted mirror sensor requires two laser interferometer measurements. In order to keep the mirror's diameter small, the two interferometers need to be placed as close as possible. Thus, we built a custom mount which packages both laser interferometers compactly. Figure 6-11 shows a picture of this mount.

Then entire metrology setup is shown in Figure 6-12. The He-Ne laser provides light for all three interferometers. Beam splitters send the laser light to each interferometer. The height of the small z-mirror interferometer and the height of the tilted-mirror interferometers differ by roughly one-half inch. It is only easy to change the beam height by amounts greater than or equal to one inch with one inch optics components; thus, we increase the height by an amount $x > 1$ inch and then decrease it by an amount $y > 1$ inch such that $x - y$ is the desired height difference of roughly one-half inch.

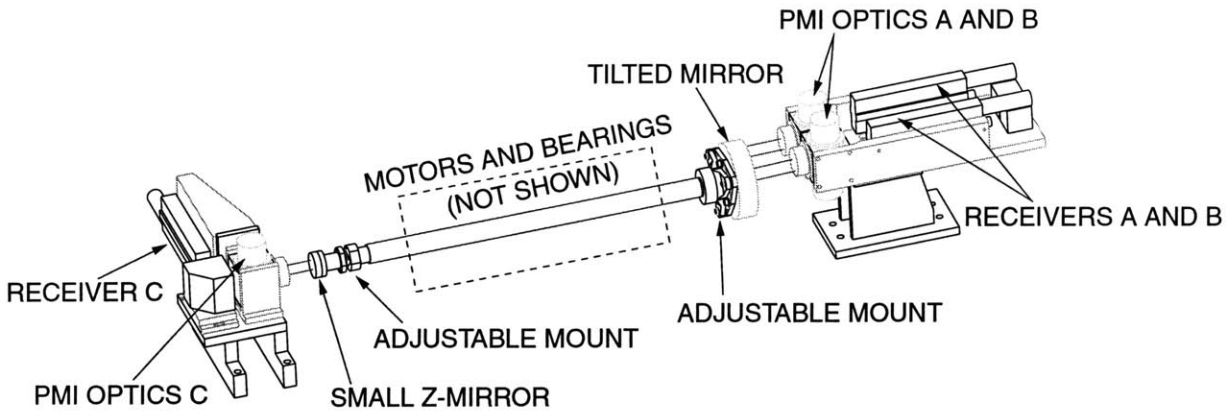

Figure 6-10: The tilted-mirror sensor and small z-mirror sensor are located on opposite ends of the shaft. The three Plane Mirror Interferometers (PMI) are shown along with their receivers. Figure drawn by Marsette Vona [70].

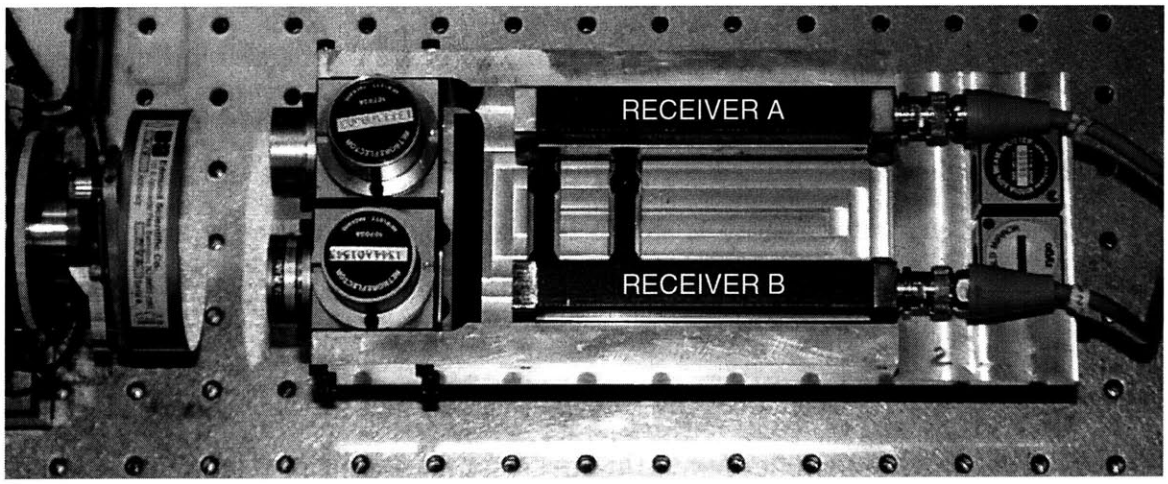

Figure 6-11: Compact mount for the tilted-mirror sensor's interferometer optics and receivers.

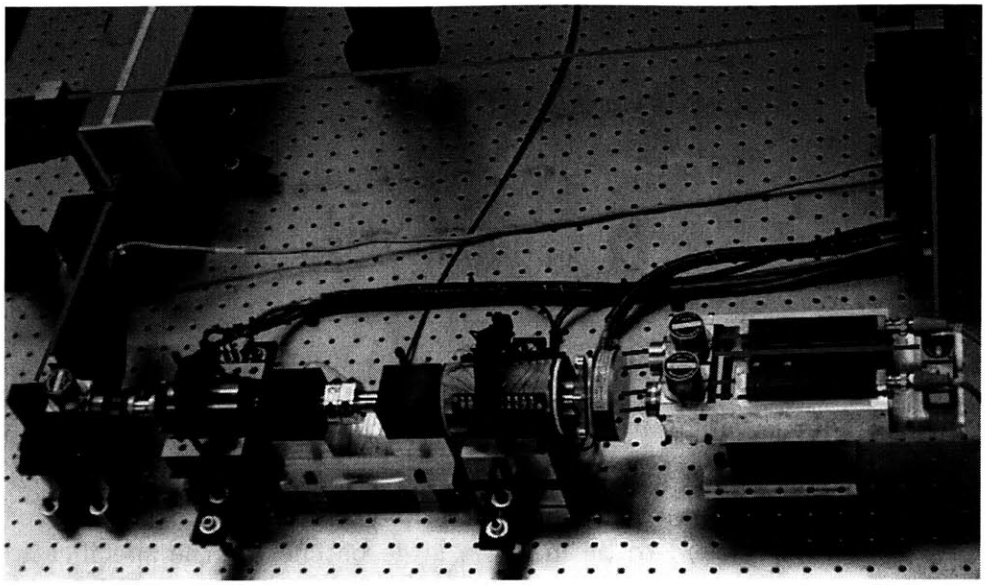

Figure 6-12: Approximate laser beam paths for the three, two-pass plane mirror interferometers.

6.5 Linear Motor Permanent Magnet Rotor

Tubular linear motors are not yet commodity items although a couple of companies make inexpensive ones for non-precision applications. Thus, we were forced to design and build a custom tubular linear motor. Fortunately, tubular linear motors are easier to construct than other types of motors, such as rotary motors, because the windings can be rings, and there are no end-turns to deal with—only coil leads. The motor is a three-phase, permanent magnet, synchronous motor. It is also a frameless motor: the stator and rotor are separate pieces which rely on some external bearing means such as the shaft's air bearings in our machine. We first describe the design and fabrication of the magnetic rotor and then in the following section we describe the design and fabrication of the stator.

Ideally, the magnetic rotor of a tubular linear motor consists of a series of ring magnets. These rings should be magnetized radially as shown in Figure 6-13. Unfortunately it is difficult to obtain small quantities of rare earth ring magnets at reasonable costs. This is due primarily to the expense of the custom magnetizing fixture required for radially magnetized ring magnets. Also, magnetic material in the

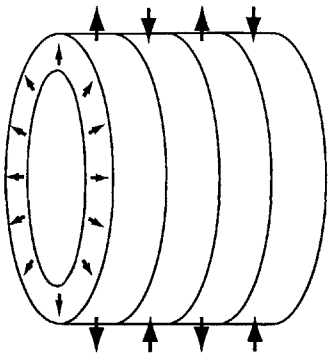

Figure 6-13: An ideal configuration of radially magnetized ring magnets for a tubular linear motor.

shape of rings and arcs tend to be made in large batches to the specifications of a particular motor manufacturer.

6.5.1 Magnets

There are several possibilities for achieving a ring magnet indirectly. One is to use a compression bonded NdFeB magnet which can be readily machined. This material can be milled into arcs which can be magnetized approximately radially in a standard solenoidal magnetizer. The disadvantage of compression bonded NdFeB is that it has a remanence of 0.5-0.6 T, about half that of sintered NdFeB. Nonetheless, it is widely used in prototype motors. Sintered NdFeB can be machined into arcs and magnetized in the standard way too. Unfortunately, it can be tricky to machine as unreacted Nd chips oxidize in an exothermic reaction and can catch fire.

A third alternative for fabricating a radially magnetized ring is to approximate the ring with a number of small rectangular magnets. Sintered NdFeB rectangular magnets are readily available at reasonable costs. We choose this method of fabrication as it provides the high fields of sintered NdFeB, but requires no machining of magnetic material, or purchase of custom magnetizers.

Michael Berhan built ring magnets for a tubular motor out of eight rectangular magnets arranged in an octagon [5]. One of his rings is shown on the left in Figure 6-14. In his tubular linear motor, the magnet array surrounds the stator and does not

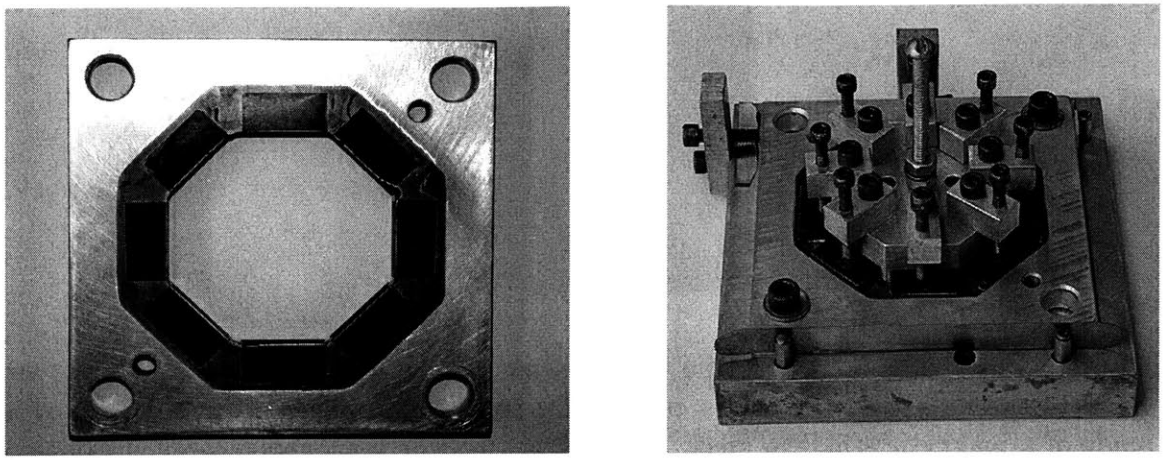

Figure 6-14: On the left is an exterior octagonal ring magnet for a tubular linear motor. On the right is the fixture used to assemble the magnets. Pictures taken by Michael Berhan [5].

have any back iron. He designed and built an elaborate fixturing system shown on the right in Figure 6-14 for assembling the octagonal magnet rings. The fixturing system locates and holds the magnets in place while a replication epoxy is applied between the magnets and an aluminum housing.

In our design, we also decided that an octagon offers a good compromise between closely approximating a circumscribing circle and using as few magnets as possible. Since our magnet array is internal to the coils and has a back iron, the assembly process is considerably easier. We have the further requirement that the magnet array be modular and removable so that we can use it again on successive generations of the z-θ axis shaft. To achieve this, our design consists of a steel back iron ring shown in Figure 6-15 which slides onto a shoulder of the shaft. The magnets are glued to the eight flats on the outside of the ring. A drawing of the completed structure is shown in Figure 6-16. The assembly of rings is axially clamped into position against the shaft shoulder.

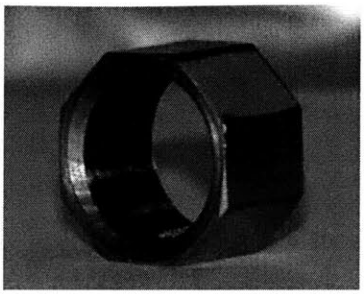

Figure 6-15: The back iron for the linear motor magnets. Eight NdFeB magnets are glued to the flats, and the center portion fits onto a shoulder of the shaft, which is made of a magnetic stainless steel.

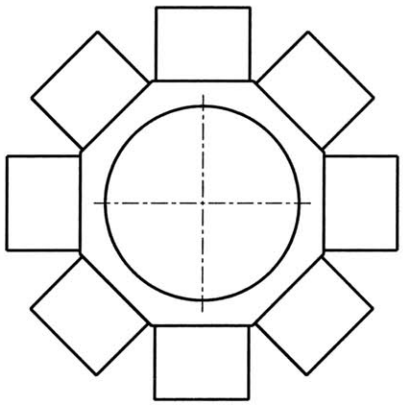

Figure 6-16: Drawing of the octagonal back iron with eight NdFeB magnets glued to it. A detailed mechanical drawing is shown in Figure D-4 of Appendix D.

6.5.2 Back Iron Octagon

The octagonal back iron shown in Figure 6-15 is machined out of low-carbon steel rod. Low-carbon steel is soft physically and magnetically, which are both desirable properties in this application. The exterior octagonal shape was first milled with an NC mill while the rod was held vertically in a V-block. Next the bar stock was placed in a lathe, and the center was drilled and then bored to diameter. Then, we cut the part to approximate height with a cutoff tool and milled it down to achieve the desired height. Finally, the central hole was counterbored. In the last milling operation, the pressure exerted by the vise was sufficient to deform the thin ring-like structure so that the bored center hole was elliptical with a major axis roughly ten

thousandths of an inch longer than the minor axis. In order to correct this, we lightly clamped the part along its major elliptical axis to return it to round and also polished the interior on a lathe to achieve the required hole diameter.

6.5.3 Octagonal Ring Assembly

In this section we describe how we assemble and align eight strong NdFeB magnets onto the octagonal nut. A mechanical drawing of the assembly is shown in Figure D-4 in Appendix D. Figure 6-17 shows our initial assembly fixture. The base is an aluminum plate with a tapped hole in the center. A screw tightened into this hole clamps the octagonal back iron between the aluminum plate and a washer. The screw also passes through a cylindrical part which fits into the center of the back iron nut and thus prevents the nut from moving sideways. This part is hidden in Figure 6-17 since it is beneath the washer and inside the nut. The octagonal back iron's height is slightly longer than the length of the magnet, so that when several rings are clamped together the clamping force will be on the rings and not the brittle magnets. A brown plastic shim with an octagonal cutout is used to space the magnet ten thousandths of an inch above the aluminum plate so that it is centered on the octagonal back iron's height. This shim is coated in mold release so that any stray glue does not stick to it.

We next describe the assembly procedure. We determine the polarity of the magnet to be assembled with a gaussmeter. Then, a drop of Maxi-Cure cyanoacrylate (Appendix F) is placed on the appropriate side of the magnet. The magnet is carefully brought into contact with the flat and centered by eye. This requires some practice as the magnetic force can be quite large, and the magnets are brittle and will crack if not touched down gently. Also, the cyanoacrylate sets in a couple of seconds so the centering must be done very quickly. We add magnets contiguously around the octagon.

After adding several magnets to the nut, it becomes noticeably harder to add further magnets. Figure 6-18 shows five magnets added to the nut. If we assume that they are all magnetized radially outwards, then the exposed portion of the nut acts like

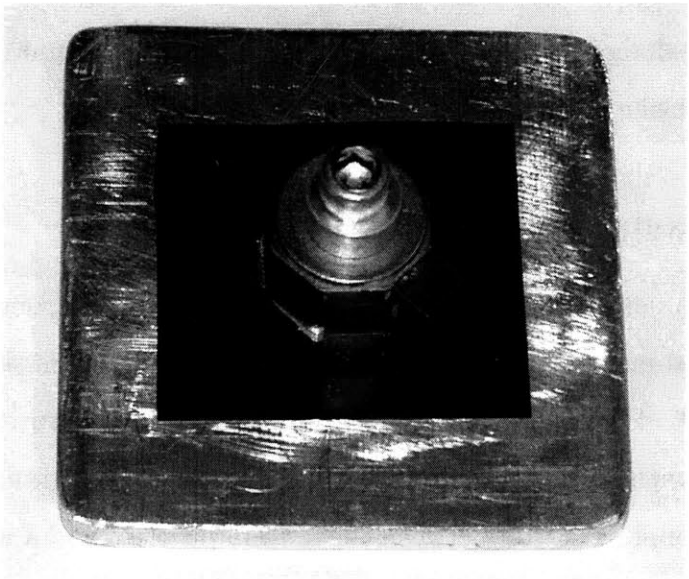

Figure 6-17: Assembly of the magnet array with the first fixture.

a south pole and its flux can be measured with a gaussmeter. As we bring in the south pole of the next magnet to be added, it repels the iron surface until it gets very close, approximately a millimeter. At this point it is close enough to induce a north pole in the iron and is suddenly attracted to the iron. This initially unanticipated behavior makes assembly of the last two magnets onto the nut significantly more difficult. For this reason, we build a second assembly fixture shown in Figure 6-18. This fixture has an extremely thin aluminum base, and the screw is tightened directly into a steel optical table. The steel table acts to short out the magnets already assembled on the nut so that they do not repel the incoming magnet as strongly. Also, the incoming magnet is attracted to the steel, and this reduces the force required to hold it centered as it is brought into position. The thin base is made extra long, so that it can be pried off the optical table once the magnet ring is complete.

The completed magnet ring is shown in Figure 6-19. We spray paint the magnet surfaces with a rust inhibitor so that the magnets do not rust. In the next section we describe how these rings are assembled onto the shaft to form the magnetic rotor of the linear motor.

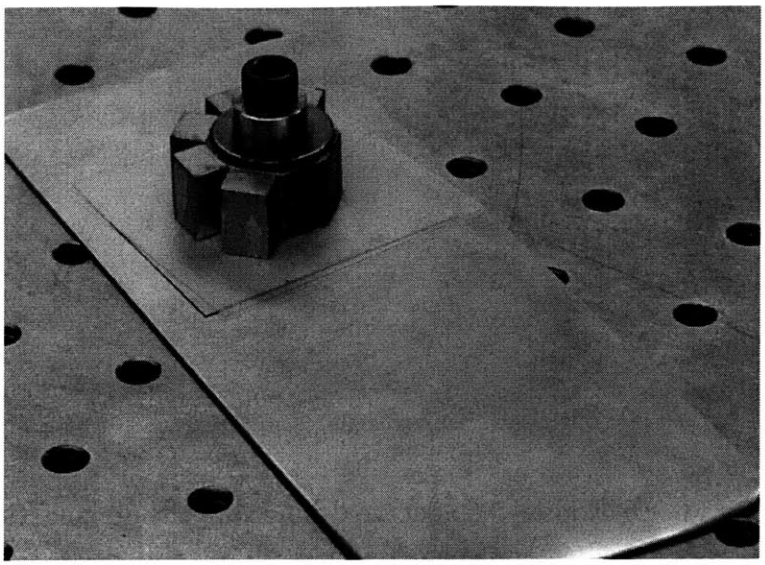

Figure 6-18: Assembly of the magnet array with the second fixture. The steel optical table partially shorts out the magnets already assembled and attracts the incoming magnet so that the force required to position it is reduced.

6.5.4 Assembly of Rings onto Shaft

Figure 6-20 shows how we assemble the rings onto the shaft using an aluminum endcap. The hollow endcap covers some of the shaft and extends beyond the end of the shaft. The endcap is a sliding linear bearing which maintains the orientation of the magnet ring as it is slid onto the shaft. With the endcap present, the large magnetic attraction between the magnet ring and the ferromagnetic shaft acts only to pull the ring onto the shaft.

The magnetic pitch of the linear motor is the distance between North poles in the magnet array. The pitch of our linear motor is equal to the width of four magnet rings, or 4×0.520 inch $= 2.080$ inch. The magnet rings could be arranged north–north–south–south, but to better approximate a segment of a longer magnet array, we arranged the rings north–south–south–north as described in more detail in section 4.3.6. Figure 4-8 of section 4.3.6, "Magnet Arrays," shows how the fields from this magnet array better approximate an ideal magnet array with multiple pitches. The first and second magnet rings attract each other as do the third and fourth. The two pairs of magnet rings repel each other, but are forced together as the locknut is

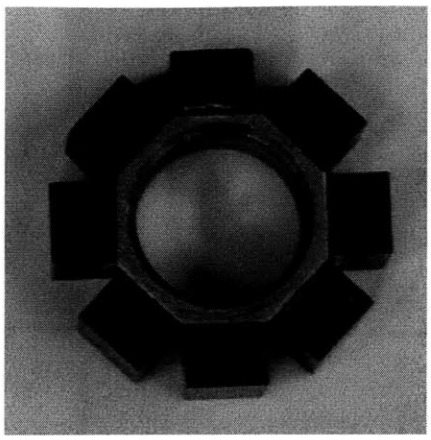

Figure 6-19: Radially magnetized linear motor magnet ring.

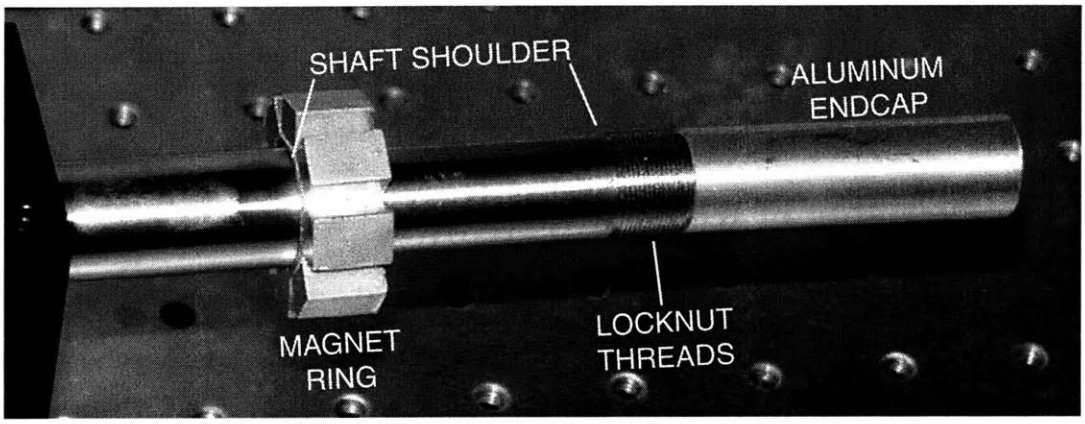

Figure 6-20: The first magnet ring has been slid onto the shaft's shoulder. The aluminum endcap centers the ring on the ferromagnetic shaft during assembly.

tightened. We use precision Bearhug Locknuts from Whittet Higgins (Appendix F). Figure 6-21 shows the completed linear motor rotor.

6.6 Linear Motor Stator

The linear motor stator essentially consists of a stack of ring coils in a steel can. Nylon spacers separate the coils, and the coil stack is axially clamped in the can. Stator design and fabrication poses a number of challenges. The wires in the coil must be well insulated from each other and from the back iron. The coils must also be

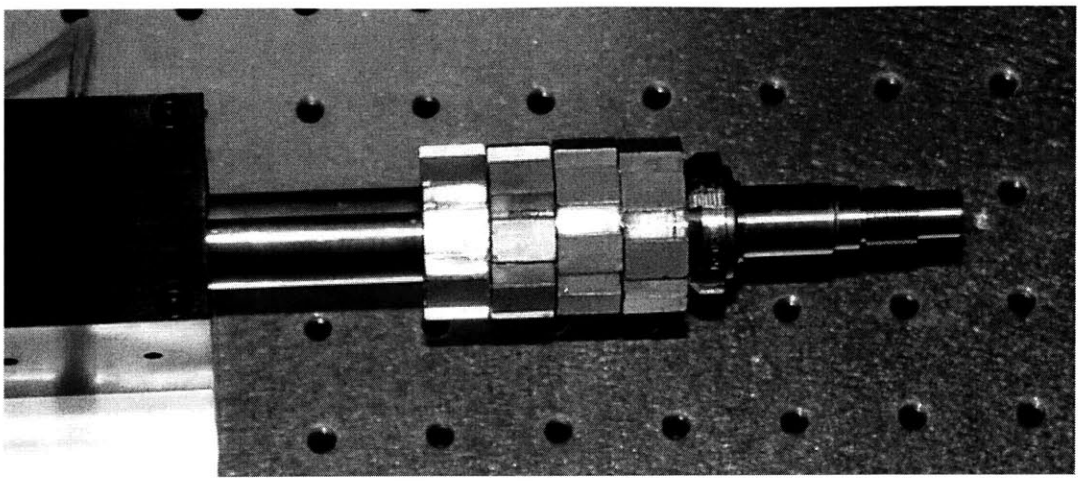

Figure 6-21: Linear motor permanent magnet rotor. The four magnet rings are axially clamped by the locknut.

protected so that they are not nicked during assembly or operation. It is often tricky to route the coil start and finish leads as well. Additionally, good heat transfer out of the stator coils is essential since stator overheating generally limits the achievable force.

6.6.1 Coils

One of the linear motor coils is shown in Figure 6-22. Each coil consists of 104 turns of 23 A.W.G. copper magnet wire. The coil has 9 layers, each of which has 11 or 12 turns per layer. Since the coil has an odd number of layers, the start and finish leads are on opposite sides of the coil, but are located at approximately the same angular position.

The mechanical drawing for the coil is shown in Figure D-3 of Appendix D. The coil has an inside diameter of 1.460 inches which leaves adequate clearance of 0.033 inches between the coil and the diagonal of the octagonal magnet ring, 1.393 inches. This amount of clearance is conservative so that the motor will be easy to align. Figure 6-23 shows the magnet ring inside the coil as they would appear inside the assembled motor. The coil thickness (radially) is 0.200 inches, and its depth (axially) is 0.300 inches.

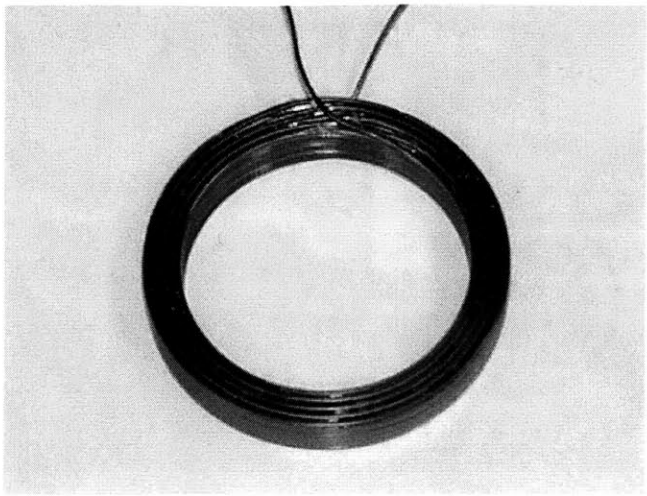

Figure 6-22: Linear motor coil. It was wound by Wirewinders (see Appendix F).

Wirewinders (see Appendix F) wound the coils for us to the dimensions specified in Figure D. We machined a custom bobbin for them with an outer diameter equal to the inner diameter of our coil, 1.460 inches. It is made of steel so that it would not be damaged as the remaining epoxy is scraped away between winding coils. As a coil is wound, Wirewinders apply a thermally conductive epoxy between each of the coil's layers. Then they bake the coils to harden the epoxy and form a solid coil. Usually this produces a flash of epoxy at one edge of the coil; this flash can be sanded away, but then the coil might be damaged. To avoid the flash, they let each coil sit overnight before baking it.

The resulting coils are very nice, but they are about 0.020 inch too thick radially in the region where the coil layers cross over. This occurs in the same angular region where the start and stop leads are located. The crossovers force the coil to be thicker in this region. We made the stator inner diameter slightly larger to accomodate this out-of-roundess in the coil's outer diameter.

6.6.2 Cooling

A stator gets hot when high currents I pass through its coils with resistance R and produce I^2R Joule heating. Typically, this heating limits the motor's maximum

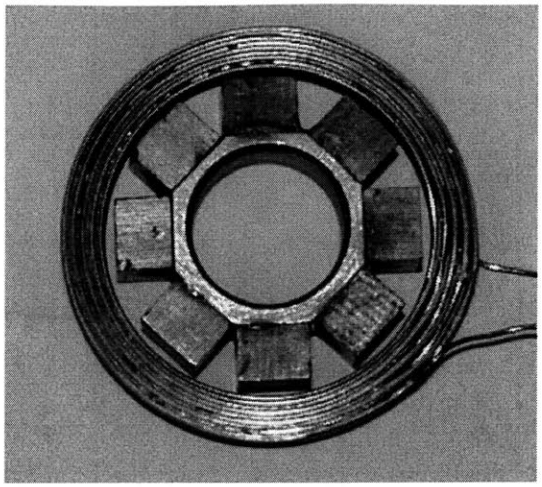

Figure 6-23: The linear motor magnet ring is shown inside the linear motor coil. This picture is similar to a cross-section of the assembled motor.

force. An active cooling system can reduce the temperature rise caused by the heat and thus allow for higher currents and forces in the motor. We did not pursue active cooling methods in our first prototype design, but they could be incorporated in future prototypes.

The author's Master's thesis, *Thermally Efficient Linear Motor Analysis & Design* [41], examines advanced cooling systems for motors. This thesis presents a simple thermal model of an electrical coil which shows that the temperature rise in it increases as the square of the number of coil layers. Thus, a coil with separated end-turns, shown in Figure 6-24, is designed so that each layer of the coil can be directly cooled. Oil flows through the gaps in the end-turns on both sides of the coil to remove heat. This design allows for nearly 6 times higher current and force in steady state and dissipates 32 times as much heat as a free-convection cooled coil. It is also possible to cool this coil with a copper comb-shaped structure inserted into the separated end-turns [41]. Heat flows from the coil to the comb's fingers and then to the comb's base where it is removed by flowing water. This design would allow 4.7 times the current of a free-convection cooled coil, and does not require sealing oil flow past the coil's end-turns.

A separated-turn coil cooling scheme would offer significantly increased force ca-

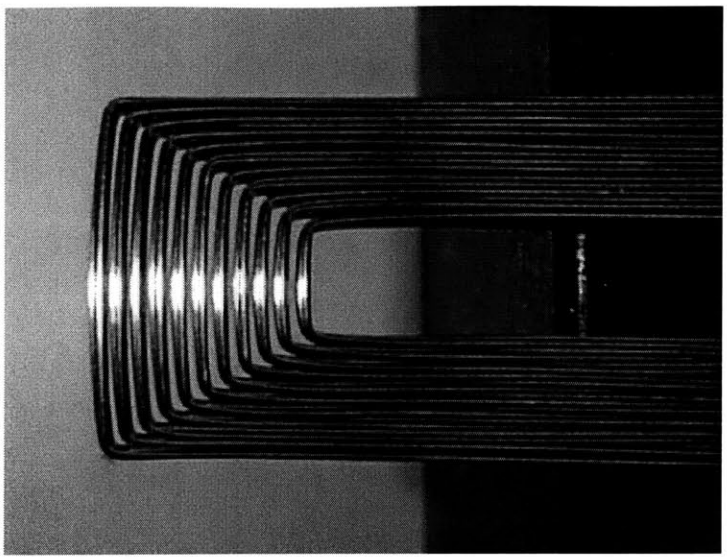

Figure 6-24: A separated end-turn coil allows each layer of the coil to be directly cooled [41]. This technique could be used in future generations of motors for the z-θ axis.

pability for our rotary-linear axis, but would complicate the coil winding and stator design. A conventional cooling scheme which flows air or water through the stator housing would probably offer only a 20%–40% improvement in current and force. In our present setup, the power amplifiers overheat well before the motor does, and they limit the prototype's force capability: continuous phase currents of 3 A cause the power amplifiers to become too hot to touch while the motor's temperature increases much more slowly.

6.6.3 Stator Back Iron

The stator back iron is made from C1018 low-carbon steel. We originally considered making a laminated back iron to reduce eddy current losses. In a tubular linear motor the eddy currents want to circulate around the stator in circular paths. Thus, radial laminations are required to break up these eddy currents, but radial laminations are difficult to form into a cylinder. Thus, we use an unlaminated stator back iron for our prototype motor. Our back iron does have one lengthwise slot, shown in Figure 6-25, which serves as a first-order lamination: The eddy currents cannot completely

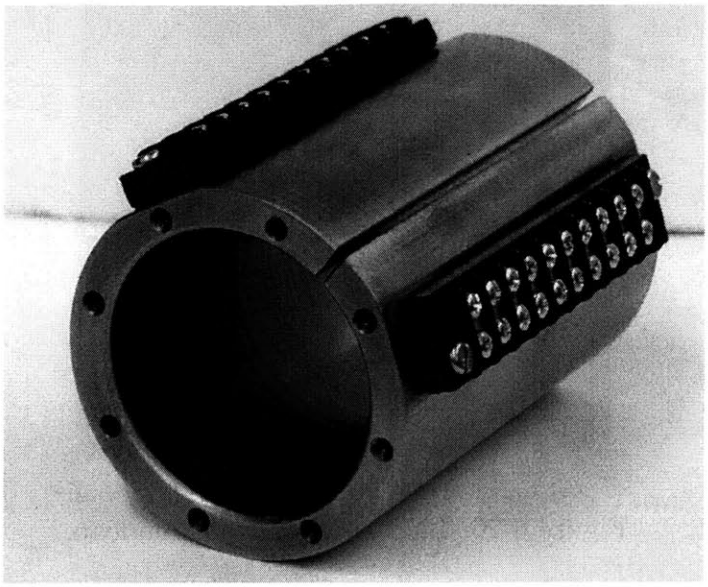

Figure 6-25: Linear motor stator back iron.

circulate around the stator due to this slot. This slot also provides access to the coil leads.

The stator back iron is an annular piece of steel with a slot in it as shown in Figure 6-25. A detailed mechanical drawing of the back iron is shown in Figure D-5 of Appendix D. The stator was machined from 2.5 inch diameter bar stock. First, we drilled out the core of the stator using a succession of larger and larger drills. Then, we bored the inside surface to achieve the inside diameter of 1.875 inches. Next we drilled and tapped eight 8-32 threaded holes on either side for attaching the endcaps. Finally, we used a slitting saw to create the lengthwise slit.

Unfortunately, residual stresses present in the steel acted to close the structure and reduce the width of the slit. Thus, we used the slitting saw again to achieve the desired slit width of 0.060 inches. We also bored the inside diameter again since it was reduced by the closing of the structure. The chips produced by this boring operation were interrupted once per revolution due to the presence of the slit, but with light cuts the boring worked fine. The closing of the structure also reduced the distance between the two tapped holes on either side of the slit. This required making new endcaps with a non-uniform hole distribution to match the hole distribution on the

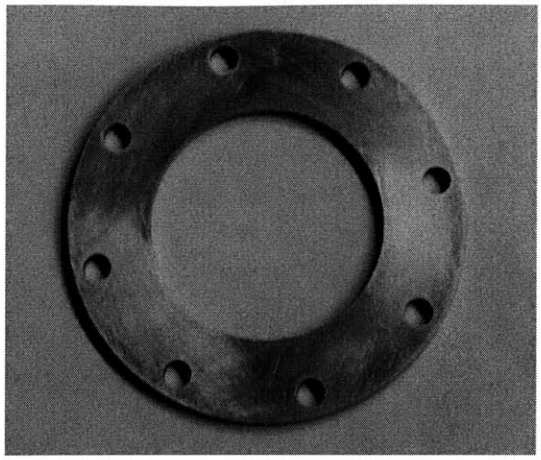

Figure 6-26: Linear motor stator endcap.

back iron. In retrospect, it would have been better to slit the stator before drilling these holes and boring the center to its final dimension.

After the machining was completed, we sanded the interior surface of the stator so that it was smooth and would not nick the coils. We especially filed and sanded the slit and the slit's corners since the coils' leads pass around these corners and through the slit. Also, as shown in Figure 6-25, we milled flats on both sides of the slit and attached two terminal blocks. The coil leads attach to these terminal blocks. Connections between the coils as well as to the power amplifiers are made through the terminal blocks. This prevents any tension from external connections from being transmitted to the motor's coil leads.

6.6.4 Stator Endcap

The two aluminum stator end-caps attach to either end of the stator back iron. One endcap is attached directly to the back iron; the other endcap axially clamps the coil stack inside the back iron. The endcaps are fabricated with a water-jet cutter. Figure 6-26 is a picture of an endcap. The spacing of holes is slightly non-uniform to match the non-uniform spacing of holes on the back iron.

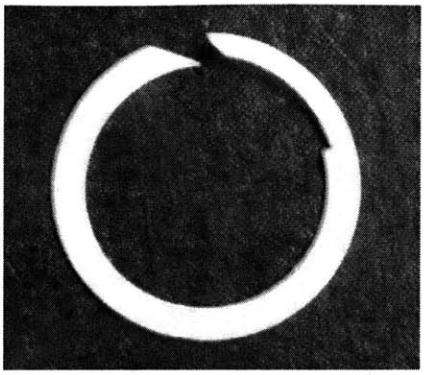

Figure 6-27: Nylon coil spacer.

6.6.5 Coil Spacers

Coil spacers electrically insulate adjacent coils and provide room for the inside coil lead to exit the stator. The inside coil lead must cross the thickness of the coil (see Figure 6-22) to reach the outside of the coil and the slit in the stator back iron. The coil spacer provides space for this lead while maintaining the axial space betwen two coils so that this lead is not compressed when the coil stack is axially clamped.

The coil spacers are 0.040 and 0.050 inch thick nylon rings with cutouts for the inside lead wire as shown in Figure 6-27. Nylon is used since it is electrically insulating, can withstand high temperatures, and won't scratch the coils . We fabricate them from nylon shim stock with a water-jet cutter. When we water-jet the nylon shim stock by itself, the shape of the resulting part is distorted due to the compliance of the nylon ring. Thus it is necessary to sandwich the nylon between two pieces of aluminum shim stock and pop-rivet the three layers together. When we water-jet the three layers together, accurate nylon spacers are produced.

6.6.6 Stator Assembly

In this section we explain how the coils are assembled into the stator back iron. Protecting the coils from damage and short circuits is the most important aspect of this assembly process. Figure 6-28 shows two pictures of the stator during assembly.

A thin pink sheet of Nomex-Kapton-Nomex 2-2-2 laminate lines the back iron and

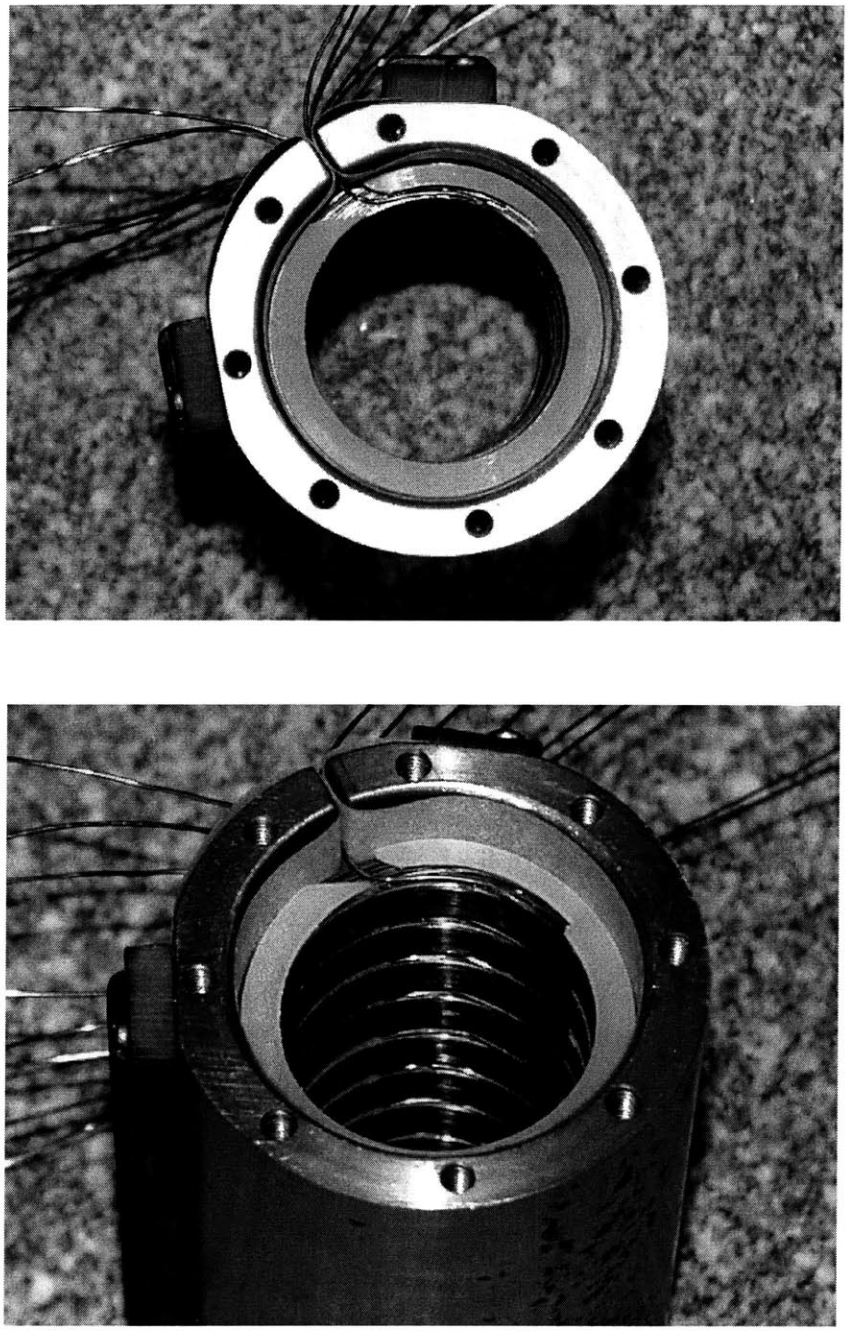

Figure 6-28: Linear motor stator assembly. Nylon spacers separate the coils. Coil leads are routed through a slit in the back iron. The stack of coils and spacers is axially clamped by endcaps (not shown).

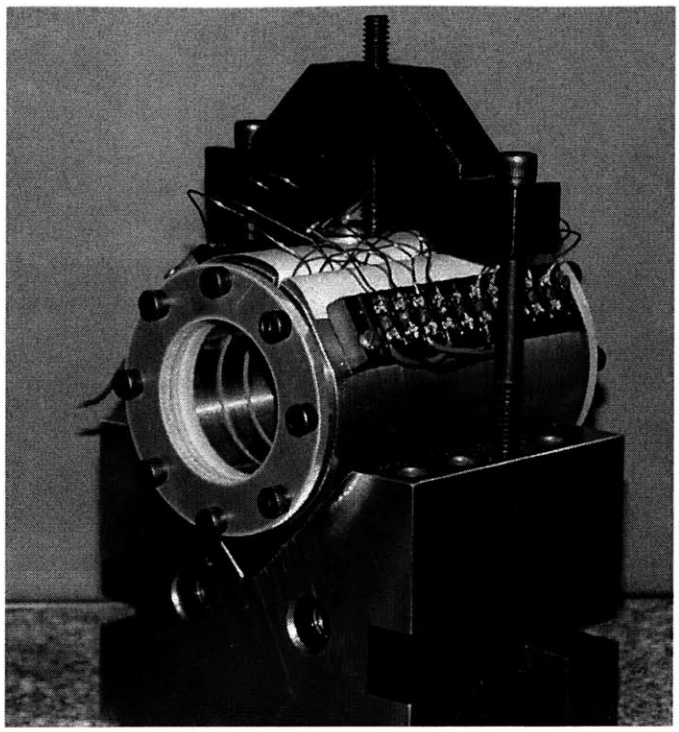

Figure 6-29: Linear motor stator.

the slit as can be seen in Figure 6-28. The triplex laminate is made of calendered aramid Nomex paper bonded to both sides of a Kapton polyimide film. The Kapton film provides high dielectric, tear, and tensile strength, while the Nomex paper provides a smooth, abrasion resistant surface. Each layer of the laminate is 2 mils thick so that the entire laminate is 6 mils thick. The laminate electrically insulates the coil and back iron and protects the coils from any roughness in the machined back iron since the laminate is highly resistant to tearing and puncture. The most likely area for nicking wires is at corners of the slit, and the laminate completely lines the slit to help prevent this. We bought this laminate from Electrical Insulation Suppliers (Appendix F).

Once the Nomex-Kapton-Nomex liner is in place, the coil stack can be assembled. First one endcap is attached to the back iron. Then some nylon spacers are inserted so that the first coil is located 0.215 inches from the endcap. Next, the nine coils are carefully inserted, each separated by a nylon coil spacer. As shown in Figue 6-28, the

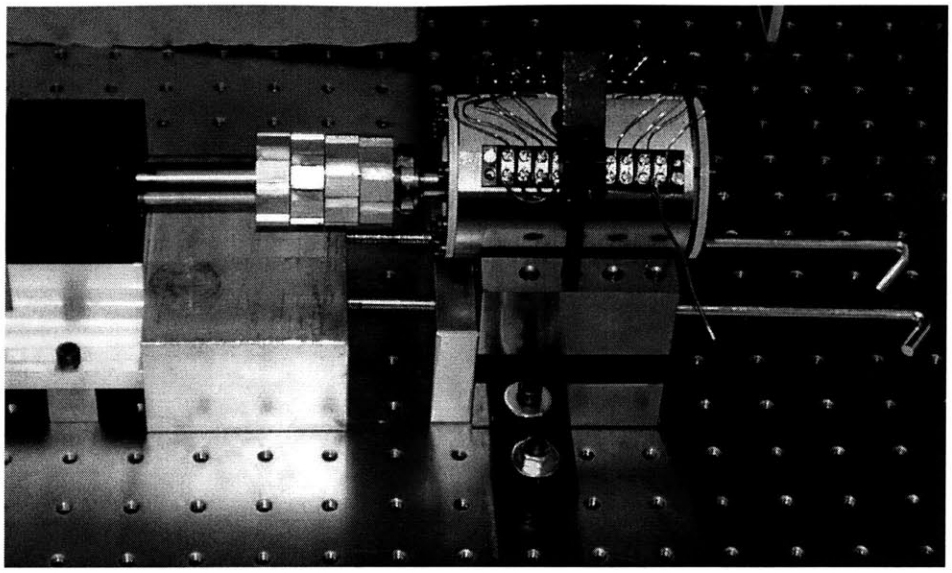

Figure 6-30: Jacking mechanism for assembling the stator around the rotor.

inside coil lead is routed through the gap in the nylon coil spacer and out the slit. The spacer protects the lead from being crunched by the next coil. After the last coil is assembled, several nylon coil spacers are inserted, and the second endcap is screwed in loosely. This endcap axially compresses the entire coil/spacer stack. Before the endcap is tightened, a smooth brass cylinder is inserted into the center of the coil stack to center the coils and spacers. The stack is axially clamped by tightening the endcap, and the brass cylinder is removed. Finally, the coil leads are cut to length, stripped of insulation, and attached to the terminal blocks on other side of the slit. The completed stator is shown in Figure 6-29.

6.6.7 Assembly of Stator around Rotor

The linear motor stator is clamped in a 90° precision V-block made by Suburban Precision (Appendix F) as shown in Figure 6-29. Shims are inserted under the V-block so that the stator is concentric with the rotor. Since the permanent magnets are so strong, we use a jacking mechanism shown in Figure 6-30 to assemble the stator around the rotor. Since the stator is surface wound, the coils act as an airgap between the permanent magnets on the rotor and the stator back iron. Thus, the attractive

force is not great, and we find that the stator can be assembled over the rotor without the jacking mechanism if the stator is kept centered during the process. After the stator is in place around the rotor, the stator's position is adjusted so that its axis is aligned with the shaft's axis, and the stator and rotor are concentric. The gap between the stator and rotor at various places is measured with plastic shim stock.

6.7 Rotary Motor

The rotary motor is a permanent magnet synchronous motor. We require that the rotor fit on the shaft, and that the stator be 1 inch longer than the rotor so that the z-θ axis can travel axially. Most frameless motors, even when listed in catalogs, are custom items. Our requirement that the stator be longer than the rotor makes our motor specifications even more unusual.

It is very difficult to find a vendor willing to sell a single custom motor. Our original motor vendor initially said they would make the motor but later reneged on this and refused to return phone calls. The president of this company told us that the engineering costs of making a custom motor made it unprofitable. Furthermore, he claimed that the company generally did not make money selling motors but made money selling the accompanying power amplifiers. We were building our own power amplifiers for just this reason, and they did not want to sell us a motor without amplifiers. In anticipation of receiving this motor we had already designed, ordered, and received our first shaft.

Fortunately, we found another vendor, Aerotech (Appendix F), which agreed to sell us the motor. Based on our previous experience, we did not ask them to build a custom motor, but rather asked for two standard motors of differing lengths. We use the rotor of the short motor, and the stator of the longer motor to create our desired motor. Their smallest 50 mm diameter frameless motor comes in two models—the 52 mm long S-50-52 and the 86 mm long S-50-86. The difference in length between the lamination stack in the stator of the long motor and the permanent magnet rotor of the short motor is 32.2 mm or 1.27 inches which is greater than our 1 inch

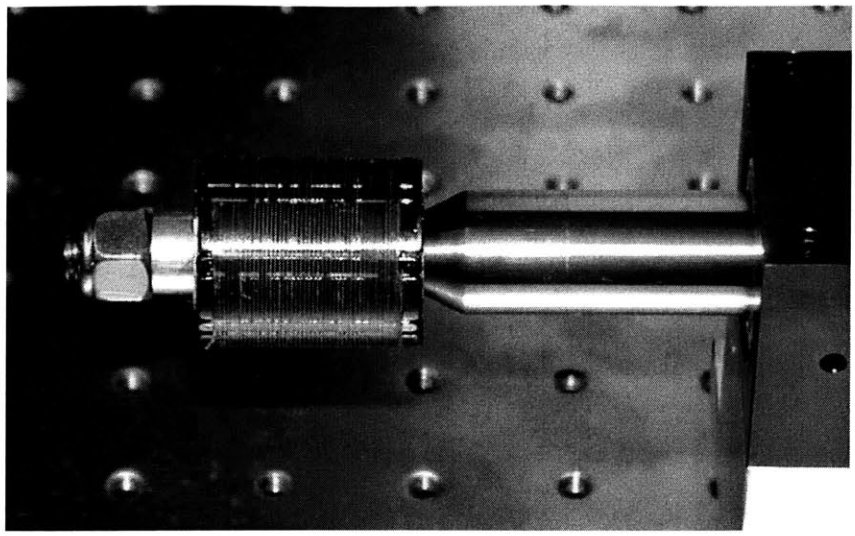

Figure 6-31: Aerotech rotary motor permanent magnet rotor mounted on shaft.

requirement.

The permanent magnet rotor slides onto one of the shaft's shoulders and is axially clamped by a locknut as shown in Figure 6-31. The rotor is wound with a fiber to retain the magnets at high speeds. The stator (shown in Figure 6-9) is surface wound, and the coils are impregnated with epoxy. This protects the coils from damage and provides better heat transfer to the stator back iron and surrounding air. The stator can be assembled around the rotor without a jacking mechanism since the attractive force between the stator and rotor is only a few pounds. The stator is mounted in a V-block similarly to the linear motor stator. Since it has a smaller diameter than the linear motor stator, the V-block sits on parallels which raise it up so that the stator and rotor are concentric. The motor leads are strain-relieved since they attach to a terminal block mounted to the V-block.

6.8 Summary

In this chapter we saw how the prototype rotary-linear axis was designed, built, and assembled. The components could not be designed in isolation but were designed to be integrated with the rest of the axis. We were also careful to make the components

modular so that they could be re-used on future rotary-linear axis prototypes. For example, to build the next prototype axis, the designer might want to re-use the tubular linear motor and rotary motor but incorporate a different rotary sensor. In this case the designer could specify a shaft with the same shoulder diameters as ours, though its length and other features might be different; the frameless rotary and linear motors could be disassembled and reassembled on the new shaft.

We were suprised to find that we could position the linear and rotary motor stators over the permanent magnet rotors by hand. Initially, we planned various jacking mechanisms and built one (shown in Figure 6-30) to allow us to position the stators around the permanent magnet rotors. We feared that the magnetic attraction would be extremely large and could damage the axis or motor if not constrained by a jacking mechanism. The surface wound nature of both motors in which the coil acts as a large air gap reduces the attraction force significantly. There is a large attraction force, but the assembly can be accomplished without a jacking mechanism if the rotor is kept centered.

We mounted the two motor stators in V-blocks so that they would be solidly supported and would not vibrate due to reaction forces. However, the stands for the interferometer mounts are made of two thin parallel plates as can be seen in Figure 6-10. We found that if the interferometer mount holding the tilted-mirror sensor was tapped while the rotary axis controller was holding an angular position, the shaft would rotate suddenly a small amount. The vibration in the interferometer mount fooled the system into thinking the axis had rotated away from its nominal position, and the controller commanded a restoring torque from the rotary motor. Interferometers should be mounted on a solid support so that they don't vibrate relative to the optical table.

The next chapter is a tutorial on field orientated control. It shows how to model and control three phase motors using a convenient set of transformations. The following chapter explains the control of the prototype rotary-linear axis we constructed in this chapter.

Chapter 7

Field Orientation Principle

This chapter is a tutorial on the field orientation principle, especially as it applies to permanent magnet synchronous motors. This tutorial is included in this thesis for two main reasons. First, it provides the equations necessary to commutate the linear and rotary permanent magnet synchronous motors we use in our rotary-linear axis. In fact, only sections 7.4.2 and 7.4.3 of this chapter are needed to do this. Second, we provide a model of the permanent magnet motor in *dq* coordinates in section 7.6 which is needed for sensorless control. We implement a sensorless control scheme for the rotary motor in section 8.5 of the next chapter. The material in this chapter also is used to simplify the calculation of the linear and rotary motor force constants in sections 4.5 and 4.7 respectively.

This review of field orientated control synthesizes material from a number of excellent sources. These include Leonhard's text, *Control of Electrical Drives* [40], and Fitzgerald, Kingsley, and Umans's text, *Electric Machinery* [18]. We also draw upon lecture notes written by MIT Professor James Kirtley [35] and notes written by MIT Professors Jeffrey Lang, George Verghese, and Marija Ilic [39]. In this tutorial chapter, we combine these different perspectives into a coherent and continuous introduction to field orientated control.

The field orientation principle allows us to control AC motors as if they were DC brushed motors. AC motors, such as synchronous and induction motors, have multiple phases and complex transient behavior, which make them difficult to control.

Under common simplifying assumptions, brushed DC motors are simple to control: the armature current is directly proportional to the rotor torque. Application of the field orientation principle allows us to transform stator currents for an AC motor into direct and quadrature currents, which are analogous to the field and armature currents in a brushed DC motor. Using these field orientation transformations yields commutation laws by which AC motors can be readily controlled.

In this chapter we first review DC motor modeling. The mechanical commutation in a DC motor makes controlling it easy: torque is proportional to armature current. We also show how field weakening control can be used to enable high-speed operation. In the remainder of the chapter we focus on a specific AC motor, the 3-phase permanent magnet synchronous motor. We first model this motor in 3-phase variables *abc*; the resulting torque expression shows that the motor ideally requires sinusoidal commutation to produce constant torque output. Next, we derive the field orientation or *dq* transformations, which transform variables from the *abc* frame to a two-phase frame rotating with the rotor called the *dq* frame. We apply these transformations to our three-phase motor model in the *abc* frame and derive an equivalent motor model in the *dq* frame. This *dq* motor model is analogous to the DC motor model since torque is directly proportional to q axis current. Using these results, in the last section we show how a 3-phase permanent magnet synchronous motor can be controlled in the same manner as a DC motor using the *dq* transformations.

7.1 DC Motor Modeling

Direct current (DC) motors are commonly used in variable speed drives. They are flexible in allowing for operation at a wide range of speeds and torques. They can be modeled simply and therefore controlled with minimal complexity. Their main disadvantage is the need for mechanical commutation which requires periodic maintenance of brushes, limits speed and power, and causes friction. We review DC motor modeling and control in this section. In the next section we show how the field orientation transformations allow AC motors to be controlled with the same conceptual

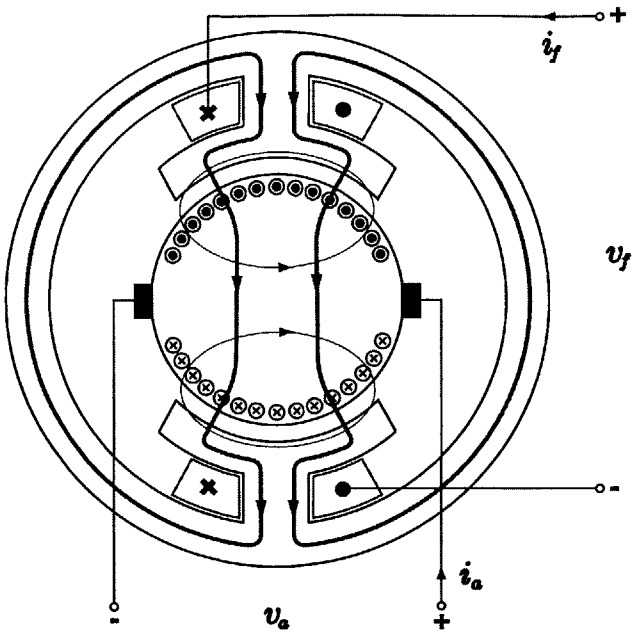

Figure 7-1: Schematic cross-section of a DC motor. The field windings and their magnetic fields are shown in red; the armature windings and their magnetic fields are shown in blue.

simplicity as DC motors.

Figure 7-1 shows a cross-section of a two-pole DC motor. The cylindrical motor consists of an outer stator and inner rotor. The stator and rotor are both magnetically permeable. The stator contains two field coils shown in red which are wound around the two poles. The magnetic field lines produced by these field coils are shown in red in Figure 7-1. They cross the small air gap between the poles and rotor radially and continue through the rotor to the opposite pole. The rotor contains armature winding currents which are essentially always oriented as shown despite the rotor's rotation. This is due to the action of the mechanical commutator and a relatively complex wiring scheme between the brushes, commutator, and armature windings. The magnetic flux created by the armature windings is shown in blue in Figure 7-1. This flux is much weaker than the flux produced by the field coils since it travels through a larger air gap. For more details on the fabrication of such motors see [40].

It is common to use permanent magnets in place of the field coils, especially in

smaller servomotors. Permanent magnets eliminate the field coils and their power supplies and are more compact than field coils in smaller motors. However, since the flux supplied by the permanent magnets cannot be varied in operation, some flexibility is lost in motor control. We will consider the more general case of a motor with field windings; a motor with permanent magnets will have the same behavior as a motor with constant current in the field windings.

Although controlling a DC motor is easy, DC motor design and analysis can be quite complicated. For example, the mechanical commutator uses brushes and a complex armature winding pattern to maintain a spatially fixed distribution of currents in the rotating rotor. In practice, the design of such DC motor armature windings is something of a black art. A second complication is that the magnetic field produced by the armature tends to distort the main air gap flux produced by the field coils. Fortunately this field is much weaker than the main flux since it has a larger effective airgap as described above. In large machines, this effect is sometimes further reduced by using compensating windings in the stator poles. These compensating windings are connected in series to the armature windings but have current flowing in the opposite direction. Thus, these windings can cancel the flux produced by the armature windings. There are other subtleties to DC motor design as described in [40, 18], but fortunately a simple analysis is all that is required for most control applications.

The ease with which DC motors can be controlled is due to the fixed spatial arrangement of the main flux and armature flux. In Figure 7-1 the main flux (in red) is directed downward. We shall call this the *direct-axis* flux. The armature flux (in blue) is oriented 90 electrical degrees from the main flux and is also therefore called the *quadrature-axis* flux. The fixed 90° angle between the direct-axis flux and the quadrature-axis flux produces maximum torque. In DC motors the mechanical commutator maintains these two axes essentially perpendicular to each other as the rotor rotates. As a result, DC motors are relatively easy to control. In AC motors, we must perform the commutation electrically, without the aid of a mechanical commutator. If we can achieve the same effect in an AC motor, with the direct and quadrature

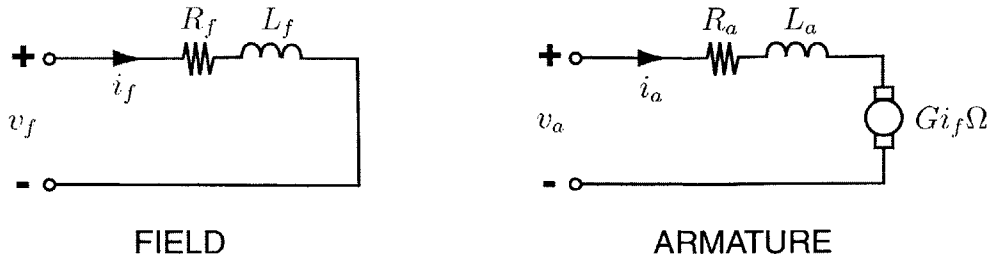

Figure 7-2: Circuit model for field windings and armature windings in a DC motor.

axes always perpendicular, it too will be easily controllable.

7.1.1 Terminal Voltages

A simple DC motor model sufficient for most applications is presented in many controls textbooks [54, 19, 15]. We assume that the field and armature windings of the DC motor shown in Figure 7-1 are separately excited. It is also possible to consider series and parallel connections of these motor windings [40]. An electrical model of the field and armature windings is shown in Figure 7-2. The field winding has resistance R_f and inductance L_f. The field winding voltage v_f and current i_f are related by the equation,

$$v_f = i_f R_f + L_f \frac{di_f}{dt}. \tag{7.1}$$

The armature winding also contains some resistance R_a and inductance L_a. As noted previously motors typically have $L_a \ll L_f$ due to the larger air gap in the armature magnetic field path. Since the armature is rotating, a backwards electromotive force (EMF), is generated which is proportional to the speed of rotation Ω and to the field current i_f. We label the proportionality constant G such that the speed voltage is $Gi_f\Omega$. This speed voltage can be derived using Faraday's Law with either a fixed or moving contour through the armature windings [76]. The proportionality constant G depends on the motor geometry, e.g., the air gap, motor radius, and the number of turns in the field and armature coils. It is this speed voltage that connects the electrical and mechanical domains and represents the energy conversion process in the motor. The armature winding voltage v_a and current i_a are thus related by the

equation,

$$v_a = i_a R_a + L_a \frac{di_a}{dt} + G i_f \Omega. \tag{7.2}$$

7.1.2 Torque

The radial magnetic flux produced by the field winding interacts with the current in the armature windings to produce a force at the radius of the rotor. The force produced is calculated using the Lorentz force density,

$$\vec{F} = \vec{J} \times \vec{B}, \tag{7.3}$$

where $\vec{F}$ is the volume force density, $\vec{J}$ is current density in the armature windings, and $\vec{B}$ is air gap magnetic flux. The resulting torque τ contains the same proportionality constant G introduced to calculate the backwards electromotive force:

$$\tau = G i_f i_a. \tag{7.4}$$

Assuming nonlinearities such as magnetic saturation in the stator are not present, the torque is directly proportional to both the field and armature windings. For smaller motors with permanent magnet excitation, the field current is essentially constant and it is common to define a motor torque constant,

$$K_t = G i_f, \tag{7.5}$$

such that torque is directly proportional to armature current,

$$\tau = K_t i_a. \tag{7.6}$$

The above Lorentz force calculation yields the correct force and torque for the motor, but there is a subtlety regarding its use [76]. Typically the armature windings are placed in teeth on the rotor surface to reduce the effective size of the motor's air gap. In fact, most of the magnetic flux crossing the air gap goes through these

permeable teeth and not through the coils. Hence, force is mainly produced in the magnetically permeable teeth of the rotor and not in the coils. Nevertheless, the true force can still be calculated exactly, by naively assuming all the magnetic flux goes through the coils. This surprising result can be explained best in terms of the Maxwell stress tensor [76]. The force on an object can be calculated by integrating the Maxwell stess tensor over the surface of the object. Since only the surface magnetic fields enter into this calculation, the details of how the magnetic fields act inside the volume do not change the net force.

7.1.3 Power

The motor directly converts electrical power absorbed by the speed voltage into mechanical power. The electrical power p_e is equal to the armature current i_a multiplied by the speed voltage, $Gi_f\Omega$,

$$p_e = Gi_f i_a \Omega. \tag{7.7}$$

The mechanical power generated p_m is equal to the torque, $\tau = Gi_f i_a$, multiplied by the angular speed Ω,

$$p_m = Gi_f i_a \Omega. \tag{7.8}$$

Earlier, we assumed that the proportionality constant G in the torque expression was identical to the proportionality constant G in the back EMF expression. The basis for this assumption was that a lumped electromechanical analysis of the motor would yield identical expressions for G in both cases. Another common way to show this equivalence is by assuming that the electrical power p_e and mechanical power p_m expressions above are equal. From this it also follows that the torque and back EMF constants are the same.

7.2 DC Motor Control

In this section, we show that a DC motor can be easily controlled using the model we have just developed. We consider the problem of controlling the angular position of

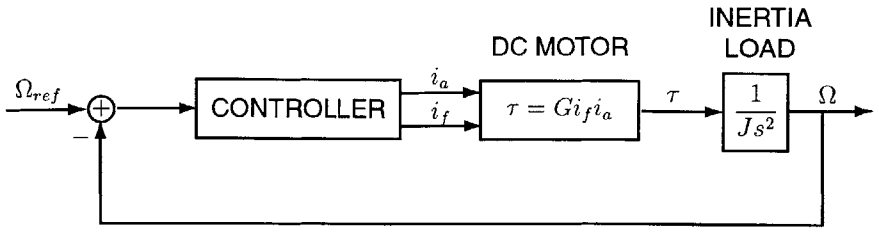

Figure 7-3: Control block diagram showing a DC motor driving an inertial load.

a load attached to a separately excited DC motor. We further assume that we have high bandwidth current controllers so that we can directly set the motor's field and armature currents. If we can accurately model the torque produced by the motor, we can include the motor and load in a standard control block diagram as shown in Figure 7-3. The torque, $\tau = Gi_f i_a$, is proportional to the field current i_f and armature current. Thus it seems we can control the motor torque by adjusting either the field current i_f, or armature current i_a, or perhaps both.

7.2.1 Armature Control

The most common DC motor control scheme holds the field current i_f constant at its maximum value and varies the armature current i_a. This situation is called armature control. Although we have assumed high bandwidth current controllers, the armature and field inductances, L_a and L_f, will limit the achievable current loop bandwidths. In particular, recall that $L_a < L_f$ so that we can achieve faster dynamic performance by varying i_a than by varying i_f. Thus, it is more common to control the armature current than the field current since better dynamic response is obtained.

7.2.2 Field Weakening Control

Armature control generally is all that is required. At high speeds Ω, however, the back EMF, $Gi_f\Omega$, generated in the armature winding can use up the entire voltage capability of the power supply. This results in an upper limit on motor speed called the no-load speed, Ω_0. It is possible to operate the motor above the no-load speed

only by reducing the field current and hence the back EMF. The price paid for this field weakening is increased armature current and associated losses, in order to maintain the same torque level as before the field current was reduced. Field weakening increases the no-load speed but decreases the stall torque. Thus, it is only useful for increasing motor speed when low torque is required. At higher torques, field weakening can actually lead to reduced speed as well as higher armature losses, which is completely undesirable [40].

7.2.3 Combined Control

We now can summarize the general control scheme for DC motors. Below the no-load speed Ω_0, armature control is used, with the field current fixed at its maximum value. Above the no-load speed, field control, or field weakening, must be used. Field weakening allows for higher speed operation in the low torque regime, but it decreases motor efficiency. Figure 7-4 shows the armature and field weakening control ranges for a DC motor in steady state.

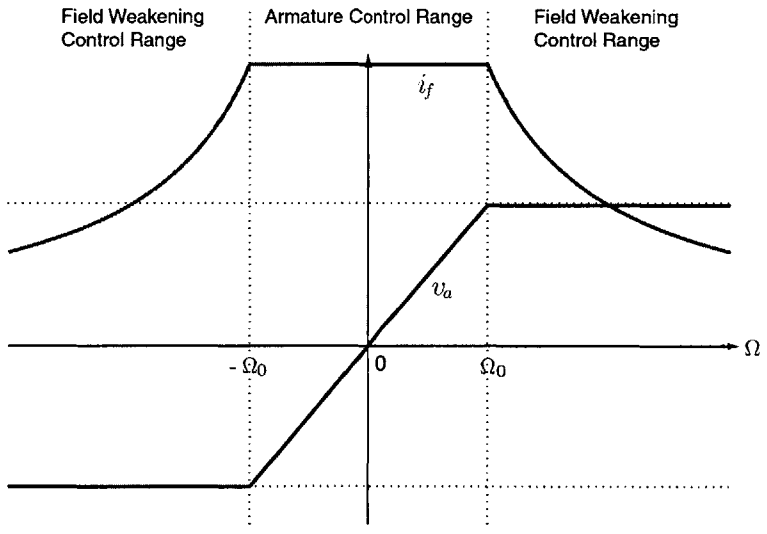

Figure 7-4: Control ranges for a DC Motor in steady state. Figure adapted from Leonhard [40].

As mentioned previously, a DC motor using permanent magnets instead of field windings to create the main flux can be thought of as a separately excited DC motor

with constant field current i_f. Thus, a permanent magnet DC motor is operated only in the armature range, and its field cannot be weakened unless auxiliary field coils are present. Typically, operation above no-load speed is not crucial, so the increased efficiency and reduced motor volume offered by permanent magnet DC motors are valuable. At higher power levels, above 10 hp, however, wound field motors are more power efficient than permanent magnet motors.

In the next section we show how AC motors can be controlled in the same manner just described for DC motors. We explain the concept of the quadrature-axis current i_q in an AC motor; it is proportional to torque just like the armature current i_a in a DC motor. Also, we introduce the direct-axis current i_d which acts similarly to the field current i_f and can be used for field weakening.

7.3 Permanent Magnet Synchronous Motor Modeling in *abc* Variables

Field orientation transformations simplify AC motor modeling and control. They can be applied to induction motors and synchronous motors. In the remainder of this chapter we show how these transformations apply to three-phase permanent magnet synchronous motors. We start off by modeling the motor in *abc* variables which correspond to the motor's actual three phase voltages, currents, and flux linkages. Then, we will introduce field orientation transformations, which transform the motor's variables into a frame fixed to the rotor, called the *dq* frame. In this frame the motor's voltages, currents, and flux linkages take on DC values for steady-state operation much like the quantities in a DC motor. We next transform our motor model from the *abc* frame into the *dq* coordinate frame. Finally, we show how easy it is to control a permanent magnet synchronous motor in the *dq* frame.

We use the rotary permanent magnet synchronous motor as an example throughout the rest of this chapter. This type of motor is commonly used today in many applications including precision machine tools. Both of the motors in our z-θ axis are

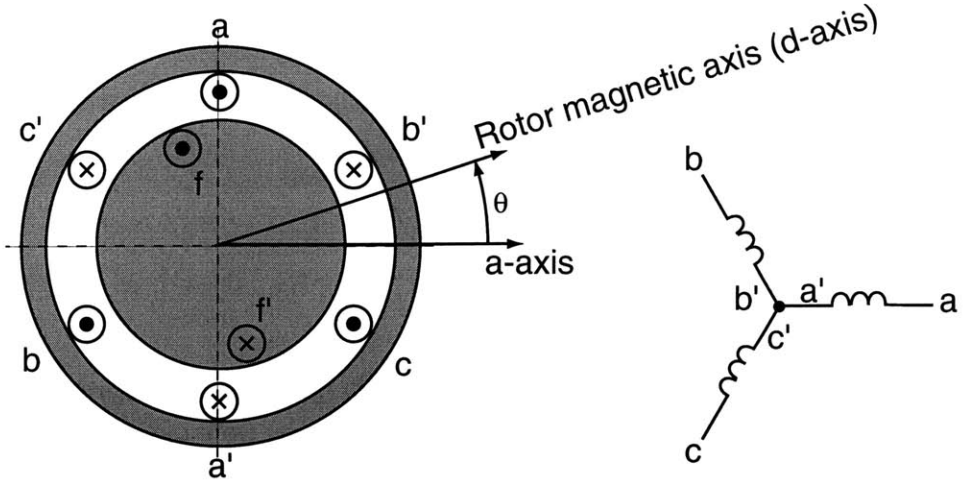

Figure 7-5: Symmetrical three-phase permanent magnet synchronous motor. The permanent magnet is modeled by a field winding on the rotor. The stator windings are typically connected in a wye configuration as shown on the right.

permanent magnet synchronous motors. This discussion applies nearly identically to field wound synchronous motors as well. Although this discussion is not sufficient to model and control induction motors, many of the concepts developed carry over to induction motors. See [40] for more details.

We examine the case of a two-pole motor. Our discussion can be extended to multi-pole motors by setting the electrical frequency ω equal to the number of pole pairs p times the mechanical frequency Ω,

$$\omega = p\Omega. \tag{7.9}$$

We generalize some of our results to motors with p poles pairs. We consider a motor with symmetrical three-phase stator windings since this is the most common case. The modeling and dq transformations for symmetrical windings of more than three phases can be derived analogously to those for symmetrical three-phase windings.

The concentrated phase a, b, and c stator windings for the example motor are shown in Figure 7-5. The permanent magnet is modeled by a field winding f on the rotor with constant current I_f. The stator windings are assumed connected in

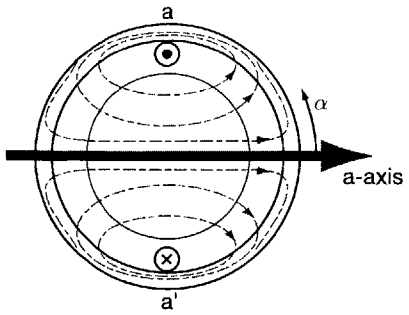

Figure 7-6: The magnetic flux lines produced by coil aa' in the stator of a cylindrical rotary motor are shown. The a-axis points in the direction of the magnetic flux produced. Actual field lines are perpendicular to the stator and rotor back irons.

the wye configuration shown in Figure 7-5. The three stator currents, i_a, i_b, i_c, are functions of time t and may vary in any way provided that they are balanced,

$$i_a + i_b + i_c = 0, \tag{7.10}$$

due to the summation of the currents at the isolated neutral point of the wye connection. Thus, only two of the three currents can be set independently. We avoid writing time dependence explicitly as $i_a(t)$ to simplify the notation. All currents, voltages and flux-linkages with lower-case letters denote time-varying quantities. It is also possible to drive the three phases independently as long as they are driven so that they are balanced.

Each concentrated coil in Figure 7-5 represents a distributed coil which produces a sinusoidal magnetic flux and magnetomotive force in the air gap. The direction of the magnetic flux defines the coil's magnetic axis. Figure 7-6 shows the a-axis corresponding to coil aa'. In Figure 7-5, the magnetic axis of rotor coil ff' is rotated by an angle θ from the magnetic axis of stator coil aa'. The magnetic axis of the rotor coil ff' rotates with the rotor. Later, we will see that this magnetic axis aligned with the rotor's flux is the d-axis of the dq coordinate frame.

We now model the flux linkages of the three stator coils, λ_a, λ_b, and λ_c, as functions of the three stator currents, i_a, i_b, i_c, and the three flux linkages between the stator

coils and the rotor, λ_{af}, λ_{bf}, and λ_{cf}:

$$\begin{bmatrix} \lambda_a \\ \lambda_b \\ \lambda_c \end{bmatrix} = \begin{bmatrix} \mathcal{L}_{aa} & \mathcal{L}_{ab} & \mathcal{L}_{ac} \\ \mathcal{L}_{ba} & \mathcal{L}_{bb} & \mathcal{L}_{bc} \\ \mathcal{L}_{ca} & \mathcal{L}_{cb} & \mathcal{L}_{cc} \end{bmatrix} \begin{bmatrix} i_a \\ i_b \\ i_c \end{bmatrix} + \begin{bmatrix} \lambda_{af} \\ \lambda_{bf} \\ \lambda_{cf} \end{bmatrix}. \tag{7.11}$$

The script $\mathcal{L}$ represents an inductance which in general could be a function of rotor angle θ. Here, $\mathcal{L}_{aa}$ denotes the self-inductance of phase a, and $\mathcal{L}_{ab}$ denotes the mutual inductance between phases a and b. This notation is the same as that used in *Electric Machinery* [18]. We could have extended the inductance matrix to be 4×4 by including the rotor coil and the stator-to-rotor mutual inductances and rotor self-inductance. For a permanent magnet rotor, this coil is imaginary so we are not interested in its internal details. Thus it is more convenient to include these terms via the stator-to-rotor flux linkages λ_{af}, λ_{bf}, and λ_{cf}. This notation reduces the model order from four to three and more closely describes the quantities of interest in a permanent magnet motor. Next, we briefly examine the stator-to-rotor flux linkages and the stator inductances in our model.

7.3.1 Stator-to-Rotor Flux Linkages

We assume the permanent magnet rotor produces only fundamental space harmonic magnetic flux so that the flux linked by the stator phases varies as the cosine of angle from each phase's magnetic axis. In a real machine there are higher-order spatial harmonics, but the fundamental harmonic provides the main torque generating terms. Later, we will see that the *dq* transformations assume this same simple fundamental space harmonic distribution of magnetic flux. The flux linkages between the rotor and the three phase windings are thus modeled as

$$\lambda_{af} = \lambda_f \cos\theta \tag{7.12}$$

$$\lambda_{bf} = \lambda_f \cos\left(\theta - \frac{2\pi}{3}\right) \tag{7.13}$$

$$\lambda_{cf} = \lambda_f \cos\left(\theta - \frac{4\pi}{3}\right), \tag{7.14}$$

where λ_f is the maximum flux produced by the magnets which links each coil.[1]

7.3.2 Stator Inductances

Our motor has a cylindrical rotor, so each stator phase has a self-inductance L which in the simplest model is independent of θ,

$$\mathcal{L}_{aa} = \mathcal{L}_{bb} = \mathcal{L}_{cc} = L. \tag{7.15}$$

The stator self-inductance L includes both self-inductance due to the space-fundamental component of flux L_0 as well as self-inductance due to the armature leakage flux L_l,

$$L = L_0 + L_l. \tag{7.16}$$

See *Electric Machinery* [18] for a model explicitly containing the leakage inductance terms. The stator mutual inductances M are also independent of θ,

$$\mathcal{L}_{ab} = \mathcal{L}_{ac} = \mathcal{L}_{ba} = \mathcal{L}_{bc} = \mathcal{L}_{ca} = \mathcal{L}_{cb} = -M, \tag{7.17}$$

where $M > 0$. The stator mutual inductances are negative since a positive current in coil aa' creates flux that links coil bb' negatively as can be seen in Figure 7-5. The mutual inductance M is the negative of one-half the space-fundamental self-inductance, L_0. This is due to the fact that the armature phases are displaced by $\frac{2\pi}{3}$: The fraction of flux produced by coil aa' and linked by coil bb' in Figure 7-5 is

$$\frac{-\int_{-\pi/6}^{\pi/6} \cos\theta d\theta}{\int_{-\pi/2}^{\pi/2} \cos\theta d\theta} = -\frac{1}{2}. \tag{7.18}$$

Here the integral from $-\pi/2$ to $\pi/2$ is the total flux produced by coil aa' and the integral from $-\pi/6$ to $\pi/6$ is the flux produced by coil aa' and linked by coil bb'.

[1] In the case of a wound-field synchronous motor, the maximum flux linked by the stator coils from the rotor, λ_f, is equal to the maximum mutual inductance between the stator coils and rotor coil, L_{af}, and the current in the rotor coil i_f, $\lambda_f = L_{af} i_f$.

The flux linkage by phase a is the sum of flux linkages due to its self-inductance, mutual inductance with coils b and c, and flux linkage with the rotor,

$$\lambda_a = Li_a - Mi_b - Mi_c + \lambda_{af}. \tag{7.19}$$

Under balanced three-phase conditions in the stator,

$$i_a = -i_b - i_c, \tag{7.20}$$

so that we can rewrite λ_a in terms of only the phase a current,

$$\lambda_a = (L + M)i_a + \lambda_{af}. \tag{7.21}$$

This is a useful simplification since we can now define a synchronous inductance,

$$L_S = L + M, \tag{7.22}$$

which is the apparent phase a self-inductance looking at phase a's terminals. In reality the synchronous inductance L_S is produced by phase a's true self-inductance L and its mutual inductance M with phases b and c along with their associated currents. However, the balanced three-phase conditions allow us to express the sum of the currents i_b and i_c in terms of i_a so that we can combine the effects of the self- and mutual-inductances. The flux linkages in phases b and c simplify in the same manner.

7.3.3 Stator Terminal Voltages

The terminal voltage v_a of phase a is the sum of its resistive drop i_aR and the time rate of change of its flux linkage, $d\lambda_a/dt$,

$$v_a = i_aR + \frac{d\lambda_a}{dt}, \tag{7.23}$$

where R is the resistance in each armature phase. Using (7.21) and (7.22), we can write the terminal relations for the three phases as

$$v_a = i_a R + L_S \frac{di_a}{dt} + \frac{d\lambda_{af}}{dt} \tag{7.24}$$

$$v_b = i_b R + L_S \frac{di_b}{dt} + \frac{d\lambda_{bf}}{dt} \tag{7.25}$$

$$v_c = i_c R + L_S \frac{di_c}{dt} + \frac{d\lambda_{cf}}{dt}. \tag{7.26}$$

Thus, we see that the phase a voltage, v_a, is the sum of a resistive drop, $i_a R$, a voltage due to the synchronous inductance, $L_s(di_a/dt)$, and a voltage due to the changing flux linkage with the rotor, $d\lambda_{af}/dt$. This last term, $d\lambda_{af}/dt$, is a speed voltage which, in light of (7.12), is proportional to $d\theta/dt$.[2]

7.3.4 Torque

We will calculate the torque produced by our motor using the energy method [76]. The coenergy of our electro-mechanical system is

$$\begin{aligned} w'(i_a, i_b, i_c, \theta) = & \\ & \frac{1}{2} L_S (i_a^2 + i_b^2 + i_c^2) + \\ & \lambda_f \cos(\theta) i_a + \lambda_f \cos\left(\theta - \frac{2\pi}{3}\right) i_b + \lambda_f \cos\left(\theta - \frac{4\pi}{3}\right) i_c. \end{aligned} \tag{7.27}$$

The first term includes the self- and mutual-inductances of the armature phases and the next three terms are the torque-producing terms representing the rotor flux linked by the armature phases. Torque τ is the partial derivative of coenergy $w'(i_a, i_b, i_c, \theta)$ with respect to θ,

$$\tau = \left. \frac{\partial w'(i_a, i_b, i_c, \theta)}{\partial \theta} \right|_{i_a, i_b, i_c} =$$

[2] In the case of a wound-field synchronous motor, $\lambda_{af} = L_{af} i_f \cos\theta$ and the term, $d\lambda_{af}/dt$, contains a transformer voltage proportional to di_f/dt and a speed voltage proportional to $d\theta/dt$. Since for a permanent magnet rotor the field current is constant, $i_f = I_f$, the transformer voltage disappears, and we have only a speed voltage.

$$-\lambda_f \left[i_a \sin(\theta) + i_b \sin\left(\theta - \frac{2\pi}{3}\right) + i_c \sin\left(\theta - \frac{4\pi}{3}\right) \right]. \tag{7.28}$$

(7.28) is a general expression for the torque τ produced in our motor as a function of the three phase currents, i_a, i_b, and i_c. Notice that this expression is complicated and that it is not immediately obvious how we should control the three currents i_a, i_b, and i_c in order to produce a given amount of torque τ. The standard solution is to drive the three phases with currents that are sinusoidal functions of rotor angle θ,

$$\begin{aligned} i_a &= -I_S \sin(\theta) \\ i_b &= -I_S \sin\left(\theta - \frac{2\pi}{3}\right) \\ i_c &= -I_S \sin\left(\theta - \frac{4\pi}{3}\right), \end{aligned} \tag{7.29}$$

where I_S is the peak amplitude of the stator phase currents. Substituting the currents in equations (7.29) into the torque expression, (7.28), and simplifying yields

$$\tau = \frac{3}{2} I_S \lambda_f. \tag{7.30}$$

Under this commutation law, torque is independent of rotation, and proportional to the strength of the permanent magnets λ_f and to the peak amplitude of the armature currents I_S in equations (7.29). By commanding the peak current amplitude I_S as a function of time, we can control the motor's torque as a function of time. The particular choice of phase currents which are sinusoidal functions of rotor angle θ given by equations (7.29) is called sinusoidal commutation. It is often used in motor drives because it simplifies the general complicated torque expression, (7.28), to a simple expression, (7.31), which can be used in motor control systems. This can also be shown to be the power optimal commutation pattern.

The torque expression in (7.31) for the permanent magnet synchronous motor with sinusoidal commutation is similar to the torque expression for the DC motor, (7.6), which we repeat here,

$$\tau = K_t i_a.$$

If we define the torque constant K_t of the permanent magnet synchronous motor to be equal to $(3/2)\lambda_f$, its torque is

$$\tau = K_t I_S. \tag{7.31}$$

Thus, just as DC motor torque is directly proportional to armature current i_a, torque produced by a synchronous motor with sinusoidal commutation is proportional to the peak current amplitude I_S.

Sinusoidal commutation is the key to transforming the complicated torque expression, (7.28), into the simple torque expression, (7.31). In the next section, we introduce the dq transformation. After that we apply it to the synchronous motor and see that it provides the same simplification in the torque equation as sinusoidal commutation does. It also gives us a better understanding of our motor. In effect, sinusoidal commutation transforms the phase currents to a frame rotating with the rotor angle θ. This is the same thing that the dq transformations do: sinusoidal commutation follows naturally from the dq transformations. We will see that the peak current amplitude I_S of sinusoidal commutation is equal to the quadrature-axis current i_q in the dq frame.

7.4 dq Transformations

In this section we derive the field orientated or dq transformations which simplify AC motor modeling and control. We continue to use the example of a two-pole, three-phase permanent magnet synchronous motor. First, we develop the $abc \leftrightarrow \alpha\beta$ transformation which transforms between a three-phase AC system, abc, and a two-phase AC system, $\alpha\beta$. Second, we develop the $\alpha\beta \leftrightarrow dq$ transformation which transforms between a two-phase AC system, $\alpha\beta$, and a two-phase DC system, dq, which rotates with the rotor. We derive these transfomations by equating the magnetomotive forces in the air gap of the motor in the three different frames. Third, we introduce a transformation matrix T which transforms currents, voltages, and flux linkages directly

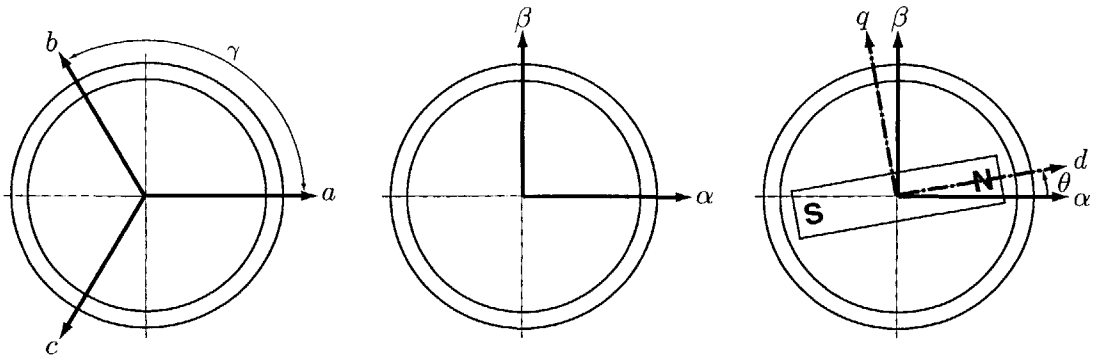

Figure 7-7: The *abc* axes form a three-phase AC system fixed in the stator frame. The $\alpha\beta$ axes represent an equivalent two-phase AC system fixed in the stator frame. The *dq* axes represent an equivalent two-phase DC system that rotates with the rotor flux.

from the *abc* frame to the *dq* frame. This matrix is useful for transforming our motor model into the *dq* frame. In this discussion we only derive the transformations between currents in the different frames. The same transformations also transform voltages and flux linkages between the frames.

The magnetic axes of the *abc*, $\alpha\beta$, and *dq* frames are shown in Figure 7-7. Recall that the magnetic axis of a coil points in the direction of the magnetic flux produced by that coil (Figure 7-6). The *abc* frame in Figure 7-7 shows the three magnetic axes corresponding to the three motor phases shown in Figure 7-5. Since the three phase coils are fixed in the stator, their three magnetic axes, *abc*, are also fixed. The angle γ represents the angular offset between the motor phases: for a three-phase motor $\gamma = 2\pi/3$. The *a*-axis is located on the real axis of the imaginary plane, the *b*-axis is located at an angle of γ with respect to the *a*-axis, and the *c*-axis is located at an angle of 2γ with respect to the *a*-axis. In general this discussion can be extended to an m phase motor by letting $\gamma = 2\pi/m$.

We define the direct axis or *d*-axis to be aligned with the rotor's flux and the quadrature axis or *q*-axis to lead the direct axis by $\pi/2$ as shown in Figure 7-7. For a motor with a permanent magnet rotor, like the one we are considering, the *d*-axis is aligned with the permanent magnet and rotates with the rotor. This discussion also applies to other AC motors. For example, although we will not consider induction

motors further here, the d-axis of induction motors is aligned with the direction of rotor flux and slips relative to the rotor position to induce rotor currents. In deriving the transformation from the abc frame to the dq frame, we will find it convenient to introduce an intermediate frame, the $\alpha\beta$ frame. The $\alpha\beta$ frame has two magnetic axes as shown in Figure 7-7. The α-axis is aligned with the a-axis, and the β-axis leads the α-axis by $\pi/2$. These axes are fixed in space.

7.4.1 Complex Current Vector

We derive the $abc \leftrightarrow \alpha\beta$ and $\alpha\beta \leftrightarrow dq$ transformations for currents, i. The transformations are derived by equating the air gap magnetomotive force in the three different frames. These same transformations also apply to voltages, v, and flux linkages, λ.

First, let's develop an expression for the air gap magnetomotive force in the abc frame. Let $\mathcal{F}(\alpha, t)$ be the number of ampere-turns enclosed by a closed loop magnetic flux path (such as the ones shown in Figure 7-6) which crosses the air gap radially at an angle α at time t. For the idealized motor shown in Figure 7-5 the coils of each phase are infinitely thin and the ampere-turns wave, which is equal to the air gap magnetomotive force, would be a square wave. In reality, the coils have some finite width, and motors are often designed such that the spatial ampere-turns distribution is sinusoidal. We will model the spatial ampere-turns distribution of each phase as sinusoidal and centered on the phase's magnetic axis. The dq transformations assume only pure sinusoidal magnetomotive force waves exist in the motor. Thus the ampere-turns of a closed loop flux path crossing the air gap at an angle α is

$$\mathcal{F}(\alpha, t) = N_{abc}\left[i_a \cos\alpha + i_b \cos(\alpha - \gamma) + i_c \cos(\alpha - 2\gamma)\right], \tag{7.32}$$

where N_{abc} is the number of turns in each coil. We can simplify the math by using complex numbers, for example, by substituting

$$\cos\alpha = \frac{1}{2}(e^{j\alpha} + e^{-j\alpha}), \tag{7.33}$$

and by introducing a time-dependent complex current vector,

$$\vec{i_S} = i_a + i_b e^{j\gamma} + i_c e^{j2\gamma} = i_S e^{j\zeta}, \tag{7.34}$$

where i_S and ζ are the time-dependent magnitude and phase of the complex current vector $\vec{i_S}$. Using (7.32), (7.33) and (7.34) we can write the ampere-turns wave $\mathcal{F}(\alpha, t)$ as

$$\mathcal{F}(\alpha, t) = \frac{1}{2} N_{abc} \left[\vec{i_S} e^{-j\alpha} + \vec{i_S^*} e^{j\alpha} \right] = N_{abc} i_S \cos(\zeta - \alpha). \tag{7.35}$$

(7.32) expresses the ampere-turns wave as a superposition of sinusoidal waves centered on the three magnetic axes with magnitudes determined by the three phase currents, i_a, i_b, and i_c. (7.35) says that the same ampere-turns wave can also be thought of as a single sinusoidal wave with instantaneous magnitude i_S whose peak is instantaneously located at an angle ζ from the a-axis.

At this point it should be stressed that the phase currents, i_a, i_b, and i_c, can vary as functions of time in any arbitrary manner provided they are balanced. Although we are using a complex vector $\vec{i_S}$, we have not specialized to steady state operation, and our complex quantities should not be mistaken for complex phasors used to describe steady state oscillation.

As an example of the formalism we have developed, let's consider the special case of steady-state rotation of the stator magnetomotive force at speed ω. If we feed the stator with balanced, three phase currents with peak amplitude I_M,

$$i_a = I_M \cos(\omega t), \tag{7.36}$$

$$i_b = I_M \cos(\omega t - \gamma), \tag{7.37}$$

$$i_c = I_M \cos(\omega t - 2\gamma), \tag{7.38}$$

(7.34) tells us that $i_S = \frac{3}{2} I_M$ and $\zeta(t) = \omega t$. Thus the magnetomotive force wave $\mathcal{F}(\alpha, t)$ has a fixed magnitude of $\frac{3}{2} N_{abc} I_M$, and rotates at constant angular velocity ω.

7.4.2 $abc \leftrightarrow \alpha\beta$ Transformation

The first transformation of interest converts between a three-phase AC system with fixed axes abc and a two-phase AC system with fixed axes $\alpha\beta$. The $abc \leftrightarrow \alpha\beta$ transformation can be derived by equating the magnetomotive forces in the two frames,

$$N_{abc}\left(i_a + i_b e^{j\frac{2\pi}{3}} + i_c e^{j\frac{4\pi}{3}}\right) = N_{\alpha\beta}(i_\alpha + j i_\beta). \tag{7.39}$$

Here $N_{\alpha\beta}$ is the number of turns in the $\alpha\beta$ frame, and i_α and i_β are equivalent currents in the two-phase $\alpha\beta$ frame. We may choose the ratio $N_{\alpha\beta}/N_{abc}$ arbitrarily, as it just changes the the current transformation by a constant factor. We adopt the most commonly used ratio of

$$\frac{N_{\alpha\beta}}{N_{abc}} = \frac{3}{2}. \tag{7.40}$$

This ratio is often used since it preserves the magnitude of currents between the two frames. This is especially useful in motor control when the magnitudes of currents are of interest. This normalization is used by Fitzgerald, Kingsley, and Umans [18], Kirtley [35], Analog Devices [4, 52], and Texas Instruments [63]. An alternative choice is

$$\frac{N_{\alpha\beta}}{N_{abc}} = \sqrt{\frac{3}{2}} \tag{7.41}$$

which is often used in more theoretical treatments because it makes the transformations unitary and power invariant. This normalization is used by Lang, Verghese, and Ilic [39] and Jones [30, 29]. Finally, Leonhard [40] uses the ratio

$$\frac{N_{\alpha\beta}}{N_{abc}} = 1, \tag{7.42}$$

possibly because the number of coil turns is constant under this transformation.

(7.39) with the normalization condition, (7.40), and the condition for balanced currents, equation (7.10), yields the $\alpha\beta \rightarrow abc$ transformation,

$$i_a = i_\alpha$$

$$
\begin{aligned}
i_b &= -\left(\frac{1}{2}\right) i_\alpha + \left(\frac{\sqrt{3}}{2}\right) i_\beta \\
i_c &= -\left(\frac{1}{2}\right) i_\alpha - \left(\frac{\sqrt{3}}{2}\right) i_\beta.
\end{aligned} \tag{7.43}
$$

The inverse $abc \rightarrow \alpha\beta$ transformation is

$$
\begin{aligned}
i_\alpha &= i_a \\
i_\beta &= \left(\frac{1}{\sqrt{3}}\right) i_b - \left(\frac{1}{\sqrt{3}}\right) i_c.
\end{aligned} \tag{7.44}
$$

7.4.3 $\alpha\beta \leftrightarrow dq$ Transformation

The second transformation converts between a two-phase AC system with fixed axes $\alpha\beta$ and a two-phase DC system with rotating axes dq. The dq system corresponds to a DC motor, and in steady state the direct and quadrature currents, voltages, are flux linkages are constant. We define θ as the angle of rotation of the dq frame from the $\alpha\beta$ frame as shown in Figure 7-7. The $\alpha\beta \leftrightarrow dq$ transformation can be derived by equating the magnetomotive force in the fixed $\alpha\beta$ frame and in the rotating dq frame,

$$
N_{\alpha\beta}(i_\alpha + j i_\beta) = N_{dq}\left((i_d + j i_q)\, e^{j\theta}\right). \tag{7.45}
$$

Setting the number of turns in the $\alpha\beta$ frame, $N_{\alpha\beta}$, equal to the number of turns in the dq frame, N_{dq},

$$
\frac{N_{dq}}{N_{\alpha\beta}} = 1, \tag{7.46}
$$

preserves current magnitudes, power, and the number of turns between these two frames. From (7.45) we can solve for the $dq \rightarrow \alpha\beta$ transformation, which is just a 2-D rotation from the dq frame to the $\alpha\beta$ frame,

$$
i_\alpha = i_d \cos\theta - i_q \sin\theta \tag{7.47}
$$

$$
i_\beta = i_d \sin\theta + i_q \cos\theta. \tag{7.48}
$$

The inverse $\alpha\beta \rightarrow dq$ transformation is

$$i_d = i_\alpha \cos\theta + i_\beta \sin\theta \tag{7.49}$$

$$i_q = -i_\alpha \sin\theta + i_\beta \cos\theta. \tag{7.50}$$

7.4.4 dq Transformation Matrix T

We can write the $abc \leftrightarrow \alpha\beta$ and $\alpha\beta \leftrightarrow dq$ transformations as matrices and multiply them to obtain a single matrix transformation T which transforms quantities from the abc frame directly to the dq frame. This transformation matrix is mainly useful in converting motor models from the abc frame to the dq frame for theoretical reasons. For example, implementing a sensorless control scheme in the dq frame requires us to convert motor variables between the abc and dq frames. Currents, voltages, and flux linkages are all transformed by the same matrix T. Also, in order to obtain a square, and hence invertible matrix, we need to include a zero-sequence component denoted by subscript 0 into the dq frame.[3] Under balanced three-phase conditions the zero-sequence components are zero and are therefore usually ignored [18]. Combining the two transformations into one matrix T is useful for theoretical reasons but is not preferred for real-time computations because it is less computationally efficient.

We define a vector U_{abc} of parameters in the abc frame, where u can represent currents i, voltages v, or flux linkages λ,

$$U_{abc} = \begin{bmatrix} u_a \\ u_b \\ u_c \end{bmatrix}. \tag{7.51}$$

We also define the vector U_{dq} of corresponding parameters in the dq frame, where

[3]This frame is sometimes called the $dq0$ frame for this reason.

again u can represent currents i, voltages v, or flux linkages λ,

$$U_{dq} = \begin{bmatrix} u_d \\ u_q \\ u_0 \end{bmatrix}. \tag{7.52}$$

The matrix T transforms variables from the *abc* frame to the *dq* frame,

$$U_{dq} = TU_{abc}, \tag{7.53}$$

and the inverse of T transforms variables from the *dq* frame to the *abc* frame,

$$U_{abc} = T^{-1}U_{dq}. \tag{7.54}$$

The matrix T is

$$T = \frac{2}{3}\begin{bmatrix} \cos\theta & \cos(\theta - \frac{2\pi}{3}) & \cos(\theta - \frac{4\pi}{3}) \\ -\sin\theta & -\sin(\theta - \frac{2\pi}{3}) & -\sin(\theta - \frac{4\pi}{3}) \\ \frac{1}{2} & \frac{1}{2} & \frac{1}{2} \end{bmatrix}, \tag{7.55}$$

and its inverse is

$$T^{-1} = \begin{bmatrix} \cos\theta & -\sin\theta & 1 \\ \cos(\theta - \frac{2\pi}{3}) & -\sin(\theta - \frac{2\pi}{3}) & 1 \\ \cos(\theta - \frac{4\pi}{3}) & -\sin(\theta - \frac{4\pi}{3}) & 1 \end{bmatrix}. \tag{7.56}$$

Note that the factor of 2/3 in the matrix T, (7.55), is the ratio of turns in the *abc* frame to turns in the $\alpha\beta$ frame, $N_{abc}/N_{\alpha\beta} = 2/3$ from (7.40). Since the number of turns in the $\alpha\beta$ and *dq* frames is the same, $N_{\alpha\beta} = N_{dq}$, we are choosing $N_{abc}/N_{dq} = 2/3$. This normalization choice preserves the magnitude of currents between the *abc* and *dq* frames, but the resulting transformation is not power invariant. This is not a problem because the power is the same in both frames, and we can still compute it as shown in section 7.5.3: we just need some extra constants.

7.5 Permanent Magnet Synchronous Motor Modeling in dq Variables

7.5.1 Stator Flux Linkages

In section 7.3 we developed a model of our motor in abc variables. Now we transform this model to dq variables. It is helpful to re-write our three-phase model in matrix form so that we can use the transformation matrix T. From (7.11) and the ensuing discussion, we have

$$\lambda_{abc} = L_{abc} I_{abc} + \lambda_{abcf}, \tag{7.57}$$

where λ_{abc} and I_{abc} are vectors of flux linkages and currents in the abc frame. Here L_{abc} is defined as the armature inductance matrix in the abc frame,

$$L_{abc} = \begin{bmatrix} L & -M & -M \\ -M & L & -M \\ -M & -M & L \end{bmatrix}, \tag{7.58}$$

and λ_{abcf} is a vector of the stator-to-rotor inductances in the abc frame,

$$\lambda_{abcf} = \begin{bmatrix} \lambda_{af} \\ \lambda_{bf} \\ \lambda_{cf} \end{bmatrix} = \begin{bmatrix} \lambda_f \cos\theta \\ \lambda_f \cos\left(\theta - \frac{2\pi}{3}\right) \\ \lambda_f \cos\left(\theta - \frac{4\pi}{3}\right) \end{bmatrix}. \tag{7.59}$$

We apply the transformation, $U_{dq} = T U_{abc}$, and its inverse to (7.57) to express the flux linkages and currents in the dq frame,

$$\begin{aligned} \lambda_{dq} &= \left[T L_{abc} T^{-1}\right] I_{dq} + \left[T \lambda_{abcf}\right] \\ &= L_{dq} I_{dq} + \lambda_{dqf}, \end{aligned} \tag{7.60}$$

where we have just defined L_{dq} and λ_{dqf}. The utility of the dq transformations is that under certain assumptions the self-inductance matrix, L_{dq}, and the rotor flux

linked by the stator, λ_{dqf}, have particularly simple forms: they do not depend on rotor angle θ and they do not contain any mutual inductance terms. A sufficient set of assumptions that lead to these simplifications in L_{dq} and λ_{dqf} are that three self-inductances in the matrix L_{abc} are the same, and the six mutual inductances in the matrix L_{abc} are also the same. In fact, we are even allowed to have saliency in the rotor such that the inductances vary as $\cos 2\theta$, but we do not consider this most general case here.[4] In our example, we have met these assumptions since all the self-inductances are equal to L and all the mutual inductances are equal to $-M$. Under these assumptions, and after much algebra[5] [18], we find that the armature inductance matrix in dq coordinates is diagonal,

$$L_{dq} = TL_{abc}T^{-1} = \begin{bmatrix} L_d & 0 & 0 \\ 0 & L_q & 0 \\ 0 & 0 & L_0 \end{bmatrix}, \tag{7.61}$$

where

$$L_d = L + M \tag{7.62}$$

$$L_q = L + M \tag{7.63}$$

$$L_0 = L - 2M. \tag{7.64}$$

If we had included rotor saliency in the analysis, the direct and quadrature inductances, L_d and L_q, would not be equal.

The form of λ_{dqf} is also particularly simple,

$$\lambda_{dqf} = T\lambda_{abcf} = \begin{bmatrix} \lambda_f \\ 0 \\ 0 \end{bmatrix}, \tag{7.65}$$

[4]See *Electric Machinery* [18] for a derivation with these saliency terms included.

[5]This tedious calculation and others in this chapter involving the matrix T are easily performed with symbolic math software such as the symbolic math toolbox in Matlab.

which indicates that the rotor only produces magnetic flux on the d axis. Since we defined the d axis to point in the direction of the rotor's flux, this makes sense.

7.5.2 Stator Terminal Voltages

We now transform the stator voltage equations from the abc frame to the dq frame. In the abc frame, we have

$$V_{abc} = \frac{d\lambda_{abc}}{dt} + R[I]I_{abc}, \tag{7.66}$$

where $[I]$ is a 3×3 identity matrix. After using the transformation rule, $U_{dq} = TU_{abc}$, and its inverse, we arrive at an expression for V_{dq},

$$\begin{aligned} V_{dq} &= T\frac{d}{dt}(T^{-1}\lambda_{dq}) + TR[I]I_{abc} \\ &= \frac{d}{dt}\lambda_{dq} + \left(T\frac{d}{dt}T^{-1}\right)\lambda_{dq} + R[I]I_{dq}, \end{aligned} \tag{7.67}$$

where the first term in (7.67) is a transformer voltage, the second term will be shown to be a speed voltage, and the third term is the resistive drop. To see that the second term leads to a speed voltage, we calculate that

$$T\frac{d}{dt}T^{-1} = \begin{bmatrix} 0 & -\frac{d\theta}{dt} & 0 \\ \frac{d\theta}{dt} & 0 & 0 \\ 0 & 0 & 0 \end{bmatrix} \tag{7.68}$$

From the matrix equation (7.60) we can summarize the flux linkages in the dq frame,

$$\lambda_d = L_d i_d + \lambda_f \tag{7.69}$$

$$\lambda_q = L_q i_q. \tag{7.70}$$

The d axis flux is produced by i_d and the rotor's permanent magnets, and q axis flux

is produced by i_q. From equations (7.67) and (7.68), the voltages in the dq frame are

$$v_d = i_d R + \frac{d}{dt}\lambda_d - \omega\lambda_q \tag{7.71}$$

$$v_q = i_q R + \frac{d}{dt}\lambda_q + \omega\lambda_d, \tag{7.72}$$

where $\omega = d\theta/dt$ is the rotor's speed. The first terms in equations (7.71) and (7.72) are the resistive drop, the second terms are transformer voltages, and the third terms are speed voltages.

7.5.3 Power

It is often easier to find motor power in the dq frame than in the abc frame. This is because the dq currents and voltages are constant in steady-state operation, while the abc currents and voltages are sinusoids. In the abc frame power p is

$$p = v_a i_a + v_b i_b + v_c i_c = V_{abc}^T I_{abc}. \tag{7.73}$$

Transforming to the dq frame, we have

$$\begin{aligned} p &= V_{abc}^T T^T \left(T^T\right)^{-1} T^{-1} T I_{abc} \\ &= V_{dq} \left[\left(T^T\right)^{-1} T^{-1}\right] I_{dq} \\ &= \frac{3}{2} v_d i_d + \frac{3}{2} v_q i_q + 3 v_0 i_0, \end{aligned} \tag{7.74}$$

since

$$\left(T^T\right)^{-1} T^{-1} = \begin{bmatrix} \frac{3}{2} & 0 & 0 \\ 0 & \frac{3}{2} & 0 \\ 0 & 0 & 3 \end{bmatrix}. \tag{7.75}$$

As mentioned in section 7.4.4, our transformation matrix T is not power invariant. We can see this because the coefficients in (7.74) are 3/2, 3/2, and 3; a power invariant transformation would have all unity coefficients. We see from this derivation that a unitary transformation matrix would lead to a power invariant transformation since

(7.75) would then be an identity matrix.

7.5.4 Torque

We can find the torque in two different ways, either by using energy arguments or transforming the torque expression in the *abc* frame. First, we find the torque using energy arguments. If we use equations (7.71) and (7.72) to substitute for v_d and v_q in the power equation, (7.74), we will find terms due to resistive loss, changes in stored energy, and electro-mechanical power conversion. The electro-mechanical power conversion or back EMF terms can be divided by mechanical speed to yield the motor torque,

$$\tau = p\frac{3}{2}(\lambda_d i_q - \lambda_q i_d), \tag{7.76}$$

where we have generalized to a motor with p pole pairs. We generalize to p pole pairs because our rotary motor has $p = 4$ pole pairs and we would like to develop a model for it in the *dq* frame. We can write this torque in terms of the motor's inductances using equations (7.69) and (7.70),

$$\tau = p\frac{3}{2}(\lambda_f + (L_d - L_q)I_d)I_q. \tag{7.77}$$

Our example permanent magnet motor has a smooth rotor so $L_d = L_q$, and its torque is thus

$$\tau = p\frac{3}{2}i_q\lambda_f. \tag{7.78}$$

The permanent magnets provide the d axis flux of λ_f, and we can control the motor torque by adjusting the quadrature current i_q which is proportional to motor torque.

We now re-derive this torque expression in a different way by using the transformation matrix T. We can write our expression for torque in the *abc* frame, (7.28), in matrix form as

$$\tau = \frac{d}{d\theta}\left(\lambda_{abcf}^T\right) I_{abc}. \tag{7.79}$$

We transform λ_{abcf} and I_{abc} to the dq frame using the transformation matrix T,

$$\begin{aligned}\tau &= \frac{d}{d\theta}\left((\lambda_{abcf}^T T^T)(T^T)^{-1}\right) T^{-1}(T I_{abc}) \\ &= \frac{d}{d\theta}\left(\lambda_{dqf}^T (T^T)^{-1}\right) T^{-1} I_{dq} \\ &= \lambda_{dqf}^T \left[\frac{d}{d\theta}\left((T^T)^{-1}\right) T^{-1}\right] I_{dq}, \end{aligned} \tag{7.80}$$

where we have used $d(\lambda_{dqf}^T)/d\theta = 0$ in going from the second to the third line. The matrix expression in square brackets simplifies to

$$\frac{d}{d\theta}\left((T^T)^{-1}\right) T^{-1} = \begin{bmatrix} 0 & \frac{3}{2} & 0 \\ -\frac{3}{2} & 0 & 0 \\ 0 & 0 & 0 \end{bmatrix}. \tag{7.81}$$

Our torque expression in the dq frame is now quite simple since $\lambda_{dqf} = [\lambda_f, 0, 0]^T$:

$$\tau = p\frac{3}{2} i_q \lambda_f. \tag{7.82}$$

This is the same torque expression we arrived at via the energy method, (7.78). We have again generalized to a motor with p pole pairs in (7.82).

We can rewrite (7.82) as

$$\tau = K_t i_q \tag{7.83}$$

where K_t is the motor torque constant,

$$K_t = p\frac{3}{2}\lambda_f. \tag{7.84}$$

The quadrature current, i_q, transforms to 3-phase currents with peak amplitudes equal to i_q since our transformation preserves current magnitudes. Thus, K_t is the motor force constant expressed in units of Newton-meters per peak amps, [N·m/A_{peak}]. Since root mean square currents, i_{rms}, are related to peak currents, i_{peak}, by $i_{rms} = (1/\sqrt{2})i_{peak}$, the motor force constant is $\sqrt{2}K_t$ in units of Newton-meters per rms

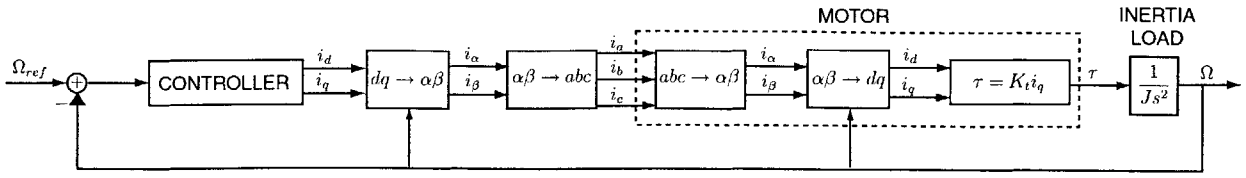

Figure 7-8: Block diagram of 3-phase permanent magnet synchronous motor control in dq variables. The transformations inside the motor block are part of the motor model.

amps, [N·m/A_{rms}]. In the next section we look controlling the permanent magnet motor using the simple expression for torque in the dq frame that we have just derived.

7.6 Permanent Magnet Synchronous Motor Control in dq Variables

We now show how the dq transformations reduce the controller design procedure for a 3-phase permanent magnet synchronous motor to the familiar procedure for a DC motor discussed in section 7.2. Figure 7-8 shows a block diagram of the motor control loop. The controller specifies direct and quadrature currents, i_d and i_q, which are transformed to 3-phase currents, i_a, i_b, and i_c, by a digital signal processor (DSP). These currents are generated by high bandwidth current amplifiers and applied to the motor's phases. From the motor model in dq coordinates we know that the motor torque is proportional to the quadrature current i_q, as expressed in (7.83),

$$\tau = K_t i_q.$$

In order to represent this in the block diagram, the motor model includes the $abc \rightarrow dq$ transformation.

For the purposes of controller design, the forward and reverse transformations in Figure 7-8 cancel each other and may be omitted as shown in Figure 7-9. This simple block diagram is analogous to the DC motor control block diagram of Figure 7-3. For

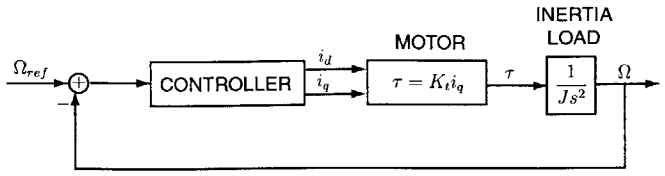

Figure 7-9: Controller design in dq variables is analogous to DC motor controller design.

a permanent magnet motor with a smooth rotor, the direct current, i_d, is set to zero since it does not produce any torque, and the quadrature current, i_q, is used to create torque. The controller may now be designed using standard classical or state-space techniques.

At high speeds, it may be desirable to reduce the d-axis flux so that the back EMF component, $\omega\lambda_d$, of v_q, (7.72), is reduced. The d-axis flux is given by (7.69),

$$\lambda_d = L_d i_d + \lambda_f.$$

Thus, at high speeds a negative direct current, i_d, can effectively weaken the field created by the permanent magnets. However, since permanent magnet motors have large effective air gaps, this field weakening is much less efficient than directly reducing the current in the field winding of a field-wound synchronous motor.

7.6.1 Homing the Motor

In Figure 7-8 the $\alpha\beta \rightarrow dq$ transformation performed by the DSP requires the electrical angle θ of the rotor. Often a relative sensor such as an encoder or laser interferometer (for linear motors) is used to sense rotor angle (or position). Since the $\alpha\beta \rightarrow dq$ transformation requires an absolute measure of angle, we must somehow zero or home the relative sensor. One option is to move the rotor until an index pulse is triggered. Another option is to use the motor phases themselves to home the motor; this is what we discuss in this section.

If we command a positive direct current, i_d, and set the angle, θ, used by the

$\alpha\beta \rightarrow dq$ transformation, we create flux along the d-axis which is at an angle θ from the a-axis (see Figure 7-7). The rotor of the motor will line up with this flux produced by stator currents. After waiting for the resulting oscillatory motion of the rotor to die down, we know that the rotor is pointing at an angle θ from the a-axis. For example, to align the rotor with the a-axis, we would set $\theta = 0$, and to align the rotor with the b-axis, we would set $\theta = 2\pi/3$.

7.7 Summary

This tutorial chapter introduces the field orientation transformations for three phase permanent magnet synchronous motors. We reviewed the standard modeling and control of brushed DC motors first since these are well understood. Later in the chapter we showed that three phase permanent magnet motors can be controlled in a similar manner using the field orientation transformations. We also developed a model for a 3-phase permanent magnet motor in *abc* coordinates and transformed it into *dq* coordinates.

Three phase permanent magnet motors can be controlled without the field orientation transformations presented in this chapter. However, the field orientation transformations simplify our understanding of these motors and make it easier for us to commutate them and measure their parameters. For example, what does it mean to speak of a three phase motor's force constant in Newtons per amp if there are three phases? What current are we talking about? As we saw in this chapter, the current level is really the amplitude of the three sinusoidal phase currents. It's much easier to think of the motor force constant as Newtons per amp of quadrature current, i_q. The quadrature current directly produces motor torque, and the field orientation transformations convert the actual phase currents into the quadrature current, or vice versa.

In addition to being used for motor commutation, the field orientation transformations provide us with a simple model of the motor in the *dq* frame. At the end of the next chapter, we will use this model to create a sensorless observer for the rotary

motor. First, though, the next chapter looks at the motor power amplifier circuits and the linear and rotary axis control design.

Chapter 8

Control System

In this chapter we look at the control system which runs the two axes of our prototype rotary-linear axis. In the first section, we look at the design of the analog power amplifier current control loop. This high bandwidth controller provides currents to each phase of the rotary and linear 3-phase motors. In the following two sections we look at the design of the linear and then rotary axis controllers. We control the linear and rotary axes separately since their dynamics are largely uncoupled. For each axis, we show measured Bode plots of the open-loop plant. We then explain the causes of initially unmodeled resonances and develop appropriate models and possible mechanisms for these modes. Using the open-loop Bode plot, we explain how we design an appropriate controller for each axis and show the resulting loop transmission Bode plot. For each axis, we then show the performance achieved via closed-loop Bode plots, step responses, and positioning noise. The linear axis has a 70 Hz closed-loop bandwidth and 2.5 nm rms positioning noise. The rotary axis has a 40 Hz closed-loop bandwidth and 3.1 μrad rms positioning noise. In the final section of the chapter we present a sensorless control scheme for spinning the rotary motor using only measurements of the motor's phase currents and voltages. Such an approach would be helpful for controlling a rotary-linear high speed spindle. In this application, precise angular positioning is not required; we only need to implement speed control and require angle only for motor commutation. We have successfully implemented sensorless control at a rotation speed of 390 rpm (40.84 rad/s) on our

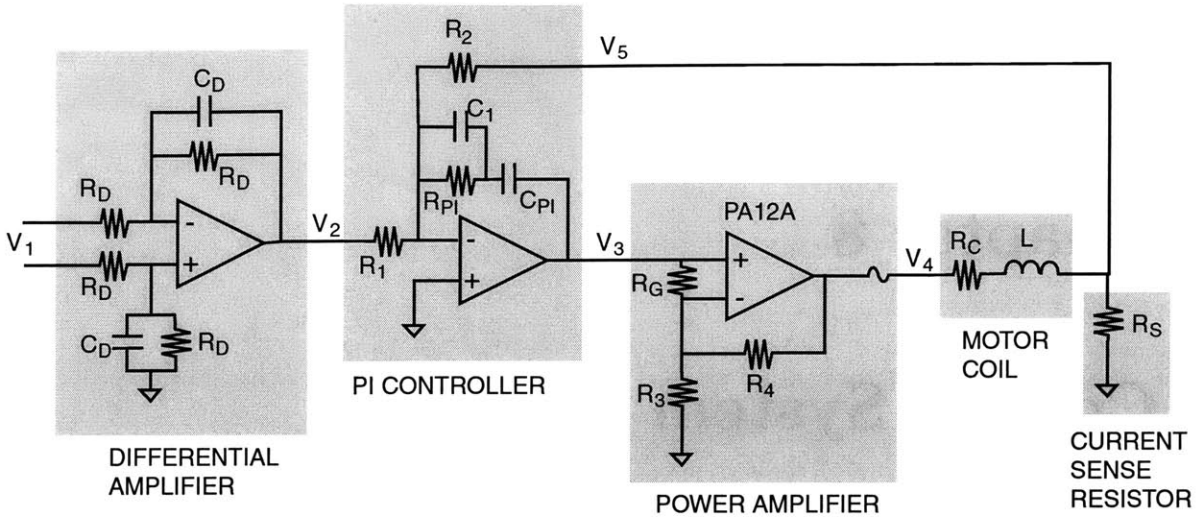

Figure 8-1: Current control circuit for each motor phase.

testbed.

8.1 Power Amplifier

A power amplifier provides current for each motor phase. The two main categories of power amplifiers are linear amplifiers and switching amplifiers. Linear amplifiers are based on a power op amp. Switching amplifiers, also called pulse-width modulated (PWM) amplifiers, use transistors to switch the voltage between two fixed levels at a high frequency (say 20 kHz). Switching amplifiers are energy efficient, but they can generate significant high frequency electrical noise. We choose to use a linear amplifier in our prototype to avoid this noise and the added complexity of implementing a switching amplifier.

Figure 8-1 shows the power amplifier circuit we use for each motor phase. It is modified from a circuit design used widely in our laboratory [75, 34, 74]. The voltage, V_1, is supplied by a D/A converter from the main DSP control board. It first passes through a differential amplifier which rejects common mode noise. Voltage V_2 serves as the reference input to a PI controller, and V_5 is a feedback signal proportional to the current in the motor coil, as measured by sense resistor R_s. The PI controller

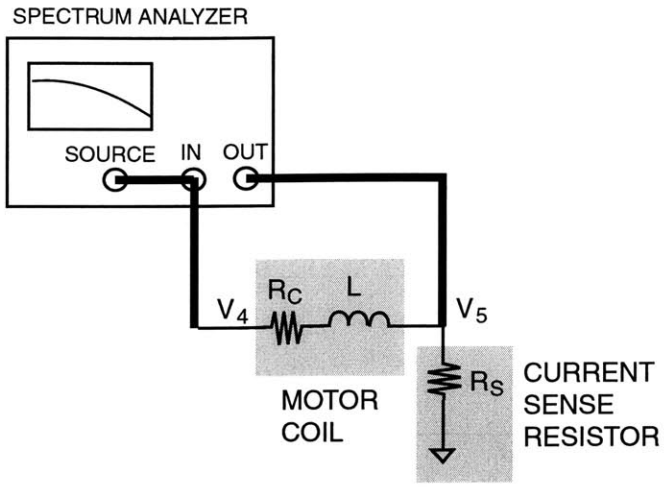

Figure 8-2: Spectrum analyzer configuration for measuring the transfer function V_5/V_4.

outputs a control effort V_3 which is amplified by the PA12A power amp to apply voltage V_4 to the motor phase in series with sense resistor R_s.

In this section we first develop a model for the motor phases. Then, we show how to design PI controllers for the current control loops. Next, we show the closed-loop Bode plots and current step responses of these controllers. Finally, we discuss the reduced gain configuration of the power amplifier that we use to eliminate a problem with power op amp oscillation.

8.1.1 Coil Model

We model the motor coils as a resistance, R_C, in series with an inductance, L, as shown in Figure 8-2. R_C is determined by measuring the resistance of the coil with a voltmeter. L is determined by adding a current sense resistor, R_S, in series with the coil and measuring the transfer function of the resulting voltage divider. This transfer function is

$$\frac{V_5}{V_4} = \frac{K}{\tau s + 1}, \tag{8.1}$$

where $K = R_S/(R_C + R_S)$ and the time constant is $\tau = L/(R_C + R_S)$. A Hewlett-Packard spectrum analyzer in swept-sine mode was used to measure this transfer

function experimentally. Figure 8-3 shows the resulting Bode plot for a linear motor phase. The Bode plot looks very much like the ideal first order system predicted by

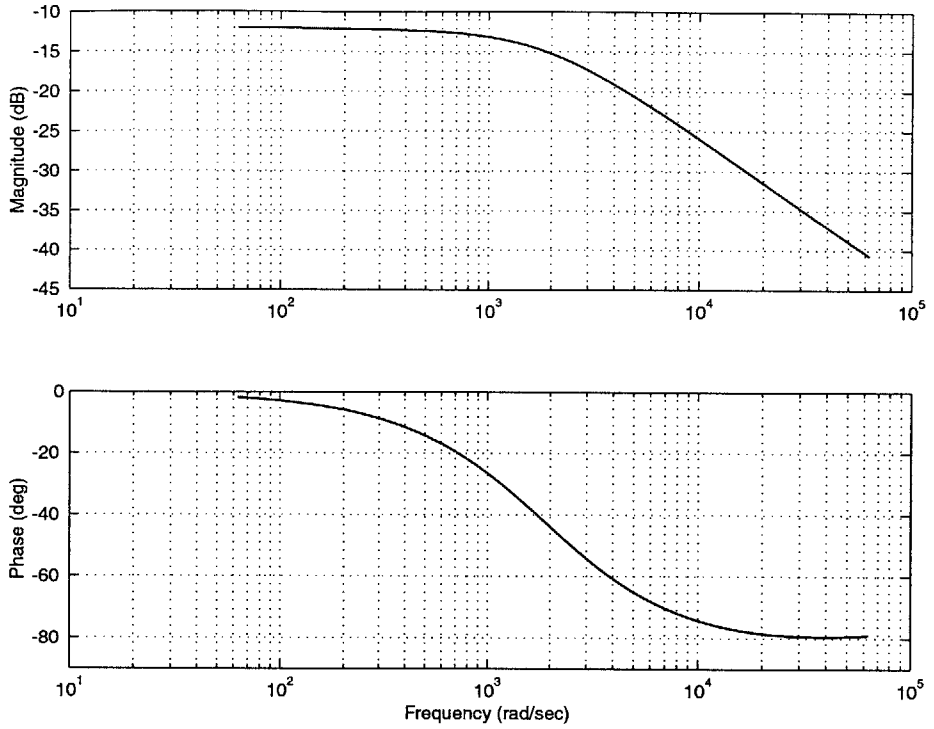

Figure 8-3: Measured bode plot for the transfer function V_5/V_4 from Figure 8-2, for one of the linear motor phases.

our model. Since the resistance R_S of the current sense resistor is known precisely, we can determine R_C and L from the Bode plot. Table 8.1 summarizes the measured resistances, inductances, and time constants for our rotary and linear motor phases.

8.1.2 PI Controller Design

If the current controller has a bandwidth approximately 20 times higher than the main control loop, its dynamics can be ignored when designing the main controller. Since our main mechanical control loop will have a bandwidth of approximately 100 Hz, the current amplifier bandwidth should be approximately 2 kHz. We would also like a highly damped step response, so we should have at least 80 degrees of phase margin at crossover. In addition, the current amplifier should map the D/A voltage range of

	Linear Motor	*Rotary Motor*
Phase Resistance, R_C	3.2 Ω	6.8 Ω
Phase Inductance, L	1.7 mH	1.66 mH
Sense Resistor, R_S	1.0 Ω	1.0 Ω
Time Constant, τ	0.513 ms	0.212 ms
DC Gain Constant, K	0.238	0.128

Table 8.1: Resistances, inductances, and time constants of motor phases.

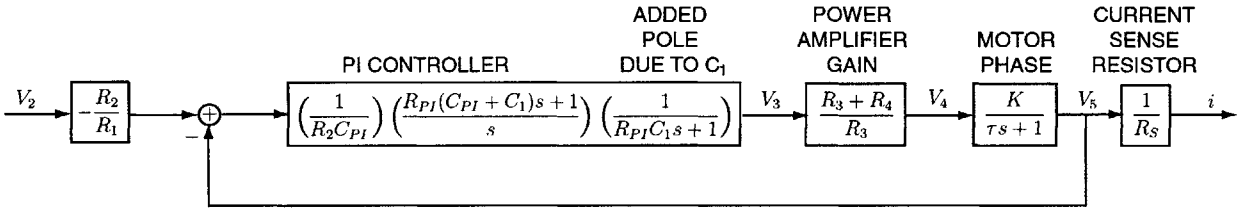

Figure 8-4: Block diagram of PI current controller.

-10 to $+10$ V into the current range of -10 to $+10$ A. Although steady-state currents may be only 3 A, we want to allow for short pulses of higher currents to achieve high peak accelerations. Thus, the overall amplifier gain should be 1 A/V.

We have identified the motor phase resistance and inductance above and can now design the proportional-integral (PI) controller. The first step is to turn the circuit diagram shown in Figure 8-1 into a block diagram.

Assuming exact componenet matching, the transfer function of the differential amplifier is

$$\frac{V_2}{V_1} = \frac{-1}{R_D C_D s + 1}. \tag{8.2}$$

This is a low-pass filter with time constant $R_D C_D$. With $R_D = 10$ kΩ and $C_D = 820$ pF, the filter bandwidth is 19.4 kHz, well above the current loop bandwidth of approximately 2 kHz. Since, the differential amplifier precedes the PI control loop, it is not included in the PI control loop transfer function.

Figure 8-4 shows a block diagram for the remainder of the current control circuit. The ratio $-R_2/R_1$ sets the gain of the circuit in A/V. The parameter, $R_{PI}C_{PI}$ (since $C_1 \ll C_{PI}$), sets the location of the PI controller zero. We locate the zero somewhat

		Linear Motor	*Rotary Motor*
Differential Amplifier	R_D	10.0 kΩ	10.0k Ω
	C_D	820 pF	820 pF
PI Controller	R_{PI}	49.9 kΩ	20.0 kΩ
	C_{PI}	0.01 μF	0.01 μF
	C_1	47 pF	47 pF
	R_1	3.32 kΩ	2.0 kΩ
	R_2	3.32 kΩ	2.0 kΩ
Power Amplifier	R_3	10.0 kΩ	10.0 kΩ
	R_4	10.0 kΩ	10.0 kΩ
	R_G	10.0 kΩ	10.0 kΩ

Table 8.2: Values of resistances and capacitances for the current amplifier circuit shown in Figure 8-1 for the two motors.

above the open-loop pole of the motor phase, $1/\tau$. The parameter, $1/(R_2C_{PI})$ allows gain adjustment to achieve the desired crossover frequency. We add the small capacitor C_1 to the circuit design. It reduces high frequency feedback around the controller op amp which improves circuit stability, and rolls off the loop gain at high frequencies.

Table 8.2 lists the resistor and capacitor values chosen for the power amplifier controllers for the linear and rotary motors. The linear motor current controller has a crossover frequency of 2.2 kHz and 90 degrees of phase margin; the rotary motor controller has a crossover frequency of 1.9 kHz and 90 degrees of phase margin.

8.1.3 Controller Performance

We measure the frequency responses and step responses of the closed-loop current amplifiers to verify their performance. Figure 8-5 shows the linear motor current amplifier closed-loop Bode plot, and Figure 8-6 shows the rotary motor current amplifier closed-loop Bode plot. The Matlab tool `dsa_tf`, written by Katie Lilienkamp in our research group, is used as a spectrum analyzer to obtain the frequency response data. This tool is described further on page 247 of section 8.2.1. A high sampling rate of 100 kHz is used to avoid phase lag due to the time delay of the discrete system.

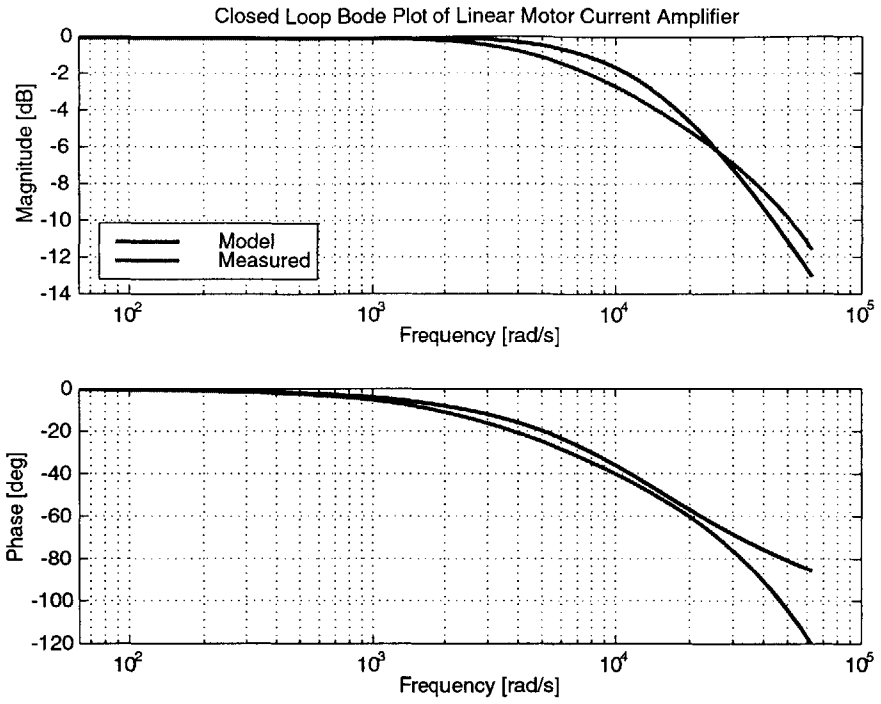

Figure 8-5: Linear motor current amplifier closed-loop Bode plot.

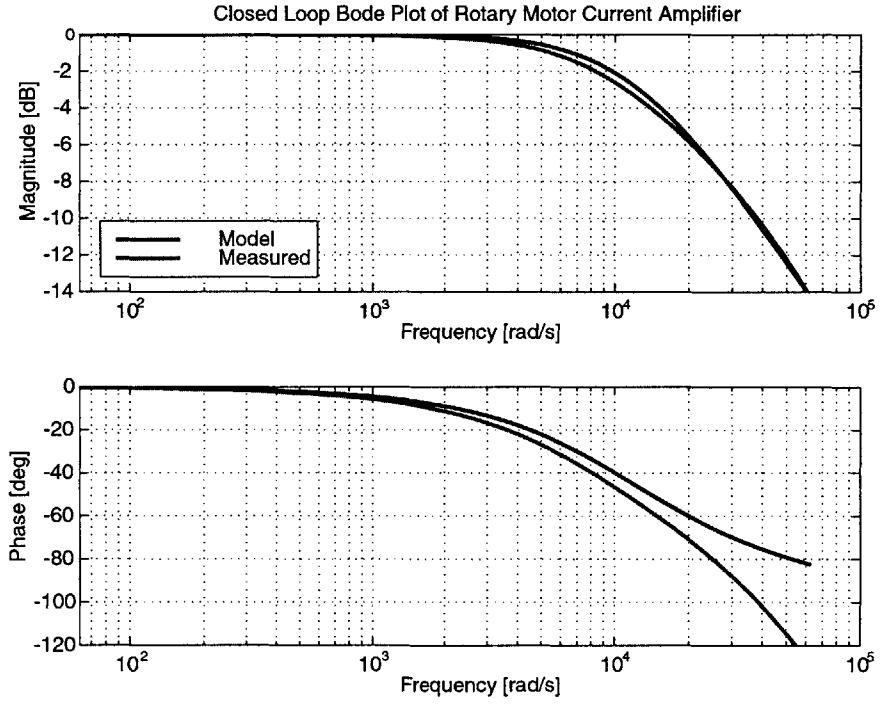

Figure 8-6: Rotary motor current amplifier closed-loop Bode plot.

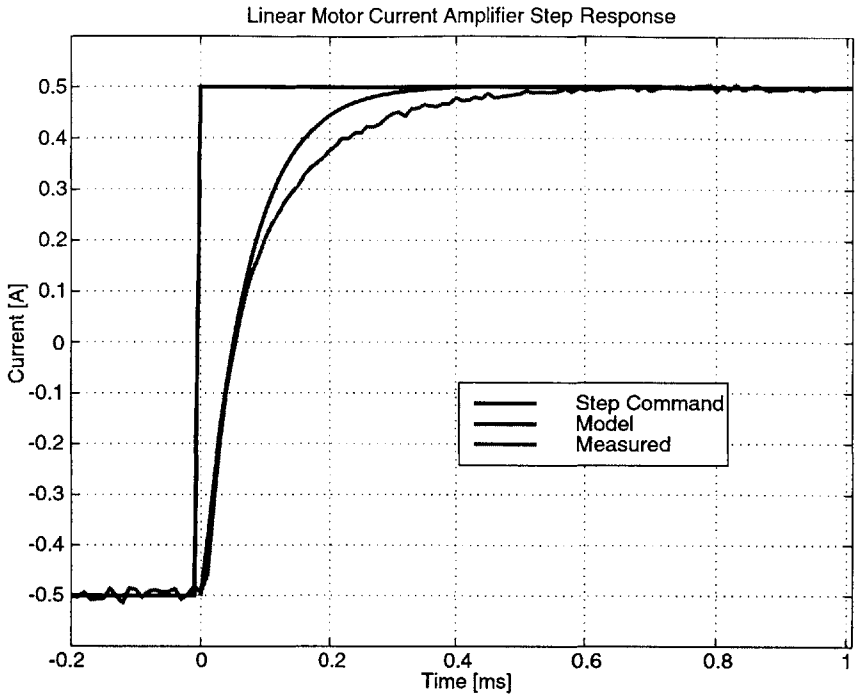

Figure 8-7: Linear motor current amplifier step response.

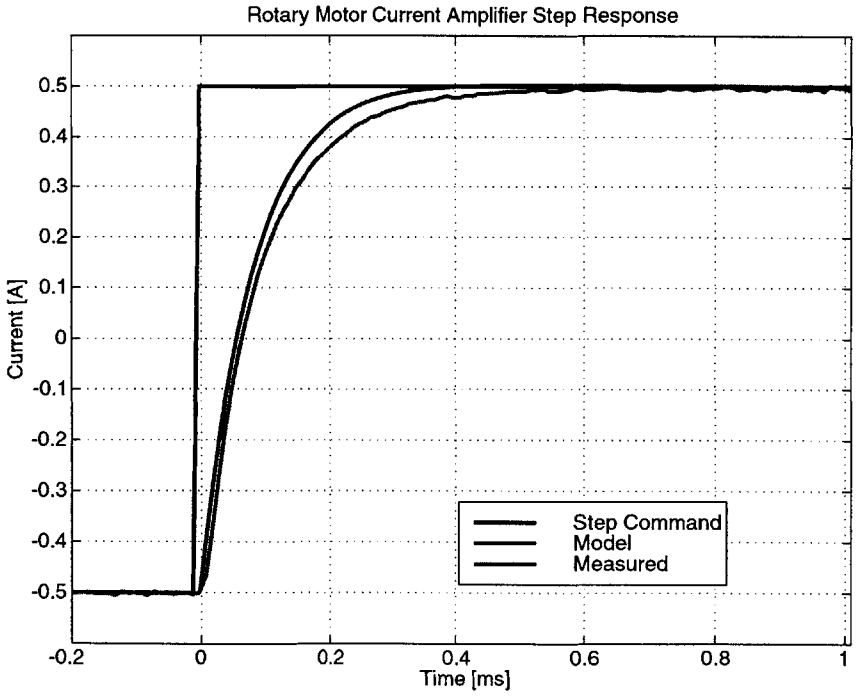

Figure 8-8: Rotary motor current amplifier step response.

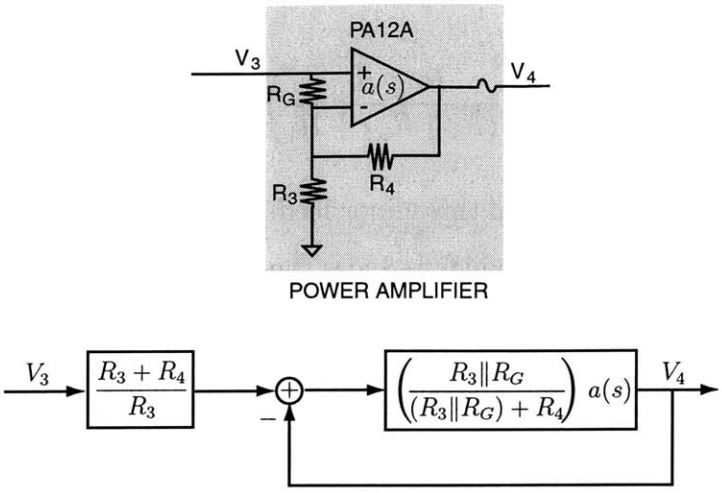

Figure 8-9: Block diagram of PA12A power amplifier loop. R_G reduces the bandwidth of the feedback loop around the op amp without affecting the gain from V_3 to V_4.

The frequency responses of both amplifiers are close to the predicted responses. The bandwidths of both current amplifiers are 1.75 kHz. The step responses are shown in Figure 8-7 and Figure 8-8. Both amplifiers have rise times on the order of 0.2 ms and have no overshoot.

8.1.4 Reduced Gain Configuration

This section explains how resistor R_G across the power op amp input terminals (Figure 8-1) eliminates an observed power op amp oscillation. The initial circuit design did not include R_G. When we tested the current control circuit, we found that the output voltage was oscillating at 2 MHz. Since the circuit oscillated at a much higher frequency than the 2 kHz bandwidth of the PI current control loop, we concluded that the oscillations were due to the minor feedback loop around the power op amp itself. We tested this hypothesis, by driving the power amplifier stage directly at V_3 and observing the output V_4. As expected, the oscillations were still there.

Figure 8-9 shows the power amplifier and its block diagram reduced to a unity-feedback form. The open-loop transfer function of the power op amp is $a(s)$ defined by $V_4(s) = a(s)(V^+ - V^-)$, where V^+ and V^- are the input voltages. The magnitude

of the loop transmission is

$$\left(\frac{R_3 \parallel R_G}{(R_3 \parallel R_G) + R_4}\right) a(s). \tag{8.3}$$

One may improve the stability of this minor feedback loop by increasing the ideal low frequency gain, $(R_3 + R_4)/R_3$, which reduces the magnitude of the loop tranmission. The ideal low frequency gain should roughly map the range of V_3, typically ± 15 V, into the range of V_4 which is determined by the power supply used with the power op amp. Thus, for a given application the ideal low frequency gain may not be able to be increased. The inclusion of R_G in the circuit provides an additional degree of freedom such that the ideal gain, $(R_3 + R_4)/R_3$, and the loop transmission can be adjusted independently [57]. Note that for any value of R_G, including inifinity (no R_G), the ideal low-frequency gain of this amplifier is

$$\frac{V_4}{V_3} = \frac{R_3 + R_4}{R_3}. \tag{8.4}$$

This is the gain shown in the Power Amplifier Gain block in Figure 8-4. The magnitude of the minor loop transmission given in equation (8.3) decreases as R_G increases. Thus, adding the resistor R_G into the circuit reduces the bandwidth and increases the stability of the minor feedback loop around the power op amp, but has no significant effect on the major PI feedback loop (Figure 8-4).

8.2 Linear axis compensator design

One of the main benefits of our rotary-linear axis is that the mechanical system is simple and therefore easy to model and control. The air bearings provide essentially frictionless guidance, and the forces and torques produced by the motors can be calculated accurately. As a first approximation, we can model the linear axis mechanical system as a mass and the rotary axis mechanical system as an inertia. Of course, there are additional resonances and other dynamics, especially at higher frequencies. In subsequent sections we examine these higher order effects in detail and see how

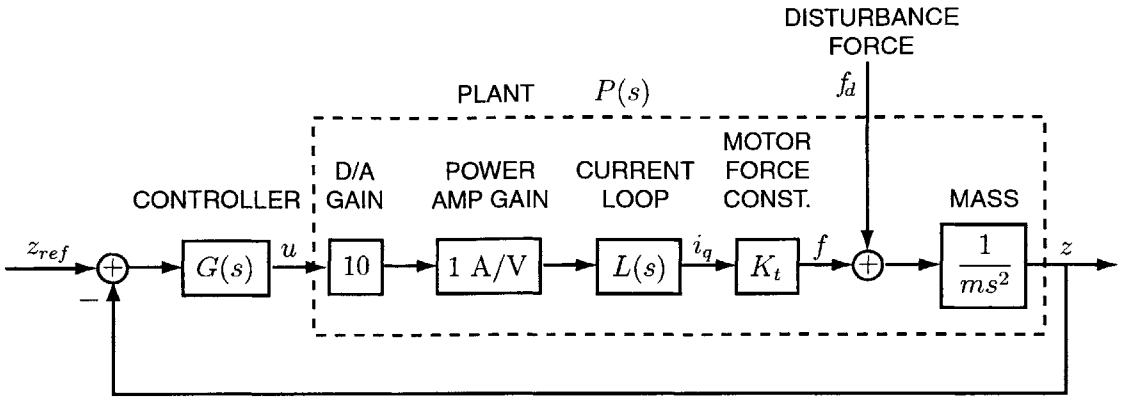

Figure 8-10: Linear axis control block diagram.

they affect the controller design. We see that to a very good approximation the linear axis can be considered a plain mass, but the rotary axis has significant low frequency resonances which limit its performance.

For both the linear and rotary axes we model the system and identify resonances. Then we use our model to develop an appropriate controller, and finally we will verify the control system's performance.

Figure 8-10 shows the control block diagram for the linear axis. The controller $G(s)$ provides a control effort u based on the error between the reference position z_{ref} and the measured position z of the axis. This control effort becomes a reference current for the inner analog current control loop discussed in section 8.1 and shown in Figure 8-1. The 1.75 kHz bandwidth of the current loop is much higher than the approximately 100 Hz bandwidth of the outer position loop. Thus, the current loop's closed loop transfer function, $L(s)$, is approximately unity in the frequency range of interest for the position loop. The control effort, u, is a proportional command of the q-axis current, i_q. As described in detail in section 7.5.4, the linear motor produces a force, $f = K_t i_q$, proportional to the q-axis current, i_q, where the proportionality constant, K_t, is the motor's force constant. This force and any external disturbance force, f_d, are applied to our shaft which we intially model as a pure mass, $1/(ms^2)$.

We are using a 3-phase brushless motor, but for the purposes of controller design, we have omitted the dq transformations for motor commutation. This simplification

is possible since the motor inherently performs the reverse dq transformations as is shown in Figure 7-8 and discussed in section 7.4. Thus, even though we are using a 3-phase brushless motor, we can design the control system as if we are using a brushed DC motor with armature current, i_q, motor constant, K_t, and force, $f = K_t i_q$. Said another way, the commutation laws are suppressed in Figure 8-10, and we treat the motor as a brushed DC motor with a single coil current i_q.

The sensor dynamics do not appear in the control block diagram. The laser interferometer has a much higher bandwidth than our position loop, and we have provided gains in our DSP so that the interferometer's counts are converted to meters.

Now that we have an initial model of the linear axis control loop, we need to verify it experimentally and see what other effects may be present in our system. In particular, we suspect that the moving mechanics will have some higher frequency resonances which we have not yet modeled. We also expect additional phase loss due to time delays associated with the zero-order hold in the D/A converter and the digitial implementation of the controller.

8.2.1 Modeling

An initial model of the linear-axis plant is shown in Figure 8-10. It consists of the D/A gain, the power amplifier gain, the analog closed-loop current control, the motor constant, and the shaft's mass. We have already measured many of these components separately. For example, the power amplifier gain and closed-loop current control transfer function are measured in section 8.1.3, and the motor constant is measured in section 4.2. The only component we have not already measured is the shaft mechanical dynamics model which initially consists of a pure mass.

In order to measure $P(s)$ we want to measure the transfer function from u to z. We can do this by applying a sine wave at different frequencies at u and measuring the amplitude and phase of z at each frequency. Since there is no mechanical spring in the system, if we attempt to measure this transfer function open-loop, the shaft will tend to wander from its intial position after executing many open-loop sinusoidal cycles. This is not usually a problem in a rotary system, but for a linear system with

short travel, the shaft may wander to the end of its travel during the measurement. The solution is to close the loop with any stable closed-loop controller $G(s)$ and measure the transfer function from u to z as z_{ref} is driven with sine waves at different frequencies.

Based on our initial model shown in Figure 8-10 we design a baseline lead-lag controller with a 20 Hz bandwidth to stabilize our plant so that we can measure the plant's frequency response. This controller is implemented on a dSPACE 1103 DSP board. We describe the dSPACE implementation in detail in Chapter 9. For now, we would like to point out that the dSPACE implementation gives us easy access to any of the variables in the DSP, including u and z. Furthermore, a software dynamic signal analyzer[1] for dSPACE was developed by Katie Lilienkamp, a student in our laboratory [42]. Just like an analog dynamic signal analyzer, this software dynamic signal analyzer measures the frequency response between its two inputs and provides a source output which can be used to drive the system.

We use this software dynamic signal analyzer to measure the frequency response of the plant transfer function $P(s)$ shown in Figure 8-10. The first input is connected to the control effort, u, and the second input is connected to the position, z. The source output provides a sinsusoidal reference position to z_{ref}. The amplitude of this sinusoidal reference position is chosen at each frequency to be high enough to achieve a good signal-to-noise ratio in the sinusoidal position response z, but low enough to avoid saturating the power amplifiers. Although some trial-and-error is involved in setting the amplitude of z_{ref} at various frequencies, we develop a simple model that works well. For frequencies below the controller's bandwidth, the position z should be close to the reference position z_{ref},

$$z \approx z_{ref} = A \sin \omega t, \tag{8.5}$$

where the reference sinewave has an amplitude, A, and frequency, ω. In order to

[1]This software may be downloaded from our lab's website, http://web.mit.edu/pmc/www/Links/download/download.html. We modified this software to run on the dSPACE 1103 board.

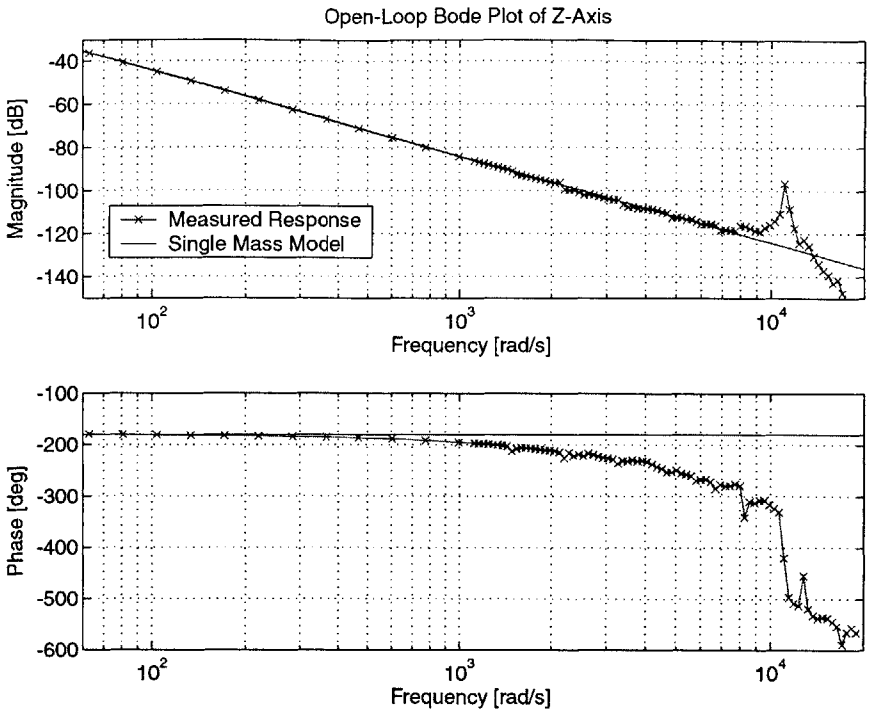

Figure 8-11: Measured linear axis open-loop Bode plot (from control effort, u, to position, z). The initial model shown for comparison consists of a single mass, the D/A gain, the power amplifier gain, and the motor force constant. The z sensor is an interferometer measuring distance from the tilted mirror.

avoid saturating the power amplifiers we need to limit the acceleration, $\ddot{z}$,

$$\ddot{z} \approx A\omega^2 \sin \omega t. \tag{8.6}$$

Thus, for frequencies below the closed-loop bandwidth, the amplitude, A, should be inversely proportional to ω^2. For frequencies above the closed-loop bandwidth, z no longer accurately follows z_{ref}, and, in fact, the closed-loop transfer function from z_{ref} to z falls off with a -2 slope. This is because above crossover, the closed-loop system transfer function approaches the forward gain transfer function, and the forward gain transfer function has two more poles than zeros. Thus, a constant reference sinewave amplitude will work for frequencies above the closed-loop bandwidth.

The measured open-loop Bode plot of our plant $P(s)$ is compared to our initial model in Figure 8-11. The initial plant model shown in Figure 8-10 includes the

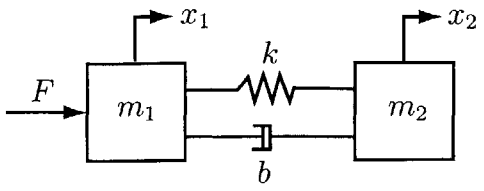

Figure 8-12: Canonical two-mass system. Measurement x_1 is collocated with the actuator; measurement x_2 is non-collocated with the actuator.

D/A gain, power amplifier gain, and motor force constant; it models the shaft as a pure mass and assumes that the current control loop is ideal by approximating its closed loop transfer function as unity, $L(s) = 1$. We used the tilted-mirror (shown in Figure 6-1) to measure z initially since we set up this mirror and its interferometers before we set up the smaller z mirror and its interferometer. The rotary axis controller prevents the shaft from rotating during the linear axis frequency response measurement.

The initial plant model agrees very well with the actual system. The excellent agreement at low frequencies indicates that we have modeled and measured the gains, force constant, and mass well.[2] We notice an unmodeled resonance at 11,020 rad/s. There is also significant phase lag at higher frequencies. In general, though, the plant is very clean and close to the simple, initial model. In the following two sections we first investigate the observed resonance and then model the phase lag.

Linear Axis Resonance

The resonance at 11,020 rad/s is a non-collocated resonance since it has two poles and no associated zeros. A non-collocated resonance arises when there is flexibility between the actuator and sensor. Figure 8-12 shows a canonical two-mass system often used to study control through a flexible structure [19]. The transfer function from force F to position x_2 is called non-collocated since a spring separates the sensor and actuator. The transfer function from force F to position x_1 is called collocated

[2]It is possible that two or more errors in these parameters cancel each other out when multiplied together, but this is unlikely.

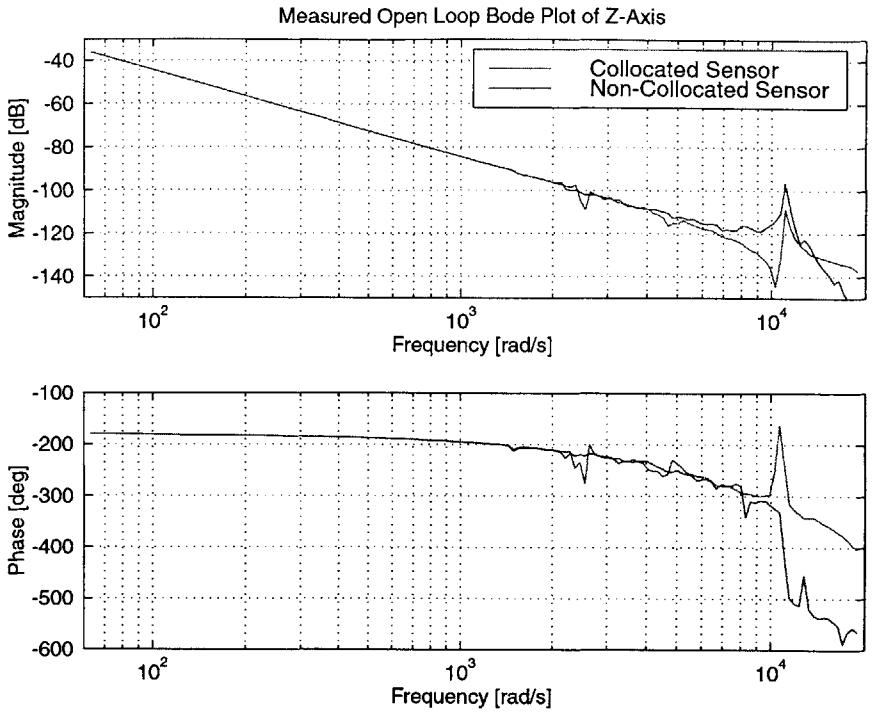

Figure 8-13: Measured linear axis open-loop Bode plots (from control effort, u, to position, z). We compare the Bode plot of the z-axis using the tilted mirror interferometer, a non-collocated sensor, with the Bode plot of the z-axis using the small z mirror interferometer on the other end of the shaft, a collocated sensor.

since the sensor is located on the same rigid body as the actuator; however, flexibility exists elsewhere in the system. Collocated resonances have two zeros in addition to two poles, leading to a more stable system as we shall see shortly.

Once we had set up the smaller z mirror and its interferometer on the other end of the shaft (as shown in Figure 6-1), we took another frequency response measurement of the linear plant $P(s)$ using this interferometer. As shown in Figure 8-13 this frequency response is similar to the one using the tilted-mirror interferometer, except that the resonance at 11,020 rad/s is now preceded by two zeros at 10,260 rad/s. The two transfer functions represent the classic collocated and non-collocated cases.

Next we developed a model to explain the observed resonance at 11,020 rad/s and the observed collocated and non-collocated sytem behavior. Since the transfer function based on the tilted mirror is non-collocated, the flexibility has to exist between

the linear motor magnets and the tilted mirror. The tilted mirror mount is a prime candidate for the location of this flexibility. We use the two-mass model shown in Figure 8-12 to model the resonance. In particular, mass m_1, represents the entire shaft and all mounted components except the tilted mirror; mass, m_2, represents the tilted mirror. The linear motor provides force F. The flexibility, k, and damping, b, are due to compliances in the tilted mirror mount. The position, x_1, of m_1 is measured by the small z mirror interferometer, and the position, x_2, of m_2 is measured by one of the tilted-mirror interferometers.

The equations of motion for the canonical two-mass system of Figure 8-12 are

$$m_1\ddot{x_1} + b(\dot{x_1} - \dot{x_2}) + k(x_1 - x_2) = F \tag{8.7}$$

$$m_2\ddot{x_2} + b(\dot{x_2} - \dot{x_1}) + k(x_2 - x_1) = 0. \tag{8.8}$$

We take the Lapace transform of both equations and solve for the collocated transfer function,

$$\frac{X_1(s)}{F(s)} = \frac{m_2s^2 + bs + k}{(m_1 + m_2)s^2\left[\left(\frac{m_1m_2}{m_1+m_2}\right)s^2 + bs + k\right]}, \tag{8.9}$$

and the non-collocated transfer function,

$$\frac{X_2(s)}{F(s)} = \frac{k + bs}{(m_1 + m_2)s^2\left[\left(\frac{m_1m_2}{m_1+m_2}\right)s^2 + bs + k\right]}. \tag{8.10}$$

Here $X_1(s)$, $X_2(s)$, and $F(s)$ are the Laplace transforms of x_1, x_2, and F, respectively. The four poles of both transfer functions are identical, as they must be, since poles describe the natural modes of the system. The two poles at the origin represent the rigid body dynamics of both masses moving together,

$$\frac{1}{(m_1 + m_2)s^2}. \tag{8.11}$$

The other two poles at the resonant frequency,

$$\omega_0 = \sqrt{\frac{k}{\left(\frac{m_1 m_2}{m_1+m_2}\right)}}, \tag{8.12}$$

represent the system's flexible mode. Note that in the collocated case, (8.9) two zeros exist at a slightly lower frequency, $\sqrt{k/m_2}$, than the flexible mode poles, but that in the non-collocated case (8.10), no such zeros exist. The collocated case is easier to control since the zeros nearly cancel the flexible mode poles.

In order to compare the collocated and non-collocated models with our measured data, we need to obtain numerical values for the masses, m_1 and m_2, the spring constant, k, and the damping constant, b. We set $m_1 = 1.256$ kg, the mass of the shaft and all components except the tilted mirror, and we set $m_2 = 0.190$ kg, the mass of the tilted-mirror. Setting $\omega_0 = 11,020$ rad/s in equation (8.12), we calculate that the spring constant is $k = 20 \times 10^6$ N/m. The damping ratio ζ can be estimated from the height of the resonant peak in the Bode Plot of the non-collocated system (Figure 8-11) to be $\zeta = 0.005$. The damping constant b is related to damping ratio ζ by,

$$b = 2\zeta\omega_0 \left(\frac{m_1 m_2}{m_1 + m_2}\right). \tag{8.13}$$

Figure 8-14 shows Bode Plots of the collocated and non-collocated models. We have included the D/A gain, power amplifier gain, and motor force constant in the transfer functions as well so that these plots are models for the linear-axis plant $P(s)$. The models in Figure 8-14 look very similar to the measured data in Figure 8-13. The only difference is that the measured data has more phase delay at higher frequencies. We model this in the following section.

The tilted mirror mount is shown in Figure 8-15. It has three fine pitch adjustment screws which control the mirror's tilt and a spring steel web to pre-load the mirror against the adjustment screws. The sping steel serves as a flexure to constrain three degrees of freedom. An aluminum plate is epoxied to the mirror and has silicon carbide inserts opposite the adjustment screws. The Hertzian contact stiffness between the

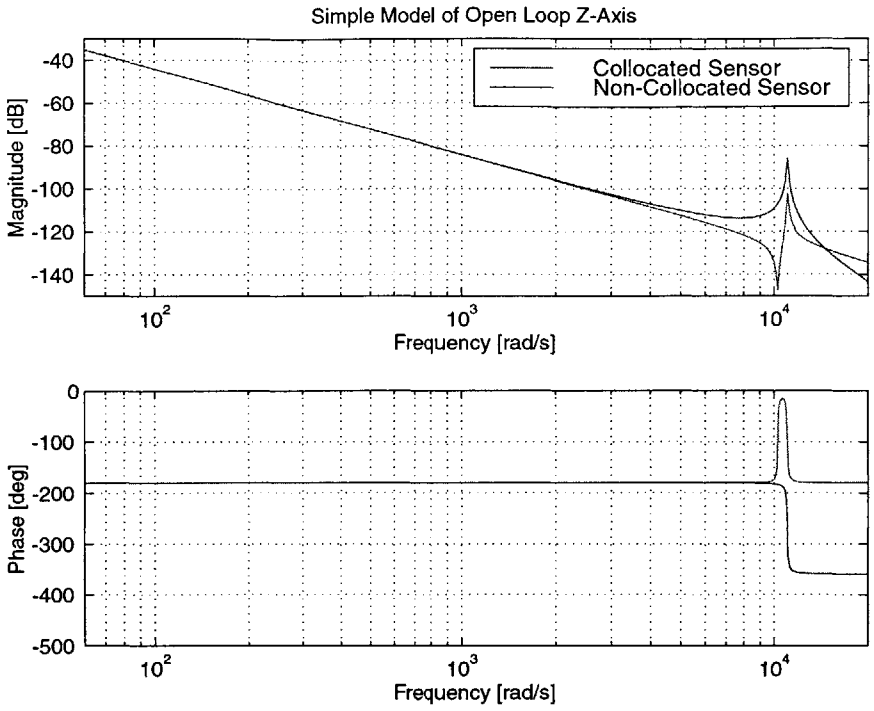

Figure 8-14: Linear axis open-loop Bode plots of collocated and non-collocated models of the z-axis.

adjustment screws and silicon carbide inserts is the source of the flexibility for the observed resonance.

Although the resonance does not limit the control system performance because it is sufficiently high in frequency, we attempted to increase its frequency further. To do this we increased the pre-load on the three adjustment screws. First we replaced the 0.010 inch thick annular spring steel web in the tilted mirror mount with two 0.020 inch thick webs to increase the pre-load force. Then we increased the distance between the mirror and the mount by increasing the length of the three adjustment screws. This placed the web under a greater stress thus increasing the pre-load. Figure 8-16 shows the effects of increasing the pre-load: the resonant frequency increased from 11,020 rad/s to 12,270 rad/s. Thus, we have increased the contact stiffness in the tilted-mirror mount 25% from $k = 20 \times 10^6$ N/m to $k = 25 \times 10^6$ N/m.

We are confident that the contact flexibility in the tilted-mirror mount causes the observed resonance for two reasons. First, a two-mass model predicts the observed

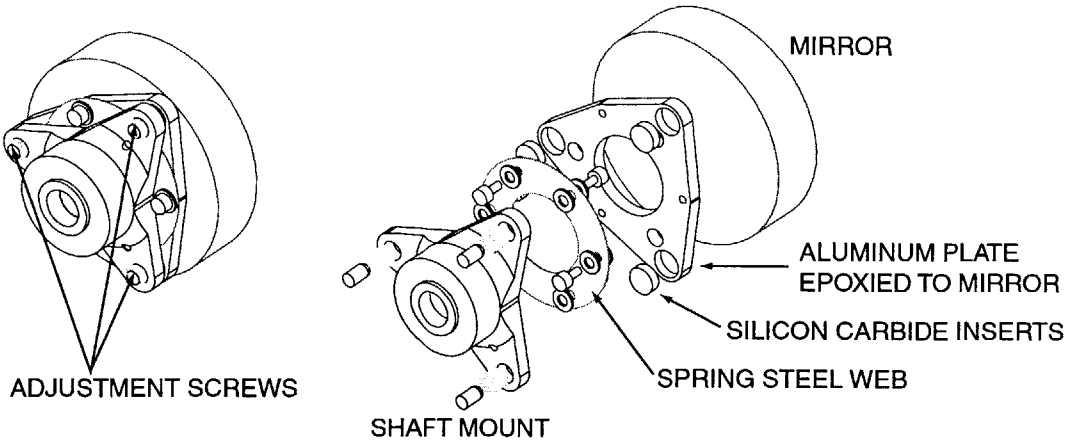

Figure 8-15: Tilted-mirror mount. Figure drawn by Marsette Vona [70].

collocated and non-collocated frequency responses. Second, increasing the pre-load on the contact zone increases the observed resonant frequency.

Modeling Phase Lag

In Figure 8-17 we compare our collocated model (cyan) with the experimental data (red x's). The amplitude plots agree quite well, but the experimental data has significant phase loss at high frequencies which is not predicted by our model. In our initial model, we assume that the power amplifier current control loop is exactly unity. In fact, though, it's closed-loop transfer function has some phase lag starting at 1000 rad/s as shown in Figure 8-5. When the power amplifier dynamics are added to our plant model, we obtain the model shown in green in Figure 8-17. The additional delay between this model and the experimental data is likely due to digital control and the zero-order hold of the D/A converter, and is thus well-modeled by a pure time delay. We model a time delay of T_d seconds using a second order Pade approximation,

$$e^{-T_d s} \approx \frac{\left(\frac{T_d^2}{12}\right) s^2 - (\frac{T_d}{2})s + 1}{\left(\frac{T_d^2}{12}\right) s^2 + (\frac{T_d}{2})s + 1}. \tag{8.14}$$

We choose the time delay, $T_d = 160$ μs, so that the model's phase matches the measured phase. This delay is reasonable given our digital sampling time of $T_s =$

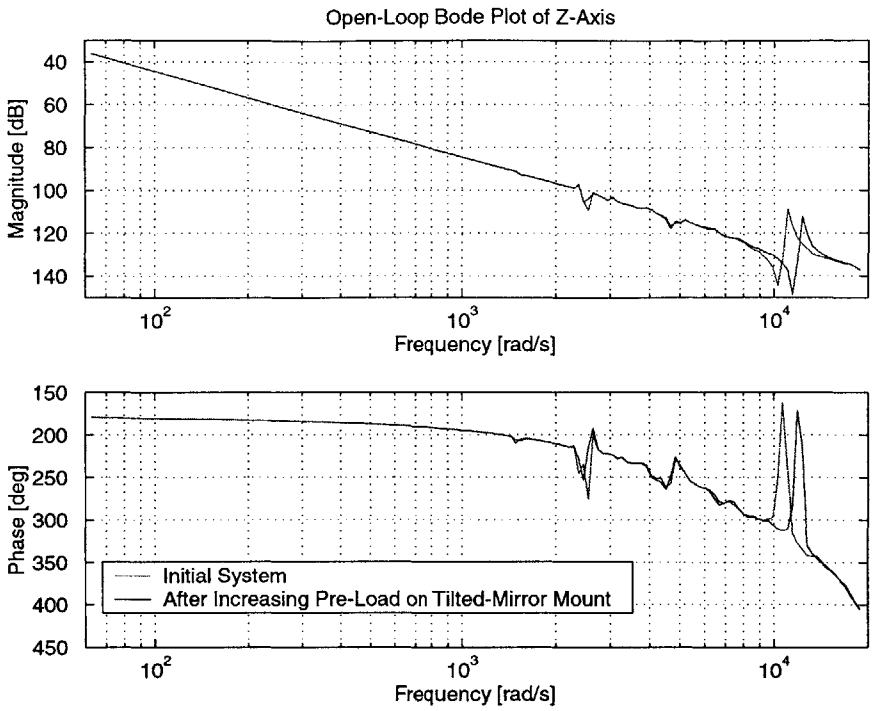

Figure 8-16: Measured linear axis open-loop Bode plots (from control effort, u, to position, z). Increasing the pre-load on the the tilted-mirror mount (shown in Figure 8-15 increases the resonant frequency.

100 μs: the delay between actuation and sensing is approximately T_s, due to the nearly 100% loading of the control processor at this sampling rate, and the delay due to the zero-order hold is $T_s/2$. There also may be some additional unmodeled phase delay in the sensor and actuator. Our final model, shown in blue in Figure 8-17, agrees very well with the experimental data.

8.2.2 Control Design

The linear axis plant is a double integrator except for the high-frequency resonance. We stabilize this plant in the standard way with a lead compensator to add phase around our desired cross-over frequency of 95 Hz. Our lead compensation term is

$$\frac{\frac{1}{220}s + 1}{\frac{1}{2200}s + 1}. \tag{8.15}$$

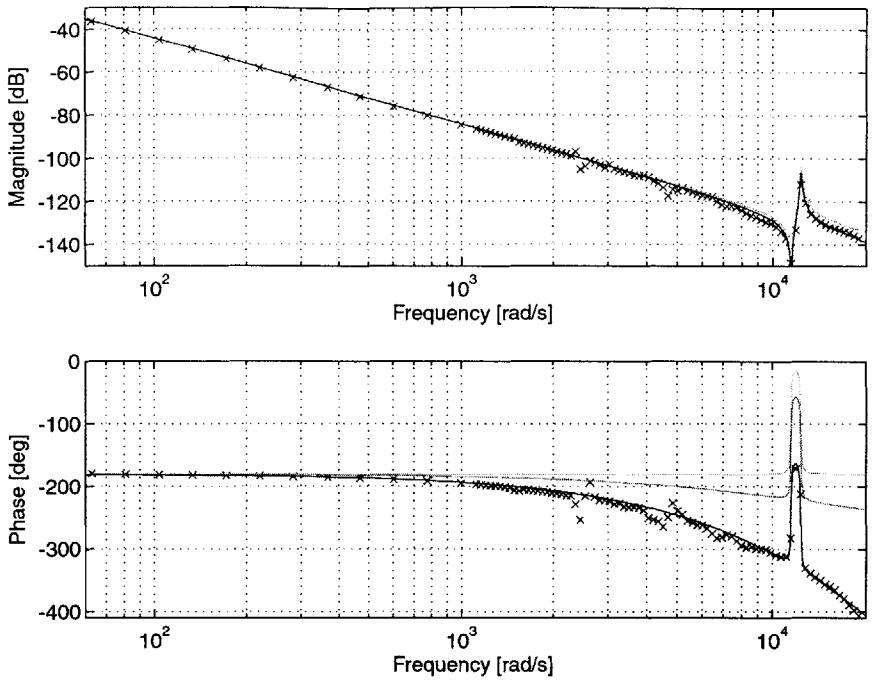

Figure 8-17: Linear axis open-loop Bode plot (from control effort, u, to position, z). The experimental measurement is shown with red x's, and the final model is shown in blue. The final model is based on an initial model with a collocated resonance shown in cyan. When the power amplifier dynamics are added, the model appears as shown in green. When a time delay due to the digital control is added, the final model in blue is obtained.

Since zeros in the forward path become zeros of the closed-loop system, if we put the lead compensation in the forward path, we will have a closed-loop zero at $s = 220$ rad/s. Since poles in the feedback path become zeros of the closed-loop system, if we put the lead compensation in the feedback path, we will have a closed-loop zero at $s = 2200$ rad/s. Thus, it is desirable to put the lead compensation in the feedback path so that the closed-loop zero is at a higher frequency and therefore does not cause as much overshoot and over-actuation in the closed-loop step response. We also add a lag compensator to increase low-frequency stiffness,

$$\frac{s+40}{40s} = \frac{1}{40} + \frac{1}{s}. \tag{8.16}$$

We implement the lag compensation in a parallel structure as given in the expression

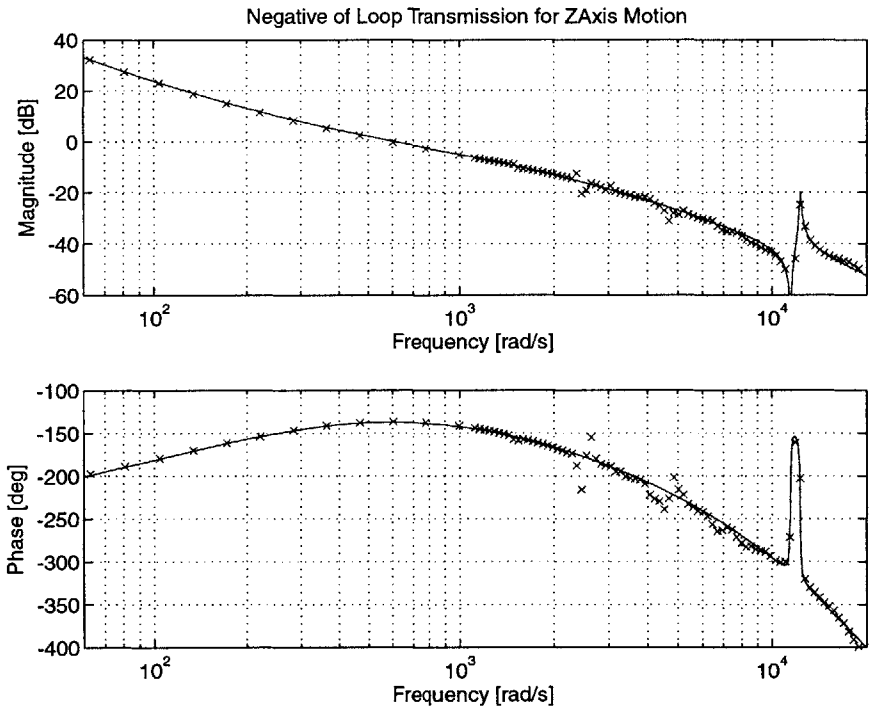

Figure 8-18: Linear axis negative loop transmission Bode plot. Red x's indicate measured data. Blue line is modeled response.

on the right above with the integrator separated so that we can implement anti-windup on this integrator. The gain required to achieve a cross-over of 95 Hz, or 597 rad/s, is 57,753. Figure 8-18 shows the Bode plot of the negative of the loop transmission for the linear axis with the lead-lag compensation included.

8.2.3 Performance

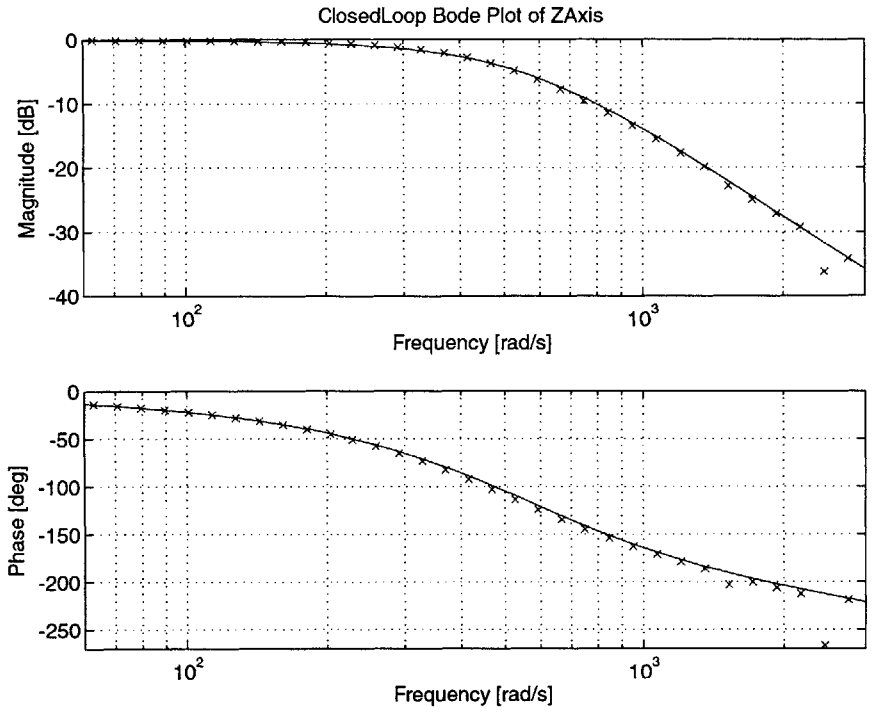

Figure 8-19: Linear axis closed-loop Bode plot.

Figure 8-19 shows the measured linear axis closed-loop Bode plot. It has a bandwidth of 70 Hz, or 440 rad/s, and agrees well with the model Bode plot. The measured linear axis step response for a 20 μm step is shown in Figure 8-20. It agrees well with the step response predicted by the model. The linear-axis closed-loop positioning noise is shown in Figure 8-21. The z-θ axis has 2.5 nm rms positioning noise over the 1/4 second time interval shown in the figure. This extremely low noise level is obtained since we are controlling a very simple, easily-modeled mechanical system mounted in air bearings with a high bandwidth controller. In addition, the laser in-

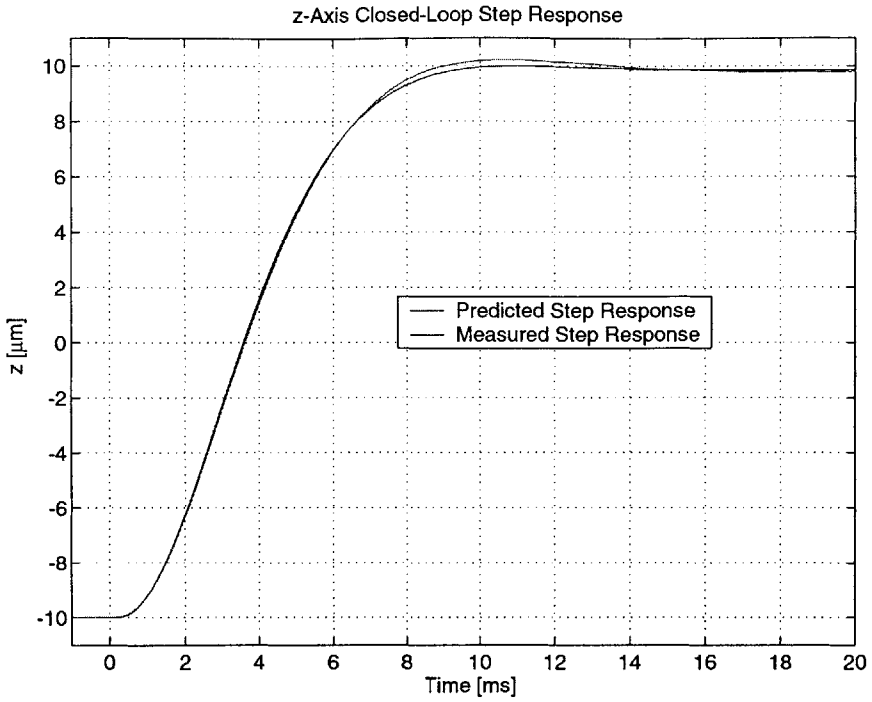

Figure 8-20: Linear axis step response.

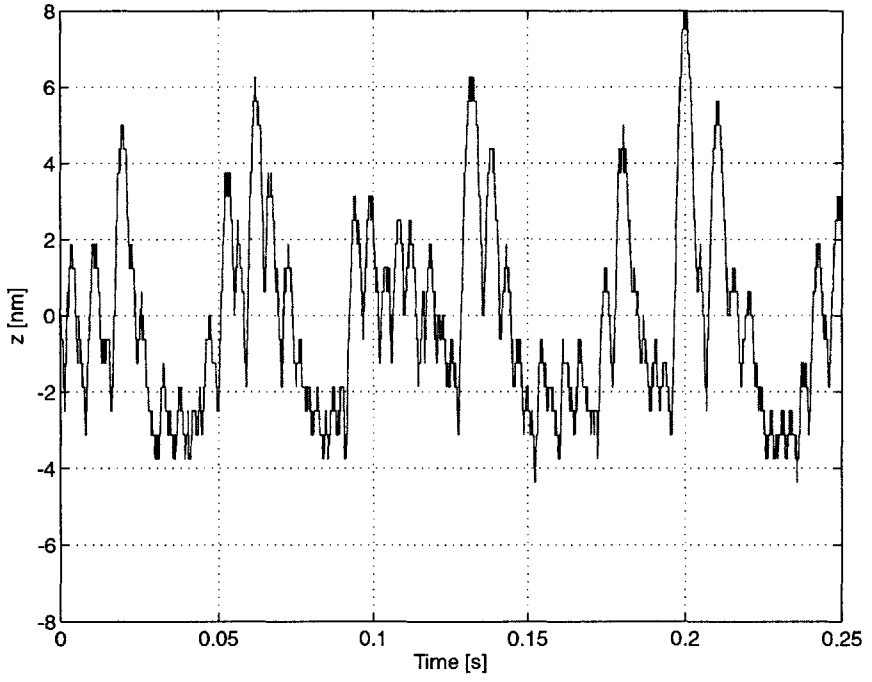

Figure 8-21: Linear axis closed-loop positioning noise of 2.5 nm rms.

terferometer measurement beam path length is very short, and thus our disturbances are minimized. Finally, the experiment is supported on an air table which attenuates floor vibrations.

8.3 Rotary Axis Compensator Design

The rotary axis controller is more difficult to design than the linear axis controller. This is because some low frequency bending mode vibrations of the shaft couple to the rotary motion and appear in the open-loop Bode plot of the rotary axis. The two lowest resonant frequencies are caused by cantilever resonances of the large tilted-mirror and the small z mirror. However, even with these resonances present we are able to obtain a 40 Hz closed-loop bandwidth. Future generations of rotary-linear axes will likely replace the tilted-mirror sensor and small z mirror sensor by a sensor of negligible mass and inertia such as a 2-D encoder. Thus, future rotary-linear axes should be able to achieve significantly higher rotary axis bandwidths.

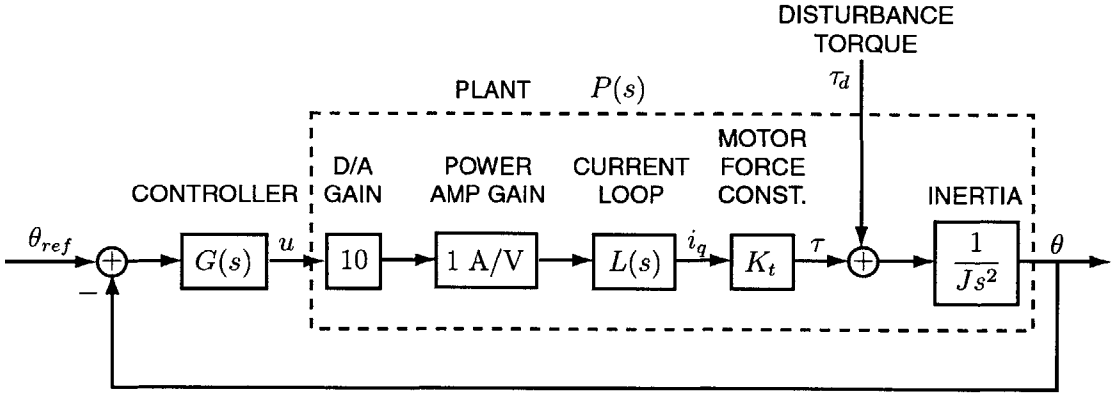

Figure 8-22: Rotary axis control block diagram.

Figure 8-22 shows the initial control block diagram for the rotary axis. It is similar to the linear axis control block diagram shown in Figure 8-10. The controller $G(s)$ provides a control effort, u, based on the error between the reference angle, θ_{ref}, and the measured angle, θ, of the axis. This control effort becomes a reference current for the inner analog current control loop discussed in section 8.1 and shown

in Figure 8-1. The 1.75 kHz bandwidth of the current loop is much higher than the 40 Hz bandwidth of the outer rotary position loop. Thus, the current loop's closed-loop transfer function, $L(s)$, is approximately unity in the frequency range of interest for the position loop. The control effort, u, proportionally commands the the q-axis current, i_q. The rotary motor produces a torque, $\tau = K_t i_q$, proportional to the q-axis current, i_q, where the proportionality constant, K_t, is the motor's torque constant as presented in more detail in section 7.5.4. This torque and any external disturbance torque, τ_d, are applied to the shaft which we intially model as a pure inertia, $1/(Js^2)$. Like the linear motor, the rotary motor is a 3-phase brushless motor, but for the purposes of controller design we can omit the dq transformations for motor commutation.

8.3.1 Modeling

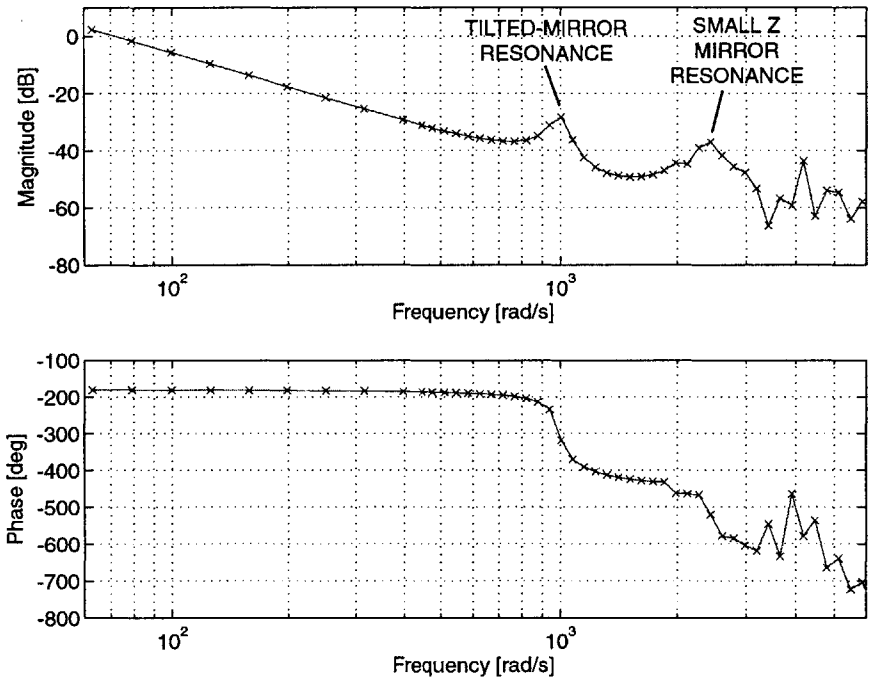

Figure 8-23: Measured rotary axis open-loop Bode plot (from control effort, u, to angle, θ).

The measured rotary axis open-loop Bode plot $P(s)$ is shown in Figure 8-23. In

the figure we identify the two lowest rotary axis resonances as cantilever vibrations of the large tilted-mirror and small z mirror on the shaft. In this section, we look at the tests and calculations that let us identify the causes of these observed resonances. In the following section we show how we compensate this system to achieve as high a closed-loop bandwidth as possible, and in the final section we look at the closed-loop performance.

Perhaps the most reliable way to identify a mechanical resonance is to drive the system at that frequency and use some sort of probe to determine the shape of the associated modes. In the simplest case, a handheld stylus or even a screwdriver allows one to directly feel the amplitude of motion. At the resonant frequency, the vibration has a relatively large amplitude and so is easy to observe. The use of a probe enhances one's sense of touch, and enables detection of even small vibrations. We used this method to help identify our resonances. When the system is driven in rotation with a 1000 rad/s sinusoid, the tilted-mirror sensor mount vibrates with the greatest amplitude. When the system is driven in rotation with a 2,513 rad/s sinusoid, the small z mirror sensor mount vibrates with the greatest amplitude.

We also find that the amplitude of vibration of the small z mirror sensor resonance changes as the shaft is translated. This lends credence to the claim that this is a cantilever resonance since we expect the cantilever resonant frequency to depend critically on the shaft length. It is harder to observe a change in vibration amplitude of the tilted-mirror resonance as the shaft translates because the 1 inch shaft travel does not change the length of the reduced diameter shaft that mostly causes the vibration. As shown in Figure 6-5, the rotary motor shoulder has half the diameter of the main part of the shaft. Thus, most of the bending flexibility occurs in this section of the shaft so that changing the length of the thicker part of the shaft does not affect the resonant frequency much.

Initially, the low-frequency resonance attributed to the tilted-mirror occurred at a frequency of 628 rad/s. At this time, the air bearings sat in O-rings in their pillowblocks as described in section 6.1. In an attempt to increase the frequency of this resonance, we potted the air bearings in a low-expansion replicating epoxy. This

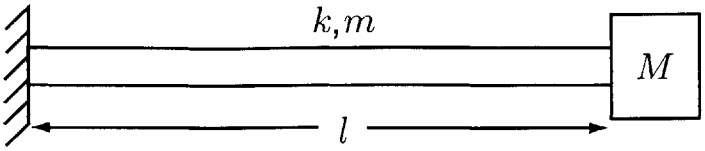

Figure 8-24: Cantilever beam with distributed mass, m, stiffness, k, length, l, and lumped mass, M.

operation increased the resonant frequency from 628 rad/s to 1000 rad/s. Initially, the cantilever beam vibration had the lower frequency of 628 rad/s since its support had some flexibility due to the O-rings. After potting the bearing in epoxy, the shaft support is stiffer, and the overall vibration frequency increases.

We now calculate the approximate bending frequency for the tilted-mirror resonance and see that it is roughly the same as the observed resonant frequency. A built-in cantilever beam with distributed beam mass, m, stiffness, k, and lumped mass, M, on its end has a vibration frequency of

$$\omega = \sqrt{\frac{k}{M + 0.23m}} \tag{8.17}$$

as given by Den Hartog [22]. Here, the beam stiffness is

$$k = \frac{3EI}{l^3}, \tag{8.18}$$

where E is the modulus of elasticity of the beam, I is its cross-sectional moment of inertia, and l is its length. For a 0.75 inch diameter steel beam with $E = 190$ GPa, we obtain a flexural rigidity of

$$EI = 1228 \text{ N} \cdot \text{m}^2. \tag{8.19}$$

In our calculation, we use a beam length approximately equal to the distance from the center of the two air bearings to the center of the tilted-mirror, $l = 21.3$ cm (8.4 inches).

This length of shaft has a bending stiffness of

$$k = 0.38 \text{ N}/\mu\text{m}. \tag{8.20}$$

We let the distributed shaft mass, m, be the sum of the shaft mass plus the mass of the linear motor magnets, $m = 0.71$ kg, and the lumped mass to be the mass of the tilted-mirror and mount, $M = 0.23$ kg. Using equation (8.17) we obtain an approximate bending mode frequency of

$$\omega = 980 \; rad/s. \tag{8.21}$$

This result agrees well with our observed resonance at 1,000 rad/s. Given the uncertainty in choosing the appropriate shaft length, l, for this calculation, this agreement is better than can be expected. This calculation mainly serves to confirm that such a cantilever resonance would have a frequency in the same range as the observed frequency.

8.3.2 Control Design

In this section we describe the design of the rotary axis compensation. Our ultimate design achieves a 30 Hz cross-over frequency and a 40 Hz bandwidth. The resonance at 1000 rad/s limits our achievable bandwidth. We use a lead-lag controller just as in the compensation of the linear axis. However, we also add another pole to reduce the magnitude of high frequency resonances and to add negative phase for phase stabilization [21] of the 1000 rad/s resonance.

At one point during the design of the rotary axis, we achieved a high 70 Hz closed-loop bandwidth controller by phase stabilizing the first resonant frequency at 1000 rad/s. Unfortunately, we discovered that the axis was unstable in some angle ranges of the rotary-linear axis although it was stable for most angles. We discovered that the resonance changes from a non-collocated resonance to a collocated resonance at different angles. Figure 8-25 shows this difference in Bode plots of the negative

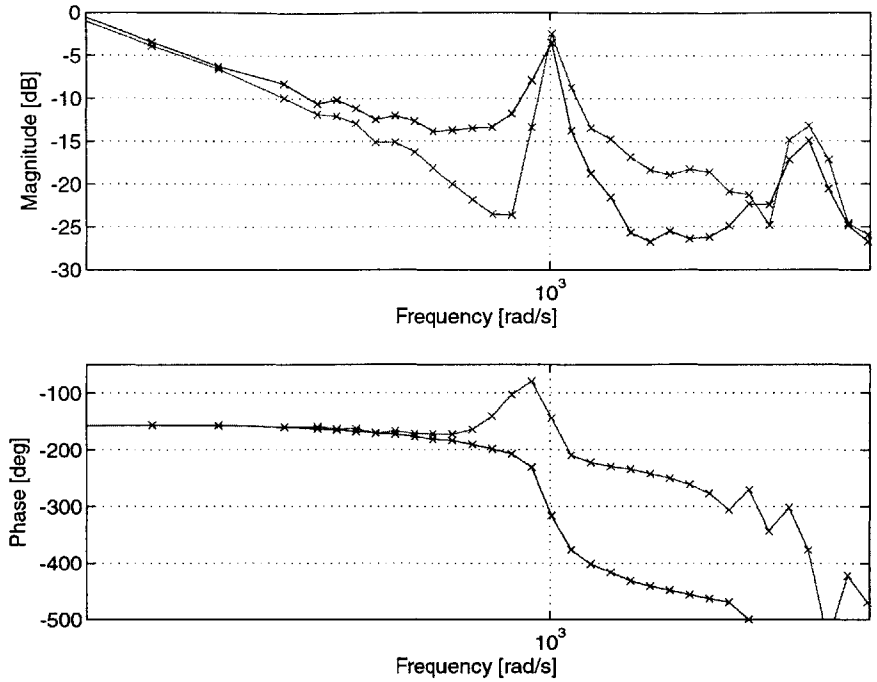

Figure 8-25: Measured rotary axis negative loop transmission Bode plots. The resonance at 1000 rad/s is non-collocated when measured at small angles around a shaft angle at $\theta = 0$ rad but is collocated when measured around $\theta = -5\pi/4$.

loop transmission taken at two different angles. At $\theta = 0$ the resonance is collocated but at $\theta = -5\pi/4$ the resonance is non-collocated. Thus, we cannot reliably phase stabilize the resonance since the phase changes as a function of rotation angle. We must instead reduce the amplitude of this resonance so that it is below 0 dB, and this constraint can only be met by reducing the control bandwidth.

We explain the behavior shown in Figure 8-25 as follows: the cantilever resonance of the beam vibrates the tilted-mirror in a vertical plane and thus affects the calculated shaft rotation angle. Since the tilted-mirror is attached to the shaft, its orientation changes with the shaft, but the cantilever resonance always shakes the mirror in the vertical plane. Thus, it is plausible that the sensor's phase will depend on shaft rotation angle for rotational frequencies near this resonance.

Our final rotary axis controller uses a lead-lag compensator and an additional pole. The lead compensator provides additional phase at the 30 Hz (188 rad/s) crossover

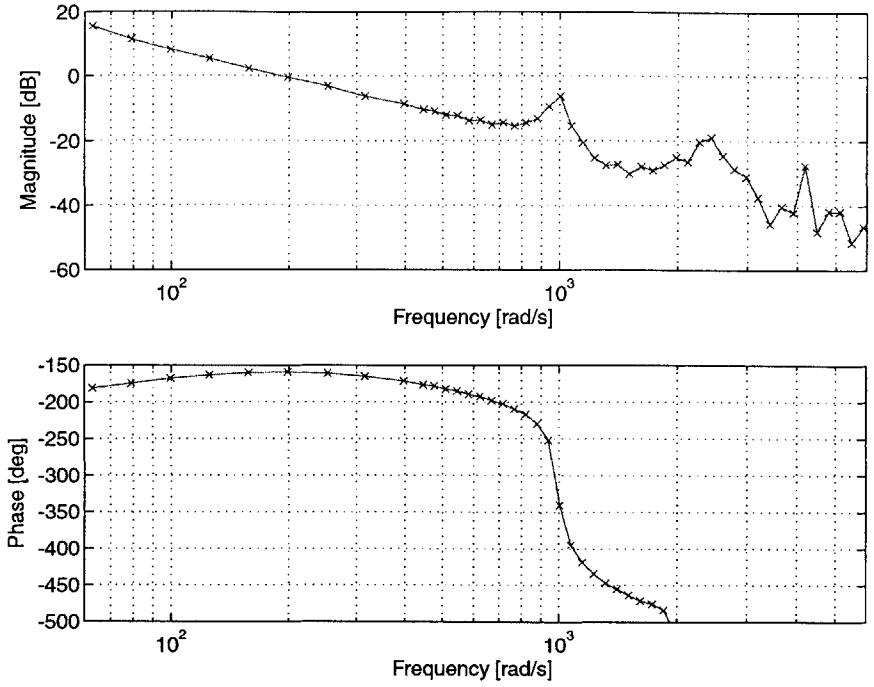

Figure 8-26: Measured rotary axis negative loop transmission Bode plot.

frequency. We use a small lead ratio, $\alpha = 4.5$, to limit the amplification of the 1000 rad/s resonance. We use a lag or PI compensator with a pole at the origin and a zero at 27 rad/s. The zero frequency is a factor of 7 below crossover so that we don't lose too much phase at crossover. We use an additional pole to reduce the magnitude of high frequency resonances. We place this pole at 1257 rad/s. This location is high enough compared to crossover that it does not reduce the phase margin much, but it is low enough compared to the high frequency resonances to provide some attenuation. In its final location, it does not reduce the magnitude of the 1,000 rad/s resonance much, but we did use this pole to provide phase stabilization in earlier controller designs. The final loop transmission Bode plot including the compensator is shown in Figure 8-26. The final compensator includes the gain, lead compensation, lag compensation, and pole,

$$G(s) = 3.5 \left(\frac{\frac{1}{100}s + 1}{\frac{1}{450}s + 1} \right) \left(\frac{s + 27}{s} \right) \left(\frac{1}{\frac{1}{1257}s + 1} \right). \tag{8.22}$$

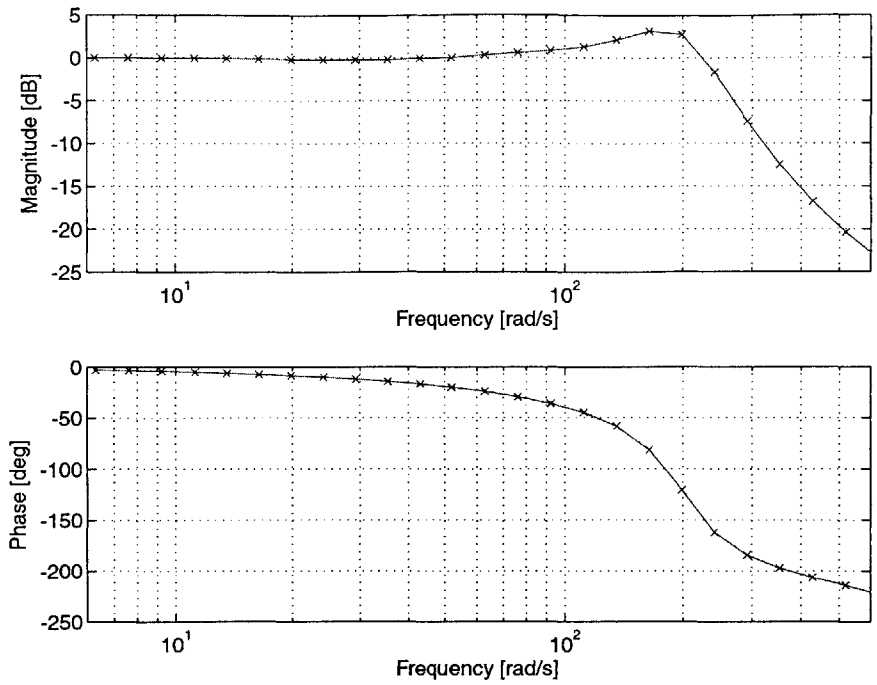

Figure 8-27: Measured rotary axis closed-loop Bode plot.

8.3.3 Performance

The rotary axis closed-loop Bode plot is shown in Figure 8-27. From this Bode plot, we see that the rotary axis has a closed-loop bandwidth of 40 Hz (250 rad/s). The step response is shown in Figure 8-28. We compare the step responses obtained when the lead compensation term is located in the feedforward and in the feedback paths. When the lead is placed in the feedback path, the overshoot is reduced since the system closed-loop zero due to the lead compensation is at a higher frequency. The rotary axis closed-loop positioning noise is shown in Figure 8-29. The z-θ axis has 3.1 μrad rms positioning noise over the 1/4 second time interval shown in the figure. This is an extremely low noise level. It corresponds to 31 nm rms positioning noise at a 1 cm radius. While acceptable for our design goals, this noise is ten times larger than that due to the linear axis.

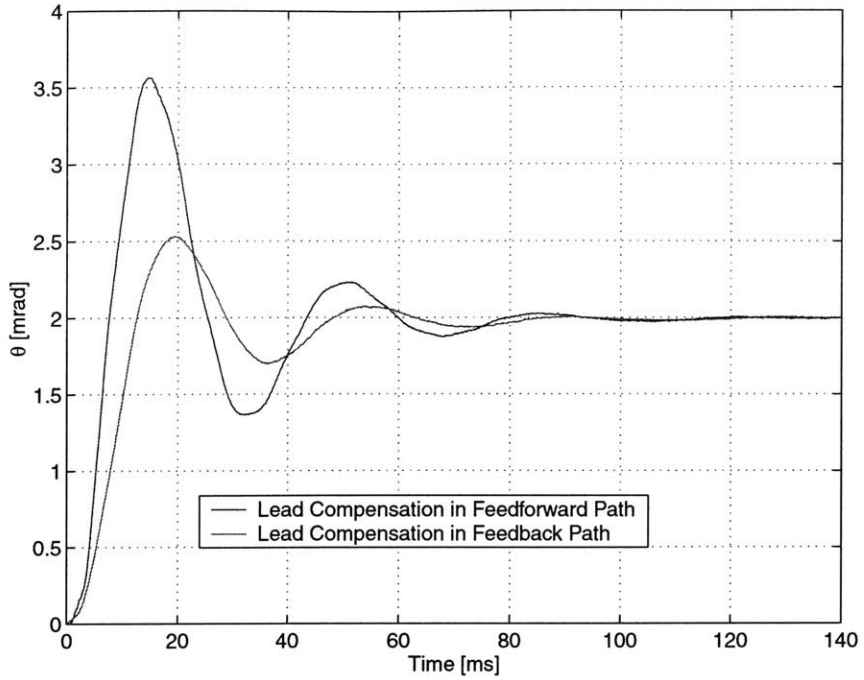

Figure 8-28: Measured rotary axis step response. Placing the lead compensation in the feedback path reduces the overshoot.

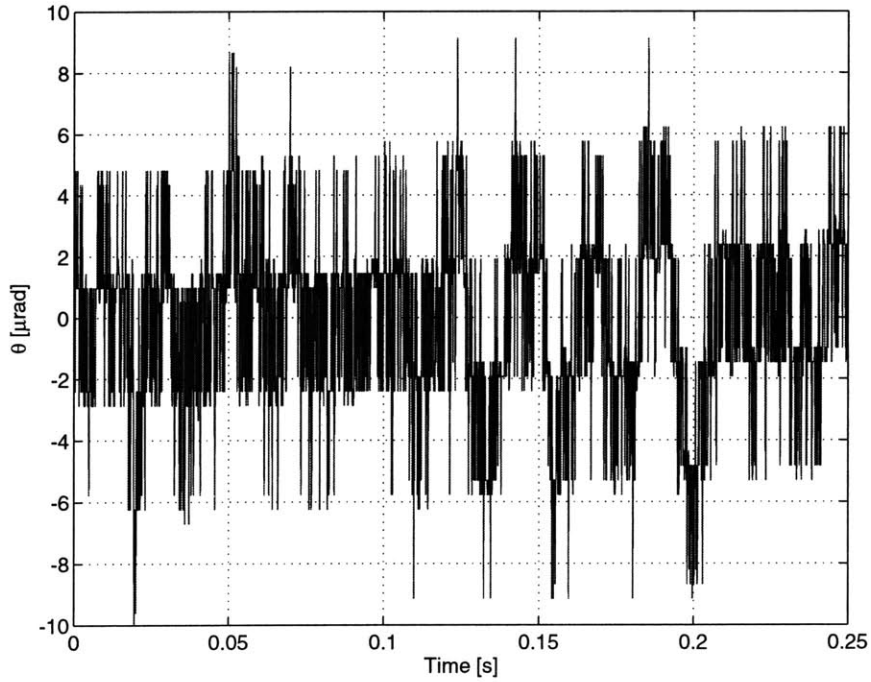

Figure 8-29: Rotary axis closed-loop positioning noise of 3.1 μrad rms.

8.4 Dynamic Stiffness

The rotary-linear axis has no inherent stiffness in its rotary and linear axes. The mass and rotary inertia of the axis provide stiffness at very high frequencies. In order to maximize linear and rotary accelerations, however, we have minimized these inertias thus reducing the stiffnesses they can provide. Low frequency stiffness must come from the closed-loop control system. In this section we first estimate the required dynamic stiffness for an example machining operation of grinding a ceramic centimeter-scale part. Then, we look at a model for our prototype axis's dynamic stiffness. We find that our linear and rotary axes need significantly higher bandwidths to achieve the required level of dynamic stiffness in this machining operation.

8.4.1 Dynamic Stiffness Required for Grinding

In this section we estimate the dynamic stiffness required for grinding a ceramic centimeter-scale part. Typical grinding wheels with thicknesses of 50 mm use 20 kW spindles. Since the spindle power P required is proportional to the width of the cut, a grinding wheel with a 1 mm thickness would require 1/50 this power, $P = 400$ W. To attain good surface finishes in ceramic, a diamond grinding wheel needs a surface speed of approximately v =30 m/s. Spindle power P is equal to the surface speed v times the cutting force F_c,

$$P = F_c v. \tag{8.23}$$

Thus, we require a cutting force of $F_c = 13.3$ N which acts tangentially to the part. According to *Modern Grinding Process Technology* [58], the normal grinding force F_n that presses the wheel into the workpiece is roughly 20 times the tangential cutting force F_c for ceramic. Thus, the normal grinding force is $F_n = 266$ N. If this were a constant force, the integral control could compensate for it and provide infinite stiffness. In fact, however, the normal force has an oscillating component that is about 20% of this value [58]. It is this dynamic component of force of about 53 N that can cause undesirable deflections in the system. For grinding a tooth, we need about 20 μm of shape accuracy. If we allow deflections due to the oscillating component of

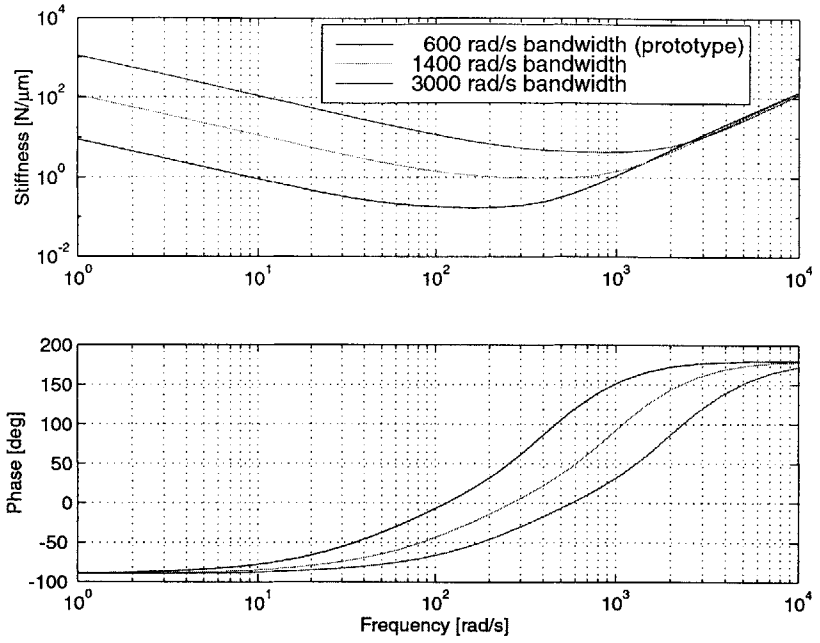

Figure 8-30: Model of linear axis dynamic stiffness for our prototype axis at different closed-loop control bandwidths. The controller we implemented has a closed-loop bandwidth of 600 rad/s.

the normal grinding force to account for 1/10 of our total error budget, we find that we need a dynamic stiffness of 27 N/μm.

Our proposed 5-axis grinding machine topology (Figure 2-13) allows the spindle to cut a centimeter-scale part from many different orientations. It is therefore possible that the normal grinding force could be aligned with the linear axis or the rotary axis of the rotary-linear axis carrying the part. Thus, the linear axis requires a dynamic stiffness of 27 N/μm, and the rotary axis requires the same stiffness at a 1 cm radius.

8.4.2 System Dynamic Stiffness Model

We use our initial plant models to study the dynamic stiffnesses of the two axes of the rotary-linear axis. Our initial linear axis plant model considers the shaft to be a pure mass, and our initial rotary axis plant model considers the shaft to be a pure inertia. The controllers we use to study dynamic stiffness are similar to the actual controllers we implemented. They use lead compensation with a lead ratio of 10 centered on the

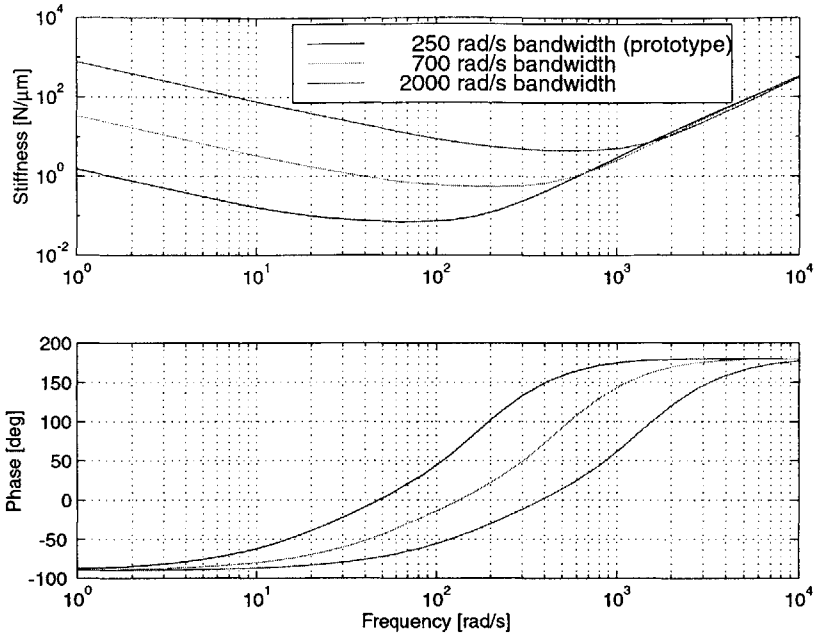

Figure 8-31: Model of rotary axis dynamic stiffness at a 1 cm radius for our prototype axis at different closed-loop control bandwidths. The controller we implemented has a closed-loop bandwidth of 250 rad/s.

crossover frequency, and a proportional-integral controller with a zero located at a frequency which is a factor of 10 below the crossover frequency.

The linear axis dynamic stiffness is the inverse of the transfer function from disturbance force f_d to linear displacement z in the block diagram shown in Figure 8-10. The linear axis dynamic stiffness is shown in Figure 8-30 for controllers $G(s)$ designed for three different closed-loop bandwidths. The controller designed for 600 rad/s models our implemented control system. The low frequency stiffness is provided by the integral term in our controller. At zero frequency, we have infinite stiffness. Without the integral control, our low frequency stiffness would be constant. The mass provides high frequency stiffness. We can increase the high frequency stiffness by increasing the system mass, but this is undesirable since it then reduces achievable accelerations.

The model for the system with our implemented linear controller has a minimum linear axis stiffness of about 0.2 N/μm. This is significantly less than our desired value of 27 N/μm. As shown in Figure 8-30, it is possible to improve the system

dynamic stiffness by increasing the closed-loop bandwidth. As shown in Figure 8-17 our linear axis plant has its first resonant frequency at 11,020 rad/s. Since this resonance is due to flexibility in the tilted-mirror mount, it will disappear when a different sensor is used in place of the tilted-mirror sensor in future prototypes. Thus, it should be possible to increase the linear axis closed-loop bandwidth greatly. In our system, minimum closed-loop bandwidth is proportional to the square root of dynamic stiffness, $\omega = \sqrt{k/m}$, where ω is the closed-loop bandwidth, k is the dynamic stiffness, and m is the mass. Thus, to obtain our target stiffness, we need a bandwidth of

$$(600 \text{ rad/s})\sqrt{\frac{27}{0.2}} = 6970 \text{ rad/s}. \tag{8.24}$$

This is a high closed-loop bandwidth but should be achievable in future prototype axes.

The rotary axis dynamic stiffness is the inverse of the transfer function from disturbance torque τ_d to angular displacement θ in the block diagram shown in Figure 8-22. In order to convert this angular stiffness to an effective linear stiffness at a radius R, we multiply the angular stiffness by a factor of $1/R^2$. One factor of R converts torque to force, and another factor of R converts angular displacement to linear displacement. Figure 8-31 shows the effective linear stiffness of the rotary axis at a 1 cm radius. The controller designed for 250 rad/s models our implemented rotary axis control system. This model has a minimum dynamic stiffness of 0.06 N/μm (at a 1 cm radius). We would need a closed-loop bandwidth of approximately

$$(250 \text{ rad/s})\sqrt{\frac{27}{0.06}} = 5300 \text{ rad/s}. \tag{8.25}$$

This approximation includes the large inertia of the tilted-mirror sensor which dominates the rotary axis dynamics. Without this sensor, the axis would have approximately 1/4 the rotary inertia, and we would require twice the closed-loop bandwidth just computed, or 10,600 rad/s in the rotary axis.

The dynamic stiffness models show that our current prototype would not be able to withstand grinding disturbances from a 400 W grinding spindle. However, future

prototypes without the resonances caused by the tilted-mirror sensor could achieve much higher closed-loop bandwidths and therefore dynamic stiffnesses. It is also possible that the grinding forces are not as great as we have estimated. If the machine uses high speed grinding, the surface speeds are greater, and the cutting and normal forces are smaller.

8.5 Sensorless Operation for z-θ Spindle

Our prototype z-θ axis is primarily intended for positioning the workpiece in a small multi-axis machine tool. For this application, precision rotary and linear sensing are required. Another application for the z-θ axis is as a spindle carrying the cutting tool. In this application, the rotary axis provides spindle high speed rotation, and the linear axis provides infeed. For use as a spindle, precision rotary sensing is no longer required. However, we do need coarse rotary sensing to be able to commutate the rotary motor and deliver power to the cutting tool. It is desirable to eliminate the mass, inertia, cost, and complexity of the rotary sensor. In this section we implement a sensorless control scheme on our prototype axis to see if it is feasible for use with a z-θ spindle. The sensorless control scheme uses measurements of the motor phase currents and voltages to estimate rotation angle. In this section we first review various sensorless control schemes and then implement one, a nonlinear observer developed by Jones and Lang [29, 30], on our prototype axis. We are successfully able to run our rotary axis under closed-loop sensorless control with their observer.

8.5.1 Sensorless Control Schemes

Numerous sensorless control schemes have been developed for permanent magnet motors. Many of these schemes only work for specific types of permanent magnet motors with specific current drives. The most popular class of sensorless control schemes uses the motor's back electromotive force (EMF) to detect motor speed. If there is no current in a motor phase, the back EMF directly provides speed voltage and hence speed information. If a phase current exists, then the back EMF can

be found using the stator phase's voltage equation and a measurement of the phase voltage. This, however, requires differentiation of the current which introduces noise into the estimate. Back EMF schemes do not work at low speeds or standstill when the speed voltage is too small and at too low a frequency.

A second technique that does work at low speeds is based on variable inductance. If the rotor has saliency, as is sometimes the case with buried magnet motors, this saliency can be detected as a function of rotation angle [10]. A third technique is to use an observer to estimate the motor's parameters. The observer also provides an estimate of some measurable quantity, and the error between this estimate and an experimentally measured value provides corrective feedback. References to papers using variations of these three sensorless control schemes are provided in articles by French and Acarnley [20] and Lorenz [44].

Sensorless drives for spindles are already being sold commercially. MTS Systems Corp. [53] sells a line of modular sensorless drives for induction motors and brushless DC motors. These drives provide velocity control up to 32,000 rpm for various machine tool applications [1].

We choose to implement a nonlinear sensorless observer for permanent magnet synchronous motors developed by Jones and Lang [29, 30]. This observer operates in the dq frame and estimates direct and quadrature currents, rotor speed, and rotor angle. The estimated rotor angle is used to transform measured phase currents and voltages into the dq frame. This makes the observer nonlinear. This paper develops the observer and performs simulations but does not use the observer to control a motor. Sepe and Lang [60, 59] extends this work to control a motor based on the sensorless observer. In addition this work adaptively estimates mechanical parameters and load torque.

8.5.2 Observer Model

In this section we develop a state-space observer for our rotary permanent magnet synchronous motor. The observer works in the dq frame and estimates motor direct current, i_d, quadrature current, i_q, rotor velocity, ω, and rotor position, θ. We denote

the estimated values with carats, $\hat{i_d}$, $\hat{i_q}$, $\hat{\omega}$, and $\hat{\theta}$. We denote measured currents and voltages transformed into the dq frame with checks, $\check{i_d}$, $\check{i_q}$, $\check{v_d}$, $\check{v_q}$, following the notation of Jones and Lang [29, 30]. We also define an estimated current vector,

$$\hat{i} = \begin{bmatrix} \hat{i_d} \\ \hat{i_q} \end{bmatrix}, \tag{8.26}$$

and an estimated voltage vector,

$$\hat{v} = \begin{bmatrix} \hat{v_d} \\ \hat{i_q} \end{bmatrix}. \tag{8.27}$$

The measured currents transformed into the dq frame also form a vector,

$$\check{i} = \begin{bmatrix} \check{i_d} \\ \check{i_q} \end{bmatrix}, \tag{8.28}$$

The two state equations for the direct and quadrature currents follow directly from the terminal voltage equations (7.71) and (7.72) and the flux linkage equations (7.69) and (7.70) in the dq frame which are developed in section 7.5.2. The mechanical equation for rotor velocity follows from Newton's 2nd Law where the applied torque is given in terms of the quadrature current as in equation (7.78). The state-space observer is

$$\frac{d\hat{i}}{dt} = \begin{bmatrix} -\frac{R}{L_d} & 0 \\ 0 & -\frac{R}{L_q} \end{bmatrix} \hat{i} + p\hat{\omega} \begin{bmatrix} 0 & \frac{L_q}{L_d} \\ -\frac{L_d}{L_q} & 0 \end{bmatrix} \hat{i} \tag{8.29}$$

$$-p\lambda_f \hat{\omega} \begin{bmatrix} 0 \\ \frac{1}{L_q} \end{bmatrix} + \begin{bmatrix} \frac{1}{L_d} & 0 \\ 0 & \frac{1}{L_q} \end{bmatrix} \check{v} + G_i(\check{i} - \hat{i}) \tag{8.30}$$

$$\frac{d\hat{\omega}}{dt} = \frac{3}{2}\left(\frac{p\lambda_f}{J}\right) \hat{i}^T \begin{bmatrix} 0 \\ 1 \end{bmatrix} - \frac{B}{J}\hat{\omega} + G_\omega(\check{i} - \hat{i}) \tag{8.31}$$

$$\frac{d\hat{\theta}}{dt} = \hat{\omega}. \tag{8.32}$$

The electrical parameters of the permanent magnet synchronous motor are the phase resistance, R, the direct- and quadrature-axis inductances, L_d and L_q, the number of pole pairs, p, the permanent magnet flux linked by the stator, λ_f, and the motor torque constant, $(3/2)p\lambda_f$. The mechanical parameters of the rotor are the shaft inertia, J, and the damping constant, B. G_i is a 2×2 matrix of controller gains, and G_ω is a 1×2 matrix of controller gains.

8.5.3 Model Parameters

In this section we explain how we obtained values for the observer model parameters. Table 8.3 lists the values we use for the model parameters.

Resistance	R	6.73	Ω
Direct-Axis Inductance	L_d	1.75	mH
Quadrature-Axis Inductance	L_q	1.75	mH
Number of Pole Pairs	p	4	
Permanent Magnet Flux Linked by Stator	λ_f	0.0248	Wb (= N·m/A)
Motor Torque Constant	$\frac{3}{2}p\lambda_f$	0.149	N·m/A
Shaft Inertia	J	3.4×10^{-4}	kg·m^2
Damping Constant	B	4.0×10^{-5}	N·m/s

Table 8.3: Model parameters for sensorless observer.

Electrical Parameters

We measure the resistance R of the motor phases with a voltmeter:

$$R = 6.73\ \Omega. \tag{8.33}$$

The inductances L_d and L_q, in the dq frame, are the sum of the self-inductance L and mutual inductance M in the abc frame as developed in equations (7.62) and (7.63),

$$L_d = L_q = L + M = 1.75\ \text{mH}. \tag{8.34}$$

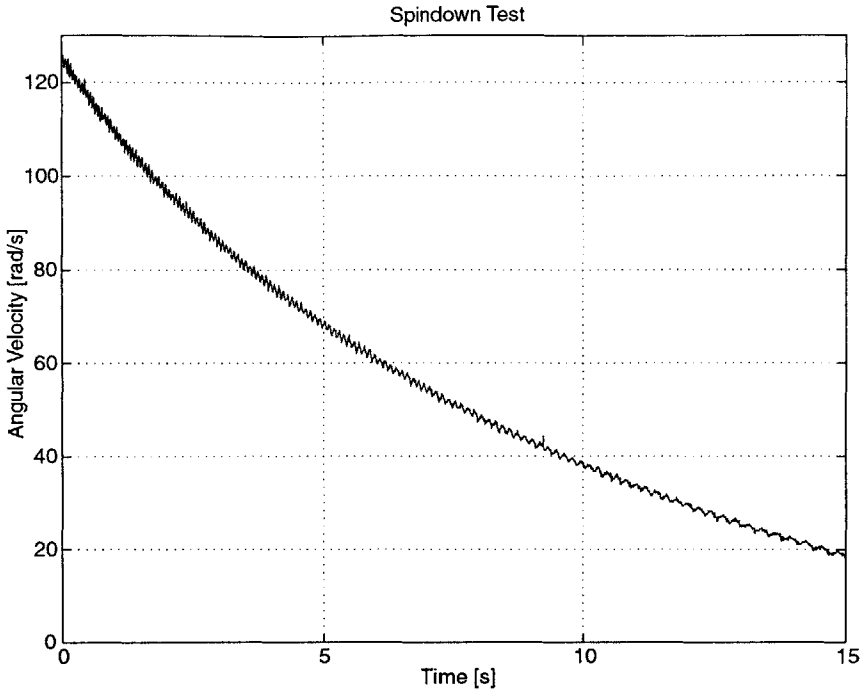

Figure 8-32: Spin-down test.

We obtain this value by measuring the inductance of two motor phases which is $2(L+M)$ with a dynamic signal analyzer as described in section (8.1.1). Our motor has

$$p = 4 \tag{8.35}$$

pole pairs, and its motor torque constant is found by measuring the back EMF as described in section 4.7,

$$K_t = \frac{3}{2} p \lambda_f = 0.149 \text{ N} \cdot \text{m/A}. \tag{8.36}$$

Mechanical Parameters

Our shaft and assembled components has a total rotary inertia of

$$J = 34 \times 10^{-5} \text{ kg} \cdot \text{m}^2. \tag{8.37}$$

We measure the damping constant, B, using a spin-down test. The dynamic equation which describes the rotor speed with only viscous damping present is

$$J\frac{d\omega}{dt} + B\omega = 0. \tag{8.38}$$

The time constant for the exponential decrease in speed is J/B. Using the first 10 second interval from the experimental data shown in Figure 8-32, we calculate that

$$B = 4.0 \times 10^{-5}\ \mathrm{N \cdot m/s}. \tag{8.39}$$

Observer Gains

With the observer gains set to zero, the observer's poles are at -6.6, $-3842 + 100i$, and $-3842 - 100i$ rad/s where we have linearized the observer about $\omega = 8\pi$ rad/s. We use pole-placement to choose the observer gains. We choose

$$G_i = \begin{bmatrix} -2000 & 100 \\ -100 & 2000 \end{bmatrix}; G_w = \begin{bmatrix} 0 & -10,000 \end{bmatrix}. \tag{8.40}$$

which results in closed-loop observer poles at -100, -1846, and -5743 rad/s.

8.5.4 Experimental Results

We first verified that our observer estimated the correct rotor velocity and angle when the motor was run under closed-loop control. We used the tilted-mirror sensor for feedback and motor commutation. We designed a 20 Hz crossover velocity control loop to run the motor at different velocities. We differentiated the tilted-mirror sensor's rotary position to obtain velocity. This introduces some noise but not that much since the tilted-mirror sensor has a high resolution of 1,366,000 counts/rev. We found that it was necessary set the observer initial states close to the physical motor states or the observer would become unstable. We zero the intial states at the same time we start the motor from rest, and the observer tracks the motor speed from standstill up to a constant speed.

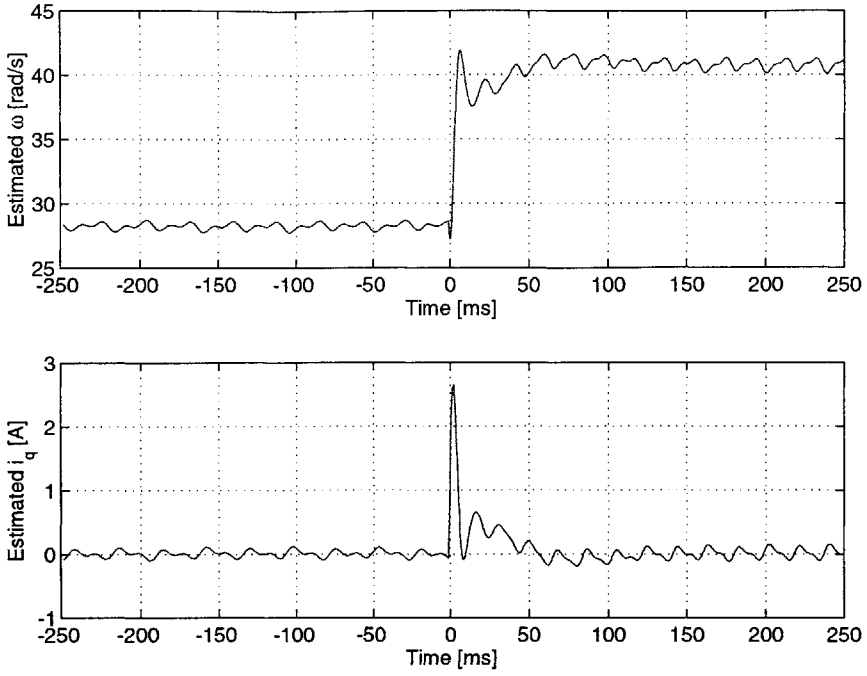

Figure 8-33: Sensorless speed control step response. Estimated speed, $\hat{\omega}$, and estimated quadrature current, $\hat{i_q}$, for a step change in reference speed from 28.27 rad/s (4.5 rev/s) to 40.84 rad/s (6.5 rev/s). The system is running under closed-loop speed control with estimated speed, $\hat{\omega}$ used as a measured signal, and estimated angle, $\hat{\theta}$, used to commutate the rotary motor.

After the observer was working, we used the estimated rotor position $\hat{\theta}$ and estimated rotor velocity $\hat{\omega}$ to implement closed-loop sensorless control. Instead of using the tilted-mirror sensor for motor commutation and velocity feedback, we use $\hat{\theta}$ and $\hat{\omega}$ respectively. Figure 8-33 shows a step response in rotor velocity to a change in reference speed from 28.27 rad/s (4.5 rev/s) to 40.84 rad/s (6.5 rev/s). The estimated quadrature current $\hat{i_q}$ is also shown. The ripple in the $\hat{\omega}$ and $\hat{i_q}$ is proportional to rotor speed.

These experimental results demonstrate that it is feasible to use a sensorless control scheme on a rotary-linear axis used as a spindle. Thus, we can eliminate the need to design and incorporate a rotary sensor in spindle applications. Since designing and integrating the rotary sensor is one of the main challenges in building rotary-linear axes, this is an extremely useful result.

8.6 Summary

The first topic of this chapter was the design of an analog power op amp current amplifier for providing current to the motor phases. We learned that we could stabilize the power op amp and eliminate its oscillation by adding a resistor R_G across the two op amp inputs. This resistor reduces the bandwidth of the minor loop feedback around the power op amp but does not affect the ideal gain of the power op amp, $(R_3 + R_4)/R_3$. Hence it improves power op amp stability but does not affect the major current amplifier PI feedback loop.

Next we modeled and controlled the linear axis. We found an initially unmodeled resonance at 11,020 rad/s and identified it as flexibility in the contact stiffness of the tilted-mirror mount. We were able to model this resonance very closely using a classic two-mass system where one mass was the tilted-mirror and the other was the rest of the axis. The linear axis closed-loop bandwidth could be made higher than our final controller design of 70 Hz since the linera axis plant is so ideal and has no low frequency resonances.

The rotary axis plant has significant low frequency resonances which limit the closed-loop bandwidth which can be obtained on our prototype axis to 40 Hz. The two main resonances are due to cantilever modes of the tilted mirror and small z mirror, respectively, on the shaft. From this we learn that we should pay particular attention to putting any significant mass at the ends of the shaft in future designs. We may also want to reduce the shaft length in future designs since these bending modes are the lowest in frequency and caused us the most trouble.

We then estimated the dynamic stiffness required in a grinding operation to be 27 N/μm. Our prototype axis has a linear axis dynamic stiffness of 0.2 N/μm and a rotary axis dynamic stiffness of 0.06 N/μm at a 1 cm radius. Thus, the current system does not have enough dynamic stiffness to withstand a grinding operation. Significant increases in closed-loop bandwidth are required to achieve the target stiffness. These may be possible with an improved shaft structure which does not have the low frequency cantilever resonances. It is also possible that the stiffness required for high

speed grinding is significantly less than the stiffness we have estimated. Nonetheless, we learned that dynamic stiffness is an important issue that needs to be addressed in future rotary-linear axes.

Finally, we showed the viability of a sensorless control scheme for spindle applications. We found that the sensorless control scheme worked well but was very sensitive to some of the model parameters. For example, a 10% change in the model rotary motor force constant would drive the estimator unstable. The main conclusion from this investigation, though, is that we can avoid using a rotary sensor in spindle applications.

In the next chapter we show how the control algorithms we developed in this chapter are implemented on a DSP to control our prototype rotary-linear axis.

Chapter 9

Control Implementation

This chapter describes the software that runs our prototype z-θ axis. Our software runs on a dSPACE 1103 DSP board (see Appendix F) that uses a 400 MHz PowerPC processor. We program this board via Matlab's Simulink and Stateflow packages. *Mastering Simulink 2* [11] is a good Simulink reference and tutorial, and the *Stateflow User's Guide* [46] is a comprehensive Stateflow reference which is available on-line at the Mathwork's website. Simulink is good for programming algebraic computations and compensation transfer functions. Stateflow provides supervisory control via finite state control; it allows the definition of system states, events, and transitions between states. Matlab's Real-Time Workshop compiles our combined graphical Simulink and Stateflow program and dSPACE supplied software takes care of hardware interfacing with the DSP. We also use dSPACE's ControlDesk software to create interactive control panels for running our prototype rotary-linear axis.

In this chapter we first present an overview of the control implementation. Next we describe the order in which we put the various pieces of the control code together. The development stages we go through are applicable to a wide range of machines with actuators and sensors, even if their controllers are implemented on a completely different system. We then describe some of the software in more detail. We look at the Stateflow controller, the closed-loop compensators, motor control, sensor processing, the automatic calibration routine, and sensorless processing.

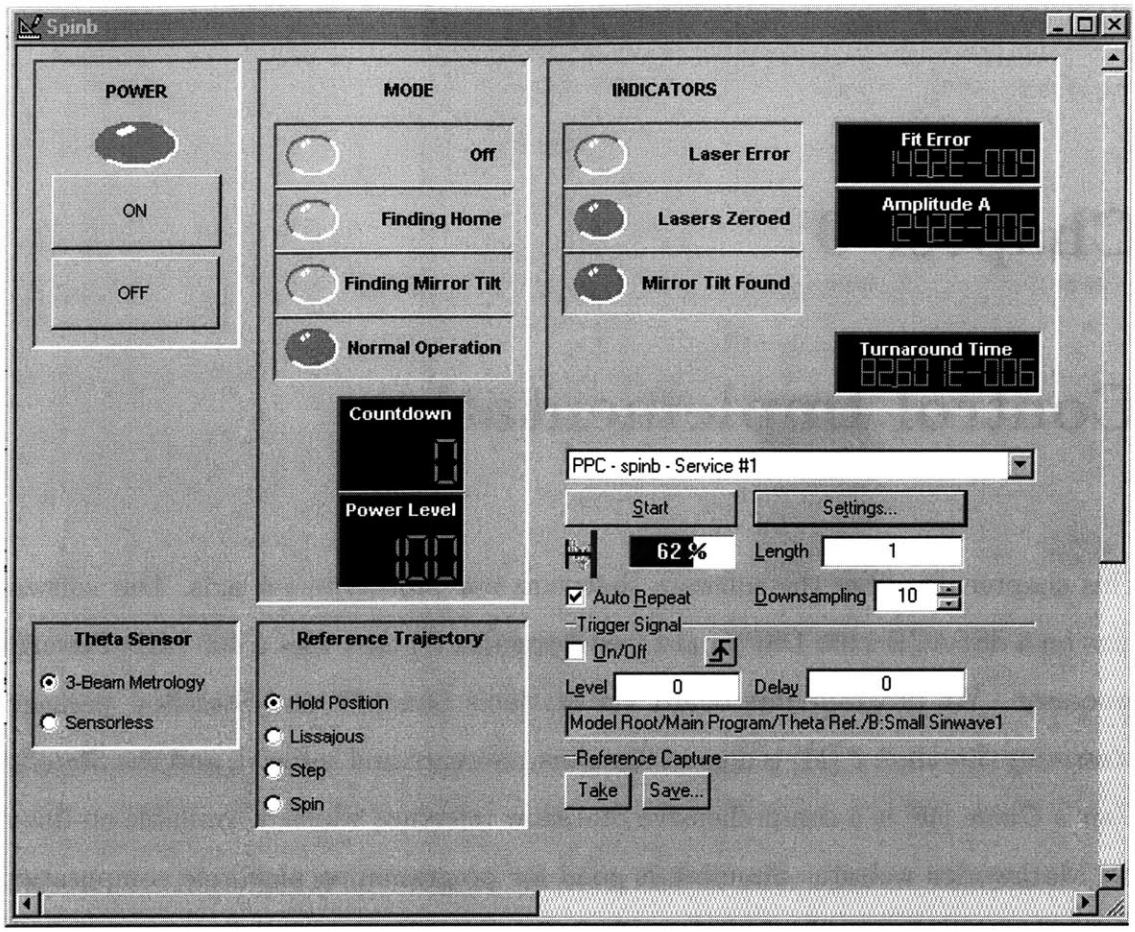

Figure 9-1: Main control panel.

9.1 Overview

The main control panel for operating the prototype rotary-linear axis is shown in Figure 9-1. The control panel is created in the dSPACE ControlDesk environment. In the upper-left is a power on-off switch and associated LED. To the right of the power switch are a set of LED's that indicate the current machine mode, *Off*, *Finding Home*, *Finding Mirror Tilt*, and *Normal Operation*. The states *Finding Home* and *Finding Mirror Tilt* correspond to homing the motor phases and automatically determining the mirror's tilt angle. The machine always goes through these modes before reaching *Normal Operation*. On the right are several indicators. If a laser error occurs, the *Laser Error* LED lights up and the machine goes to the *Off* mode. After the *Finding*

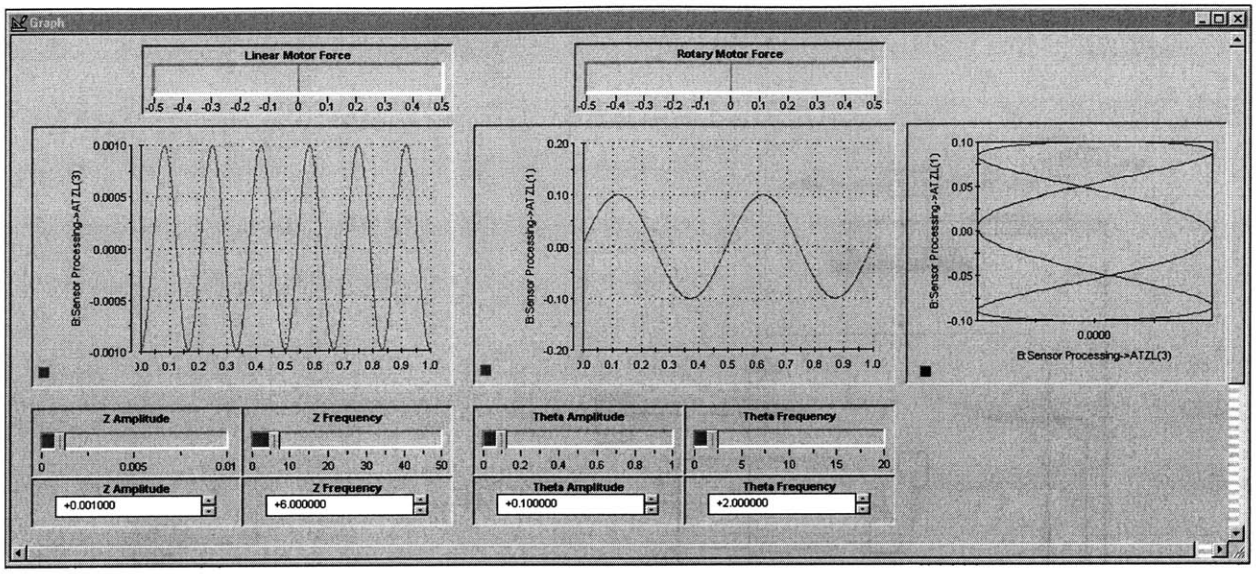

Figure 9-2: Control panel which allows control of sinusoidal motion in both z and θ.

Home mode is complete, the *Lasers Zeroed* indicator turns green. The *Mirror Tilt Found* indicator turns green when the mirror tilt has been determined by the *Finding Mirror Tilt* mode.

We can choose various reference trajectories. *Hold Position* holds both z and θ constant, *Lissajous* drives both z and θ with sinusoids, *Step* is used to obtain step responses, and *Spin* spins the axis while its z position is held constant. The main control panel also allows a choice of θ sensor: standard 3-beam metrology using the tilted-mirror sensor or sensorless operation. z and θ are plotted as functions of time in the *Graph* ControlDesk panel shown in Figure 9-2. Here we see the stage is running with a *Lissajous* reference trajectory. We can control the amplitudes and frequencies of the z and θ sinusoids independently. The bar charts on top show the control effort exerted by the two motors.

The top level combined Simulink and Stateflow program (named *spinb*) that runs the rotary-linear axis is shown in Figure 9-3. The stateflow block is called "states" and has rounded corners. It provides the supervisory control and determines what mode the axis is in. The output variable, *operation_mode*, carries this mode information to a mulitport switch. The dq currents for both motors corresponding to the

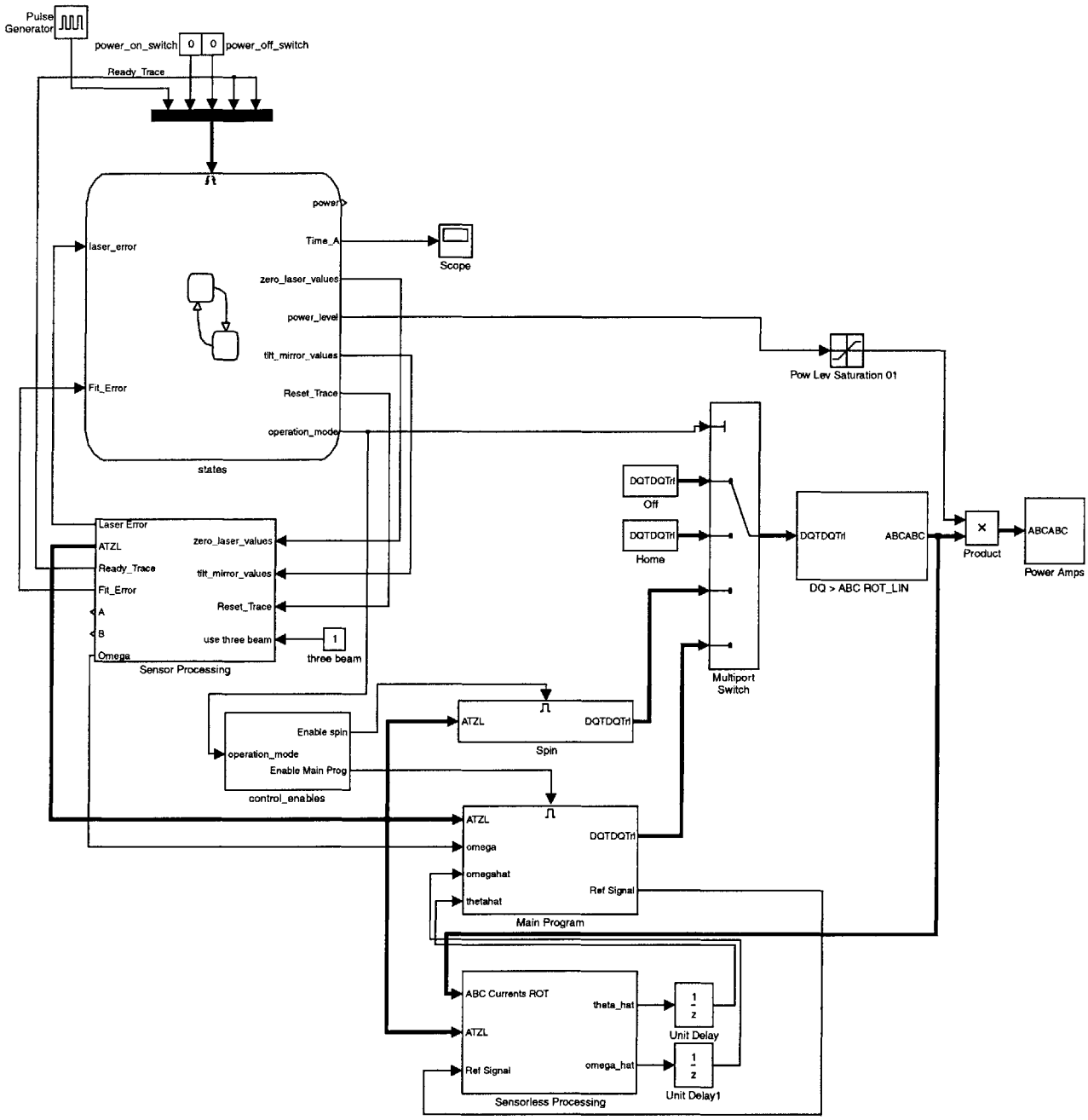

Figure 9-3: Top level of the combined Simulink & Stateflow program which controls the prototype z-θ axis.

current operation mode are passed through this multiport switch. They are then converted to *abc* phase currents and sent to the power amplifiers. The *Sensor Processing* subsystem's main function is to output a vector labeled *ATZL* which has the current shaft angle (A), the rotary motor electrical angle (T), the linear position (Z), and the linear motor electrical angle (L). This position information is fed to the *Main Program* subsystem which has the rotary and linear compensators in it. The *Sensorless Processing* subsystem provides estimates of rotary electrical angle, *theta_hat*, and shaft speed, *omega_hat*, which can be used to control the motor in the *Main Program* subsystem. Next we look at how this complex system can be developed one piece at a time.

9.2 Development Stages

Developing a complex controller like the one shown in Figure 9-3 may seem to be a daunting task, but it can readily be built up in simple stages. This section describes just one possible ordering that makes sense; there are certainly alternative development strategies. Often, for example, it makes sense to start controlling whatever hardware one receives first.

9.2.1 Homing Motor

As a first step, we connect the D/A channels on the dSPACE 1103 board to our power amplifiers. We command a constant current in one of the three phases in each motor and check that the motors respond by oscillating about fixed home positions.

9.2.2 Commutating Motor

The next step is to implement the *dq* transformations, or motor commutation laws, described in sections 7.4.2 and 7.4.3. These transformations require a measurement of motor electrical angle so any sensor processing needs to be done as well. It is possible to intially commutate the motor "open-loop" by specifying the electrical angle if the

sensor is not yet available.

With sensing of electrical angle, a constant quadrature current should provide a constant force or torque in one direction. If the force or torque is not constant the signs of the motor phases should be checked, and also the calculation of electrical angle might be wrong. It is essential to solve all these problems here so that smooth force and torque are obtained before closing the loop around the motors.

9.2.3 Sensor

The sensor software can be developed simultaneously with the initial motor software. The amount of software required will depend greatly on the sensor type and the DSP system. For example an encoder requires very little user processing if the DSP has encoder interface electronics built-in. Our custom tilted-mirror sensor requires a great deal of software to process the laser interferometer measurements. Later we added even more software to automatically measure the mirror tilt.

9.2.4 Closed-Loop Control

Once the motor and sensor are both working well, we can design a controller and close the loop. The frequency response of the plant should be measured from actuator command to sensor response. Based on this Bode plot, a controller can be designed. This data should also be compared to a plant model, and unexpected behavior should be investigated. This process is described for our linear axis in section 8.2 and for our rotary axis in section 8.3. The closed-loop controller can then be implemented. It is always a good idea to measure the Bode plot of the negative of the loop transfer function to ensure that the desired crossover and phase margin have been achieved.

9.2.5 Stateflow Controller

If desired, a supervisory control routine can be added at any stage of development. In fact, for some applications, this might be done as one of the first steps. We use the Stateflow controller to switch between different operation modes, detect laser

errors, and sequence the automatic calibration routine for our sensor. We look at this controller in more detail next.

9.3 Stateflow Controller

Our Stateflow controller is shown in Figures 9-4 and 9-5. It consists of two main states, the *Power_On* state of Figure 9-4 and the *Power_Off* state of Figure 9-5. As shown in Figure 9-5 there are several transitions between these two states. For example, if the *Off* button in ControlDesk is hit, the system goes into the *Power_Off* state. Likewise, if the *On* button in ControlDesk is hit, the system goes into the *Power_On* state after checking that there are no laser errors. If a laser error occurs while the system is in the *Power_On* state, the top transition sends the controller to the *Power_Off* state and sets flags indicating that the initial calibration routines need to be re-run.

The *Power_On* state consists of two sub-states that run at the same time, *Timer* and *Series*. The *Timer* state acts as a countdown timer. The *Series* state has a series of states relating to machine start-up and calibration. For example, the *Initialization* state, sets *operation_mode* to 2 and starts the timer. As shown in the top level model in Figure 9-3, *operation_mode* equal to 2 selects the *dq* currents for homing the motor to pass through the multiport switch.

9.4 Motor Control

The "Main Program" subsystem in the top level control program (Figure 9-3) is shown in Figure 9-6. It contains the rotary and linear axis compensation as well as the generation of reference trajectories. A speed control loop for spinning the motor is also included on the bottom and can be used instead of the angular position loop. The compensation for the rotary axis is contained in the block labeled "leadlag controller 1." It is shown in Figure 9-7.

Note that the rotary axis error passes through a block labeled "Smallest Angle

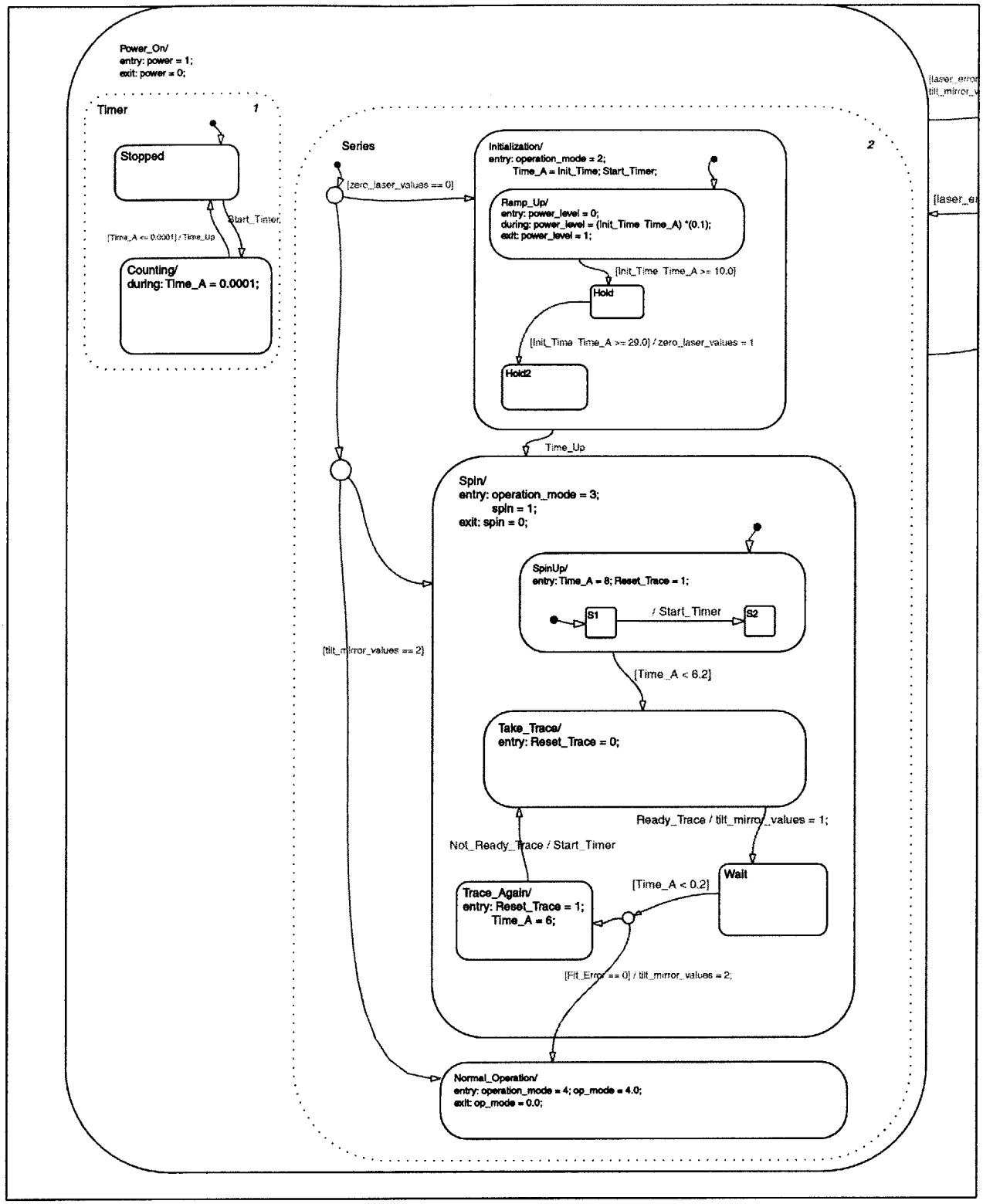

Figure 9-4: Stateflow Power On state.

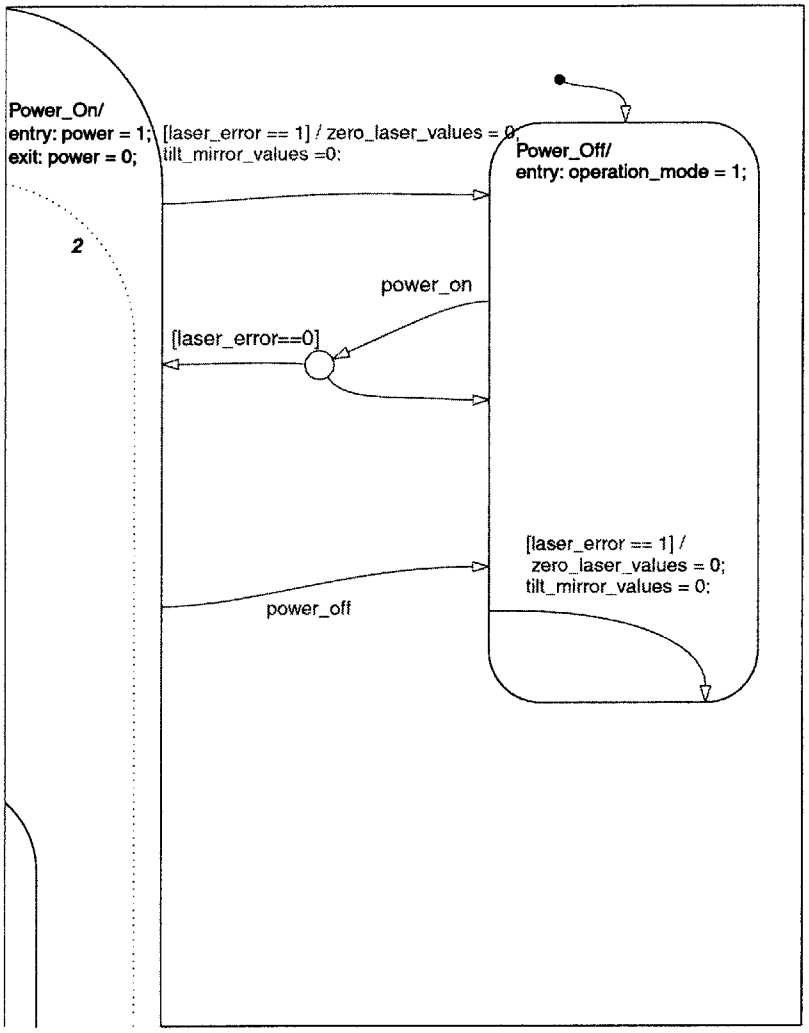

Figure 9-5: Stateflow Power Off state.

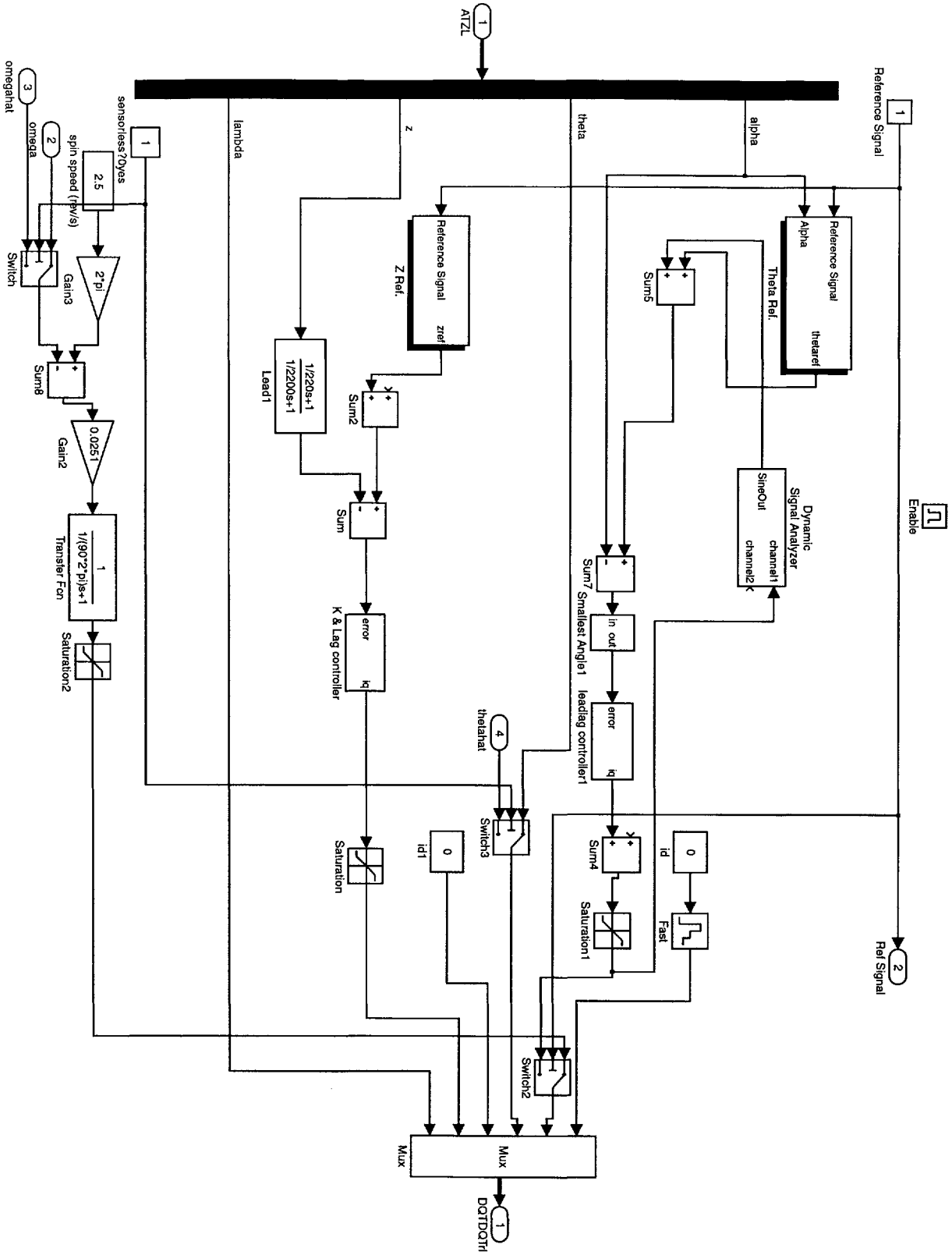

Figure 9-6: Main Program subsystem. This subsystem contains the control algorithms for the linear and rotary axes.

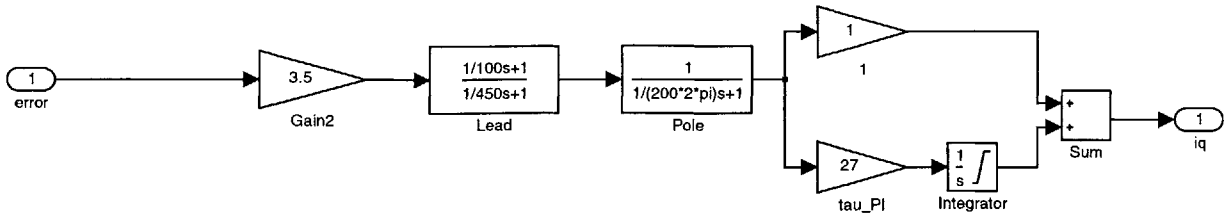

Figure 9-7: The rotary axis compensator is shown here. This compensator is contained in the "leadlag controller 1" block in Figure 9-6.

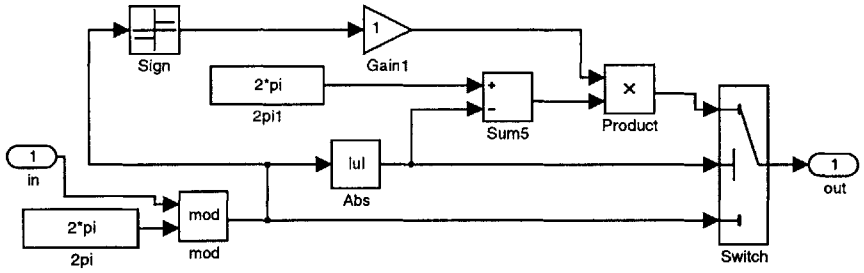

Figure 9-8: Smallest Angle subsystem. This subsystem brings the angular error between the reference and sensed angles back into the range $-\pi$ to π.

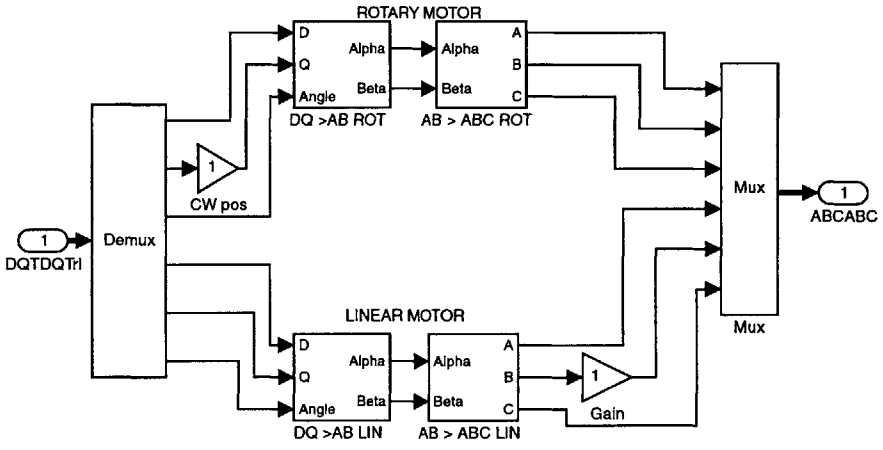

Figure 9-9: Motor Commutation subsystem. The *dq* transformations for motor commutation are contained in this subsystem labeled "DQ $->$ ABC ROT_LIN."

1." If the reference angle is $9\pi/4$ and the measured angle is 0, their difference is $9\pi/4$ even though the physical difference in angle is $-\pi/4$. This "smallest angle" block brings the angular error back into the range of $-\pi$ to π. It is shown in Figure 9-8. Unfortunately, we cannot use this block if we put the lead compensation in the feedback path since then the error signal is not an angle. Thus, for rotary motion with large angular travels, we are constrained to have the lead compensation in the feedforward path.

The "DQ $->$ ABC ROT_LIN" block in the top level control program is shown in Figure 9-9. It contains the *dq* transformations for motor commutation. These transformations are described in sections 7.4.2 and 7.4.3.

9.5 Sensor Processing

The "Sensor Processing" subsystem is shown in Figure 9-10. The "PMI" subsystem reads the laser interferometer counts from the laser axis boards. The interferometer data comes over a custom high speed parallel link to the dSPACE control board. This link is built by Marsette Vona and documented in his thesis [70]. The *SetZero* port on the "PMI" subsystem enables the laser values to be zeroed in the software. The Stateflow controller controls *zero_laser_values* so that the interferometers are zeroed after the motors have been homed. The "Mirror Tilt Parameters" subsystem outputs the six tilted-mirror calibration constants listed in Table 5.2. This subsystem also contains the calibration fit routine described in section 5.3 which fits the calibration constants to measured data taken while the mirror is spinning at constant speed. Stateflow uses *Fit_Error* to determine if the calibration constants have been fit accurately enough. If not, Stateflow calls for another measurement of the calibration constants. This time, however, the calibration constants determined by the previous fit are used so that the speed is controlled more accurately allowing for a better fit. This bootstrapping process continues until the *Fit_Error* is below a threshold value. The "Three Beam Transformation" subsystem contains the equations derived in section 5.2.3 which calculate θ, $\sin(\theta)$, and $\cos(\theta)$. Futher details of the sensor processing

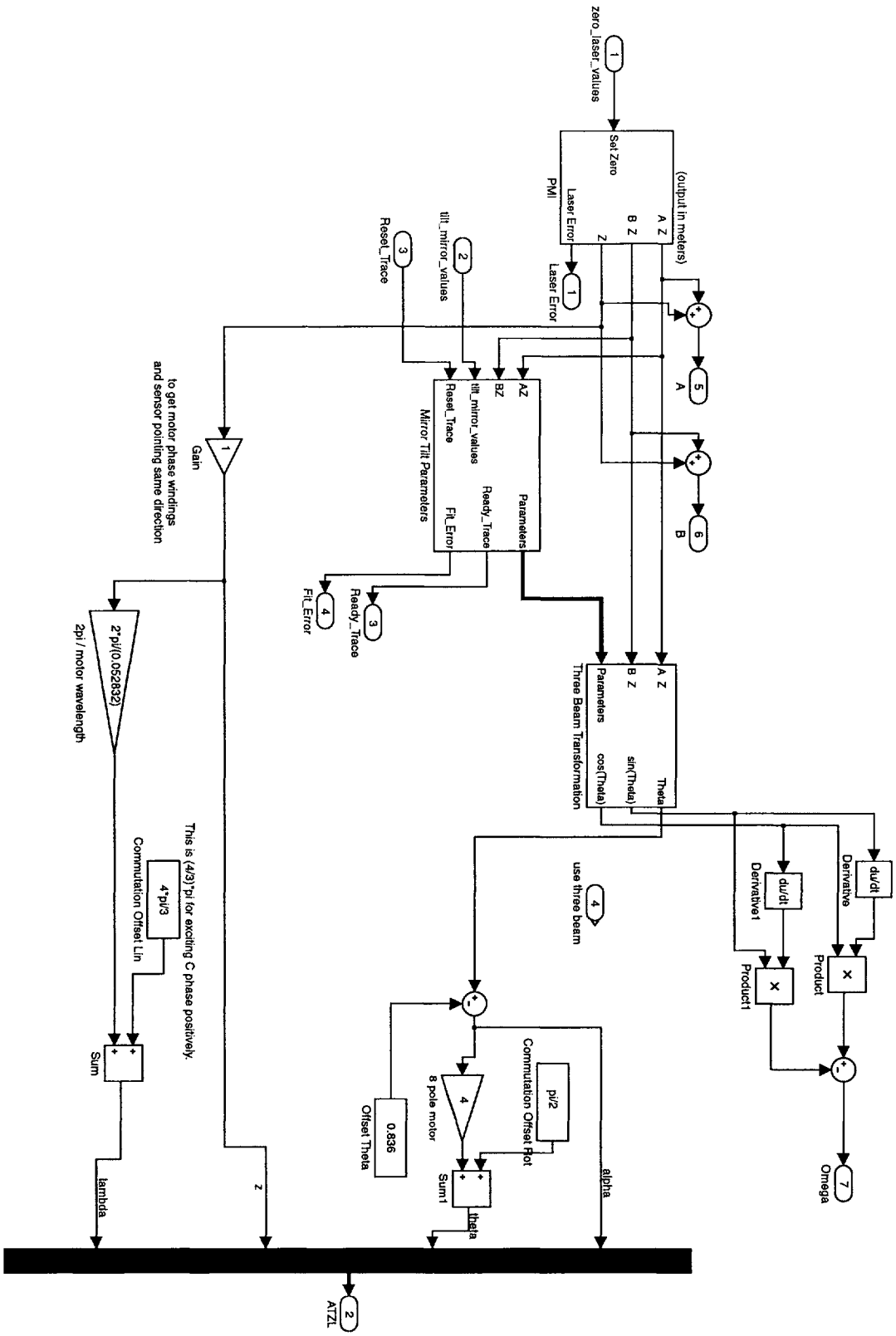

Figure 9-10: Sensor Processing subsystem.

implementation and fitting of calibration constants are contained in Vona's thesis [70].

9.6 Automatic Calibration Routine

The automatic calibration routine is run by the *Series* state (shown in Figure 9-4) in Stateflow. If the lasers have not been zeroed, the *Initialization* state is run. This state provides power to the motor phases. The power level is ramped up over 10 seconds to reduce the resulting mechanical stage oscillations. The currents are held at full power for another 19 seconds, and then the current values of the laser interferometers are remembered in the software and considered to be the zero locations.

The next stage of calibration is run by the *Spin* state. In this state the rotary motor spins the motor while the linear motor holds z position constant. This occurs via the *operation_mode* parameter which is set upon entry into this state. This parameter controls the multiport switch in the Simulink portion of top level of the program (Figure 9-3). In the *Take_Trace* state, the parameter *Reset_Trace* is taken low which tells the Simulink model to take data for the calibration fit. When this is done, the process is repeated until the *Fit_Error* is zero indicating that the calibration constants provide an acceptable fit to the measured data. At this point, the calibration routine is finished, and the axis enters the *Normal_Operation* state.

9.7 Sensorless Processing

The sensorless observer described in section 8.5.2 is implemented in the subsystem shown in Figure 9-11. The four observer state space variables—direct current, $\hat{i_d}$, quadrature current, $\hat{i_q}$, mechanical speed, $\hat{\omega}$, and electrical angle, $\hat{\theta}$—are outputs of the four integrators. The estimated electrical angle, $\hat{\theta}$, is used to transform measured voltages and commanded currents from the *abc* frame to the *dq* frame for use in this observer. The estimated electrical angle, $\hat{\theta}$, is also used to commutate the rotary motor. The estimated speed, $\hat{\omega}$ is used as feedback for the speed control loop in the "Main Program" subsystem.

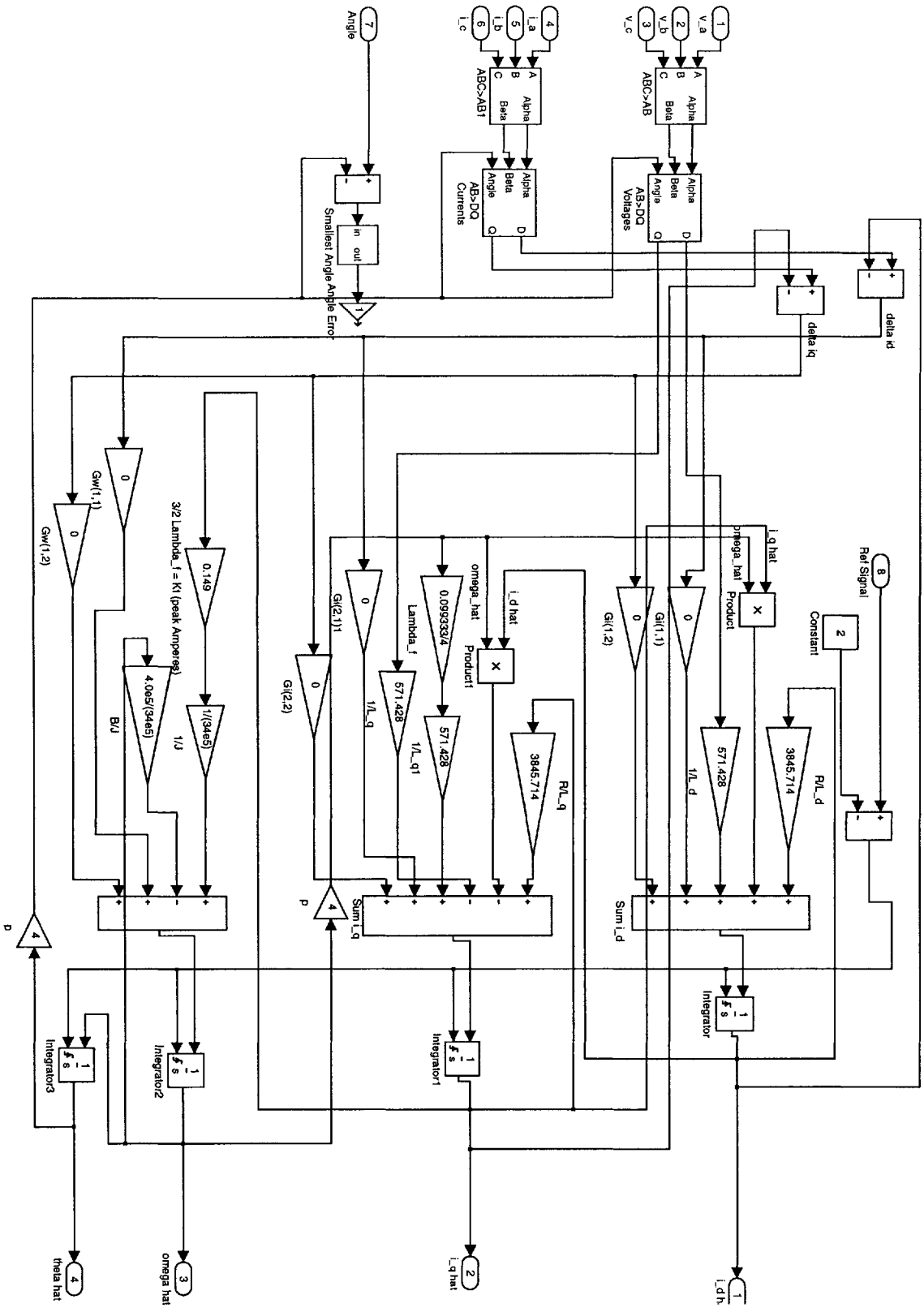

Figure 9-11: Sensorless observer subsystem.

9.8 Summary

There is no question that the dSPACE system greatly simplified our control implementation. For example, it took us just minutes to change control transfer functions. Overall, it definitely saved us months of work over implementing the controller directly in C or assembly language.

In some respects, however, the dSPACE system is non-ideal. The graphical programming language of Simulink and Stateflow is good for algorithmic calculations, but implementing conditional branching and control structures is cumbersome. Although Stateflow helps significantly in this regard, it can be extremely difficult to program. This is because it is easy to design an infinite loop into the Stateflow diagram without realizing it. The cause of the infinite loop is often subtle and requires consideration of the order in which Stateflow evaluates entries and exits of states during each execution cycle. We found that the Stateflow debugger helped us greatly to identify these loops. Unfortunately the debugger does not work when the code is run in real-time, so the model must be debugged in simulation. Once we got the Stateflow component working, it did a very nice job of controlling the machine states, sequencing events, and shutting down the machine in case of laser errors.

Another major difficulty with the dSPACE controller is that the programmer loses control over the order in which code runs during the sample time. For simple programs, this is not generally a problem. As the complexity of the program increases and the full sample time is used, however, the programmer generally would like to have more control over the order and timing of code execution. We found that in our final controller implementations our code execution time was bumping up against the 100 μs sample time. Thus, we would sometimes get task overruns, and it was not clear how we could best avoid this and why it only occurred during certain tasks such as at the end of the initial calibration routine.

In the final chapter of this thesis we look at what we have learned and future research directions for continuing work on rotary-linear axes.

Chapter 10

Conclusions & Suggestions for Future Work

10.1 Summary

The precision positioning and high acceleration capabilities of rotary-linear axes make them an enabling technology for rapidly producing complex parts to micron-level accuracies. In this thesis, we introduced rotary-linear axes as key components for use in novel multi-axis machine tools. We reviewed and classified existing 5-axis machine tool topologies and realized that topologies that stack machine tool axes can achieve only limited accelerations. By combining the rotational and translational degrees of freedom into one moving part, the rotary-linear axis offers higher accelerations and higher control bandwidths than are currently achievable.

We presented a general investigation into rotary-linear motion. Precision actuation and sensing of rotary-linear motion is especially challenging. We reviewed existing rotary-linear stage designs and found many interesting designs for achieving rotary-linear actuation and sensing. However, these designs do not have the force, precision sensing, and precision positioning capabilities required for use in high-performance machine tools. Thus, in this thesis we developed a rotary-linear axis as a key subsystem for precision, multi-axis machine tools. We fabricated a prototype axis and controlled both axes to test the feasibility of our rotary-linear axis design.

Overall, this thesis shows that rotary-linear axes are a viable component for use in precision, multi-axis machine tools. Our prototype rotary-linear axis achieves a linear acceleration of 3 g's and a rotary acceleration of 1,300 rad/s^2. These acceleration levels are far higher than today's most capable multi-axis machine tools can achieve. Furthermore, with higher power current amplifiers and reduced sensor inertia, we predict the axis could attain peak accelerations of 12 g's and 17,500 rad/s^2 at low duty cycles.

Our prototype axis uses a plane mirror interferometer with a resolution of 0.625 nm to measure linear motion. The axis uses a novel tilted-mirror sensor with a resolution of 4.6 μrad (1,336,000 counts/rev). This sensor uses two laser interferometers to measure the orientation of a tilted mirror attached to the rotary-linear shaft. The axis's simple mechanical system allows for high bandwidth controllers, 40 Hz for the rotary axis and 70 Hz for the linear axis. Under closed-loop control, the axis achieves 2.5 nm of linear positioning noise and 3.1 μrad of rotary positioning noise.

We have developed a framework for designing rotary-linear motors. We showed that for small force levels, permanent magnet synchronous motors are more power efficient than induction motors. Also, for short axial travels like ours, separate rotary and linear permanent magnet motors are more power efficient than a combined permanent magnet motor. We developeded a scaling analysis that shows that long, skinny motors are preferred for achieving high linear and rotary accelerations. We used this analysis to select commercially available rotary motor parts that maximized the axis's accelerations. We derived a continuum electromechanical analysis for a permanent magnet linear motor with iron backing. The results of this analysis allowed us to optimize the linear motor for high accelerations.

Our prototype rotary and linear motors perform exceptionally well. The rotary motor is composed of commercially available parts; the tubular linear motor is completely custom-built. Both motors have a solid construction and have not had any electrical shorts. The short rotor, long stator concept used to allow axial travel in both motors does not have any undesirable side effects. It is important to make sure that at the extremes of the axial travel, the permanent magnet rotor is still within the

stator, as in our prototype; otherwise the magnetic attraction between the permanent magnet rotor and the stator back iron can overwhelm the linear motor.

We investigated many rotary sensor concepts that can tolerate axial travel. Most of our ideas are based on plane-mirror interferometry. The prism-mirror sensor uses a prism to refract the laser beam so that it always reflects normally off a tilted mirror attached to the shaft. Unfortunately, the optical path length does not depend on rotation angle so this sensor will not sense shaft rotation. The helicoid mirror sensor seems promising, but the fabrication of the helicoid mirror would be difficult and expensive. The resolution offered by this sensor is not much greater than our prototype tilted-mirror sensor.

Our prototype tilted-mirror sensor achieves high resolution and allows us to control and test our prototype rotary-linear axis. However, it is not likely to be a final solution. It's inertia accounts for 74% of the prototype axis's total inertia. It's mass accounts for only 20% of the axis's total mass, but its location at the end of the axis causes a low frequency, 1000 rad/s, cantilever resonance. This resonance shows up in the rotary-axis plant and limits the rotary axis closed-loop bandwidth to 40 Hz. Thus, a next generation rotary-linear prototype axis would likely use a different rotary sensor. We have also shown the viability of rotary sensorless control for use with rotary-linear axes designed for a spindle applications.

We have developed many concepts and analyses related to rotary-linear actuation and sensing. Furthermore, we have successfully integrated these analyses and designs into a prototype axis which demonstrates the high accelerations and precision positioning performance rotary-linear axes can achieve.

10.2 Conclusions

We learned a great deal about rotary-linear motion that will affect the design of future rotary-linear axes. One of the most important lessons we learned was that interferometric sensors using large mirrors are not the ultimate solution for rotary sensing on these axes. Our tilted-mirror sensor is successful in measuring rotation

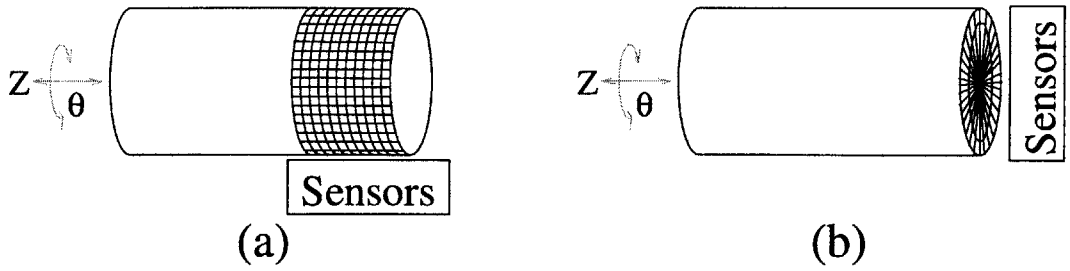

Figure 10-1: Two types of rotary-linear sensors: (a) surface area and (b) end-on. Figure drawn by Marsette Vona.

angle with sufficient resolution, but it causes a number of other problems. We knew that its inertia would be much larger than that of the rest of the axis and that therefore our achievable rotary accelerations would be reduced. We did not, however, expect the cantilever resonance modes caused by the mass of the tilted-mirror at the end of a length of the flexible shaft. These modes significantly limit the rotary axis closed-loop bandwidth we can achieve on our prototype axis. Also, our rotational measurement is compromised by the vibration of the tilted mirror since the rotary measurement measures the orientation of this mirror. If the mirror's orientation is changing due to cantilever vibrations, we will see this as changes in shaft angle.

One of the reasons we pursued interferometric sensors is that they are end-on sensors as shown schematically in Figure 10-1 (b). We reasoned that end-on sensors require much less shaft length compared to surface area sensors which are shown schematically in Figure 10-1 (a). We can now see the fallacy of this assumption, at least in some cases. Although depicted as requiring no shaft length in Figure 10-1 (b), our end-on tilted-mirror sensor takes up 1 3/4 inches of axial travel. This is nearly double that of the surface area sensor which need be only as long as the shaft travel of 1 inch. Thus, we should reconsider surface area sensors as viable solutions for future axes.

In our design we concentrated on optimizing the rotary-linear axis for high rotary and linear accelerations. We were successful in this endeavor, but perhaps sacrificed too much by allowing low frequency resonances to occur. Future designs will need shorter, more compact shafts without any significant mass at the ends to avoid bend-

ing resonances. Futhermore, although increasing the shaft diameter reduces rotary and linear accelerations, it may be necessary to do this to achieve higher bending stiffnesses. We will need to increase the frequency of these bending resonances to achieve higher closed-loop bandwidths. These higher bandwidths are required for achieving sufficient dynamic stiffness to tolerate the oscillating component of grinding forces.

We learned some valuable techniques for fabricating permanent magnet motors. We found that using an iron backing plate to short out some of flux from the permanent magnets made it easier to attach the last few magnets in a ring configuration for the rotor. We also found that cyanoacrylate works well for attaching the magnets to the backiron. None of the magnets has fallen off our rotor since fabrication. Of course, we are not spinning the motor at high speeds, but the system has survived impulses of force. These occur when a laser is blocked while the axis is running, and it hits a stop at one end of travel after the controller shuts off the power.

We found that our method for insulating the stator coils and routing the motor's lead wires worked well also. The slot in the stator for the entry and exit of coil leads did not cause any noticeable motor cogging. This is because the motor is surface wound and there is therefore a large effective air gap between permanent magnet rotor and the stator. The Nomex-Kapton-Nomex protective film and nylon coil separators insulated and protected the motor coils from damage, nicks, and shorts.

We developed a general design procedure for permanent magnet synchronous motors. In particular, we learned that permanent magnet synchronous motor shear stress increases proportionally to the motor pitch length, l, if we consider motors whose dimensions scale with l. Thus one generally wants to choose the largest pitch length possible. Of course, since the motor's layer thicknesses scale with l, this imposes a limit on how large l can be made. We learned that the power optimal coil thickness is $l/10$ for permanent magnet synchronous motors with iron backing. Others have shown that the power optimal coil thickness for permanent magnet synchronous motors with not iron backing is $l/5$. In keeping with this comparison, our analysis shows that we can achieve the same force in an iron-backed motor with half the magnet thickness and half the coil thickness of an ironless motor. This result is reasonable

since the iron backing layer produces the image of the coil or magnet, thus effectively doubling its size.

The tilted-mirror sensor achieved much higher resolution than we initially thought. This was due primarily to the large tilt angle of 4.6 mrad we were able to achieve. We discovered that our two-pass plane mirror interferometers are designed to accept some tilt in the target mirror. Tilt in the target mirror offsets the measurement beam from its nominal position but surprisingly does not change the returning measurement beam direction. In the end we found that the tilt angle of our tilted-mirror sensor was nearly the same as for the proposed helicoid sensor. This was surprising since the helicoid mirror sensor was supposed to have a large tilt angle whereas we had thought of the tilted-mirror sensor as having only a very slight tilt angle. Thus, the helicoid sensor would not offer much more resolution. Initially, we had planned that the tilted-mirror sensor would only be an interim sensor until the helicoid mirror sensor could be fabricated.

10.3 Suggestions for Future Work

Future research and development of rotary-linear axes can proceed in many directions. In this section we present several of these research directions. The ultimate goal of future research and development will be to achieve a modular rotary-linear axis machine tool subsystem that can be incorporated into precision multi-axis machine tools for fabricating centimeter-scale parts. We hope such machines will prove valuable in a wide variety of applications. In particular, we hope that the fabrication of dental restorations may be automated by such a machine.

One of the most exciting aspects of this research is that it cuts across many disciplines including dynamics, controls, electromechanics, optics, and precision machine design. Therefore, it offers numerous challenges and opportunities for researchers who are interested in these disciplines and enjoy combining them to achieve balanced designs. Depending on the interests of future researchers, research on rotary-linear axes can proceed along several directions. In the following sections we describe each

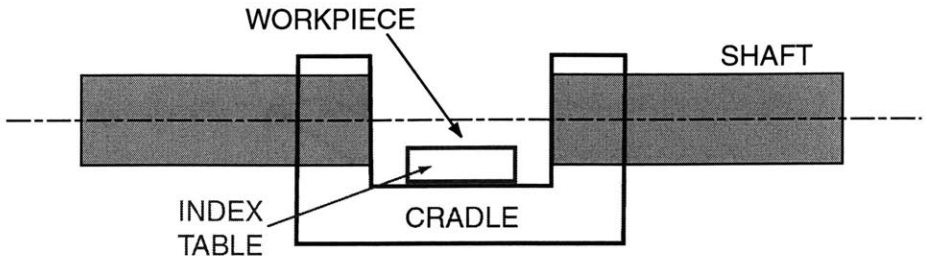

Figure 10-2: A cradle mounted on the rotary-linear axis holds a small index table and the workpiece.

of these future research directions in more detail.

10.3.1 2-D Encoder Sensor

Our tilted-mirror sensor is not intended to be an ultimate sensor solution. Its inertia and the cantilever resonance it creates limit the axis's performance. Initially, we rejected sensors that required surface area on the shaft in favor of sensors that required only an end-on measurement. These two different types of rotary-linear sensors are shown schematically in Figure 10-1. Although our tilted-mirror sensor is an end-on sensor, the mirror and mount take up 1 3/4 inches of axial shaft length. A surface area sensor need only be as long as the shaft's axial travel, in our case 1 inch. Thus, in retrospect, it seems that a surface area sensor might have been a better solution since it is smaller and adds little or no mass and inertia to the shaft.

One specific type of surface area sensor is a 2-D encoder such as that used by Anorad [8] (see section 3.1.5). A reflective 2-D encoder grid has negligible mass and inertia and can possibly be integrated into the motor or air bearing surfaces. Thus, its use would significantly reduce shaft mass and inertia. Not only would we eliminate the tilted-mirror's mass and inertia, but the shaft length would probably be reduced a couple of inches as well. Furthermore, without the tilted-mirror mass, the cantilever resonance would disappear, and the rotary axis bandwidth would be higher.

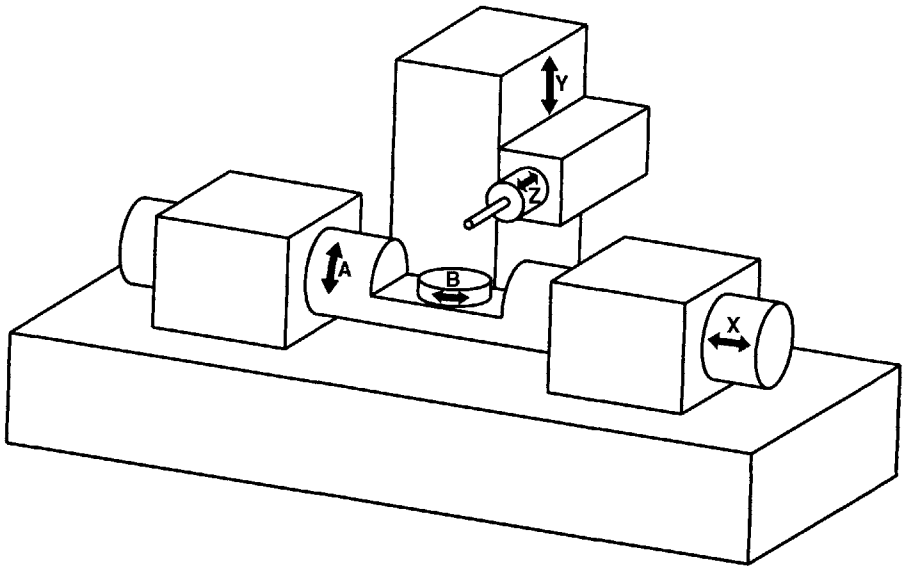

Figure 10-3: z-θ horizontal trunnion 5-axis grinding machine.

10.3.2 Cradle on z-θ Axis

Our prototype rotary-linear axis is intended to move the centimeter-scale workpiece in a 5-axis machine tool. We want the workpiece to be located approximately on the rotation axis of the rotary-linear axis. In this location the workpiece can be approximately rotated about the spindle tip so that workpiece rotation is minimally coupled to translation. If we cut out a region of the 3/4 inch diameter shaft so that the workpiece is located on the rotation axis, there will not be much shaft material left in this region. Thus, we need a cradle structure such as the one shown in Figure 10-2 to hold the workpiece and possibly also hold a small index table discussed in the next section. This cradle structure could be fabricated by epoxying it to a solid shaft and then cutting away the solid shaft in the central region. With this method, we assure that the centerlines of the shafts on either side of the cradle are not offset or at different angles from each other.

10.3.3 Index Table with Reach-In Actuator

Our envisioned 5-axis machine topology is shown in Figure 10-3. As discussed in section 2.7, the B-axis can be an index table to allow for five-sided machining. We can reduce the added inertia of this index table by offloading its actuator. In order to index the table, the rotary-linear axis would return to a home position, and the reach-in actuator would engage the index table. The design of this index table and associated reach-in actuator form another research project related to rotary-linear axes. Existing index tables do not come in sizes smaller than 2 1/2 inches in diameter.

10.3.4 z-θ Spindle Prototype

Another avenue of research is to design a prototype rotary-linear axis specialized for use as a high-speed spindle combined with infeed. Our prototype axis is primarily intended to be used for positioning the workpiece. For use as a spindle, the rotary-linear axis might have both motors next to each other and bearings on either end. Precision rotary sensing is no longer required, and the sensorless control scheme developed by Jones & Lang [29] and implemented in this thesis can be used. The z-θ spindle should be mainly optimized for high linear accelerations since rotation will generally be maintained at a constant speed.

10.3.5 z-θ Horizontal Trunnion 5-Axis Grinding Machine

It would be very exciting to integrate the rotary-linear positioning axis into a 5-axis machine tool such as the one shown in Figure 10-3. This machine ideally also has a z-θ spindle and a cradle with a small index table as have already been discussed. However, an initial prototype machine might use conventional axes instead.

To machine parts with complex surfaces, we will need to have efficient geometric algorithms to generate toolpaths which incorporate the specific kinematic and dynamic properties of the machine tool. The rotary-linear axis provides extremely high accelerations in two axes, and the toolpath generation algorithm should take advantage of this capability.

Controlling the machine tool to follow complex surfaces at very high speeds also requires significant research in control theory. We will need to develop algorithms for following high-acceleration, high-frequency trajectories with small errors. Furthermore, we will need to avoid resonances induced by the grinding process. Some form of adaptive feedforward control may well allow this. The machine's simplicity allows it to be modeled accurately which makes it easier to develop advanced control schemes.

In designing this machine we should work with researchers and manufacturers in the machine tool and dental fields in order to see our concepts used in practical devices and have a significant impact on these industries.

Appendix A

Continuum Electromechanical Analysis of Permanent Magnet Synchronous Linear Motor with Iron Backing

This Appendix presents the continuum electromechanical analysis of a permanent magnet synchronous linear motor with iron backing. The analytical expressions for motor force and power derived in this Appendix are used in Chapter 4 to design and optimize the linear motor of the z-θ axis. We use the analytical framework of Melcher [48] in which layers of electromagnetic material such as magnets, air gap, and coils are described by transfer relations. This analysis extends prior anaylses [66, 67, 34] of ironless linear motors by including iron backing behind the magnet and coil arrays. The analysis in this Appendix first appeared in Chapter 2 of the author's Master's thesis, *Thermally Efficient Linear Motor Analysis & Design* [41].

One of the main results of prior analyses [66, 67, 34] motors is that the power optimal coil thickness for an ironless stator in a single-sided motor is approximately $l/5$ where l is the magnet pitch. There is some confusion in the industry about the definition of magnet pitch. For example, for a N-S magnet array, some vendors define

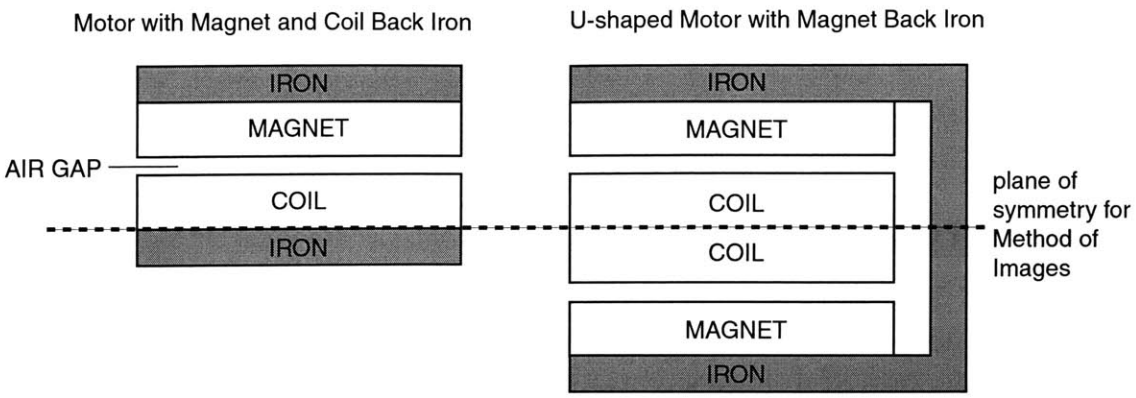

Figure A-1: The analysis of this appendix is developed for the motor on the left with magnet and coil back iron. Due to the symmetry between this motor and the U-shaped motor geometry on the right, the analysis applies to U-shaped motors as well.

the magnet pitch as the length of a single N or S magnet. In theoretical work, it is more useful to define the magnet pitch as the periodicity length of the array and thus the length of both a N and S magnet. This is the definition we use in this thesis. The analysis presented in this appendix is modified from [66] to include an iron backing behind both the magnet array and the coils. The transfer relation formulation is solved symbolically with the help of Maple [73, 25], a popular computer algebra program. The most exciting result of this computation is that the power optimal coil thickness for a single-sided linear motor with iron backing behind the magnets and the coils is approximately $l/10$.

The analysis in this appendix applies to the two different motor geometries shown in Figure A-1. The analysis in developed for the geometry on the left, a motor with magnet and coil back iron, but due to the symmetry between this motor and the U-shaped motor geometry on the right, the analysis also applies to U-shaped motors as well. The method of images allows these two quite different structures to be analyzed with the same electromechanical analysis. For the case of the U-shaped motor, a plane of symmetry cuts through the middle of the coil (Figure A-1). According to the method of images, the magnetic fields produced above this plane of symmetry are the same as those produced in a geometry which is the same above the plane of

symmetry but has iron below. Thus the power optimal coil thickness for the U-shaped motor is twice that of the single-sided motor, or $l/5$. In the next section we present the details of the motor continuum electromechanics.

A.1 Magnetoquasistatics and Fourier Series Notation

A permanent magnet motor is a magnetoquasistatic (MQS) system [23]. Under this approximation Maxwell's Equations for the magnetic field intensity H, magnetic flux density B, electric displacement D, and electric field E are:

$$\nabla \times H = J_f \tag{A.1}$$

$$\nabla \cdot B = 0 \tag{A.2}$$

$$\nabla \times E = -\frac{\partial B}{\partial t} \tag{A.3}$$

where J_f is the free current density and M is the magnetization. We also have continuity of free charge,

$$\nabla \cdot J_f = 0, \tag{A.4}$$

and a constitutive law relating magnetization, M, field intensity, H, and flux density, B,

$$B = \mu_0(H + M). \tag{A.5}$$

We assume that the system is periodic and represent the periodic fields in our problem with Fourier series. We follow Melcher's notation [48] for a field quantity Φ:

$$\Phi(z,t) = \sum_{n=-\infty}^{\infty} \tilde{\Phi}_n(t) e^{-jk_n z} \tag{A.6}$$

where

$$k_n = \frac{2\pi n}{l} \tag{A.7}$$

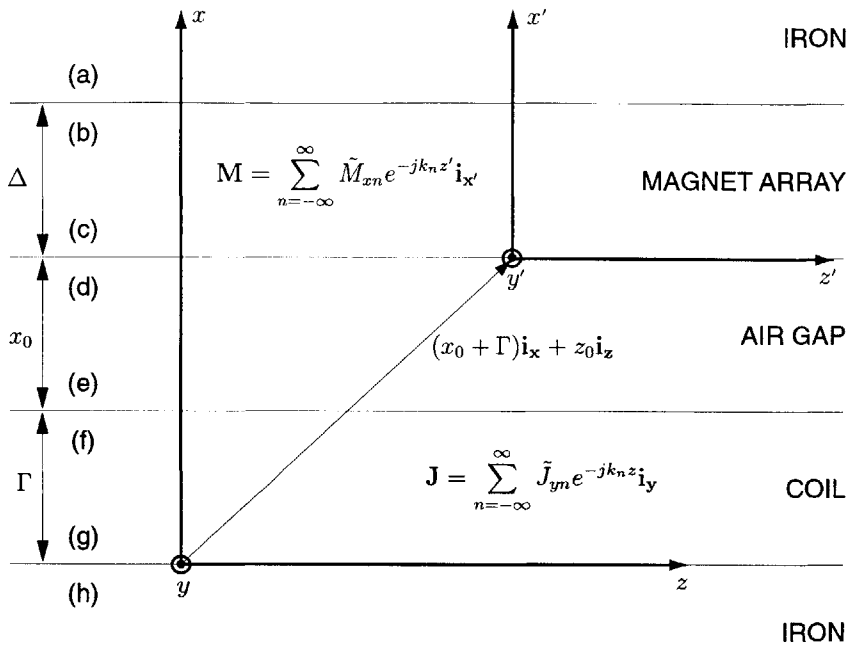

Figure A-2: Here are the five layers used in the continuum electromechanical analysis of our linear motor. The Fourier expansions for the magnetization and current density are given. Also note the two coordinate systems and the layer thicknesses, Γ, x_0, and Δ. The primed frame moves with the magnet array.

for a field whose period is l. Further, γ_n is defined as

$$\gamma_n \equiv |k_n|. \tag{A.8}$$

A.2 Transfer Relations and Boundary Conditions

A cross-sectional model of our linear motor is shown in Figure A-2. The three middle layers represent the magnet array, air gap, and coils of the linear motor. In previous analyses [66, 67, 34] the outer two layers are semi-infinite free space since the authors are modeling ironless motors. Here, we model a motor with iron layers behind the magnets and behind the coils. We make a common engineering approximation that the iron layers have infinite permeability, $\mu \to \infty$. In this limit the thickness of the iron layer does not affect the analysis so we can model the thickness as semi-infinite. In the real design this will be a good approximation for the magnetic back iron as

long as we make the iron layer thick enough to avoid saturation. It is interesting to note that for the coil back iron which models the symmetry of the U-shaped motor (Figure A-1), the condition $\mu \to \infty$ is not an approximation but is in fact exact. This is because physically there is no coil back iron in the U-shaped motor; we include this layer so that we need only analyze half of a symmetric structure. We saw that this conclusion followed from the Method of Images (Figure A-1).

The upper and lower sides of the boundaries are labeled with the letters (a) through (h). The first step of our analysis involves finding the vector potential A_y and the magnetic field intensity H_z at the top and bottom of each surface. From these surface variables we will see that we can find the field distributions everywhere. Thus we have sixteen unknowns and will need sixteen simultaneous linear equations to solve the problem. Melcher's transfer relations describe the fields within the layers. They relate the H_z's and A_y's for the two edges of a layer via two coupled equations. The semi-infinite layers provide only one equation each. This gives us eight equations. Four more equations come from jump conditions for A_y across the four boundaries (separating the five layers). An additional four equations come from jump conditions on H_z across the four boundaries.

Our ultimate goal is to find $\tilde{H}^d_{zn}$ and $\tilde{H}^d_{xn}$ so that we can evaluate the stress tensor along this plane to find an expression for the force produced on the magnets by the motor. In order to simplify the analysis, we solve the layer problem first for the fields due to the magnet and then for the fields due to the coils. These two solutions can then be superposed because the problem is linear. The primed coordinate frame shown in Figure A-2 contains the magnet array and moves relative to the coils thus allowing motion between the two parts of the motor.

A.3 Field Solutions for Magnets

We follow previous convention and use a superscript S to denote the field due to the coils only (which are part of the stator in the original analyses). Likewise a superscript of M will denote a field due only to the magnets. In this section we solve for the

fields due to the magnets alone. These fields are denoted by a left superscript M, e.g. ${}^{M}\tilde{H}^{a}_{zn}$.

A.3.1 Transfer Relations

Due to the semi-infinite plane of material at boundary (a) with $\mu \to \infty$ we have

$$ {}^{M}\tilde{H}^{a}_{zn} = 0. \tag{A.9} $$

As given in [34, 66], transfer relations for the magnet region are

$$ \begin{bmatrix} {}^{M}\tilde{H}^{b}_{zn} \\ {}^{M}\tilde{H}^{c}_{zn} \end{bmatrix} = \frac{k_n}{\mu_0} \begin{bmatrix} -\coth(k\Delta) & \frac{1}{\sinh(k\Delta)} \\ -\frac{1}{\sinh(k\Delta)} & \coth(k\Delta) \end{bmatrix} \begin{bmatrix} {}^{M}\tilde{A}^{b}_{yn} \\ {}^{M}\tilde{A}^{c}_{yn} \end{bmatrix} + \begin{bmatrix} \frac{\cosh(k_n\Delta)-1}{\sinh(k_n\Delta)} \\ -\frac{\cosh(k_n\Delta)-1}{\sinh(k_n\Delta)} \end{bmatrix} j\mu_0 \tilde{M}_{xn}. \tag{A.10} $$

The air gap transfer relations are

$$ \begin{bmatrix} {}^{M}\tilde{H}^{d}_{zn} \\ {}^{M}\tilde{H}^{e}_{zn} \end{bmatrix} = \frac{k_n}{\mu_0} \begin{bmatrix} -\coth(kx_0) & \frac{1}{\sinh(kx_0)} \\ -\frac{1}{\sinh(kx_0)} & \coth(kx_0) \end{bmatrix} \begin{bmatrix} {}^{M}\tilde{A}^{d}_{yn} \\ {}^{M}\tilde{A}^{e}_{yn} \end{bmatrix}. \tag{A.11} $$

The transfer relations for the current carrying layer assuming zero current density are

$$ \begin{bmatrix} {}^{M}\tilde{H}^{f}_{zn} \\ {}^{M}\tilde{H}^{g}_{zn} \end{bmatrix} = \frac{k_n}{\mu_0} \begin{bmatrix} -\coth(k\Gamma) & \frac{1}{\sinh(k\Gamma)} \\ -\frac{1}{\sinh(k\Gamma)} & \coth(k\Gamma) \end{bmatrix} \begin{bmatrix} {}^{M}\tilde{A}^{f}_{yn} \\ {}^{M}\tilde{A}^{g}_{yn} \end{bmatrix}. \tag{A.12} $$

We have left out the source term for the current here since this part of the analysis is only concerned with the fields caused by the magnet. The relation for the bottom $\mu \to \infty$ material is

$$ {}^{M}\tilde{H}^{h}_{zn} = 0. \tag{A.13} $$

A.3.2 Continuity of Magnetic Vector Potential

Since there are no impulsive fields, the magnetic vector potential is continuous everywhere. This gives us the following four trivial equations,

$$\begin{aligned} {}^{M}\tilde{A}^{a}_{yn} &= {}^{M}\tilde{A}^{b}_{yn}, \\ {}^{M}\tilde{A}^{c}_{yn} &= {}^{M}\tilde{A}^{d}_{yn}, \\ {}^{M}\tilde{A}^{e}_{yn} &= {}^{M}\tilde{A}^{f}_{yn}, \\ {}^{M}\tilde{A}^{g}_{yn} &= {}^{M}\tilde{A}^{h}_{yn}. \end{aligned} \tag{A.14}$$

A.3.3 Jump Conditions

In this analysis we consider only a N-S magnet array such that $\tilde{M}_{zn} = 0$. Under this condition the parallel component of the magnetic field intensity is continuous across boundaries since we have no equivalent surface currents representing the termination of horizontal magnetization. Again this gives us a set of trivial equations,

$$\begin{aligned} {}^{M}\tilde{H}^{a}_{zn} &= {}^{M}\tilde{H}^{b}_{zn}, \\ {}^{M}\tilde{H}^{c}_{zn} &= {}^{M}\tilde{H}^{d}_{zn}, \\ {}^{M}\tilde{H}^{e}_{zn} &= {}^{M}\tilde{H}^{f}_{zn}, \\ {}^{M}\tilde{H}^{g}_{zn} &= {}^{M}\tilde{H}^{h}_{zn}. \end{aligned} \tag{A.15}$$

A.3.4 Solutions

The solution of the above sixteen equations is carried out in the software package Maple [25, 73]. We only need expressions for $\tilde{H}^{d}_{zn}$ and $\tilde{H}^{d}_{xn}$ to calculate the stress tensor at surface (d). $\tilde{H}^{d}_{zn}$ is one of the sixteen variables we have solved for, and $\tilde{H}^{d}_{xn}$ is directly related to $\tilde{A}^{d}_{yn}$ which is one of the sixteen variables. This relationship comes from the definition $\mathbf{B} = \nabla \times \mathbf{A}$ and from the fact that in this type of problem $\mathbf{A}$ has only a y-directed component, from which it follows that:

$$H_{xn} = -\frac{1}{\mu_0}\frac{\partial}{\partial z}A_{yn} \tag{A.16}$$

and thus

$$\tilde{H}_{xn} = \frac{jk_n}{\mu_0}\tilde{A}_{yn}. \tag{A.17}$$

Omitting the intermediate details, the solutions for the complex amplitudes of the field quantities at surface (d) due to the magnet array are:

$${}^{M}\tilde{H}^{d}_{zn} = \left(\frac{j\tilde{M}_{vn}}{2}\right)\left(\frac{e^{2k_n g} + e^{2k_n \Delta} - e^{2k_n(\Delta+g)} - 1}{e^{2k_n(\Delta+g)} - 1}\right) \tag{A.18}$$

$${}^{M}\tilde{H}^{d}_{xn} = \left(-\frac{\coth(kg)\tilde{M}_{vn}}{2}\right)\left(\frac{e^{2k_n g} + e^{2k_n \Delta} - e^{2k_n(\Delta+g)} - 1}{e^{2k_n(\Delta+g)} - 1}\right), \tag{A.19}$$

where $g \equiv x_0 + \Gamma$ is the gap between the magnets and stator back iron.

The Fourier components of the vertical magnetization for a magnet array are given by

$$\tilde{M}_{xn} = \frac{1}{l}\int_0^l M_x e^{jk_n z'} dz'. \tag{A.20}$$

For a N-S magnet array, the fundamental Fourier coefficients of $\tilde{M}_{vn}$ for the square wave representing the magnetization are

$$\begin{aligned} \tilde{M}_{x1} &= \frac{2}{\pi}M_0 j \\ \tilde{M}_{x-1} &= -\frac{2}{\pi}M_0 j, \end{aligned} \tag{A.21}$$

where $\mu_0 M_0$ is the remanence of the permanent magnets.

A.4 Field Solutions for Coils

In this section we solve for the fields due to the coils alone with the permanent magnets removed. These quantities are indicated with a left superscript S, e.g., ${}^{S}\tilde{H}^{a}_{zn}$.

A.4.1 Transfer Relations

For a semi-infinite plane of material with $\mu \to \infty$ we have

$$ {}^{S}\tilde{H}^{a}_{zn} = 0. \tag{A.22} $$

The transfer relations for the magnet region are given in [66],

$$ \begin{bmatrix} {}^{S}\tilde{H}^{b}_{zn} \\ {}^{S}\tilde{H}^{c}_{zn} \end{bmatrix} = \frac{k_n}{\mu_0} \begin{bmatrix} -\coth(k\Delta) & \frac{1}{\sinh(k\Delta)} \\ -\frac{1}{\sinh(k\Delta)} & \coth(k\Delta) \end{bmatrix} \begin{bmatrix} {}^{S}\tilde{A}^{b}_{yn} \\ {}^{S}\tilde{A}^{c}_{yn} \end{bmatrix}. \tag{A.23} $$

Note that we have omitted the permanent magnet source term since in this part of the problem we are only finding the fields due to the coils. The air gap transfer relations are

$$ \begin{bmatrix} {}^{S}\tilde{H}^{d}_{zn} \\ {}^{S}\tilde{H}^{e}_{zn} \end{bmatrix} = \frac{k_n}{\mu_0} \begin{bmatrix} -\coth(kx_0) & \frac{1}{\sinh(kx_0)} \\ -\frac{1}{\sinh(kx_0)} & \coth(kx_0) \end{bmatrix} \begin{bmatrix} {}^{S}\tilde{A}^{d}_{yn} \\ {}^{S}\tilde{A}^{e}_{yn} \end{bmatrix}. \tag{A.24} $$

The transfer relations for the current carrying layer are

$$ \begin{bmatrix} {}^{S}\tilde{H}^{f}_{zn} \\ {}^{S}\tilde{H}^{g}_{zn} \end{bmatrix} = \frac{k_n}{\mu_0} \begin{bmatrix} -\coth(k\Gamma) & \frac{1}{\sinh(k\Gamma)} \\ -\frac{1}{\sinh(k\Gamma)} & \coth(k\Gamma) \end{bmatrix} \begin{bmatrix} {}^{S}\tilde{A}^{f}_{yn} \\ {}^{S}\tilde{A}^{g}_{yn} \end{bmatrix} + \begin{bmatrix} \frac{\cosh(k_n\Gamma)-1}{\sinh(k_n\Gamma)} \\ -\frac{\cosh(k_n\Gamma)-1}{\sinh(k_n\Gamma)} \end{bmatrix} \frac{\mu_0}{k_n} \tilde{J}_{yn}. \tag{A.25} $$

The relation for the bottom $\mu \to \infty$ material is

$$ {}^{S}\tilde{H}^{h}_{zn} = 0. \tag{A.26} $$

A.4.2 Continuity of Magnetic Vector Potential

These are the same as in the permanent magnet case, i.e.,

$$ \begin{aligned} {}^{S}\tilde{A}^{a}_{yn} &= {}^{S}\tilde{A}^{b}_{yn} \\ {}^{S}\tilde{A}^{c}_{yn} &= {}^{S}\tilde{A}^{d}_{yn} \\ {}^{S}\tilde{A}^{e}_{yn} &= {}^{S}\tilde{A}^{f}_{yn} \\ {}^{S}\tilde{A}^{g}_{yn} &= {}^{S}\tilde{A}^{h}_{yn} \end{aligned} . \tag{A.27} $$

A.4.3 Jump Conditions

These are the same as in the permanent magnet case, i.e.,

$$\begin{aligned} {}^{S}\tilde{H}^{a}_{zn} &= {}^{S}\tilde{H}^{b}_{zn} \\ {}^{S}\tilde{H}^{c}_{zn} &= {}^{S}\tilde{H}^{d}_{zn} \\ {}^{S}\tilde{H}^{e}_{zn} &= {}^{S}\tilde{H}^{f}_{zn} \\ {}^{S}\tilde{H}^{g}_{zn} &= {}^{S}\tilde{H}^{h}_{zn} \end{aligned} \quad . \tag{A.28}$$

A.4.4 Solutions

The sixteen unknowns are found by the computer algebra program Maple [73, 25]. Appendix A of [41] lists the Maple code used to perform this calculation. We are only interested in finding ${}^{S}\tilde{H}^{d}_{zn}$ and ${}^{S}\tilde{H}^{d}_{xn}$. The first coefficient is one of our unknowns, and after some simplification can be solved for as

$${}^{S}\tilde{H}^{d}_{zn} = \left(\frac{-\tilde{J}_{yn}}{2k_n}\right)\left(\frac{(e^{2k_n\Gamma}-1)(e^{2k_n\Delta}-1)e^{k_n x_0}}{e^{2k_n(\Gamma+\Delta+x_0)}-1}\right) \text{ (iron).} \tag{A.29}$$

For comparison, we provide the value of this same parameter found in previous (ironless) analyses [66, 67]:

$${}^{S}\tilde{H}^{d}_{zn} = \left(\frac{-\tilde{J}_{yn}}{2\gamma_n}\right) e^{-\gamma_n x_0}(1-e^{-\gamma_n\Gamma}) \text{ (ironless).} \tag{A.30}$$

The easiest way to see that these two expressions are in fact quite similar is to note that for typical values of Γ, Δ, and x_0, and specializing to $n > 0$, the approximation, $e^{2k_n(\Gamma+\Delta+x_0)} \gg 1$, holds. Recall that $\gamma_n = |k_n|$ so for $n > 0$ we have $\gamma_n = k_n$. We can then (temporarily) ignore the 1 in the denominator of equation (A.29) using our approximation. We now have

$${}^{S}\tilde{H}^{d}_{zn} = \left(\frac{-\tilde{J}_{yn}}{2k_n}\right) e^{-k_n x_0}(1-e^{-2k_n\Gamma})(1-e^{-2k_n\Delta}) \text{ (iron, approximate, } n>0) \tag{A.31}$$

which when compared with the ironless case (A.30) gives us a preview of the differences we will find between the solutions with and without iron. In particular, we

note:

1. The $e^{-k_n x_0}$ dependence is recovered in the approximation.

2. The term $(1-e^{-2k_n\Gamma})$ is similar to the Γ term in the ironless case, but note that Γ is now replaced by 2Γ. Recall that our final result will be that the optimal layer thickness is half of the ironless case ($l/10$ versus $l/5$); this shows why this result holds.

3. There is a new dependence on Δ in the term, $(1-e^{-2k_n\Delta})$, not found in the ironless case. This makes sense because the distance to the iron layer behind the magnets should matter. In the ironless case, there is only non-magnetic material above the coils so this distance is irrelevant.

4. The stator-driven fields are larger with the back iron because $e^{-2k_n\Gamma} < e^{-k_n\Gamma}$ and $e^{-2k_n\Delta} < e^{-k_n\Delta}$.

We can next find $\tilde{H}^d_{xn}$ by applying equation (A.17) yielding

$$ {}^{S}\tilde{H}^d_{xn} = \left(\frac{j\tilde{J}_{yn}}{2k_n}\right)\frac{(e^{2k_n\Gamma}-1)(e^{2k_n\Delta}+1)e^{k_n x_0}}{e^{2k_n(\Gamma+\Delta+x_0)}-1}. \tag{A.32} $$

A.5 Total Fields

We can now superpose equations (A.18) and (A.29) for ${}^{M}\tilde{H}^d_{zn}$ and ${}^{S}\tilde{H}^d_{zn}$ to yield the combined field due to magnet array and stator, $\tilde{H}^d_{zn}$. Likewise, equations (A.19) and (A.32) for ${}^{M}\tilde{H}^d_{xn}$ and ${}^{S}\tilde{H}^d_{xn}$ are combined to yield $\tilde{H}^d_{xn}$. For convenience, we consider the superposed field to be stationary in the magnet frame. Thus, we must use $z = z_0 + z'$ for the stator fields which results in a multiplicative term of $e^{-jk_n z_0}$ in these terms. The total fields at boundary (d) are thus

$$ \begin{aligned} \tilde{H}^d_{zn} &= \left(\frac{j\tilde{M}_{vn}}{2}\right)\left(\frac{e^{2k_n(\Gamma+x_0)}+e^{2k_n\Delta}-e^{2k_n(\Gamma+\Delta+x_0)}-1}{e^{2k_n(\Gamma+\Delta+x_0)}-1}\right) \\ &\quad + \left(\frac{-\tilde{J}_{yn}}{2k_n}\right)\left(\frac{(e^{2k_n\Gamma}-1)e^{k_n x_0}}{e^{2k_n(\Gamma+\Delta+x_0)}-1}\right)(e^{2k_n\Delta}-1)e^{-jk_n z_0} \end{aligned} \tag{A.33} $$

$$\tilde{H}^d_{xn} = \left(-\frac{\coth(k_n(\Gamma+x_0))\tilde{M}_{vn}}{2}\right)\left(\frac{e^{2k_n(\Gamma+x_0)}+e^{2k_n\Delta}-e^{2k_n(\Gamma+\Delta+x_0)}-1}{e^{2k_n(\Gamma+\Delta+x_0)}-1}\right) + \left(\frac{j\tilde{J}_{yn}}{2k_n}\right)\left(\frac{(e^{2k_n\Gamma}-1)e^{k_n x_0}}{e^{2k_n(\Gamma+\Delta+x_0)}-1}\right)(e^{2k_n\Delta}+1)e^{-jk_n z_0}. \quad \text{(A.34)}$$

A.6 Motor Force via Maxwell Stress Tensor

Now we are ready to use the Maxwell stress tensor to find the motor force. The theory underlying this analysis is given in [48]. The force F_i in the ith direction on a material is

$$F_i = \oint_S T_{ij} n_j da \quad \text{(A.35)}$$

where n_j is the jth component of the normal vector to the surface S which is being integrated over. The Maxwell stress tensor T_{ij} is given by

$$T_{ij} = \mu H_i H_j - \frac{\mu}{2}\delta_{ij}\sum_k H_k H_k, \quad \text{(A.36)}$$

where δ_{ij} is the Kronecker delta[1]. We enclose the magnet array in an imaginary box with one side at surface (d) where we have just calculated the fields and the opposite side at infinity where the fields are zero as shown in Figure A-3. The edges of the box are chosen to include an integral number of magnet periods so that by symmetry the stresses along these sides cancel. The surface integral thus simplifies to evaluating the spatial average of the stress tensor at surface (d) and multiplying by the area A:

$$F_z = -A\mu_0\langle T^d_{xz}\rangle_z = -A\mu_0\langle H^d_x H^d_z\rangle_z, \quad \text{(A.37)}$$

where $\langle\cdot\rangle$ denotes a spatial average in z. We thus need to calculate

$$F_z = -A\mu_0(\tilde{H}^d_{x(-1)}\tilde{H}^{d*}_{z(-1)} + \tilde{H}^d_{x(1)}\tilde{H}^{d*}_{z(1)}) \quad \text{(A.38)}$$

[1] $\delta_{ij} = \begin{cases} 1, & i=j \\ 0, & i\neq j \end{cases}$

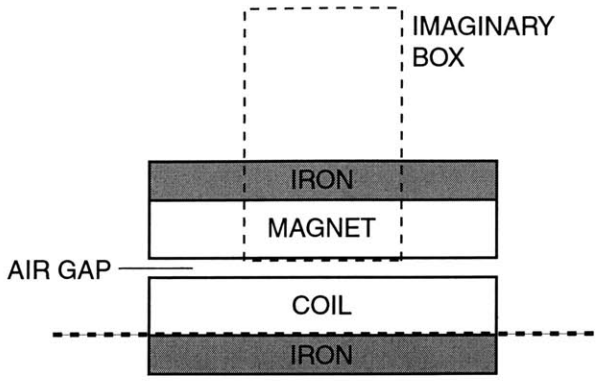

Figure A-3: We calculate the forces on this imaginary box. From our analysis we know the fields for the side of the box in the air gap. The opposite side is at inifinity where the fields are zero. The remaining two edges of the box enclose an integral number of magnet periods so that by symmetry the stresses along these sides cancel.

where we have used the spatial averaging theorem [48],

$$\left\langle \sum_{n=-\infty}^{\infty} \tilde{A}_n e^{-jk_n z} \sum_{m=-\infty}^{\infty} \tilde{B}_m e^{-jk_m z} \right\rangle_z = \sum_{n=-\infty}^{\infty} \tilde{A}_n \tilde{B}_{-n} = \sum_{n=-\infty}^{\infty} \tilde{A}_n \tilde{B}_n^*. \tag{A.39}$$

We assume a sinusoidal current density with a period l in the coils. Although we do not actually have a sinusoidal excitation, this fundamental harmonic approximates the real distribution and allows the force solution to be written down in a simple analytical form. For a pure sinusoidal excitation, all components $\tilde{J}_{yn}$ are zero except for the fundamental components, $n = \pm 1$:

$$\begin{aligned} \tilde{J}_{y1} &= J_a + jJ_b \\ \tilde{J}_{y-1} &= J_a - jJ_b. \end{aligned} \tag{A.40}$$

Here, $2J_a$ and $2J_b$ are the peak current densities for the two sinusoidally distributed phases.

We substitute for $\tilde{H}^d_{zn}$ and $\tilde{H}^d_{xn}$ in equation (A.38) using equations (A.33), (A.34), (A.40), and (A.21). A considerable amount of algebra using Maple [73, 25] yields (see

Appendix A of [41])

$$F_z = \mu_0 M_0 \frac{wl^2}{\pi^2} \left[\frac{e^{\gamma x_0}(e^{2\gamma\Delta} - 1)(e^{2\gamma\Gamma} - 1)}{e^{2\gamma(\Delta+\Gamma+x_0)} - 1} \right] (J_a \cos \gamma z_0 + J_b \sin \gamma z_0). \qquad \text{(A.41)}$$

This equation is the key result of this analysis. It predicts the force per spatial wavelength produced by a motor with iron behind the magnets and coils, and with a sinusoidally distributed stator winding. This result is an extension of the results in [66, 67] which accounts for the back iron. Our analysis was for a N-S magnet array, but a simple adjustment of equation (A.21) will allow for other arrays such as the Halbach configuration. For comparison, we repeat—in a suggestive form—the solution for the ironless case with a Halbach magnet array which has appeared in several papers [66, 67]:

$$F_z = \mu M_0 \frac{\sqrt{2} wl^2}{\pi^2} \left[(1 - e^{-\gamma\Gamma})(1 - e^{-\gamma\Delta}) e^{-\gamma x_0} \right] (J_a \cos \gamma z_0 + J_b \sin \gamma z_0). \qquad \text{(A.42)}$$

Some comments are in order:

- The $\sqrt{2}$ in equation (A.42) is there since this equation applies to a motor using a Halbach magnet array. For ironless motors, the Halbach magnet array produces a field that is $\sqrt{2}$ times stronger than a conventional N-S magnet array. Had a normal N-S array been used in that computation, the $\sqrt{2}$ would not appear. A comparison of four magnet arrays—regular N-S, four block Halbach, ideal Halbach, and vertical sinusoidal—is done in a paper by Trumper et. al. [67]. Note well, however, that in the case of a motor with iron (A.41) the substitution of a Halbach array for a N-S array will *not* improve the force by a factor of $\sqrt{2}$. The improvement will be much less. An intuitive explanation for this is that the magnetic back iron is placed on the low-field side of the Halbach array and thus affects the field less than for a N-S array. John Ofori offers another intuitive explanation for the effects of back iron on magnet arrays using the Method of Images [55].

  This leads to the following pedantic point. The proper way to compare equa-

tions (A.41) and (A.42) is by removing the $\sqrt{2}$ from the second equation thus converting a Halbach ironless motor into a N-S ironless motor. It would be incorrect, albeit algebraically the same, to add a $\sqrt{2}$ to the first equation in a mistaken attempt to convert a N-S iron-backed motor into a Halbach iron-backed motor.

- It is illuminating to examine the limit where $e^{2\gamma(\Delta+\Gamma+x_0)} \gg 1$. As an example, we use the motor of [41] with parameters listed in Table ??. We have $\gamma = 2\pi/l = 2\pi/(60\text{ mm})$, $\Delta = 11.43$ mm, $\Gamma = 3.81$ mm, $x_0 = 1.02$ mm yielding $e^{2\gamma(\Delta+\Gamma+x_0)} = 30.1$. In this case, $e^{2\gamma(\Delta+\Gamma+x_0)} \gg 1$ is a very good approximation.

  Assuming that our parameters are such that the limit $e^{2\gamma(\Delta+\Gamma+x_0)} \gg 1$ holds, we have $e^{2\gamma(\Delta+\Gamma+x_0)} - 1 \approx e^{2\gamma(\Delta+\Gamma+x_0)}$ in the denominator of equation (A.41). Under this approximation, the force equation (A.41) simplifies to

$$F_z = \mu M_0 \frac{wl^2}{\pi^2} \left[(1-e^{-2\gamma\Gamma})(1-e^{-2\gamma\Delta})e^{-\gamma x_0}\right](J_a \cos\gamma z_0 + J_b \sin\gamma z_0). \quad \text{(A.43)}$$

  Equations (A.43) and (A.42) for the iron-backed motor and the ironless motor, respectively, are quite similar. Apart from the $\sqrt{2}$, which was discussed previously, they can be made identical by the following equalities:

$$\Gamma_{ironless} = 2\Gamma_{iron} \quad \text{(A.44)}$$

$$\Delta_{ironless} = 2\Delta_{iron} \quad \text{(A.45)}$$

  The advantages of an iron-backed motor are clear: We can achieve the same force in an iron-backed motor with half the magnets and half the coil thickness as compared with an ironless motor. This result is reasonable since an iron layer behind a magnet produces the image of that magnet, thus effectively doubling its size. The same is true for the coil. Remember that this result is only strictly true when the limit $e^{2\gamma(\Delta+\Gamma+x_0)} \gg 1$ holds, as will be the case in practical implementations.

- In an ironless motor, the force equation for F_x is similar to the equation for F_z (A.42) and the two are often written in matrix form. For a motor containing iron, the F_x force is quite different from the F_z force. In fact, F_x has a term proportional to J^2 and one proportional to J. Since F_x is nonlinear in J, it cannot be written in matrix form.

A.7 Power Optimal Coil Thickness

A.7.1 Analytical Results

In this section, we derive an expression for the power dissipation in the motor as a function of the various motor parameters. We can invert equation (A.41) to yield the commutation law for our motor. We then can calculate the power dissipation using an average value of J^2/σ [67]. We introduce the variables N_s for the number of spatial periods l of the coils and N_m for the number of spatial periods l of the magnets which interact with the coils. The power dissipation P_t for the motor with iron is thereby found to be

$$P_t = \frac{(3)2N_s\pi^4\Gamma}{N_m^2\sigma(\mu_0 M_0)^2 w l^3}\left[\frac{e^{2\gamma(\Delta+\Gamma+x_0)}-1}{e^{\gamma x_0}(e^{2\gamma\Delta}-1)(e^{2\gamma\Gamma}-1)}\right]^2 F_z^2. \tag{A.46}$$

For comparison, we repeat the result from [67] for the ironless motor as well:

$$P_t = \frac{(3)N_s\pi^4\Gamma}{N_m^2\sigma(\mu_0 M_0)^2 w l^3}\left[\frac{e^{2\gamma x_0}}{(1-e^{-\gamma\Gamma})^2(1-e^{-\gamma\Delta})^2}\right] F_z^2. \tag{A.47}$$

The factor of three in equations (A.46) and (A.47) is added in the original analysis by Trumper, Williams, and Nguyen [67] to account for non-idealities in the packing factor of the windings, winding length in the end-turns, and fringing fields.

We next attempt to find the power optimal thickness of the coils by setting $\partial P_t/\partial\Gamma = 0$. In the ironless case (A.47), this derivative involves only the parameter l (via $\gamma = 2\pi/l$) and Γ. The physics is different for the motor with iron; the derivative involves x_0 and Δ as well as l and Γ. We will see that this dependence is

small in many practical cases, but it is interesting that the power optimal thickness depends on new variables—the magnet thickness and air gap—in the motor with iron.

We now apply the same approximation, $e^{2\gamma(\Delta+\Gamma+x_0)} \gg 1$, that we used previously (in section A.6). We find that this approximation eliminates the x_0 and Δ dependence just mentioned. That is, pulling out the term which depends on Γ gives

$$P_t(\Gamma) \propto \Gamma \frac{1}{(1-e^{-2\gamma\Gamma})^2}. \tag{A.48}$$

For comparison, the result in the ironless case is [67]:

$$P_t(\Gamma) \propto \Gamma \frac{1}{(1-e^{-\gamma\Gamma})^2}. \tag{A.49}$$

The difference between the expressions for the iron-backed and ironless cases is a factor of 2 in front of the Γ in the exponent. Setting $\partial P_t/\partial\Gamma = 0$ yields a transcendental equation whose solution is $2\gamma\Gamma \approx 1.25$, or

$$\Gamma_{optimal} \approx \frac{l}{10}. \tag{A.50}$$

This is the result we alluded to at the beginning of the appendix. The power optimal coil thickness for an iron-backed motor is half that of an equivalent ironless motor.

A.7.2 Coil Thickness Selection

Although we have found the optimal thickness, it is important to realize that the power vs. coil thickness plot is very flat near this minimum. Thus, while the power optimal result, $l/10$, is important, one misses a lot of design alternatives by focusing solely on this single value. The most useful way to think about this is to define a tolerance on the power dissipated. For example, we might consider coil thicknesses that dissipate no more than 10% more than the minimum power dissipation level. This can lead to a wide acceptable range of coil thicknesses. For typical coils, the temperature difference across the coil goes as the thickness squared [41]. Thus, one would want to choose the thinnest coil in the acceptable range.

However, if a cooling system such as the separated end-turn cooling scheme shown in Figure 6-24 and documented in [41] is used, the coil temperature rise does not depend on coil thickness. In this case, we want to choose the thickest coil in our acceptable range defined by power dissipation. We do this because each coil thickness in the acceptable range dissipates roughly the same power and produces exactly the same force. If we are producing the same force with a thicker coil, the current density must be smaller than it would be for a thin coil. If the coil is thicker by a factor of k, it will produce k times more force if the magnetic field and current density are the same. The magnetic field will be reduced since there is now a larger effective air gap. However, the magnetic field falls off slower than $1/k$, and so the current density in the coil must also be smaller. Hence, we can probably increase the current density in the thicker coil until we again reach the limit of our cooling system.

Appendix B

Induction Motor Optimization

In this Appendix we introduce Melcher's analysis for an induction motor [48] and then show how to select the power optimal slip speed and rotor thickness. These results are used in section 3.2.1 to design a power optimal induction motor. We can then compare the power efficiency of permanent magnet and induction motors at different force levels.

B.1 Induction Motor Model

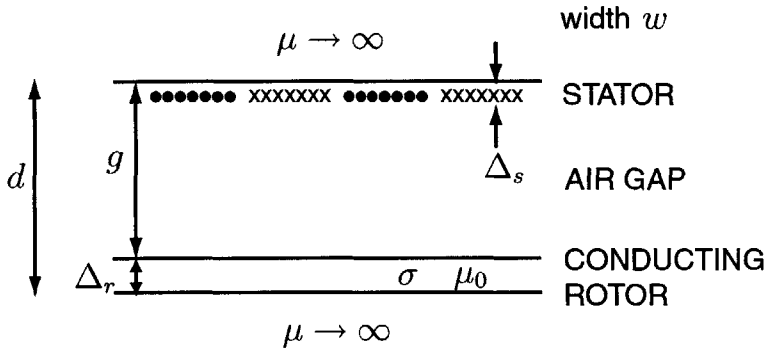

Figure B-1: Schematic showing induction motor model. The stator's windings are modeled by a thin current sheet, and the rotor is also modeled as a thin current sheet.

The induction motor model we use is shown in Figure B-1. The stator's windings are modeled by a thin surface current, and the rotor is also modeled as a thin sruface

current. The actual stator windings have a thickness, Δ_s, and the actual rotor has a thickness, Δ_r. The motor's actual air gap is g, but since our motor analysis assumes an infinitely thin rotor, we account for the rotor's actual thickness, Δ_r, by using an effective air gap,

$$d = g + \Delta_r. \tag{B.1}$$

We do not include the stator thickness, since we assume that the stator windings are wound in slots. The motor has a width, w. The rotor has conductivity, σ, and permeability, μ_0. For simplicity we assume the stator windings have the same conductivity, σ, as the rotor. The stator and rotor are backed by infinitely permeable backiron.

The wavelength of the stator coils is l, and it is convenient to define the wavenumber $k = 2\pi/l$. The stator is excited with balanced sinusoidal two phase currents with frequency ω such that the resulting current density wave is a pure traveling wave. Phase a has N_a peak turns per unit length and current amplitude I_a. The rotor moves with linear speed U relative to the stator. We define a dimensionless number, S_+, following [48] which is proportional to the slip speed, $\omega/k - U$. This slip occurs between the speed of the traveling wave of stator currents, ω/k, and the rotor mechanical speed, U. The dimensionless slip speed is

$$S_+ = \frac{\mu_0 \Delta_r \sigma}{k} (\omega - kU). \tag{B.2}$$

As derived by Melcher [48], the induction motor produces a force,

$$F = \frac{lw\mu_0}{2\sinh^2(kd)} \left(\frac{S_+ N_a^2 I_a^2}{1 + S_+^2 \coth^2(kd)} \right). \tag{B.3}$$

By integrating the Joule heating in the two current sheets we obtain an expression for the total power, P, dissipated in the induction motor,

$$P = \frac{lwI_a^2 N_a^2}{2} \left(\frac{1}{\Delta_s \sigma} + \frac{S_+^2}{\Delta_r \sigma \sinh^2(kd) \left(1 + S_+^2 \coth^2(kd)\right)} \right). \tag{B.4}$$

Here the first term is due to power dissipated on the stator, and the second term is due to power dissipated on the rotor. Solving equation (B.3) for $N_a^2 I_a^2$ and substituting into equation (B.4) yields power for a given force,

$$\frac{P}{F} = \frac{\sinh^2(kd)\left(1 + S_+^2 \coth^2(kd)\right)}{\Delta_s \sigma \mu_0 S_+} + \frac{S_+}{\Delta_r \sigma \mu_0}. \tag{B.5}$$

We use this expression to find the power optimal slip speed, S_+, and rotor thickness, Δ_r.

B.2 Power Optimal Slip Speed

We find the power optimal slip speed, $\tilde{S}_+$, by finding the slip speed which minimizes power dissipation, equation (B.5),

$$\frac{\partial}{\partial S_+}\left(\frac{P}{F}\right) = 0. \tag{B.6}$$

After some algebra, we find that the power optimal slip speed, $\tilde{S}_+$, is a function of rotor thickness, Δ_r, stator thickness, Δ_s, and kd,

$$\tilde{S}_+(\Delta_r, \Delta_s, kd) = \pm\left(\frac{\Delta_r \sinh^2(kd)}{\Delta_r \cosh^2(kd) + \Delta_s}\right)^{\frac{1}{2}}. \tag{B.7}$$

B.3 Power Optimal Rotor Thickness

We try to find the power optimal rotor thickness, $\tilde{\Delta}_r$, in the same way by solving,

$$\frac{\partial}{\partial \Delta_r}\left(\frac{P}{F}\right) = 0. \tag{B.8}$$

However, this results in an algebraic equation which is fourth order in Δ_r. Since it is difficult to solve this equation analytically, we solve it numerically by plotting P/F as a function of Δ_r as shown in Figure B-2. Since power optimal slip frequency, $\tilde{S}_+$, is a function of rotor thickness, Δ_r, we calculate $\tilde{S}_+(\Delta_r, \Delta_s, kd)$ for each value of Δ_r.

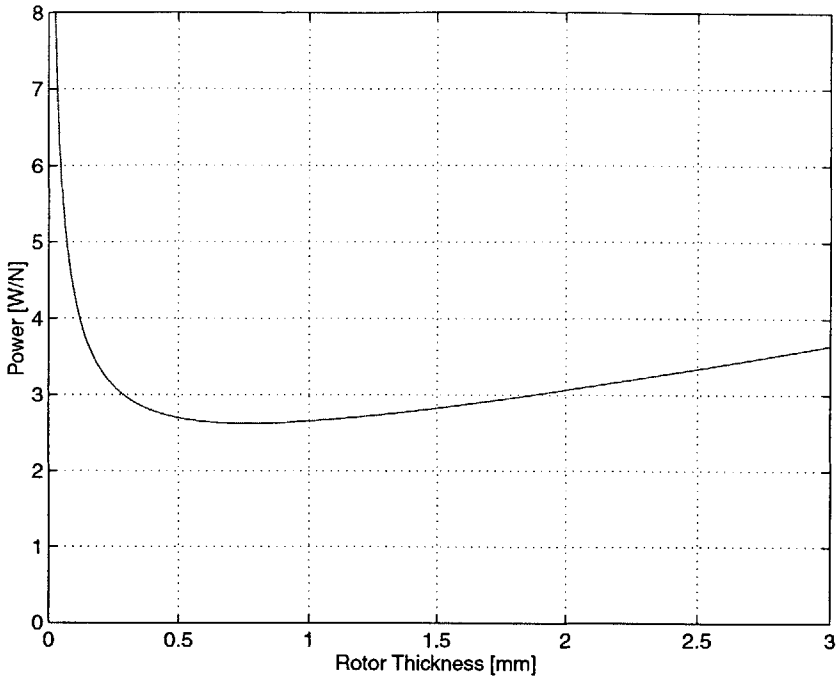

Figure B-2: Induction motor power dissipation per force, P/F, as a function of Rotor Thickness, Δ_r. The power optimal slip, $\tilde{S}_+(\Delta_r, \Delta_s, kd)$, is calculated for each rotor thickness.

Note that the plot is flat near the optimum value so that we have a wide range of near-optimal rotor thicknesses to choose from.

Appendix C

Magnetic Circuit Analysis Approximation of Magnetic Fields

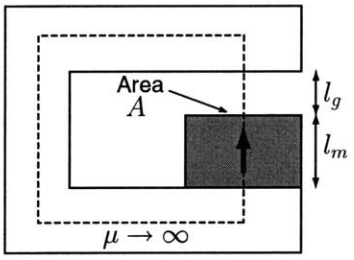

Figure C-1: Magnetic circuit with permanent magnet.

In this appendix we derive that the magnetic field in the air gap of Figure C-1, B_g, is a fraction of the permanent magnet's remanent magnetic field, B_r[1]:

$$B_g = \left(\frac{l_m}{l_m + l_g}\right) B_r. \tag{C.1}$$

Here, l_m and l_g are the thicknesses of the permanent magnet and air gap, respectively.

[1]We sometimes write the remanence, B_r, as $\mu_0 M_0$, where M_0 is the magnetization.

C.1 Assumptions

This approximation makes the following assumptions:

- The magnetic circuit consists of a high permeability, $\mu \rightarrow \infty$, core.
- The air gap, l_g, is small enought that B_g is constant over the air gap and fringing fields are negligible. However, even if l_g is relatively large, this magnetic circuit analysis is still useful since it provides a quick, rough estimate of B_g.
- The permanent magnet has approximately a straight line magnetization B-H characteristic in the second quadrant [18, 43]. This is true of rare earth permanent magnets such as neodymium-iron-boron (NdFeB) magnets and somarium cobalt (SmCo) magnets, but not, for example, Alnico magnets.

C.2 Magnetic Circuit Analysis

From Ampere's Law we know that the integral of the magnetic field intensity, $\mathbf{H}$, around a closed loop is equal to the surface integral of current density through this loop. This surface integral is equal to the number of ampere-turns, Ni, which cross the surface, and we also call this quantity the magnetomotive force, $\mathcal{F}$,

$$\mathcal{F} = Ni = \oint \mathbf{H} \cdot \mathbf{dl}. \tag{C.2}$$

In Figure C-1 we integrate $\mathbf{H}$ around the dashed contour. Since we have no coil in this problem, the magnetomotive force, $\mathcal{F}$, is zero,

$$\mathcal{F} = 0 = H_g l_g + H_m l_m, \tag{C.3}$$

where H_g and H_m are the magnetic field intensities in the air gap and magnet, respectively.

From Gauss's Law for magnetic fields, we know that the magnetic flux, Φ, is

continuous, so

$$\Phi = B_g A = B_m A, \tag{C.4}$$

or

$$B_g = B_m \tag{C.5}$$

since the areas are equal in this example.

The only other relationships we need to solve the problem are the constitutive laws for the air gap and permanent magnet which relate magnetic field, B, to magnetic field intensity, H. For the air gap, we assume a pemeability of μ_0,

$$B_g = \mu_0 H_g. \tag{C.6}$$

For the permanent magnet, we assume a straight line B-H characterisitc in the second quadrant,

$$B_m = B_r + \mu_0 H_m. \tag{C.7}$$

Combining equations (C.3), (C.5), (C.6), and (C.7) and solving for B_g yields the result, equation (C.1),

$$B_g = \left(\frac{l_m}{l_m + l_g} \right) B_r.$$

Appendix D

Mechanical Drawings

D.1 Shaft

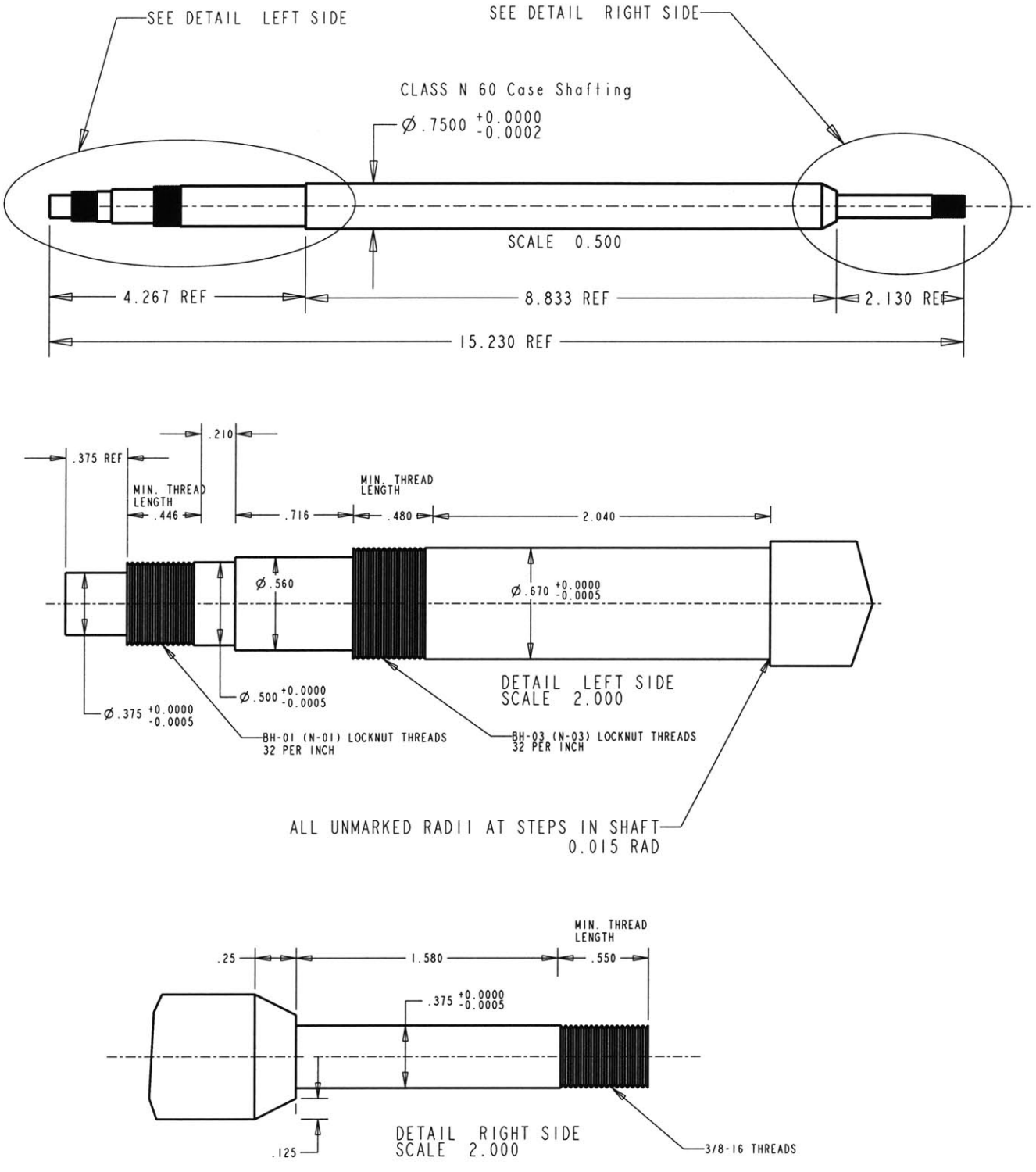

Figure D-1: Shaft mechanical drawing

D.2 Machine Base

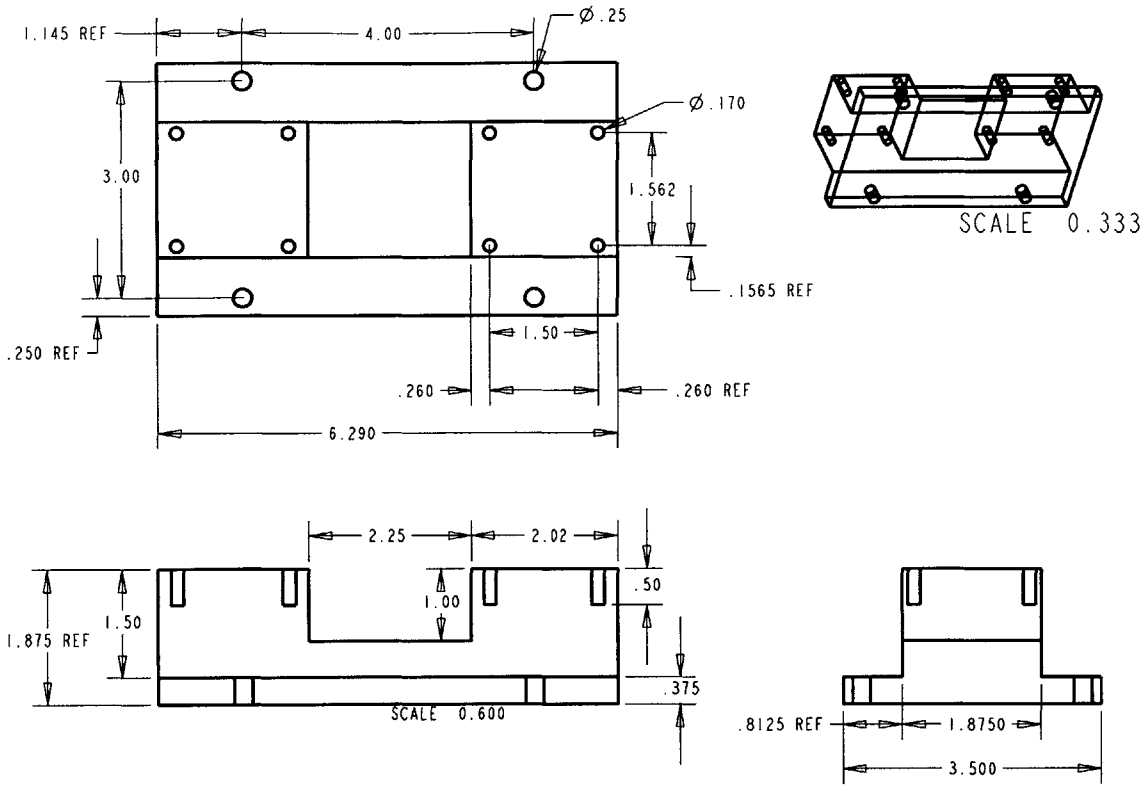

Figure D-2: Machine base mechanical drawing

D.3 Linear Motor Coil

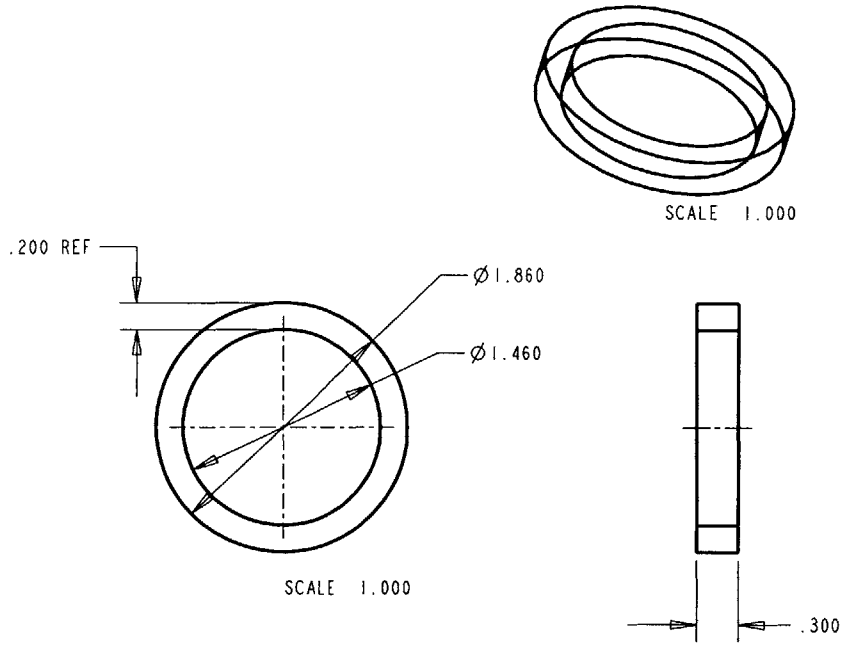

Figure D-3: Linear motor coil mechanical drawing

D.4 Linear Motor Magnet Array

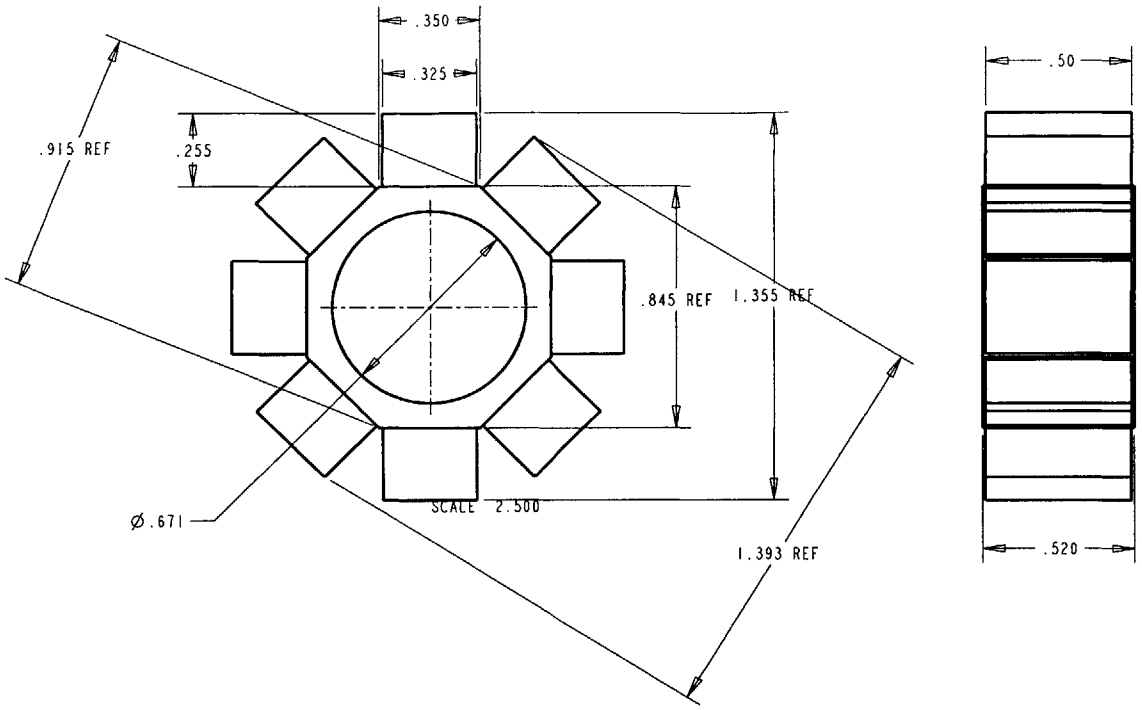

Figure D-4: Linear motor magnet array mechanical drawing

D.5 Linear Motor Stator Backiron

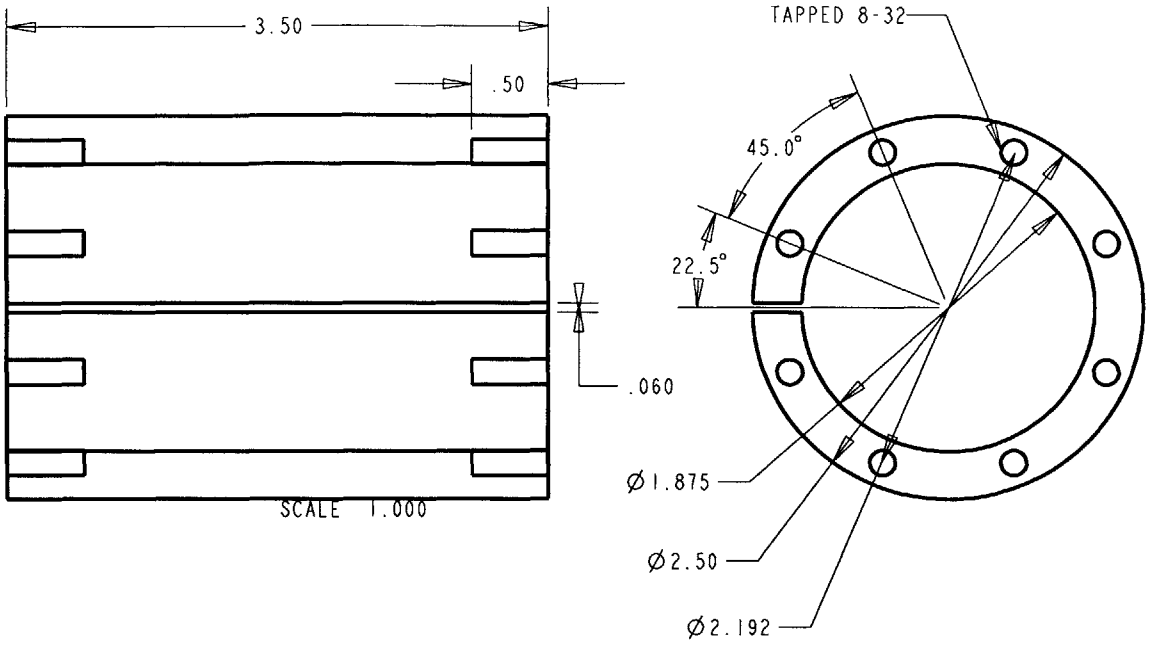

Figure D-5: Linear motor stator back iron mechanical drawing

D.6 Helicoid Mirror

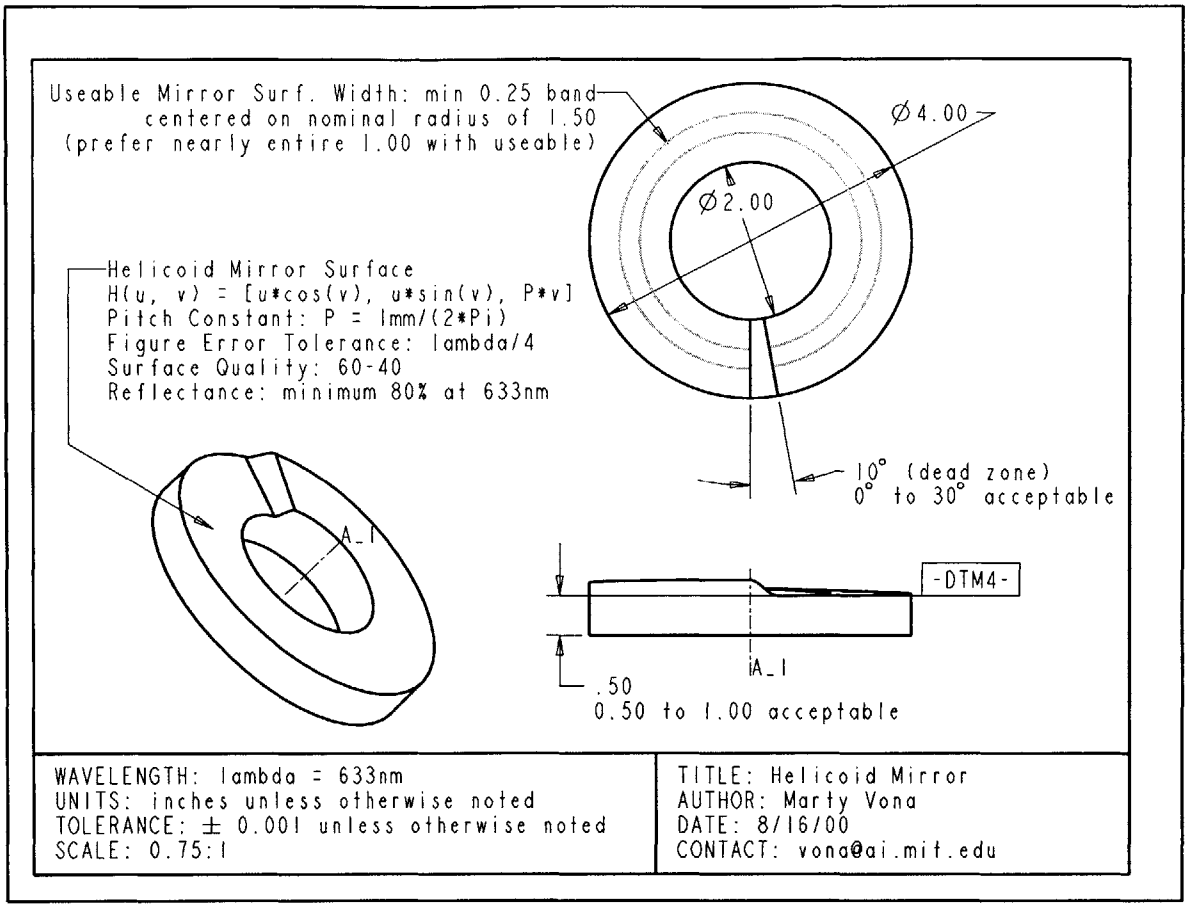

Figure D-6: Helicoid mirror mechanical drawing. Figure drawn by Marsette Vona.

Appendix E

Electrical Schematics

E.1 Motor Phases, Power Amplifiers, and dSPACE Signal Connections

Motor	*Phase*	*Power Amplifier*	*Current Command dSPACE DAC*	*Phase Voltage dSPACE ADC*	*Phase Current dSPACE ADC*
ROTARY	A	0	DACH1	ADC5	ADC2
ROTARY	B	1	DACH3	ADC9	ADC6
ROTARY	C	2	DACH5	ADC13	ADC14
LINEAR	A	6	DACH2	—	—
LINEAR	B	7	DACH4	—	—
LIENAR	C	8	DACH6	—	—

Table E.1: Motor phases, power amplifiers, and dSPACE signal connections.

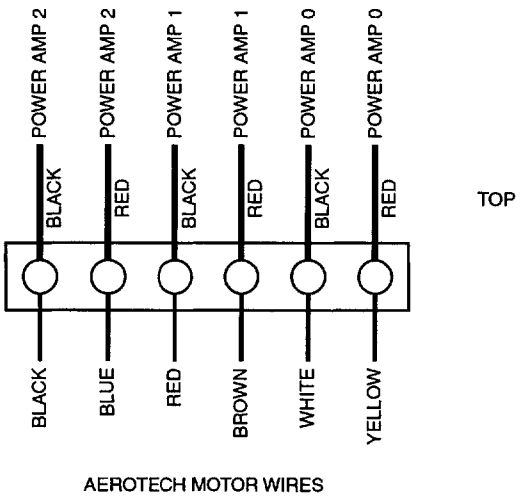

Figure E-1: Rotary motor terminal block connections.

E.2 dSPACE DAC Connector Pinouts

Connection	*dSPACE Signal*	*dSPACE D-SUB Pin*	*Description*
Power Amplifier 0	DACH1	P1B 25	14-bit DAC / 6 μs
	GND	P1B 26	
Power Amplifier 6	DACH2	P1A 25	14-bit DAC / 6 μs
	GND	P1A 26	
Power Amplifier 1	DACH3	P1B 42	14-bit DAC / 6 μs
	GND	P1B 41	
Power Amplifier 7	DACH4	P1A 42	14-bit DAC / 6 μs
	GND	P1A 41	
Power Amplifier 2	DACH5	P1B 10	14-bit DAC / 6 μs
	GND	P1B 09	
Power Amplifier 8	DACH6	P1A 10	14-bit DAC / 6 μs
	GND	P1A 09	

Table E.2: dSPACE DAC connector pinouts.

E.3 dSPACE ADC Connector Pinouts

Connection	*dSPACE Signal*	*dSPACE D-SUB Pin*	*Description*
Generic Input Voltage	ADCH1	P1B 34	16-bit ADC / 4 μs
	GND	P1B 35	
Rotary Motor Phase A Current	ADCH2	P1A 34	16-bit ADC / 4 μs
	GND	P1A 35	
Rotary Motor Temperature	ADCH4	P1A 02	16-bit ADC / 4 μs
	GND	P1A 01	
Rotary Motor Phase A Voltage	ADCH5	P1B 19	16-bit ADC / 4 μs
	GND	P1B 18	
Rotary Motor Phase B Current	ADCH6	P1A 19	16-bit ADC / 4 μs
	GND	P1A 18	
Rotary Motor Phase B Voltage	ADCH9	P1B 04	16-bit ADC / 4 μs
	GND	P1B 03	
Linear Motor Temperature	ADCH10	P1A 04	16-bit ADC / 4 μs
	GND	P1A 03	
Rotary Motor Phase C Voltage	ADCH13	P1B 38	16-bit ADC / 4 μs
	GND	P1B 37	
Rotary Motor Phase C Current	ADCH14	P1A 38	16-bit ADC / 4 μs
	GND	P1A 37	

Table E.3: dSPACE ADC connector pinouts. Note that channels 1, 5, 9, and 13 are measured simultaneously, and then channels 2, 6, 10, and 14 are read next.

E.4 RS-422 Data Link: 4284 DSP to dSPACE

4284 Connection	*dSPACE Signal*	*dSPACE D-SUB Pin*	*Description*
Data	IO 0–7		Digital I/O
$\overline{\text{STB}}$	IO 8		Digital I/O
TCLK1	IO 9		Digital I/O
$\overline{\text{RDY}}$	IO 16		Digital I/O
TCLK0	IO 17		Digital I/O
TCLK1	IO 18		Digital I/O
GND	GND	P2B 01	GND
VCC	VCC1	P2A 33	5V / 500 mA

Table E.4: RS-422 data link between 4284 DSP board and dSPACE. See [70] for more details.

Appendix F

Vendors

Aerotech, Inc.
101 Zeta Drive, Pittsburgh, PA 15238
Telephone: 412-963-7470
Webpage: www.aerotechinc.com
Product: Frameless Rotary Synchronous Motor S-50-52, S-50-86

Anorad Corporation
110 Oser Ave., Hauppauge, NY
Telephone: 516-231-1995
Webpage: www.anorad.com
Product: Rotary-Linear Actuator

Devitt Machinery Co.
4009-G Market Street, Aston, PA 19014
Telephone: 800-749-3135
Webpage: www.moglice.com
Product: Moglice FL/P

Dexter Magnetics
700 Technology Park Drive, Billerica, MA 01821
Telephone: 800-345-4082
Webpage: www.dextermag.com
Product: NdFeB Magnets CM41030-3714

dSPACE Inc.
22260 Haggerty Road, Suite 120, Northville, MI 48167
Telephone: 248-344-0096
Webpage: www.dspaceinc.com
Product: DS1103 PPC Controller Board

Electrical Insulation Suppliers/ Electronic Materials Division
1220-H Kennestone Corners Circle, Marietta, GA 30066
Telephone: 800-289-6015
Product: Nomex-Kapton-Nomex 2-2-2 Laminate

Kaman Industrial Technologies 35 Industrial Parkway, Woburn, MA 01801
Telephone: 781-935-7590
Webpage: www.kamandirect.com
Product: Whittet-Higgins Bearhug Locknuts BH-03, BH-01;
Clamp Collars SC-12A

New Way Bearings, Inc.
4009-I Market Street, Aston, PA 19014
Telephone: 800-394-1046
Webpage: www.newwaybearings.com
Product: S301901 3/4 inch ID Air Bushing

Professional Instruments Company
4601 Highway 7, Minneapolis, MN 55416
Telephone: 952-933-1222
Webpage: www.pico.thomasregister.com
Product: E.P. 750 Air Bearing

Suburban Precision
Telephone: 1-888-647-8665
Product: $3 \times 4 \times 3$ 90° Precision Vee Block

Thomson Industries, Inc.
2 Channel Drive, Port Washington, NY 11050
Telephone: 800-554-8466
Webpage: www.thomsonindustries.com
Product: Class N 60 Case Shafting with Precision Machining

Toys 'N' Stuff
55 Main St., West Lebanon, NH 03784
Telephone: 603-298-6111
Product: Maxi-Cure Cyanoacrylate

Whittet-Higgins Co.
33 Higginson Avenue, Central Falls, RI 02863
Telephone: 401-728-0700
Webpage: www.whittet-higgins.com
Product: Bearhug Locknuts BH-03, BH-01; Clamp Collars SC-12A
Distributor: Kaman Industrial Technologies (see separate listing)

Wirewinders
151 Mont Vernon Rd., Milford, NH 03055
Telephone: 603-673-1763
Product: Linear Motor Coils

Bibliography

[1] Sensorless drives improve spindles. *American Machinist*, page 15, April 2001.

[2] Aerotech, Inc., 101 Zeta Drive, Pittsburgh, PA, 15238. *S-Series Frameless Motor User's Manual*, August 2000.

[3] American Society of Mechanical Engineers, New York. *Methods for Performance Evaluation of Computer Numerically Controlled Machining Centers*, March 1993. ASME B5.54-1992.

[4] Analog Devices. *Reference Frame Conversions with the ADMC401*, June 1999. Application Note: AN401-11.

[5] Michael Tekletsion Berhan. Implementation of a halbach array in a tubular linear motor. Master's thesis, Mechanical Engineering Dept., Massachusetts Institute of Technology, June 1996.

[6] C. R. Boer, L. Molinari-Tosatti, and K. S. Smith, editors. *Parallel Kinematic Machines.* Springer-Verlag, New York, 1999.

[7] Boston Digital Corporation, Granite Park, Milford, MA 01757. *BostoMatic 505.*

[8] Anwar Chitayat. Rotary-linear actuator. U. S. Pat. No. 5,982,053, Anorad Corporation, 1999.

[9] B. K. Choi, J. W. Park, and C. S. Jun. Cutter-location data optimization in 5-axis machining. *Computer-Aided Design*, 25(6):377–386, June 1993.

[10] M. J. Corley and R. D. Lorenz. Rotor position and velocity estimation for a permanent magnet synchronous machine at standstill and high speeds. *IEEE Transactions on Industry Applications*, 34(4):784–789, July 1998.

[11] Jame B. Dabney and Thomas L. Harman. *Mastering Simulink 2.* Prentice Hall, Upper Saddle River, NJ, 1998.

[12] Paul de Wit, Johannes van Dijk, Tim Blomer, and Peter Rutgers. Mechatronic design of a z-ϕ induction actuator. In *1997 Eighth International Conference on Electrical Machines and Drives*, pages 279–283, Stevenage, England, 1997.

[13] Deckel Maho Gildemeister America Inc., 13509 South Point Blvd., Charlotte, NC 28273. *DMC U Series, DMU-P Series.*

[14] Drew Devitt. History of air bearings. *PT Design Motion Systems*, April 1999.

[15] Richard C. Dorf. *Modern Control Systems.* Addison-Wesley Publishing Company, New York, 1995.

[16] Gershon Elber. Freeform surface region optimization for 3-axis and 5-axis milling. *Computer-Aided Design*, 27(6):465–470, June 1995.

[17] Gershon Elber and Elaine Cohen. Toolpath generation for freeform surface models. *Computer-Aided Design*, 26(6):490–496, June 1994.

[18] A. E. Fitzgerald, Jr. Charles Kingsley, and Stephen D. Umans. *Electric Machinery.* McGraw-Hill, Inc., New York, 1990.

[19] Gene F. Franklin, J. David Powell, and Michael Workman. *Digital Control of Dynamic Systems.* Addison-Wesley, Reading, Massachusetts, 1998.

[20] Chris French and Paul Acarnley. Control of permanent magnet motor drives using a new position estimation technique. *IEEE Transactions on Industry Applications*, 32(5):1089–1097, September 1996.

[21] L. A. Gould, W. R. Markey, J. K. Roberge, and D. L. Trumper. Control systems theory. Technical report, Massachusetts Institute of Technology, 1997.

[22] J. P. Den Hartog. *Mechanical Vibrations.* Dover Publications, Inc., New York, 1985.

[23] Hermann A. Haus and James R. Melcher. *Electromagnetic Fields and Energy.* Prentice-Hall, Englewood Cliffs, New Jersey, 1989.

[24] Eugene Hecht. *Optics.* Addison Wesley Longman, Inc., New York, 1998.

[25] André Heck. *Introduction to Maple.* Springer, New York, 1996.

[26] Hermle Machine Co., 9600 S. Franklin Drive, Franklin, WI 53132. *C600U, C800U, C1200U.*

[27] Ingersoll Milling Machine Company, 707 Fulton Ave., Rockford, IL 61103. *High Velocity Profiler, High Velocity Gantry.*

[28] JOBS, Inc., 1397 Piedmont Suite 100, Troy, MI 48083. *Jo 'Tech, Jo 'Mach.*

[29] Lawrence A. Jones and Jeffrey H. Lang. A state observer for the permanent-magnet synchronous motor. *IEEE Transactions on Industrial Electronics*, 36(3):374–382, August 1989.

[30] Lawrence Anthony Jones. A state observer for the permanent magnet motor. Master's thesis, Electrical Engineering and Computer Science Dept., Massachusetts Institute of Technology, May 1988.

[31] Edward Kelby, Jr. and Alan G. Wallskog. Rotary & linear magnetomotive positioning mechanism. U. S. Pat. No. 3,745,433, Teletype Corporation, 1971.

[32] Taejung Kim. *Time-Optimal CNC Tool Paths: A Mathematical Model of Machining.* PhD thesis, Mechanical Engineering Dept., Massachusetts Institute of Technology, February 2001.

[33] Taejung Kim and Sanjay E. Sarma. Toolpath generation along directions of maximum kinematic performance; a first cut at machine-optimal paths. Accepted by *Computer Aided Design*, 2001.

[34] Won-jong Kim. *High-Precision Planar Magnetic Levitation.* PhD thesis, Electrical Engineering and Computer Science Dept., Massachusetts Institute of Technology, June 1997.

[35] James L. Kirtley Jr. *6.685 Electric Machinery Lecture Notes.* Technical report, Massachusetts Institute of Technology, 2000.

[36] Wojciech B. Kosmowski. High speed drilling spindle with reciprocating ceramic shaft and double-gripping centrifugal chuck. U. S. Pat. No. 5,997,223, Electro-Scientific Industries, 1999.

[37] Markku S. Kotilainen. *Design and Manufacturing of Modular Self-Compensating Hydrostatic Journal Bearings.* PhD thesis, Mechanical Engineering Dept., Massachusetts Institute of Technology, May 2000.

[38] Markku S. Kotilainen and Alexander H. Slocum. Manufacturing of cast monolithic hydrostatic journal bearings. *Precision Engineering*, 25(3):235–244, July 2001.

[39] Jeffrey H. Lang, George C. Verghese, and Marija D. Ilic. *Electrical Machine Systems: Dynamics, Estimation, and Control.* Technical report, Massachusetts Institute of Technology, 2000.

[40] Werner Leonhard. *Control of Electrical Drives.* Springer, New York, 1997.

[41] Michael Kevin Liebman. Thermally efficient linear motor analysis & design. Master's thesis, Mechanical Engineering Dept., Massachusetts Institute of Technology, February 1998.

[42] Katie A. Lilienkamp and David L. Trumper. Dynamic signal analyzer for dspace. In *Proceedings of the dSPACE User's Conference*, May 2000.

[43] James D. Livingston. *Driving Force: The Natural Magic of Magnets.* Harvard University Press, Cambridge, MA, 1996.

[44] Robert D. Lorenz. Advances in electric drive control. In *Electric Machines and Drives*, pages 9–16, 1999.

[45] Makino Inc., 7680 Innovation Way, Mason, OH 45040. *V55-5XA, MC-5XA, MC-5XB.*

[46] The Mathworks Inc. *Stateflow User's Guide*, September 2000. http://www.mathworks.com.

[47] Mazak Corporation, 8025 Production Drive, Florence, KY 41042. *Mazatech H-630 5X, Mazatech V-815 5X.*

[48] James R. Melcher. *Continuum Electromechanics.* The MIT Press, Cambridge, Massachusetts, 1981.

[49] Mikron Corp., 600 Pepper Street USA-Monroe, CT 06468. *UCP710.*

[50] Mori Seiki U.S.A., Inc., 9145 Currency Street, Irving, Texas 75063. *M-400C1.*

[51] K. Morishige, Y. Takeuchi, and K. Kase. Tool path generation using c-space for 5-axis control machining. *Journal of Manufacturing Science and Engineering*, 121:144–149, February 1999.

[52] J. F. Moynihan, P. Kettle, and A. Murray. High performance control of ac servomotors using an integrated dsp. *Intelligent Motion*, pages 213–222, May 1998.

[53] MTS Systems Corp., Automation Division, Eden Prairie, MN. *SpindleBlok, DriveBlok, IndexBlock.*

[54] Norman S. Nise. *Control Systems Engineering.* Addison-Wesley Publishing Company, New York, 1995.

[55] John Ofori-Tenkorang. *Permanent-Magnet Synchronous Motors and Associated Power Electronics for Direct-Drive Vehicle Propulsion.* PhD thesis, Electrical Engineering and Computer Science Dept., Massachusetts Institute of Technology, September 1996.

[56] Alan V. Oppenheim and Alan S. Willsky. *Signals & Systems.* Prentice Hall, Upper Saddle River, NJ, 1997.

[57] James K. Roberge. *Operational Amplifiers, Theory and Practice.* John Wiley & Sons, Inc., New York, 1975.

[58] Stuart C. Salmon. *Modern Grinding Process Technology.* McGraw-Hill, Inc., New York, 1992.

[59] Raymond B. Sepe. *Adaptive Control of the Permanent-Magnet Synchronous Motor.* PhD thesis, Electrical Engineering and Computer Science Dept., Massachusetts Institute of Technology, September 1990.

[60] Raymond B. Sepe and Jeffrey H. Lang. Real-time observer-based (adaptive) control of a permanent-magnet synchronous motor without mechanical sensors. *IEEE Transactions on Industry Applications*, 28(6):1345–1352, November 1992.

[61] S. T. Smith and D. G. Chetwynd. *Foundations of Ultraprecision Mechanism Design.* Gordon and Breach Science Publishers, Canda, 1997.

[62] Suk-Hwan Suh and Jung-Jae Lee. Five-axis part machining with three-axis cnc machine and indexing table. *Transactions of the ASME, Journal of Manufacturing Science and Engineering*, 120(22):120–128, February 1988.

[63] Texas Instruments Europe. *Field Orientated Control of 3-Phase AC-Motors*, February 1998. Literature Number: BPRA073.

[64] Jiri Tlusty, John Ziegert, and Shannon Ridgeway. Fundamental comparison of the use of serial and parallel kinematics for machine tools. *Annals of CIRP*, 48(1):351–356, 1999.

[65] Toshiba Machine Co., America, 755 Greenleaf Ave., Elk Grove Village, IL 60007. *BMC 1000 (5), MPF-5A.*

[66] David L. Trumper, Won-jong Kim, and Mark E. Williams. Design and analysis framework for linear permanent-magnet machines. *IEEE Transactions on Industry Applications*, 32(2):371–379, March/April 1996.

[67] David L. Trumper, Mark E. Williams, and Tiep H. Nguyen. Magnet arrays for synchronous machines. In *Proceedings of the IEEE IAS 28th Annual Meeting*, pages 216–223, Toronto, Canada, October 1993.

[68] Johannes M. A. M. Van Geel, Johan C. Compter, and Volker Kessler. Electromagnetic actuator having a cylindrical translation coil and a toroidal rotation coil, actuator unit comprising the actuator and a measurement system, and machine comprising the actuator or the actuator unit. U. S. Pat. No. 5,600,189, U. S. Philips Corporation, 1997.

[69] G. W. Vickers and K. W. Quan. Ball-mills versus end-mills for curved surface machining. *Transactions of ASME, Journal of Engineering for Industry*, 111(22):22–26, February 1989.

[70] Marsette Arthur Vona. Metrology techniques for compound rotary-linear motion. Master's thesis, Electrical Engineering and Computer Science Dept., Massachusetts Institute of Technology, June 2001.

[71] A. Warkentin, S. Bedi, and F. Ismail. Five-axis milling of spherical surfaces. *International Journal of Machine Tools Manufacture*, 36(2):229–243, 1996.

[72] Kevin L. Wasson. *Hydrostatic Machine Tool Spindles.* PhD thesis, Mechanical Engineering Dept., Massachusetts Institute of Technology, May 1996.

[73] Waterloo Maple Inc. *Maple V Release 4*, 1996.

[74] Ming-chih Weng. *Magnetic Suspension and Vibration Control of Flexible Structures for Non-contact Processing.* PhD thesis, Mechanical Engineering Dept., Massachusetts Institute of Technology, February 2000.

[75] Mark E. Williams. *Precision Six Degree of Freedom Magnetically-Levitated Photolithography Stage.* PhD thesis, Mechanical Engineering Dept., Massachusetts Institute of Technology, October 1997.

[76] Herbert Woodson and James Melcher. *Electromechanical Dynamics.* Krieger Publishing Company, Malabar, Florida, 1990.

[77] Amnon Yariv. *Optical Electronics.* Saunders College Publishing, A Division of Holt, Rinehart and Winston, Inc., Chicago, 1991.

[78] Yasda Precision America Corp., 751 Landmeier Road, Elk Grove Village, IL 60007. *YBM-700NTT, YBM-900NTT, H30i.*